

# AGARD

ADVISORY GROUP FOR AEROSPACE RESEARCH & DEVELOPMENT

7 RUE ANCELLE, 92200 NEUILLY-SUR-SEINE, FRANCE

**DISTRIBUTION STATEMENT A**

Approved for public release  
Distribution Unlimited

**AGARD CONFERENCE PROCEEDINGS 589**

## **Tribology for Aerospace Systems**

(la Tribologie pour les systèmes aérospatiaux)

*Papers presented at the 82nd Meeting of the AGARD Structures and Materials Panel,  
held in Sesimbra, Portugal, 6-7 May 1996.*

19961216 041



**NORTH ATLANTIC TREATY ORGANIZATION**

Published October 1996

*Distribution and Availability on Back Cover*

# DISCLAIMER NOTICE



**THIS DOCUMENT IS BEST  
QUALITY AVAILABLE. THE  
COPY FURNISHED TO DTIC  
CONTAINED A SIGNIFICANT  
NUMBER OF PAGES WHICH DO  
NOT REPRODUCE LEGIBLY.**

# AGARD

ADVISORY GROUP FOR AEROSPACE RESEARCH & DEVELOPMENT

7 RUE ANCELLE, 92200 NEUILLY-SUR-SEINE, FRANCE

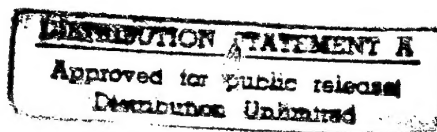
---

## AGARD CONFERENCE PROCEEDINGS 589

### Tribology for Aerospace Systems

(la Tribologie pour les systèmes aérospatiaux)

Papers presented at the 82nd Meeting of the AGARD Structures and Materials Panel,  
held in Sesimbra, Portugal, 6-7 May 1996.



DTIC QUALITY INSPECTED 2



North Atlantic Treaty Organization  
*Organisation du Traité de l'Atlantique Nord*

---

# The Mission of AGARD

According to its Charter, the mission of AGARD is to bring together the leading personalities of the NATO nations in the fields of science and technology relating to aerospace for the following purposes:

- Recommending effective ways for the member nations to use their research and development capabilities for the common benefit of the NATO community;
- Providing scientific and technical advice and assistance to the Military Committee in the field of aerospace research and development (with particular regard to its military application);
- Continuously stimulating advances in the aerospace sciences relevant to strengthening the common defence posture;
- Improving the co-operation among member nations in aerospace research and development;
- Exchange of scientific and technical information;
- Providing assistance to member nations for the purpose of increasing their scientific and technical potential;
- Rendering scientific and technical assistance, as requested, to other NATO bodies and to member nations in connection with research and development problems in the aerospace field.

The highest authority within AGARD is the National Delegates Board consisting of officially appointed senior representatives from each member nation. The mission of AGARD is carried out through the Panels which are composed of experts appointed by the National Delegates, the Consultant and Exchange Programme and the Aerospace Applications Studies Programme. The results of AGARD work are reported to the member nations and the NATO Authorities through the AGARD series of publications of which this is one.

Participation in AGARD activities is by invitation only and is normally limited to citizens of the NATO nations.

The content of this publication has been reproduced  
directly from material supplied by AGARD or the authors.

Published October 1996

Copyright © AGARD 1996  
All Rights Reserved

ISBN 92-836-0029-0



*Printed by Canada Communication Group  
45 Sacré-Cœur Blvd., Hull (Québec), Canada K1A 0S7*



# **Tribology for Aerospace Systems**

## **(AGARD CP-589)**

### **Executive Summary**

Tribology deals with the design, friction, wear, and lubrication of interacting surfaces in relative motion, as bearings or gears. This definition sheds light on problems that tribological phenomena may cause in NATO's armaments, for example, systems failures and downtime repairs, supply and resupply with their costs in the permanent and/or temporary loss of trained personnel, and reoccurring materials and labor costs. In general solutions to these problems include redesign of components, replacement of materials with harder and/or lower friction materials, and improved lubricants.

The objective of this AGARD Specialists' Meeting on Tribology for Aerospace Systems was twofold:

- discuss the technology problems by having a meeting among specialists of new technologies (such as coatings, lubrication) and people dealing with practical problems in NATO systems (airframe, engines, etc...);
- improve the knowledge of Tribology by engineers designing or maintaining NATO systems.

The scope of the Meeting was broader than aerospace because papers on reciprocating engines in land based systems were also included. It must be realized that tribological phenomena such as friction and wear are problems that will never be completely overcome by technology but can be put in "remission" through some of the approaches outlined here.

Rain and dust erosion were not included in the Terms of Reference and should be the subject of a future AGARD activity.

# **La Tribologie pour les systèmes aérospatiaux**

## **(AGARD CP-589)**

### **Synthèse**

La tribologie concerne la conception, l'interaction, l'usure par frottement et la lubrification des surfaces en mouvement relatif, telles que les galets et les engrenages. Cette définition permet d'appréhender plus clairement les problèmes qui peuvent être posés par les phénomènes tribologiques au niveau des systèmes d'armes de l'OTAN, comme par exemple, les pannes des systèmes, les temps morts demandés pour les réparations, l'approvisionnement et le réapprovisionnement avec les coûts occasionnés par la perte provisoire et/ou permanente du personnel qualifié, ainsi que les coûts récurrents des matériaux et de la main d'œuvre. En général, les solutions proposées par rapport à ces problèmes comprennent la redéfinition des composants, le remplacement des matériaux usuels par des matériaux plus durs et/ou à coefficient de frottement réduit, et l'emploi de lubrifiants améliorés.

L'objectif de cette réunion de spécialistes AGARD sur la tribologie pour systèmes aérospatiaux était double, à savoir:

- discuter des problèmes technologiques lors d'une réunion rassemblant, d'une part, les spécialistes des nouvelles technologies (telles que les revêtements, la lubrification...), et, d'autre part, ceux qui sont appelés à traiter les problèmes d'ordre pratique posés par les systèmes militaires de l'OTAN (cellule, moteur, etc...);
- élargir les connaissances en tribologie des ingénieurs responsables de la conception et de la maintenance des systèmes militaires de l'OTAN.

Les sujets examinés lors de la réunion ont débordé le domaine purement aérospatial puisque des présentations sur les moteurs semblables des systèmes terrestres ont été données. Force est de constater que si certains phénomènes tribologiques tels que l'usure par le frottement ne pourront jamais être totalement résolus technologiquement, ils pourraient néanmoins être "mis en veilleuse" par l'adoption de certaines approches décrites ici.

L'érosion par la pluie et la poussière, qui n'a pas été incluse dans les termes de référence de la réunion, mériterait de faire l'objet d'une activité future de l'AGARD.

# Contents

	<b>Page</b>
<b>Executive Summary</b>	<b>iii</b>
<b>Synthèse</b>	<b>iv</b>
<b>Preface/Préface</b>	<b>vii</b>
<b>Structures and Materials Panel</b>	<b>viii</b>
<b>Technical Evaluation Report</b> by D.J. Viechnicki	<b>T</b>
	<b>Reference</b>
<b>SESSION I: NEW TECHNOLOGIES</b>	
<b>Paper not available</b>	<b>1</b>
<b>Tribological Behaviour of Silicon Nitride-based Ceramics</b> by J.R. Gomes, A.S. Miranda, R.F. Silva and J.M. Vieira	<b>2</b>
<b>Advanced Solid Lubricant Coatings for Aerospace Systems</b> by J.S. Zabinski, S.V. Prasad and N.T. McDevitt	<b>3</b>
<b>Advanced Hard Coatings and Wear Resistant Materials for Aerospace Systems</b> by J.S. Zabinski, A.A. Voevodin and M.A. Capano	<b>4</b>
<b>An Investigation on Surface Treatments for Improving the Fretting Fatigue Resistance of Titanium Alloys</b> by A.K. Koul, L. Xue, W. Wallace, M. Bibby, S. Chakravarty, R.G. Andrews and P.C. Patnaik	<b>5</b>
<b>Thin Film Lubrication of Non-Smooth Surfaces</b> by B. Jacobson	<b>6</b>
<b>Machining and Slip-Rolling of Ceramics</b> by M. Woydt and U. Effner	<b>7</b>
<b>Sputter-Deposited Lubricant Thin Films Operating at Elevated Temperatures in Air</b> by C. Zimmermann and Y. Pauleau	<b>8</b>
<b>SESSION II: APPLICATIONS: GEARS AND BEARINGS</b>	
<b>Paper 9 Withdrawn</b>	
<b>Tribological Problems in Spacecrafts</b> by A. Borrien	<b>10</b>
<b>Metallic and Non-Metallic Protection Systems for Reduction of Tribologic Influences in Several Areas on Tornado Aircraft</b> by C.D. Hamm and K. Blomeier	<b>11</b>

<b>Improving Solid Lubricated Aerospace Bearings</b>	<b>12</b>
by B. Mortimer and S. Mason	
<b>Analysis of Fretting and Fretting Corrosion in Airframe Riveted Connections</b>	<b>13</b>
by K. Iyer, M. Xue, P.C. Bastias, C.A. Rubin and G.T. Hahn	
<b>SESSION III: APPLICATIONS ENGINES</b>	
<b>EHD Analysis of a Roller/Inner Ring Contact in a Jet Engine Roller Bearing</b>	<b>14</b>
by J. Seabra and A. Campos	
<b>Rolling Contact Testing of Vapor Phase Lubricants</b>	<b>15</b>
by N.H. Forster	
<b>La fiabilité des roulements des petites et moyennes turbines de plus en plus dépendante de la tribologie</b>	<b>16</b>
by G. Paty and B. Cheftel	
<b>Airseals for Advanced Military Jet Engines</b>	<b>17</b>
by T.J. Uihlein	
<b>High Temperature Tribology for Future Diesel Engines</b>	<b>18</b>
by W. Bryzik and R. Kamo	
<b>Tribological Assessments and Concepts for an Oilfree Internal Combustion Engine</b>	<b>19</b>
by M. Woydt	

## Preface

The fretting and wear of hinges, tracks, bearings, gearboxes in airframes and engines is a constant problem for aircraft or other defense systems, as it causes breakages and jamming, necessitating costly in-service inspections and replacement of parts.

As a result, there is ample room for improvement both for in-service systems and new systems being developed.

The meeting was divided into three sessions:

- one session on new technologies such as coatings, new materials, lubrication;
- one session on practical applications for airframes and their mechanical systems;
- one session on practical applications for engines.

The meeting closed with a round table discussion.

D. Chaumette  
Chairman Sub-Committee  
on Tribology for Aerospace Systems

## Préface

L'usure par frottement et contact des articulations, des rails, des galets, des supports et des engrenages dans les cellules aéronautiques et dans les moteurs est un problème constant pour les aéronefs et les autres systèmes de défense, car elle induit des ruptures et des grippages qui nécessitent des inspections coûteuses en service et des remplacements de pièces.

De ce fait, il existe de sérieuses possibilités d'amélioration aussi bien pour les systèmes en service que pour les nouveaux systèmes en cours de développement.

La conférence est divisée en trois sessions:

- Une session sur les nouvelles technologies telles que les revêtements, les matériaux, la lubrification;
- Une session sur les applications pratiques dans les cellules d'aéronefs et leurs systèmes mécaniques;
- Une session sur les applications pratiques aux moteurs.

La conférence s'est terminée par une discussion - table ronde.

D. Chaumette  
Président du Sous-Comité  
La tribologie pour les systèmes aérospatiaux

# Structures and Materials Panel

**Chairman:** Prof. O. Sensburg  
Chief Engineer  
Daimler Benz Aerospace  
Militaerflugzeuge LM2  
Postfach 80 11 60  
81663 Munich  
Germany

**Deputy Chairman:** Prof. S. Paipetis  
Prof. of Applied Mechanics  
School of Engineering  
Dept. of Mechanical Engineering  
University of Patras  
26110 Patras  
Greece

## SUB-COMMITTEE MEMBERS

**Chairman:** Mr. D. Chaumette  
Chef des Etudes Générales  
Direction Technique Aéronef  
Dassault Aviation  
78, Quai Marcel Dassault  
92214 Saint-Cloud  
France

<b>Members:</b>	P. Armando	—	FR	C.A. Moura Branco	—	PO
	E. Campo	—	IT	S. Paipetis	—	GR
	M. Curbillon	—	FR	C. Perron	—	CA
	B. Eksi	—	TU	A. Rodriguez Villa	—	SP
	C.R. Gostelow	—	UK	O. Sensburg	—	GE
	W. Van der Hoeven	—	NE	R. Servent	—	SP
	R. Kochendörfer	—	GE	E.A. Starke	—	US
	A. Lasalmonie	—	FR	D. Viechnicki	—	US

## PANEL EXECUTIVE

Dr Jose M. CARBALLAL, SP

**Mail from Europe:**  
AGARD-OTAN  
7, rue Ancelle  
92200 Neuilly-sur-Seine  
France

**Mail from US and Canada:**  
AGARD-NATO/SMP  
PSC 116  
APO AE 09777

Tel: 33 (1) 4738 5790 & 5792  
Telefax: 33 (1) 4738 5799  
Telex: 610176F

## RECORDER'S REPORT OF THE SPECIALISTS' MEETING ON TRIBOLOGY FOR AEROSPACE SYSTEMS

by

Dr. Dennis J. Viechnicki  
US Army Research Laboratory/Materials Directorate  
Aberdeen Proving Ground, Maryland 21005-5069, USA

### I. INTRODUCTION

Tribology is defined as a study that deals with the design, friction, wear, and lubrication of interacting surfaces in relative motion, as in bearings or gears. The definition sheds light on the problems that tribological phenomena will cause in NATO's fighting forces, for example systems failures and downtime, repairs, supply and resupply with their costs in the permanent and/or temporary loss of trained personnel, and reoccurring materials and labor costs. In general solutions to these problems include redesign of components, replacement of materials with harder and/or lower friction materials, and improved lubricants, and these types of solutions have been covered in this AGARD Specialist's Meeting on Tribology for Aerospace Systems. The scope of the meeting was broader than aerospace because two papers on reciprocating engines in land based systems were included. It must also be realized that tribological phenomena such as friction and wear are problems that will never be completely overcome by technology but rather ones that can be put in "remission" through some of the approaches outlined here.

The meeting was divided into three sessions:

New technologies to reduce the deleterious effects of friction and wear through use of new materials, lubricants, coatings, including innovative processing techniques, and machining methods for new materials, and

Two applications oriented sessions,

Friction and wear problems and solutions in gears and bearings in space vehicles and aircraft, and riveted airframe connections, and

Friction and wear problems and solutions in engines including engine bearings in large, medium, and small gas turbines, lubrication of gas turbines, jet engine airseals, and wear and lubrication in reciprocating engines.

After reading the papers and listening to the presentations as Meeting Recorder and because of my background in ceramics and hard materials, I felt it would

better reflect the tenor of the meeting if I structured my report according to the following technical areas:

New materials, coatings, processes, machining,

Lubricants,

Aerospace applications,

New reciprocating engine concepts, and

Roundtable discussion.

### II. NEW MATERIALS, COATINGS, PROCESSES, AND MACHINING

Papers [1, 2, 4, 5, 7, 8, and 11] fall in this technical area. [1] was an excellent paper to start the meeting since it dealt with the basic aspects of tribology of thin film lubricants and of fretting and pointed out future goals for tribological research. Fretting is the repeated contact of two surfaces at low amplitude and depends upon the mechanical system, the materials and their surfaces, and the environment in which the fretting occurs. Failure modes in materials and means of characterizing them were discussed. Tribology research is studying materials at the nano- and atomic scales and should lead to future materials with very low coefficients of friction in severe environments exhibiting almost no wear. [2] discussed the tribological behavior of a new wear resistant ceramic, hot pressed silicon nitride containing silica, ceria, and aluminum nitride additions, in contact with annealed tool steel or gray cast iron. In unlubricated conditions the wear resistance of the ceramic measured with a pin-on-disk tester is controlled by the build-up of a layer of wear debris on the ceramic. Relative humidity, sliding speed, and temperature of the materials also influence wear rates before the layer of wear debris is completely formed. After it is completely formed, they play a lesser role. Without the layer of wear debris, the ceramic wears more against the rough gray cast iron than against the annealed tool steel. [4] Increasing demands placed on aerospace systems require new harder wear resistant coating materials such as titanium nitride, titanium carbide, titanium carbonitride, and diamond-like coatings. New processing techniques are required to produce defect-free coatings.

Pulsed laser deposition and magnetron sputtering pulsed laser deposition are used to produce hard, chemically resistant layers of these materials with low coefficients of friction. [5] A variety of surface treatments were used to improve the fretting fatigue life of two titanium alloys, Ti-6Al-4V and Ti-17. These included ultrasonic shot peening, coatings of copper/nickel/indium and/or molybdenum disulfide, carbon and nitrogen ion implantation, and laser shock treatment. The ultrasonic shot peening demonstrates the most dramatic improvement of fretting fatigue life. These improvements are diminished when used in conjunction with the coatings or ion implantation, a case of leave well enough alone. The machining and slip rolling of ceramic is discussed in [7]. Machining can constitute between 15 and 80% of the cost of a finished ceramic component. Hot isostatically pressed silicon nitride, silicon carbide, and silicon nitride - titanium nitride were studied with a twin disk wear tester. Wear coefficients for these materials are low and dependent upon surface geometry, ambient media, surface roughness, the machining process and material removal rate. The author argues that expensive finishing costs may be reduced by eliminating the final polishing of the ceramics if finely ground ceramics are given a certain amount of time for running-in wear. [11] Dry bearings found in aircraft and rotorcraft consist of plastic liners mated against steel counterfaces. These were simulated by a tri-pin on disk tester to study the effects of surface roughness of the steel and some harder counterface materials on liner wear. For cobalt bounded tungsten carbide and alumina, hard smooth surfaces decreased liner wear. Physical vapor deposited titanium nitride physical vapor on steel does not decrease liner wear because it could not be made smooth enough. The presence of water greatly increases liner wear.

General conclusions that can be drawn from this group of papers show the importance of surface roughness and hardness, and the influence of water on increasing wear. This is especially important for while we have control of the surface roughness and hardness of wear surfaces in combat aircraft, rotorcraft, and ground vehicles, we have little control of the relative humidity and the amount of water that these combat systems will encounter above or on the battlefield.

### III. LUBRICANTS

Papers [1, 3, 6, 8, and 14] stress high temperature lubricant applications, modeling, and experimental studies. [1] discussed some basic aspects of the tribology of thin film lubricants such as the friction and energy dissipation on an atomic scale as well as the type of chemical bonding and pointed out that the future will bring universal surface treatments that can be applied to nearly any material to give it, for all intents and purposes, an infinite lifetime. [3] dealt with the problem that current lubricants cannot span the operating temperature range and lifetime requirements that will be needed in future aerospace systems. Two approaches were taken. One relied on the phenomenon that

normally brittle oxides such as zinc oxide, exhibit plasticity and are very lubricious when they are in the form of nano-phase thin films made by pulsed laser deposition. While the principal was demonstrated, the difficulty remains of preventing grain growth in these materials at operating temperatures. The second approach was that of adaptive lubricants. Here the solid lubricants undergo chemical reactions under wear conditions at elevated temperatures, and produce reaction products that are solid lubricants stable at elevated temperatures. Thus nano-phase zinc oxide reacts with molybdenum disulfide to produce zinc molybdate. Stacks of different adaptive lubricants could be laid down by physical laser deposition which could result in a solid lubricant system capable of operating over 1000C temperature range. The behavior of thin film lubricants, both oils and greases, on non-smooth surfaces is the subject of [6]. The ability of a lubricant to lubricate a contact between two surfaces is calculated by the ratio of the calculated film thickness and the combined surface roughness. Liquid lubricants and greases trapped by the asperities of rough surfaces are subjected to very high pressures, high enough to change the nature of the liquid from a Newtonian to a non-Newtonian or glassy state, which effects its ability to keep the two surfaces separate. If the surfaces come in contact, plastic deformation, smoothing of the rough surfaces and scratching can occur, and the aforementioned ratio is not a satisfactory way to determine the safe/unsafe operating limits for a lubricated contact. The author illustrates this with an ingenious experimental technique and computer modeling. He adds that actual details of the surface structure and the amount of lubricant available must also be known. [8] has RF sputter deposited in air lubricant thin films of chromium carbide, calcium fluoride, and silver on cobalt based super alloy substrates for aerospace and industrial applications at elevated temperatures such as rolling mill bearings (700C), turbopump dynamic seals (500-700C), blast furnace sliding gates (600-1000C), and hot gas extractors (200-700C). Dense thin films of these solid lubricants can be used for these high temperature applications and especially for the HERMES space shuttle control surface bearings. [14] screened a series of vapor phase deposited lubricants using rolling contact testing for high temperature turbine engine applications. The lubricants were selected for study considering toxicity, fire resistance, boundary/lubricant characteristics, thermal/oxidation stability, and temperature/viscosity index. The lubricants were a blend of tertiary-butyl phenyl phosphate isomers (TBPP), a blend of cyclophosphazine isomers (X-1P), a 2 eSt unformulated polyalphaolefin (PAO), and the PAO fluid blended with 15% TBPP(PAO+). Overall the (PAO+) shows the best performance under these specific test conditions.

The strength of this group of papers is definitely the many innovative processing techniques that have been developed for producing these high temperature lubricants.

### IV. AEROSPACE APPLICATIONS



Papers [9, 10, 12, 13, 15, and 16] cover aerospace applications. The role that tribology and friction play in space satellites is discussed in [9], and it is not all bad. Tribological phenomena are effected by the ultra-high vacuum in space. Surfaces of like metals should not be put in contact with each other. Fluid lubricants migrate because of the microgravity, so dry lubricants are preferred. Satellite subsystems must withstand fretting induced by launch vibrations, or must be locked in place. The latter requires materials with a high coefficient of friction and a low residual adherence force after release. Lubricants must operate over a wide temperature range, -20 to +60C inside the satellite and -100 to +100C outside. All these subsystems must operate for the lifetime of the satellite, usually fifteen years; and sometimes they must withstand nine years of ground storage before launch. The special demands put on lubricants and materials used in various subsystems are detailed in the paper. [10] looks at some specific friction and wear problems and their solutions in the swept wing TORNADO aircraft. The aircraft has a variable wing sweep capability which causes sliding and wear in the wing carry box, wing fairing panels, wing nib roller bearings, and the flap track trails. Solutions ranged from silver plating, and teflon liners, to actual redesign of the component. [12] Fretting and fretting corrosion in a riveted airframe connection was modeled using a relatively coarse 3-dimensional finite element analysis. Fit with experiment was good. Problem areas in the steel rivet-aluminum panel and aluminum panel-aluminum panel interfaces are highlighted. [13] deals with the analysis of an electrohydrodynamic (EHD) roller/inner ring contact in a jet engine roller bearing. A simple EHL model which takes into account some but not all of the phenomena occurring during the roller/inner ring contact is used to evaluate the lubricant film thickness and pressure inside the EHD contact. The roller geometry, along the traverse direction, plays a very important role in the EHD behavior of the roller/inner ring contact. Surface roughness produces a considerable perturbation of the normal pressure distribution with high local pressures inside the EHD contact. The center and minimum lubricant film thickness show a small reduction due to the surface roughness. In the past the reliability of high speed turbine engine bearings was dependent upon materials fatigue, but with the advent of cleaner steels, defects leading to failure are more likely to be found at the bearing surfaces rather than in the bulk [15]. Despite a better understanding of the turbine engine bearings' environment and the ability to predict behavior with improved computer codes friction and wear related defects still occur such as: skidding, poor lubrication, polluted oil systems, contact conditions in bearing cages exceeding design and materials capabilities, and surface and subsurface stresses leading to fatigue failure. In the latter case a new non-destructive analysis technique employing Barkhausen noise shows promise. An important application of friction and wear in gas turbine engines is in abrasible airseals [16]. The performance and efficiencies of these engines depend upon the

clearances between the stationary gas path seal components and the rotating blade tips of the labyrinth seals. The approach taken to maintain these seals is using abrasible materials that can withstand abrasion at speeds up to 500m/s without self-destructing from the high temperatures and stresses generated. Several materials concepts are discussed to address future requirements.

This group of papers has focused on a variety of aerospace applications and specific solutions to friction and wear problems. In the cases of space satellites and abrasible airseals, friction and wear are necessary for success.

## V. NEW RECIPROCATING ENGINE CONCEPTS

[17 and 18] discuss new engine reciprocating engine concepts, their lubrication, and surface finish requirements. The lubrication and materials requirements of a prototype adiabatic diesel engine are the subject of [17]. The adiabatic diesel is not water cooled, and while the current prototype operates above 300C, future designs incorporating advanced ceramics will operate above 500C. Current lubricating oil with thermal oxidative stability of 204C is inadequate. Future liquid and solid lubricants that can meet these engine requirements are outlined. [18] asks the question whether an oil free commercial internal combustion engine can be developed. Pollution from lubricating oil is a major concern, and environmental laws in many countries are becoming more stringent. The author believes the answer is "yes" if sliding couples of materials with very low wear coefficients independent of ambient temperature and sliding speed can be developed along with high temperature dry lubricants.

## VI. ROUNDTABLE DISCUSSION

The roundtable discussion had sixteen participants and was led by Mr. D. Chaumette, Meeting Chairman, who noted the large number of processes (plasma spraying, pulsed laser deposition, magnetron sputtering, RF sputtering, ion implantation, and detonation guns) to produce a large number of coatings (diamond-like carbon, lubricant thin films, plastic based liners, and adaptive lubricant layers). He asked if this were too many, too few, or the right number. A consensus emerged that because of the range of tribological problems covered, the numbers reflected the solutions necessary to overcome each one, and that no attempt had been made to find solutions common to several. Adherence of coatings to substrates was discussed and general agreement was reached on the need for more characterization of coatings and their defects. Lubricants, coatings, and substrates should be viewed as a materials system designed to counter wear and erosion and not just as individual components. As an example, while a coating may be very hard and wear resistant by itself, if it does not adhere to the substrate it is intended to protect, it is of little value. Similarly, if a high temperature lubricant had a deleterious chemical reaction

with a coating or substrate, it could not be used to counter wear in that particular application.

The most heated discussion arose over testing of these friction and wear resistant materials systems. It was noted that it was difficult to compare test results from different laboratories and round-robin testing was proposed. It was also pointed out that it was very difficult to extrapolate from laboratory test results to real life. Many tests are used just for screening prior to expensive component testing. No solutions were proposed for this dilemma other than a call for closer communications between systems designers and technology developers. There was some discussion on the best way to measure surface roughness for tribological applications. Should there be contact or not? Which energy criteria was preferred? The subject of residual stresses in coatings was raised as one that can effect test results, but something that is not normally quoted by coatings vendors. It is left to the individual investigator to measure them himself. This is a difficult task, and because there are no standard techniques available, the data may be of little value.

In summary that participants thought that the meeting was a success and addressed a variety of NATO defense systems issues. They felt that there should have been more said about materials characterization and adhesion of coatings. Rain and dust erosion were not included in the terms of reference and should be the subject of a future AGARD activity.

## VII. PAPERS PRESENTED AT THE MEETING

[1] "Some Scientific Aspects about Actual Research in Tribology," P. Kapsa, Laboratoire de Tribologie et Dynamique des Systems UMR CNRS 5513, Ecole Centrale de Lyon, Ecully, France.

[2] "Tribological Behavior of Silicon Nitride-Based Ceramics," J. R. Gomes\*, A. S. Miranda\*, R. F. Silva+, and J. M. Viera+, \*Department of Mechanical Engineering, Minho University, 4810 Guimaraes, and +Department of Glass and Ceramic Engineering, Aveiro University, 3810 Aveiro, Portugal.

[3] "Advanced Solid Lubricant Coatings for Aerospace Systems," J. S. Zabinski\*, S. V. Prasad\*, N. T. McDevitt+, \*WL/MLBT Materials Directorate, Wright-Patterson Air Force Base, OH 45433, + Ramspec Research, 2491 E. Mohave Dr., Dayton, OH 45424, USA.

[4] "Advanced Hard Coatings and Wear Resistant Materials for Aerospace Systems" J. S. Zabinski, A. A. Voevodin, and M. A. Capano, WL/MLBT Materials Directorate, Wright-Patterson Air Force Base, OH, USA.

[5] "An Investigation of Surface Treatments for Improving the Fretting Fatigue Resistance of Titanium Alloys," A. K. Koul\*, L. Xue\*, W. Wallace\*, M. Bibby+, S. Chakravarty^, R. G. Andrews^, and P. C.

Patnaik^, \*The Institute for Aerospace Research, National Research Council of Canada, Ottawa, K1A 0R6, + The Department of Mechanical and Aerospace Engineering, Carleton University, Ottawa, K1S 5B6, and ^ Hawker Siddeley Canada Inc., Orenda Division, Ottawa, Canada, K1J 9L8.

[6] "Thin Film Lubrication of Non-Smooth Surfaces," Bo Jacobson, SKF Engineering and Research Centre B. V., Postbus 2350, 3430 Nieuwegein, The Netherlands.

[7] "Machining and Slip-Rolling of Ceramics," M. Woydt and U. Effner, Federal Institute for Materials Research and Testing (BAM), 12200 Berlin, Germany.

[8] "Sputter-Deposited Lubricant Thin Films Operating at Elevated Temperatures in Air," C. Zimmermann\* and Yves Pauleau+, \* Dassault Aviation, 78 Quai Marcel Dassault CEDEX 300, 92552 SAINT CLOUD, and + CEA/Grenoble, CERAM 38054 GRENOBLE CEDEX 9 FRANCE.

[9] Tribological Problems in Spacecraft," A. Borrien, CNES 18 Avenue Edouard Belin, 31055 TOULOUSE CEDEX FRANCE.

[10] "Metallic and Nonmetallic Protection Systems for Reduction of Tribologic Influences in Several Areas on Tornado Aircraft," C. D. Hamm\* and K. Blomeier+, \* Daimler-Benz Aerospace AG, Military Aircraft, D-81663 Munchen, Postfach 801160, and + Daimler-Benz Aerospace AG, Airbus, D-28199 Bremen, Hunefelderstr. 1-5, Germany.

[11] "Improving Solid Lubricated Aerospace Bearings," B. Mortimer and S. Mason, Structural Materials Centre, Defence Research Agency, Farnborough, Hants, UK, GU14 6TD.

[12] "Analysis of Fretting and Fretting Corrosion in Airframe Riveted Connections," K. Iyer, M. Xue, P. C. Bastias, C. A. Rubin, and G. T. Hahn, Department of Mechanical Engineering, Box 1592, Station B, Vanderbilt University, Nashville, TN 37235, USA.

[13] "EHD Analysis of a Roller/Inner Ring Contact in a Jet Engine Roller Bearing," J. Seabra and A. Campos, Faculdade de Engenharia da Universidade do Porto, Rua dos Bragas - 4099 PORTO CODEX - PORTUGAL

[14] "Rolling Contact Testing of Vapor Phase Lubricants," N. H. Forster, Aero Propulsion and Power Directorate, Wright Laboratory, Wright-Patterson Air Force Base, OH 45433, USA.

[15] "The Dependence of Bearing Reliability in Small and Medium Turbines Upon Tribology," G. Paty and B. Cheftel, Turbomeca - 64511 BORDES CEDEX FRANCE.

[16] "Airseals for Advanced Military Jet Engines," T. J. Uihlein, Daimler-Benz Aerospace, MTU Motoren-und

Turbinen-Union, Munchen GmbH, 80995 Munchen, Germany.

[17] "High Temperature Tribology for Future Diesel Engines," W. Bryzik\* and R. Kamo+, \* US Army Tank-Automotive RDE Center (TARDEC), AMSTA-TR, Bldg 212, Mail Stop 121, Warren , MI 48397-5000, and + Adiabatics, Inc., 3385 Commerce Dr., Columbus, IN 47201, USA.

[18] "Tribological Assessments and Concepts for an Oil-Free Internal Combustion Engine," M. Woydt, Federal Institute for Materials Research and Testing (BAM), 12200 Berlin, Germany.

## TRIBOLOGICAL BEHAVIOUR OF SILICON NITRIDE-BASED CERAMICS

J.R. Gomes\*  
A.S. Miranda\*  
R.F. Silva<sup>+</sup>  
J.M. Vieira<sup>+</sup>

\* Department of Mechanical Engineering, Minho University, 4810 Guimarães - Portugal  
<sup>+</sup> Department of Glass and Ceramics Engineering, Aveiro University, 3810 Aveiro - Portugal

### SUMMARY

Engineering ceramics have enjoyed a growing technological interest in the last decades as high temperature, wear resistant materials. Their low density, low thermal expansion and high hardness associated with a high chemical and mechanical stability in a broad range of temperatures, make them superior candidates as alternative materials for cutting tool inserts, abrasion resistant components, automotive engine parts and aerospace vehicles.

It was investigated the tribological behaviour of a  $\text{Si}_3\text{N}_4$ -based ceramic in sliding against tool steel and grey cast iron. The influence of environmental humidity, sliding speed and temperature on wear of the ceramic is presented and discussed. Laboratory tests were carried out in a pin-on-disc tribometer at variable environmental humidity ranging from 2% to 98%, sliding speed varying from  $0.05 \text{ ms}^{-1}$  to  $3.5 \text{ ms}^{-1}$  and disc temperatures in the range  $22^\circ\text{C}$  -  $600^\circ\text{C}$ . The wear mechanisms were investigated using scanning electron microscopy (SEM) with energy dispersive X-ray analysis (EDS).

The formation of a tribolayer of wear debris adherent to the contact surface of the ceramic was found to be determinant in keeping the wear coefficient low. The conditions leading to the formation of such protective layers are identified and discussed.

### 1. INTRODUCTION

Low density, low thermal expansion, high specific stiffness, high hardness, excellent chemical and mechanical stability in a very broad range of temperatures are useful properties of  $\text{Si}_3\text{N}_4$ , as well as of a selection of fine ceramics and coatings, that make them superior candidate materials for machine elements in energy efficient, light weight equipments and in aerospace vehicles [1-4].

Developments of  $\text{Si}_3\text{N}_4$  materials are being considered for ball and roller elements, in particular for bearing elements, for unlubricated applications such as vacuum instruments and as friction drive elements for high accuracy transmission systems [5,6]. Other applications of  $\text{Si}_3\text{N}_4$  include heat exchangers, pumps for cryogenic fluids, rocket arm pads, inlet and exhaust valves of internal combustion engines [7-9]. Valves operate at

fairly extreme conditions of temperature, pressure and mechanical loads in a severe environment, as a result wear is a significant problem with conventional metallic valves. In vacuum the wear resistance of ceramics does not decrease, and the coefficient of friction does not increase, due to adhesion as in metals. This advantage makes them more promising as components in vacuum for precision equipments [6].

Among high technology ceramics the silicon nitride and sialons became known for their high wear resistance both in lubricated and dry contact applications [4,10]. The wear mechanisms of silicon nitride, as for many other hard-brittle ceramics [11], depend on microstructural characteristics namely on the amount and composition of intergranular phase, grain size,  $\alpha/\beta$ - $\text{Si}_3\text{N}_4$  conversion and porosity [10-13]. Abrasion resistance of this ceramic is directly correlated to the  $H^{3/4}K_{Ic}^{1/2}$  product where  $H$  is hardness and  $K_{Ic}$  is the fracture toughness. This product is at the highest value at room temperature in the nitride ceramics but, above all, it stays high for surface contact temperatures that often rise above  $1200^\circ\text{C}$  [10,12].

Resistance to chemical wear may indeed turn the weak point of  $\text{Si}_3\text{N}_4$  for more specific applications, knowing that intergranular glass softening point, diffusion and oxygen born reactions became noticeable just above  $900^\circ\text{C}$  in less refractory silicon nitride compositions [10,13,14].

The tribological performance of  $\text{Si}_3\text{N}_4$  is complex and could be controlled by a set of different mechanisms such as plastic deformation, microfracture, oxidation and tribochemical reactions [12,15]. The tribochemical reactions lead to the formation of coherent interfacial films that protect the ceramic surface from further oxidation and abrasion effects. A similar protection results from tribolayers formed of agglomerates of fine wear debris present in the contact interface. These surface layers are usually called transfer films, tribofilms or third body layers. As these layers become compacted, they control both friction and wear [16-20].

Ceramics are difficult to machine and expensive. The application of ceramic homologous couples would be limited but the coupling of a ceramic with highly wear resistant metallic alloys may have great potential [6]. Therefore, a study of wear of ceramic/metal is valuable.

If unlubricated ceramic/metal combinations such as bearings are used in engine applications a lubricious action is afforded by the oxide films that are formed on the metal surface, increasing the life time of the component at high temperatures. For effective use of these materials detailed research of the interaction of the ceramic/metal couples, deep understanding and clear identification of the dominant wear mechanisms are needed [7,21,22]. Data on silicon nitride/metal tribopairs are sparse comparing to published data on silicon nitride self-mated pairs [4,10]. Concerning the ceramic/cast iron tribosystem little work has been reported. In fact cast iron is a commonly used tribological material in conventional industry, that is often replaced by light weight, special alloys if one seeks advanced technological applications [23].

Many effects such as atmospheric humidity, sliding speed, contact load and temperature, strongly influence the wear mechanisms of  $\text{Si}_3\text{N}_4$ . There is no consensus in literature about the effect of humidity. Humidity plays a variety of roles in special as far as crack propagation, reactions with the sliding surfaces and modifications to the third body layers are concerned [18,24-27]. The presence of humidity in the atmosphere is reported to be detrimental or beneficial depending on the sliding system and the operating conditions. The wear rate of ceramics is frequently reported to be larger at high humidity [4,10,28]. The increasing wear with moisture was explained by corrosion effects or weakening of adhesion of oxidized wear debris to the ceramic surface [10]. When the sliding speed is increased the contact surface becomes dry due to frictional heating. Adhesion of the protecting film and extensive smearing of the wear debris over the ceramic surface extends life of both the ceramic surface and the opposing surface [4,10,26,28]. The protective effect is similar either if steel or the more brittle graphite bearing GCI are in use. Oxygen and water vapour are not available in the outer space vacuum, but these gases will be found in biospheres, cabins, combustion gases of rocket engines, fuel cells or in any internal combustion engine.

The work described in the present paper is a part of a broader investigation on the nature of unlubricated wear of  $\text{Si}_3\text{N}_4$  based ceramics sliding against tool steel and grey cast iron. The effect of humidity, sliding speed and disc temperature under mild loading and speed conditions, have been investigated using a pin-on-disc tribometer. The discussion is focused on the role of wear debris entrapped in the contact interface, in controlling the tribological behaviour of the ceramic.

## 2. TEST MATERIALS

The ceramic material used in this work was produced by the authors and belongs to the system  $\text{Si}_3\text{N}_4\text{-CeO}_2\text{-AlN}$ . The ceramic pins were machined from discs that were uniaxially hot-pressed at 30 MPa of applied pressure, at 1500 °C. Chemical composition, volume fraction ( $V_L$ )

and nitrogen content of the intergranular glassy phase are given in Table 1.

Table 1. Composition of  $\text{Si}_3\text{N}_4$  and intergranular phase volume

Composition (mol.%)				$V_L$ (%)	N (at.%)
$\text{Si}_3\text{N}_4$	$\text{SiO}_2$	$\text{Ce}_2\text{O}_3$	AlN		
76.2	7.3	0.9	15.6	10.1	27.1

Raw materials:  $\text{Si}_3\text{N}_4$ , HcStarck LC12;  $\text{CeO}_2$ , Fluka puriss; AlN, HcStarck grade C.

The volume fraction of the intergranular phase and its N-content were calculated from the amount and composition of the sintering aids, using densities of glasses of similar compositions [14]. The hardness (H) and fracture toughness ( $K_{Ic}$ ) of the ceramic are shown in Table 2. The hardness was measured using a Vickers indenter with a load of 9.8 N, taking the average from 20 indentations. For each indentation the Palmqvist-type crack lengths were measured and ( $K_{Ic}$ ) was determined according to Niiara's expression [29]. The  $\alpha\text{-Si}_3\text{N}_4$  weight fraction was calculated from the peak heights of the X-ray diffraction patterns using the calibration method of Gazzara and Messier [30].

Table 2. Hot pressing temperature, microstructural and mechanical properties of  $\text{Si}_3\text{N}_4$

T (°C)	Relative density (%)	$\alpha\text{-Si}_3\text{N}_4$ (weight %)	H (GPa)	$K_{Ic}$ (MPam <sup>1/2</sup> )
1500	98.92	61.4	19.7 (0.8)*	4.1 (0.3)*

\* Standard deviation in brackets.

The counterface discs were machined from commercial grade rods of tool steel (TS) and grey cast iron (GCI). The composition and properties of these alloys are shown in Table 3.

Table 3. Properties of tool steel and cast iron discs

Material	Code	Composition	H(GPa)
Annealed Tool Steel (TS)	DIN 1.2080	2.0%C; 12%Cr	2.5
Grey Cast Iron (GCI)	Grade 200	3.9%C; 2.9%Si; 0.9%Mn; 0.04% (max) S; 0.1% (max) P	1.9

The contact surface of the discs was polished with 800 grit silicon carbide paper followed by finishing with 1  $\mu\text{m}$  diamond paste. The final surface roughness, as

measured by profilometry, was  $0.05\text{ }\mu\text{m}$  and  $0.3\text{ }\mu\text{m}$  Ra for the steel disc and the cast iron disc, respectively.

### 3. EXPERIMENTAL PROCEDURE

Unlubricated friction and wear tests were carried out in a PLINT TE67 HT tribometer. A ceramic pin was loaded against a rotating disc with a normal contact force ( $F_n$ ) of 5 N, which was kept constant in all tests. The pin had a conical tip with an area of contact of 1 mm in diameter. Pin and disc geometries are shown in Fig 1. The disc was driven by a 2.35 kW d.c. motor of infinitely variable speed.

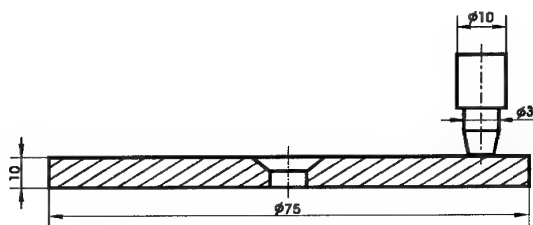


Fig 1 - The pin-on-disc test geometry used in the present study.

The use of an acrylic chamber to isolate the area of test from the atmospheric environment, allowed the control of the relative humidity (RH) in that area. High relative humidity environments (98% RH) were obtained by blowing air through a water reservoir at controlled temperature. Low humidity conditions (2% RH) were achieved by purging the chamber with air passed through a bed of silica gel desiccant. Intermediate values of RH were obtained by controlling the flow of air entering the chamber.

A data acquisition system was used to record the frictional force acting on the pin/disc interface. The friction force ( $F_f$ ) was proportional to the output signal of a bending-type load cell which counteracted the pin holder arm.

Before testing, all samples were cleaned in a ultrasonic bath with pure ethyl alcohol and dried in blown hot air. The tests were stopped at regular time intervals and the weight loss of the pin was measured using an analytical balance with an accuracy of  $10\text{ }\mu\text{g}$ . Pin wear volume at the end of each run was calculated from its weight loss and the density of the material. Disc wear volume was evaluated by profilometry [31].

After an initial running-in period, the sliding couple entered a steady state regime where the volume of wear ( $V$ ) became proportional to the sliding distance ( $x$ ). The wear coefficient ( $K$ ) in this regime was calculated by  $K=V/(F_n \cdot x)$ . The friction coefficient ( $f$ ) was given by  $f=F_f/F_n$ .

Variable speed tests were carried out at room temperature with a constant relative humidity of 50%. Sliding speeds varying from  $0.05$  to  $3.5\text{ ms}^{-1}$  were used, which were

obtained by combining the rotational speed of the disc with the radius of the contact track on the disc surface.

Tests of variable relative humidity were carried out at a constant sliding speed of  $0.5\text{ ms}^{-1}$  for RH values of 2%, 50% and 98%, with a precision allowance of  $\pm 2\%$ . A portable digital hygrometer was used to measure RH.

High temperature tests were carried out at  $100\text{ }^\circ\text{C}$ ,  $200\text{ }^\circ\text{C}$ ,  $400\text{ }^\circ\text{C}$  and  $600\text{ }^\circ\text{C}$ . Up to  $400\text{ }^\circ\text{C}$  the disc was heated using an electric air blower which directed a stream of heated air into an air box involving the disc carrier. For temperatures higher than  $400\text{ }^\circ\text{C}$ , the air heater was replaced by a propane gas burner. The gas system consisted on the burner itself and a control circuit comprising a solenoid valve and a needle valve bypass. For tests above  $200\text{ }^\circ\text{C}$  a lid was fitted to the air box covering the disc specimen and allowing access for the pin. Disc temperature was measured using a non-contact type IR radiation thermometer, and controlled by a digital controller which regulated the electric power and the gas flow supplied to the air heater and to the gas burner, respectively. The worn surface of the pins, and the wear track of the discs, were observed by optical microscopy after each test run. At the end of the test they were examined, as well as the wear debris, by analytical scanning electron microscopy (SEM) with EDS X-ray analysis, to provide evidence permitting the identification of the mechanisms of material removal and the interpretation of results.

## 4. RESULTS

### 4.1 Relative humidity

Table 4 shows experimental values of friction and wear coefficients obtained at various RH conditions. A typical variation of the coefficient of friction during a test run is shown in Fig 2.

Table 4. Friction coefficient,  $f$ , pin wear coefficient,  $K_p$ , and disc wear coefficient  $K_D$  ( $\times 10^{-15}\text{ Pa}^{-1}$ ) for different humidity conditions ( $v=0.5\text{ ms}^{-1}$ ,  $F_n=5\text{ N}$ )

RH (%)	Si <sub>3</sub> N <sub>4</sub> /TS			Si <sub>3</sub> N <sub>4</sub> /GCI		
	$f$	$K_p$	$K_D$	$f$	$K_p$	$K_D$
2	0.81	3.3	24.9	0.74	4.3	6.2
50	0.77	10.9	1.3	0.77	18.0	1.3
98	0.89	12.0	3.0	0.74	15.0	2.0

The frictional behaviour in each test run was characterized by a quick rise in friction to a stationary regime in which the coefficient of friction remained approximately constant to a value dependent on the test conditions. There is no direct correlation between the environmental RH and the value of friction coefficient measured. The disc material, however, affects the value of ( $f$ ) which was generally lower for the ceramic/GCI pair.

The effect of RH on the wear behaviour of the ceramic pin is plotted in Fig 3. It can be observed (see also Table 4) that when RH increased from 2% to 50%, pin wear coefficient ( $K_p$ ) raised by a factor of 3.3 for the ceramic/TS contact and by a factor of 4.2 for the ceramic/GCI contact. A further increase in RH did not significantly affect ( $K_p$ ). The influence of the counterface material on the wear behaviour of the ceramic pin has also been determined by the environmental RH. Thus, in dry air (RH=2%) pin wear was practically the same for both ceramic/TS and ceramic/GCI pairs. For RH equal to 50% and higher, however, pin wear coefficient was higher in contact with GCI than when in contact with TS. In dry air (RH=2%) the wear of the GCI disc was significantly lower than the wear of the TS disc. The former was also associated to a lower value of the coefficient of friction. For increasing values of RH disc wear decreased, remaining ( $K_D$ ) similar for both TS and GCI discs.

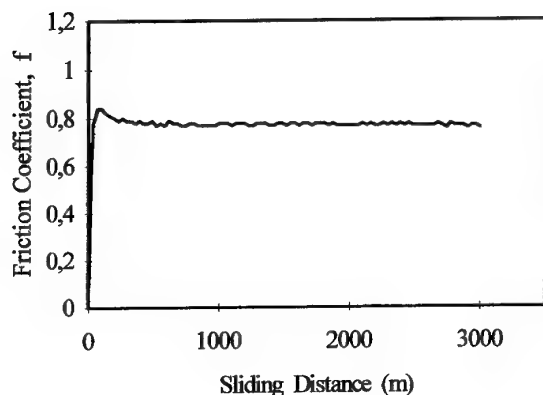


Fig 2 - Typical variation of the coefficient of friction during a test run (pair  $\text{Si}_3\text{N}_4$ /TS, RH=50%).

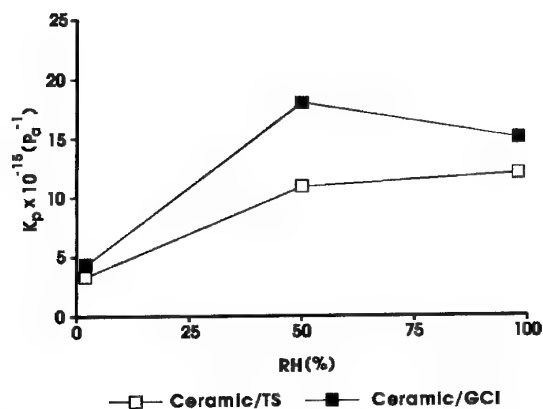


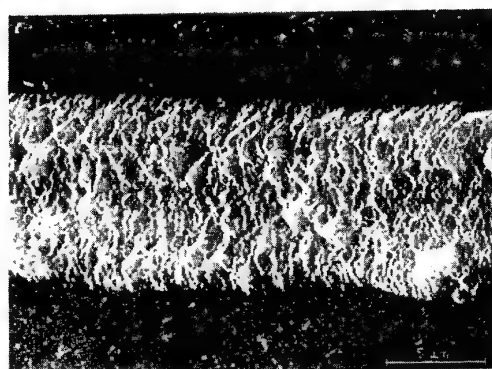
Fig 3 - Variation of the wear coefficient,  $K_p$ , of  $\text{Si}_3\text{N}_4$  in different humidity environments, against tool steel (TS) and grey cast iron (GCI).

The wear coefficient of the discs ( $K_D$ ) has been determined according to the same expression as for pin wear coefficient ( $K_p$ ). Therefore, because the total sliding distance ( $x$ ) is not the same for contacting points of pin and disc surfaces, the values presented for ( $K_p$ ) and ( $K_D$ ) are not directly comparable.

Under the lower RH conditions, and for both TS and GCI disc materials, the observation of the wear surface of the ceramic pins by SEM revealed the existence of adherent layers of wear debris (Fig 4a) which the EDS analysis showed to be rich in iron (Fig 5). A more close observation of these layers put in evidence the occurrence of microfracture in a direction perpendicular to the direction of sliding (Fig 4b)). For RH of 50% and 98% only very small aggregates of wear debris adherent to the worn surface of the pin have been observed. After all tests the worn surface of the ceramic pin was polished showing abrasion marks in the direction of sliding. The morphology of the worn surface of the discs was similar for all tests. The surface was polished, with fine abrasion grooves in the direction of sliding. No layers adherent to the surface have been observed.



a)



b)

Fig 4 - Secondary electron images (SEM/SE) of a worn  $\text{Si}_3\text{N}_4$  surface tested against GCI (RH=2%); a) extensive layers of iron-rich wear debris adherent to the ceramic surface; b) microfracture of the adherent layers.

The observation of the wear debris by SEM showed a similar morphology for all RH conditions tested. As



shown in Fig 6 for a ceramic/GCI contact, they were constituted by fine particles and some relatively large flakes. The debris produced from ceramic/TS contacts were, generally, smaller in size. The EDS analysis of the wear debris permitted the identification of the presence of constituting elements of both materials in contact (Fig 7).

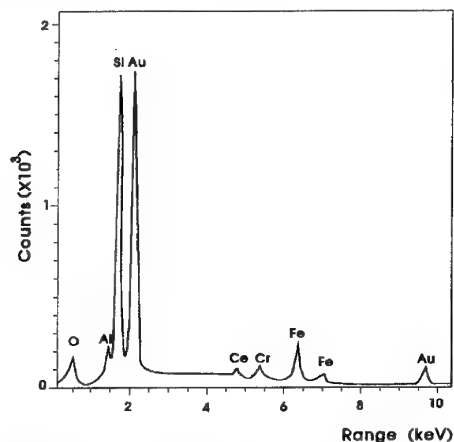


Fig 5 - SEM-EDS spectrum of the worn  $\text{Si}_3\text{N}_4$  surface after sliding against TS (RH=2%).

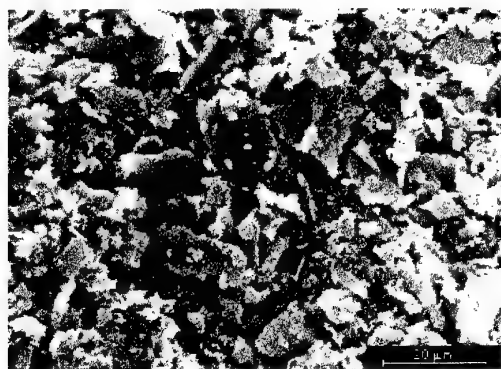


Fig 6 - Secondary electron image (SEM/SE) of the loose wear debris resulting from the contact  $\text{Si}_3\text{N}_4$  / GCI (RH=50%).

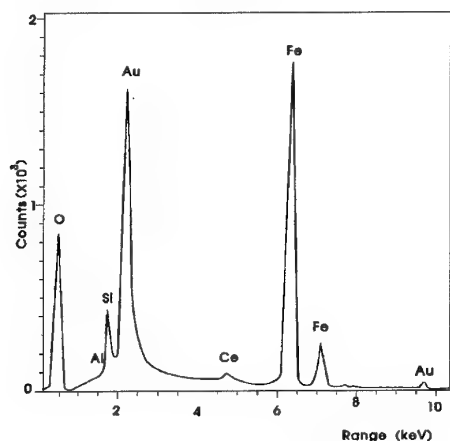


Fig 7 - SEM-EDS spectrum of the wear debris resulting from the contact  $\text{Si}_3\text{N}_4$  / GCI (RH=50%).

#### 4.2 Sliding speed

Experimental values of friction and wear coefficients obtained for ceramic pins and metallic discs tested at different sliding speeds, are given in Table 5. The effect of sliding speed on wear for both ceramic/TS and ceramic /GCI contacts, is shown in Fig 8.

It can be observed (Table 5) that for the ceramic/TS contact the coefficient of friction has not been significantly affected by sliding speed, whereas for the ceramic/GCI contact there was a decrease on (f) for sliding speeds greater than  $0.5 \text{ ms}^{-1}$ . The measured pin wear was similar for both contact pairs. Pin wear coefficient ( $K_p$ ) decreased by more than one order of magnitude as sliding speed increased from  $0.2 \text{ ms}^{-1}$  to  $3.5 \text{ ms}^{-1}$ . The wear of the GCI disc was not significantly affected by the speed of sliding. The wear coefficient of the TS disc varied slightly with the variation of sliding speed, the minimum of ( $K_D$ ) occurring for  $v=0.5 \text{ ms}^{-1}$ .

Table 5. Friction coefficient, f, pin wear coefficient,  $K_p$ , and disc wear coefficient  $K_D$  ( $\times 10^{-15} \text{ Pa}^{-1}$ ) at different sliding speeds ( $F_n=5 \text{ N}$ , RH=50%)

v ( $\text{ms}^{-1}$ )	$\text{Si}_3\text{N}_4$ / TS			$\text{Si}_3\text{N}_4$ / GCI		
	f	$K_p$	$K_D$	f	$K_p$	$K_D$
0.05	0.78	17.0	14.0	0.75	20.0	4.2
0.2	0.79	22.0	6.6	0.85	20.0	2.3
0.5	0.77	10.9	1.3	0.77	18.0	1.3
2.0	0.83	2.3	11.7	0.65	2.5	4.5
3.5	0.80	1.5	3.8	0.67	0.9	4.7

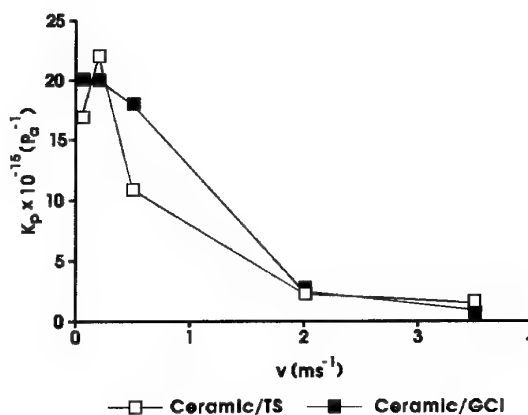


Fig 8 - Dependence of  $\text{Si}_3\text{N}_4$  pin wear coefficient,  $K_p$ , on sliding speed, against tool steel (TS) and grey cast iron (GCI).

The observation of the contact surfaces by optical microscopy and by SEM, showed features which depended on the sliding speed. At low sliding speeds ( $v \leq 0.5 \text{ ms}^{-1}$ ) the worn surfaces of the pins after testing were clean, with very small amounts of material adhered, showing fine abrasion marks characteristic of wear by micropolishing. The contact surfaces of the metallic discs



were also polished, without adherent material. The wear debris were constituted by a mixture of fine particles and medium size flakes. For higher sliding speeds ( $v > 0.5 \text{ ms}^{-1}$ ) the contact surface of the pins showed some evidence of wear by micropolishing, as well as iron-rich layers of material adhered to the surface, as shown in Fig 9. The wear surface of the discs showed evidence of plastic deformation which is more pronounced in the case of the GCI disc, tending to close the graphite flake cavities. At  $v = 3.5 \text{ ms}^{-1}$  some removal of material from the disc surface by delamination was observed, in conjunction with substantial amounts of plastic deformation (Fig 10).

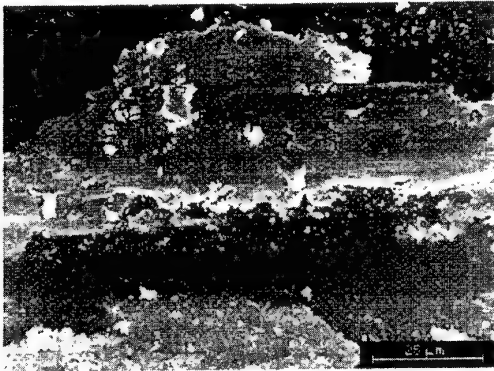


Fig 9 - Secondary electron image (SEM/SE) of a worn  $\text{Si}_3\text{N}_4$  surface tested against TS at  $3.5 \text{ ms}^{-1}$  sliding speed ( $\text{RH}=50\%$ ).



Fig 10 - Secondary electron image (SEM/SE) of the contact surface of the GCI disc ( $\text{RH}=50\%$ ,  $v=3.5 \text{ ms}^{-1}$ ).

The wear debris formed under these testing conditions were mainly constituted by fine particles, with some loose flakes and cylindrical rolls. For all testing conditions the EDS analysis of the wear debris revealed the presence of elements of both materials of the pair.

#### 4.3 Temperature

Table 6 shows friction and wear coefficients obtained from tests at variable disc temperature. The effect of

temperature on the wear of the ceramic pin against TS and GCI discs is shown in Fig 11.

There is no clear effect of temperature on friction. When temperature increased from room temperature to  $600^\circ\text{C}$  pin wear coefficient decreased by a factor of 5.4 for the ceramic/TS pair, and by a factor of 20 for ceramic/GCI pair. This decrease in ( $K_p$ ) occurred mainly in the temperature range  $22^\circ\text{C} - 200^\circ\text{C}$ . Disc temperatures over  $200^\circ\text{C}$  had only a slight effect in decreasing ( $K_p$ ).

Table 6. Friction coefficient,  $f$ , pin wear coefficient,  $K_p$ , and disc wear coefficient  $K_D (\times 10^{-15} \text{ Pa}^{-1})$  at different temperatures ( $v=0.5 \text{ ms}^{-1}$ ,  $F_n=5 \text{ N}$ )

T ( $^\circ\text{C}$ )	$\text{Si}_3\text{N}_4/\text{TS}$			$\text{Si}_3\text{N}_4/\text{GCI}$		
	$f$	$K_p$	$K_D$	$f$	$K_p$	$K_D$
22	0.77	10.9	1.3	0.77	18.0	1.3
100	0.99	6.5	25.0	0.76	3.2	10.8
200	0.78	2.9	13.8	0.78	2.5	24.0
400	0.70	2.5	15.1	0.57	2.0	77.4
600	0.73	2.0	14.1	0.86	0.9	72.6

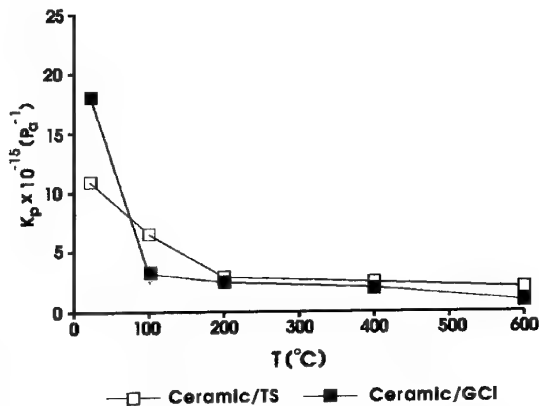


Fig. 11 - Dependence of  $\text{Si}_3\text{N}_4$  pin wear coefficient,  $K_p$ , on disc temperature, against tool steel (TS) and grey cast iron (GCI).

With respect to disc wear, different behaviours were observed for TS and GCI. The wear coefficient of the GCI disc increased almost two orders of magnitude when temperature increased from  $22^\circ\text{C}$  to  $600^\circ\text{C}$ . The wear coefficient of the TS disc increased of about one order of magnitude as temperature raised from  $22^\circ\text{C}$  to  $200^\circ\text{C}$ , staying practically constant at higher values of temperature. A peak value of ( $K_D$ ) equal to  $2.5 \times 10^{-14} \text{ Pa}^{-1}$  was observed for a disc temperature of  $100^\circ\text{C}$ , which corresponded to the highest value of friction coefficient measured ( $f=0.99$ ).

The worn surfaces of the ceramic pins were observed by SEM/EDS and their final morphology can be characterized as follows. At low and intermediate disc temperatures (temperature up to  $200^\circ\text{C}$ ) an inchoerent layer of laminated wear debris on the pin surface has

been observed. For disc temperatures of 400 °C and 600 °C an extensive tribolayer spreading on the pin surface along the sliding direction has formed (Fig 12). EDS analysis of a debris-free area of the ceramic surface tested at 600 °C revealed the presence of the ceramic elements Si, Al and Ce, and small traces of Fe from the disc. A similar analysis of the tribolayer has clearly demonstrated its metallic origin and oxidized nature by the intensity of the Fe and O peaks on the EDS spectrum. This is also corroborated by the SEM/BS of the same area (Fig 12b)). The features observed on the contact surface of the ceramic pin were similar for both ceramic/TS and ceramic/GCI pairs.

At temperatures of 100 °C and higher the surface of both TS and GCI discs suffered plastic deformation which was more pronounced at higher temperatures for the GCI disc. The contact surface was characterized by smooth deformed regions and areas where surface material had been partially removed.

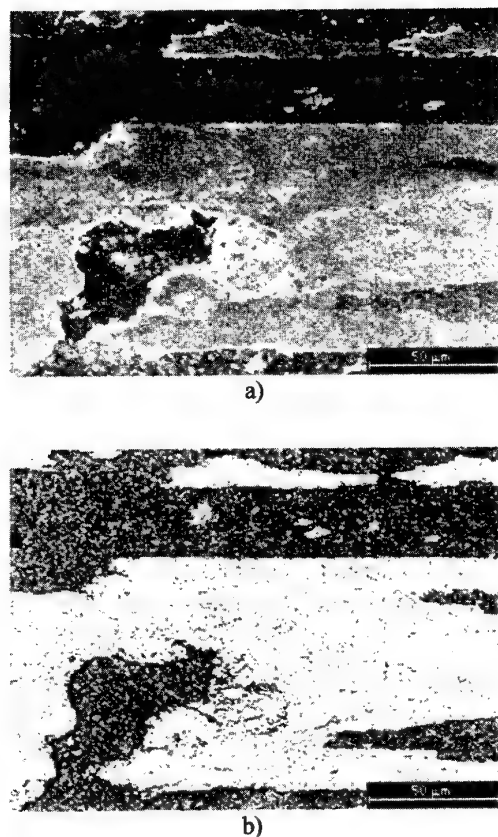


Fig 12 - Worn surface of a Si<sub>3</sub>N<sub>4</sub> pin tested against GCI at 600 °C ( $v=0.5 \text{ ms}^{-1}$ ); a) SEM/SE micrograph showing flat layers of adherent wear debris; b) A backscattered electron (SEM/BS) image of the worn surface. An iron-rich film transfer is evident as a white area on the ceramic darker background.

## 5. DISCUSSION

### 5.1 Formation of tribolayers

The wear resistance of Si<sub>3</sub>N<sub>4</sub> under the test conditions investigated in this work was found to be controlled by the formation of a tribolayer adherent to the contact surface of the ceramic. Sets of operating and environmental conditions leading to the formation of such layers originated low wear. Testing conditions inhibiting the formation of these layers resulted in higher wear of the ceramic. Similar tribological behaviour has been reported by other researchers [7, 18,19,32-36].

Wear debris, which have formed in all tests, were constituted by particles of various geometries and dimensions (Fig 6) originated from both contact surfaces, as demonstrated by EDS spectra as the one shown in Fig 7. The debris originated from the ceramic pin surface were the result of micropolishing of the surface caused by sliding indentation action of loose ceramic grains [4] and loose chromium carbide particles of the TS disc, or due to mechanical interaction with the surface of the GCI disc which became rougher as graphite flakes were pulled out the surface due to sliding and heat generation in the contact [38,39]. Debris originated from the surface of the discs resulted of: (i) micropolishing in a similar manner as described above for the pin surface; (ii) oxidation (revealed by the intense oxygen peak on the EDS spectrum as shown in Fig 7 for a particular set of test conditions), which increases as RH and temperature increase [27,34,40,41]; (iii) plastic deformation followed by surface delamination (Fig 10), especially at high sliding speeds and ambient temperatures [6,42].

Increasing sliding speed and ambient temperature affect the rheology of the wear debris promoting the formation of aggregates [17,18,43] which are subsequently laminated in the contact due to the sliding action under the operating contact stresses. In this way a tribolayer is formed adherent to one of the surfaces, protecting it against wear [16,35,36]. Figs 4, 9 and 12 show tribolayers formed on the ceramic pin surface under different test conditions.

Humidity leads to the disruption of the tribolayer of wear debris, or prevents its formation, by promoting the nucleation and growth of microcracks [18], weakening the adhesion bonds and altering the tribolayer's rheology [32,34,44,45]. High contact temperatures (flash temperatures), which can be originated either at low sliding speeds and high ambient temperatures or at high sliding speeds and room temperature, were found to promote the formation of tribolayers of wear debris adherent to the surface of the Si<sub>3</sub>N<sub>4</sub> pin (Figs 9 and 12).

### 5.2 Wear behaviour

The wear coefficient of Si<sub>3</sub>N<sub>4</sub> was not significantly affected by the counterface materials used (Figs 3, 8 and 11). The reason for this is that when a tribolayer was formed on the ceramic surface, the wear behaviour was

mostly dependent on the tribology of this layer and less dependent on the opposing surface. Under conditions which did not facilitate the formation of a tribolayer the ceramic wear coefficient was slightly higher against GCI than against TS, due to the higher surface roughness of the GCI counterface.

Humidity played an important role in controlling the formation of tribolayers as described before. Pin-on-disc contacts are open-type contacts allowing a strong interaction between the adsorbed gaseous species of the atmosphere and the contact surface. In humid air (RH of 50% and 98%), tribolayers of debris agglomerates were not present to protect the pin surface. The wear of the pin increased due to micropolishing and mechanical interaction with the disc surface. The sliding action and heat generation by friction caused the removal of graphite flakes from the GCI contact surface, leaving large cavities on the disc wear track, thus increasing surface roughness [38,39]. A considerable amount of the debris formed were of the flake-like type [46,47] as shown in Fig 6. This led to higher wear coefficients (Fig 3), the solid lubrication effect of graphite being secondary. Debris formed on the  $\text{Si}_3\text{N}_4$ /TS contact were of the powder-like type [46,47] meaning less contact severity and lower wear. In dry air (RH=2%) a layer of agglomerated wear debris adherent to the pin surface has formed which protected the ceramic keeping the wear coefficient low (Fig 4a)). Repeated sliding can originate the disruption of the protecting tribolayers by microcracking (Fig 4b)), which will reform again if environmental and sliding conditions stay favorable.

Looking at Tables 5 and 6, and Figs 8 and 11, it is interesting to note that there is a transition value of sliding speed (which for this set of results is  $v=2 \text{ ms}^{-1}$ , Fig 8) and a corresponding transition temperature (equal to  $200^\circ\text{C}$ , Fig 11) to which the wear coefficient of  $\text{Si}_3\text{N}_4$  stabilizes to a low value, similar for both cases and practically independent of the counterface material. The transition sliding speed and ambient temperature mentioned above corresponded to conditions at which a coherent tribolayer adherent to the pin surface has formed (Figs 9 and 12). This suggests that for a given RH the influential parameter in the formation of a tribolayer might be the contact temperature (flash temperature). The tribolayers formed were mainly constituted by metallic oxidized particles (Fig 12b)) and its extension over the contact surface increased with increasing sliding speed and ambient temperature.

All sliding speed tests were carried out at RH=50%. The frictional heat generated makes the contact surface to become dry. At low sliding speeds the effect of humidity on the formation of a tribolayer prevailed. No protecting layer of debris, or only a incoherent one, adhered to the pin surface and the wear coefficient was high. At high sliding speeds the tribocontact became dry and an extensive layer of wear debris adhered to the ceramic surface, resulting in low wear. A similar wear behaviour occurred in the temperature tests.

The disc material is subjected to oxidation which originates the formation of iron oxide films on the wear track. The sliding action causes the disruption of this film producing loose oxidized particles (Fig 7). The kinetics of oxidation increases as RH and temperature increase [27,34,35]. In humid air (RH of 50% and 98%) disc wear coefficient ( $K_D$ ) was lower than in dry air (Table 4) due to the influence of humidity in the formation of a more effective oxide film on the disc surface [27,40]. In dry air the wear coefficient observed was lower for the GCI disc than for the TS disc. This was attributed to the solid lubrication effect of graphite which also contributed to a lower friction coefficient [38,48,49].

At sliding speeds  $v \leq 0.5 \text{ ms}^{-1}$ , the slight decrease in ( $K_D$ ) observed for both disc materials (Table 5) could be attributed to the increasing effectiveness of the oxide films in protecting the surfaces. For  $v > 0.5 \text{ ms}^{-1}$ , heat generation by friction in the contact increases, leading to plastic deformation and delamination of the disc surface (Fig 10) thus increasing wear [4,50].

At increasing ambient temperature (Table 6), the GCI disc showed a significant increase in wear coefficient. This was attributed to the decrease in bulk mechanical resistance of the disc material with increasing temperature, originating extensive plastic deformation and delamination of the surface at the higher values of temperature. At high ambient temperature ( $T \geq 200^\circ\text{C}$ ) the TS disc experienced lower wear than the GCI disc, which was nearly independent of temperature in the range  $200^\circ\text{C} - 600^\circ\text{C}$ . The TS disc material is a hot working tool steel which sustains its mechanical resistance at relatively high temperatures, thus accounting for the good wear behaviour observed.

## 6. CONCLUSIONS

The wear resistance of  $\text{Si}_3\text{N}_4$  sliding against tool steel (TS) and grey cast iron (GCI) in unlubricated conditions was found to be controlled by the formation of a tribolayer of wear debris adherent to the sliding surface of the ceramic. Sets of operating and environmental conditions leading to the formation of such a layer originated low wear. Conditions inhibiting its formation resulted in higher wear.

Relative humidity (RH), sliding speed ( $v$ ) and disc temperature ( $T$ ) were found to affect the formation of tribolayers. Humidity has a deleterious effect by promoting the nucleation and growth of microcracks, weakening the adhesion bonds and altering the tribolayer's rheology. At increasing sliding speed ( $v \geq 2 \text{ ms}^{-1}$ ) the heat generated by friction dries up the contact and affects the wear debris' rheology, promoting the formation of tribolayers. Similar effect was observed at high disc temperatures ( $T \geq 200^\circ\text{C}$ ). This suggests that for a given RH the influential parameter controlling the formation of tribolayers of wear debris might be the contact temperature (flash temperature).

When a tribolayer has formed the wear coefficient of the ceramic was in the range of  $10^{-15} \text{ Pa}^{-1}$ , being practically independent of sliding speed, disc temperature and counterface material. In the absence of a protective tribolayer the wear coefficient of the ceramic rose to the range of  $10^{-14} \text{ Pa}^{-1}$ , being higher against GCI than against TS.

The main mechanisms of wear of the ceramic surface were micropolishing by loose hard particles and mechanical interaction with the rough surface of the GCI disc. Disc wear was due to micropolishing, surface oxidation and plastic deformation associated to removal of material from the surface by delamination. The latter was more pronounced for the GCI disc at high sliding speeds and disc temperatures, due to the effect of temperature on the mechanical resistance of the material.

#### ACKNOWLEDGEMENTS

This work was financially supported by JNICT under contract STRDA/C/CTM/607/92.

#### REFERENCES

- Bai, M., Zhang, X. and Qi, S., "Tribological Properties of Silicon Nitride Ceramics Coated with Molybdenum Films under Boundary Lubrication", *Wear*, 169, 1993, pp 181-187.
- Tucci, A. and Esposito, L., "Microstructure and Tribological Properties of  $\text{ZrO}_2$  Ceramics", *Wear*, 172, 1994, pp 111-119.
- Wang, H., Kimura, Y. and Okada, K., "Sliding Friction and Wear of Ceramics at Elevated Temperatures up to  $1000^\circ\text{C}$ ", in "Proc. of the Japan Int. Tribology Conference", Nagoya, 1990, pp 1389-1394.
- Lee, K.H. and Kim, K.W., "Effects of Humidity and Sliding Speed on the Wear Properties of  $\text{Si}_3\text{N}_4$  Ceramics", *Mat. Sci. Eng.*, A186, 1994, pp 185-191.
- Adachi, K., Hokkirigawa, K. and Kato, K., "The Wear Mechanism of Silicon Nitride in Rolling-sliding Contact", *Wear*, 151, 1991, pp 291-300.
- Zhou, L., Fang, L., Wang, N.X. and Zhou, J.E., "Unlubricated Sliding Wear Mechanism of Fine Ceramic  $\text{Si}_3\text{N}_4$  Against High-chromium Cast Iron", *Tribol. Int.*, 27, 5, 1994, pp 349-357.
- He, Y.J., Winnubst, A.J.A., Schipper, D.J., Bakker, P.M.V., Burggraaf, A.J. and Verweij, H., "Friction and Wear Behaviour of Ceramic-Hardened Steel Couples under Reciprocating Sliding Motion", *Wear*, 184, 1995, pp 33-43.
- Srinivasan, S.R. and Blau, P.J., "Effect of Relative Humidity on Impact Behavior of Machined Silicon Nitride", *J. Am. Ceram. Soc.*, 77, 3, 1994, pp 683-688.
- Park, D.S., Danyluk, S. and McNallan, M.J., "Influence of Tribochemical Reaction Products on Friction and Wear of Silicon Nitride at Elevated Temperatures in Reactive Environments", *J. Am. Ceram. Soc.*, 75, 11, 1992, pp 3033-3039.
- Gomes, J.R., Miranda, A.S., Silva, R.F. and Vieira, J.M., "Tribological Properties of  $\text{AlN-CeO}_2\text{-Si}_3\text{N}_4$  Cutting Materials in Unlubricated Sliding Against Tool Steel and Cast Iron", *Mat. Sci. Eng.*, A209, 1996, pp 277-286.
- Rice, R.W., "Micromechanics of Microstructural Aspects of Ceramic Wear", *Ceram. Eng. Proc.*, 6, 7-8, 1985, pp 940-958.
- Dong, X. and Jahanmir, S., "Wear Transition Diagram for Silicon Nitride", *Wear*, 165, 1993, pp 169-180.
- Silva, R.F. and Vieira, J.M., "Cutting Performance and Hot Hardness of  $\text{Si}_3\text{N}_4$ -based Ceramic Inserts", *J. Hard Mater.*, 3, 1, 1992, pp 63-72.
- Silva, R.F., Moreira, A.P., Gomes, J.M., Miranda, A.S. and Vieira, J.M., "The Role of Nitrogen in the Intergranular Glass Phase of  $\text{Si}_3\text{N}_4$  on High Temperature Applications and Wear", *Mat. Sci. Eng.*, A168, 1993, pp 55-59.
- Denape, J., Marzinotto, A. and Petit, J.A., "Roughness Effect of Silicon Nitride Sliding on Steel under Boundary Lubrication", *Wear*, 159, 1992, pp 173-184.
- Blomberg, A., Olsson, M., Bratthäll, J. and Hogmark, S., "Characterization of Surface Films Formed on Ceramics During Dry Sliding Contact", in "Proc. Int. Tribology Conference", Brisbane, 1990, Vol. 1, pp 79-84.
- Blomberg, A., Hogmark, S. and Lu, J., "An Electron Microscopy Study of Worn Ceramic Surfaces", *Tribol. Int.*, 26, 6, 1993, pp 369-381.
- Komvopoulos, K. and Li, H., "The Effect of Tribofilm Formation and Humidity on the Friction and Wear Properties of Ceramic Materials", *ASME J. Tribol.*, 114, January 1992, pp 131-140.
- Stachowiak, G.W., Stachowiak, G.B. and Batchelor, A.W., "Metallic Film Transfer During Metal-Ceramic Unlubricated Sliding", *Wear*, 132, 1989, pp 361-381.
- Boch, P., Platon, F., Kapelski, G., Godet, M., Berthier, Y., Trabelsi, R., Briggs, J., Arbabi, H. and Azema, O., "Tribology and Velocity Accommodation Mechanisms of Ceramics ( $\text{SiC}$  and  $\text{Si}_3\text{N}_4$ ) as a Function of Temperature and Environment" in "Proc. of the Japan Int. Tribology Conference", Nagoya, 1990, pp 1395-1400.
- Jen, M. and Yan, L., "Environmental Effects on Wear Behaviour of Alumina", *Wear*, 161, 1993, pp 111-119.
- Sliney, H.E. and Dellacorte, C., "The Friction and Wear of Ceramic/Ceramic and Ceramic/Metal Combinations in Sliding Contact", *Lubr. Eng.*, 50, 7, July 1994, pp 571-576.
- Wu, H., Jin, Y., Nicoll, A.R. and Barbezat, G., "Friction and Wear of a Plasma Sprayed  $\text{Al}_2\text{O}_3\text{-40\%ZrO}_2$ -Cast Iron System", *Wear*, 176, 1994, pp 49-60.
- Lancaster, J.K., Mashal, Y.A.-H. and Atkins, A.G., "The Role of Water in the Wear of Ceramics", *J. Phys. D: Appl. Phys.*, 25, 1992, pp A205-A211.

25. Lin, J.F. and Chen, Y.N., "Tribological Reaction Generated on Ceramic-stellite Couples under Dry Sliding Contact and Water- and Oil-lubricated Conditions", *Wear*, 177, 1994, pp 139-149.
26. Gee, M.G. and Butterfield, D., "The Combined Effect of Speed and Humidity on the Wear and Friction of Silicon Nitride", *Wear*, 162-164, 1993, pp 234-245.
27. Papaphilippou, C., Vardavoulis, M. and Jeandin, M., "The Influence of Humidity and the Role of Debris in the Unlubricated Wear of Ductile Cast Iron Against Alumina", *Wear*, 177, 1994, pp 151-157.
28. Chen, Y.M., Pavy, J.C. and Rigaut, B., "Effets de L'Humidité sur le Comportement des Céramiques  $Al_2O_3$ ,  $Si_3N_4$  et PSZ en Frottement à Grande Vitesse sur Acier", *Matériaux et Techniques - Spécial Tribologie*, December 1991, pp 40-44.
29. Niihara, K., Morena, R. and Hasselman, D.P., "Evaluation of  $K_{IC}$  of brittle solids by the indentation method with low crack-to-indenter ratios", *J. Mat. Sci. Lett.*, 1, 1982, pp 13-16.
30. Gazzara, C.P. and Messier, D.R., "Determination of phase content of  $Si_3N_4$  by X-ray diffraction analysis", *Am. Ceram. Soc. Bull.*, 56, 9, 1977, pp 777-780.
31. Silva, R.F., Gomes, J.M., Miranda, A.S. and Vieira, J.M., "Resistance of  $Si_3N_4$  Ceramic Tools to Thermal and Mechanical Loading in Cutting of Iron Alloys", *Wear*, 148, 1991, pp 69-89.
32. Ajayi, O.O. and Ludema, K.C., "Mechanism of Transfer Film Formation During Repeat Pass Sliding of Ceramic Materials", *Wear*, 140, 1990, pp 191-206.
33. Godet, M., "The Third-body Approach: A Mechanical View of Wear", *Wear*, 100, 1984, 437-452.
34. Lancaster, J.K., "A Review of the Influence of Environmental Humidity and Water on Friction, Lubrication and Wear", *Tribol. Int.*, 23, 6, 1990, pp 371-389.
35. Childs, T.H.C. and Mimaroglu, A., "Sliding Friction and Wear up to 600 °C of High Speed Steels and Silicon Nitrides for Gas Turbine Bearings", *Wear*, 162-164, 1993, pp 890-896.
36. Melandri, C., Gee, M.G., Portu, G. and Guicciardi, S., "High Temperature Friction and Wear Testing of Silicon Nitride Ceramics", *Tribol. Int.*, 28, 6, 1995, pp 403-413.
37. Wani, M.F., Mukerji, J., Prakash, B. and Bandopadhyay, S., "Friction and Wear Behavior of Hot-Pressed SiAlON-Steel Ball Tribopair under Reciprocating Sliding Conditions", *Am. Ceram. Soc. Bull.*, 72, 9, September 1993, pp 82-87.
38. Fang, L., Gao, Y., Zhou, L. and Li, P., "Unlubricated Sliding Wear of Ceramics Against Graphitized Cast Irons", *Wear*, 171, 1994, pp 129-134.
39. Luo, Q., Xie, J. and Song Y., "Effects of Microstructures on the Abrasive Wear Behaviour of Spheroidal Cast Iron", *Wear*, 184, 1995, pp 1-10.
40. Czichos, H., Becker, S. and Lexow, J., "International Multilaboratory Sliding Wear Tests with Ceramics and Steel", *Wear*, 135, 1989, pp 171-191.
41. Quinn, T.F.J., "Oxidational Wear Modelling: Part II. The General Theory of Oxidational Wear", *Wear*, 175, 1994, pp 199-208.
42. Nakamura, Y. and Hirayama, S., "Wear Tests of Grey Cast Iron Against Ceramics", *Wear*, 132, 1989, pp 337-345.
43. Kapsa, P. and Viot, J.F., "Frottement à Sec de Couples Acier/Céramique: Phénomènes Importants", *Rev. Int. Hautes Tempér. Réfract. Fr.*, 21, 1984, pp 47-61.
44. Kapelski, G., Platon, F. and Boch, P., "Wear and Friction Properties of some Engineering Ceramics", in "Science of Ceramics", 14, ed. Derek Taylor. The Institute of Ceramics, Stoke-on-Trent, UK, 1988, pp 781-786.
45. Fischer, T.E., Liang, H. and Mullins, W.M., "Tribocchemical Lubricious Oxides on Silicon Nitride", in "Mat. Res. Soc. Symp. Proc., Materials Research Society, Vol. 140, 1989, pp 339-344.
46. Kato, K., "Tribology of Ceramics", *Wear*, 136, 1990, pp 117-133.
47. Hokkirigawa, K., "Wear Mode Map of Ceramics", *Wear*, 151, 1991, 219-228.
48. Sugishita, J. and Fujiyoshi, S., "The Effect of Cast Iron Graphites on Friction and Wear Performance II: Variables Influencing Graphite Film Formation", *Wear*, 68, 1981, pp 7-20.
49. Eyre, T.S., "Wear Characteristics of Flake and Nodular Graphite Cast Iron", British Cast Iron Research Association, BCIRA Report 942, January 1969.
50. So, H., "The Mechanism of Oxidational Wear", *Wear*, 184, 1995, pp 161-167.

## ADVANCED SOLID LUBRICANT COATINGS FOR AEROSPACE SYSTEMS

J.S. Zabinski and S.V. Prasad, WL/MLBT Materials Directorate, WPAFB, OH 45433  
N.T. McDevitt, Ramspec Research, 2491 E. Mohave Dr., Dayton, OH 45424

### SUMMARY

Advances in solid lubricant technology are required for aerospace systems operating in extreme environments. Targeted operational temperature and lifetime requirements are beyond current capabilities. For example, to increase the thrust to weight ratio in expendable turbine engines, solid lubricants are under development for operation at temperatures to about 800°C. Increases in performance and lifetime for lubricated space based systems are also required. Technological advancements may be achieved through development of new coating materials, processes, and coatings strategies. New materials discussed in this report are oxides and adaptive lubricants. Adaptive lubricants undergo designed chemical reactions with the environment as temperature changes to continually maintain low friction and low wear. Pulsed laser deposition is discussed as an emerging process for growing solid lubricant thin films with complex chemistries and microstructures. Finally, multi-layer coatings that are under evaluation for improving adaptive lubricant performance are discussed.

### 1 INTRODUCTION

Lubricants that are effective over an extreme range of operating temperatures are necessary for the development of new generation high performance gas turbine engines with increased propulsion capability. If suitable lubricant materials were available, engines could be run at higher temperatures and therefore more efficiently. Unfortunately, there is no single known lubricant that can provide low friction over the desired range, from subambient to 800°C. Liquids and polymers can only function in moderate temperature regimes. Even the well known solid lubricants such as graphite and molybdenum disulfide ( $\text{MoS}_2$ ) oxidize in air at temperatures above 400 or 450°C and thereby lose their lubricating properties.

A compilation of lubricant materials by McMertry reveals that most solid lubricant formulations consist of  $\text{MoS}_2$  or graphite [1].  $\text{WS}_2$  is sometimes used because it has been reported to have an upper operating temperature limit of about 100°C higher than  $\text{MoS}_2$ . For the most part, few new lubricants or lubricant systems have been reported. There are several notable exceptions: (1) King reports on the tribological properties of a number of candidate solid lubricants and found that Cs and Zn thiomolybdates and thiotungstates have promising properties (2), Gardos reports on the potential of  $\text{TiO}_x$  materials specially formulated to have oxygen deficiencies and, therefore, mechanically weak shear planes [3,4], and (3) Peterson et al. have investigated oxides and double oxides for their high temperature lubricating properties [5,6].

New materials are only one consideration for providing improved lubrication in extreme environments. Suitable

techniques for depositing solid lubricants on mechanical elements are equally important. Early techniques involved burnishing and bonding the films. Film thickness was difficult to control and adhesion was marginal. For precision applications, sputter deposition has proven more effective. There are aspects of the sputter process that limit film quality. Some of the deficiencies are: (1) contamination by background gases (i.e.,  $\text{H}_2\text{O}$ ,  $\text{O}_2$ , etc.), (2) contamination by elements used in prior depositions and (3) porous morphology [7-13]. Contamination from any source can compromise film integrity and prohibit good control of film properties. The porosity and morphology of some sputter deposited films exposes reactive edge planes to the environment where they are susceptible to degradation by oxidants [10-13]. Some of the deficiencies discussed above have been addressed in recent studies of sputter deposition operating conditions [14] and of ion beam assisted sputter deposition (IBAD) [15-17]. In both cases, the formation of dense, "basal" oriented  $\text{MoS}_2$  films was reported. In general, high energy deposition technologies produce good thin film solid lubricants. Pulsed laser deposition (PLD) is a high energy technique that provides coatings that are free from the deficiencies discussed above. The relative merits of PLD films have been discussed and it is important to note that stoichiometry and microstructure are easily controlled [18].

The purpose of this report is to discuss recent advances in solid lubrication in the authors' laboratory. The discussion is organized to first present the pulsed laser deposition (PLD) process. New materials that have been designed using the PLD process are then discussed. These include ZnO and adaptive lubricants. ZnO is discussed as a new material even though its friction properties were discussed around 1960 [5,6]. Reported values of friction coefficient at 704°C were between 0.33 and 0.5. Clearly, this material did not generate further interest as a thin film solid lubricant. Here, PLD has been used to create substoichiometric ZnO with fine grains and dual-phase microstructures. Material with tailored microstructure has low friction and good wear properties. Adaptive lubricants were designed, using thermodynamics as a guide, to permit operation over a broad temperature range. The idea exploited is to design a lubricant system that has good performance at low temperature and, as temperature increases, its components react with each other and the atmosphere to form a high temperature lubricant. In this way, the lubricant adapts to its environment, continually providing lubrication over a wide temperature range. The  $\text{PbO-MoS}_2$ ,  $\text{ZnO-MoS}_2$  and the  $\text{ZnO-WS}_2$  adaptive lubricant systems are discussed.

### 2. EXPERIMENTAL

#### 2.1 Pulsed Laser Deposition.

The system used for pulsed laser deposition is constructed from a stainless steel vacuum chamber that was specially instrumented for pulsed laser deposition. There are four key



components: (1) a laser, (2) optical beam steering and focusing, (3) an instrumented chamber, and (4) a computer data collection and process control system. For the experiments discussed in this manuscript, a Lambda Physik LPX 110i excimer laser was filled with a Ne, KrF mixture to provide a beam of UV radiation at 248 nm. The beam was pulsed at a rate of 10 Hz (17 ns pulse width) and it was focused to a 2.0 by 4.0 mm rectangle on the target face providing a fluence of between 1 and 2.5 J/cm<sup>2</sup> depending on the laser power setting. Beam steering was accomplished using a computer controlled raster mirror. The beam was brought into the deposition system through an MgO window and directed toward the target. Film uniformity was maximized by: (1) rotating the target and the substrate during deposition and (2) rastering the laser beam across the target under computer control. Targets were polished prior to each deposition to minimize roughness and increase deposition rates; they were cleaned using the laser with the sample shutter closed. Deposition was commenced by opening the shutter. The base pressure in the chamber was  $9 \times 10^{-7}$  Pa. A calibrated quartz crystal oscillator was used to measure film thickness. Resistive heating was employed to degas and/or anneal the specimens; temperature was measured using a calibrated infrared pyrometer. Reactive gases were input to the system through a leak valve and pressure monitored using a capacitance manometer. At high vacuum, pressure was measured by a Bayert Alpert gauge. System parameters were monitored using a computer: film thickness, growth rate, system pressure, laser power, laser pulse rate, and residual gas concentrations. In some instances, optical fluorescence signals were used to control film quality and improve deposition rate [19].

## 2.2 Sample Preparation and Analysis

Substrates for tribo-tests were fabricated from 440C stainless steel (SS) coupons that were polished to 1  $\mu\text{m}$ . Materials were cleaned in soap and water and then ultrasonically washed in acetone and methanol.

Surface chemistry was studied with a Surface Science Instruments (SSI) M-probe XPS instrument operated at a base pressure of  $3 \times 10^{-7}$  Pa. Using an Al anode, a 400 X 1000  $\mu\text{m}$  line spot, and a 25 eV pass energy, the full width at half maximum (FWHM) of the Au 4f<sub>7/2</sub> peak was 0.71 eV. Binding energy positions were calibrated against the Au 4f<sub>7/2</sub> peak and energy separations were calibrated using the Cu 3s and Cu 2p<sub>3/2</sub> peaks at 122.39 and 932.47 eV, respectively. Bulk chemistry and film crystallinity were investigated by Raman spectroscopy using a SPEX 1877 spectrometer and the incident light of a 514.5 nm Ar<sup>+</sup> laser. An intensified 1024 element, diode array detector was used to collect the Raman signal. Crystal structures were determined using data acquired by a Rigaku D/max -1B diffractometer equipped with a thin film attachment and a monochromator. High resolution scanning electron microscopy (SEM) was performed on the films using a Leica 360 field emission SEM equipped with an energy dispersive x-ray analyzer.

Room temperature friction and wear data were collected using a ball-on-flat tribometer. The ball was held in a lever arm, and the friction force was measured using strain gauge circuitry. The normal load was computed from the dead weight hung in the cantilever assembly. In order to maintain a constant humidity level in the test environment, the ball-disk assembly was enclosed in a chamber. Flow rates of dry air and saturated humid air were adjusted to control relative humidity from near zero to almost 100%. The percentage relative humidity was measured by a high performance sensor inserted in the chamber. The tests reported here were run in dry nitrogen, dry air, or moist air.

## 3 LUBRICIOUS ZnO FILMS

### 3.1 Background

As discussed earlier, many oxides are stable in air at high temperatures. However, their behavior as thin film solid lubricants has not been extensively investigated. Another obstacle to exploiting oxides is that they are brittle. Their inability to deform plastically or shear easily hinders them from forming smooth friction reducing third-body films on wear surfaces. In addition, the wear debris from an oxide is usually abrasive. Gleiter and coworkers (20,21) presented a new approach to overcome the brittleness in ceramic materials. They reported that conventionally brittle ceramics could become ductile if a polycrystalline ceramic with a crystal size of a few nanometers was generated. The nanocrystalline material could permit large plastic deformation at low temperatures. The development of a ductile nanophase oxide coating for mechanical elements would be a major breakthrough in high temperature lubrication.

Gardos (3,4) proposed an alternate mechanism for turning oxides, particularly substoichiometric rutile (TiO<sub>2-x</sub>), into lubricants. Gardos hypothesized that the energetics, including bond length changes, which depend on electronic properties associated with vacancies in the lattice, are ultimately responsible for variations in shear strength.

In a number of previous studies, the authors have reported the synthesis of pulsed laser deposited (PLD) thin films for tribological applications [18]. It was demonstrated that the crystallinity of thin films could be controlled by selecting the substrate temperature, and in the case of oxide films, the stoichiometry could be adjusted by controlling the oxygen partial pressure in the deposition [22,23]. Thus PLD offers the potential for growing both nanocrystalline oxide as well as nonstoichiometric films for tribological applications.

The high temperature (i.e., 700°C) friction coefficient of ZnO is about 0.3; it melts at 1800°C [6]. ZnO was therefore selected for further research as a thin film solid lubricant with the intention of using PLD to adjust film microstructure and stoichiometry. Although ZnO has been grown by a variety of techniques, including PLD [24,25], no systematic tribological study of well characterized thin films has been reported. The objective of the current study then, was to evaluate the friction

behavior of ZnO films grown by PLD. Several permutations of deposition conditions, namely the substrate temperature and oxygen partial pressure were employed to grow films with different crystal size and oxygen content.

### 3.2 Experimental Details

The major objective of this research was to grow oxide films with different stoichiometries and varying degrees of crystallinity. In order to achieve this objective, four different deposition conditions were employed, as listed below:

Table 1: Deposition parameters for ZnO film

	Temperature (°C)	Pressure O <sub>2</sub> (Pa)
RT, vac	RT	9x10 <sup>-7</sup>
RT, O <sub>2</sub>	RT	6.7x10 <sup>-1</sup>
300°C, vac	300	9x10 <sup>-7</sup>
300°C, O <sub>2</sub>	300	6.7x10 <sup>-1</sup>

RT: room temperature

A commercial hot pressed ZnO disk (99.9% purity, hexagonal crystal structure) obtained from *Cerac Inc.* was used as the target material.

Friction measurements were made using a ball-on-disk tribometer in which a stationary ball was held against a rotating disk. The disk was comprised of a 25 mm diameter steel substrate on which a PLD ZnO film was deposited. A 3.125 mm diameter 440C steel ball was used as the counterface. For each friction track, the rotational speed was adjusted to get a constant sliding speed of 50 mm/s. The majority of the friction measurements were made at a normal load of 1 N. For steel-on-steel, a normal load of 1 N on a 3.125 mm diameter ball corresponds to a Hertzian contact pressure of 675 MPa. The relative humidity in the current study was maintained at 50%, and measurements were made at room temperature.

### 3.3 Results

Surface chemistry and stoichiometry were determined from analyses of the Zn 4f<sub>5/2-7/2</sub> and O 1s XPS spectra and the Zn LMM Auger line. The ZnO target underwent charging and an electron flood gun was used to neutralize the surface. Peak

positions in this instance were referenced to adventitious carbon. Peaks were fitted to Voight functions by minimizing the Chi-squared value; binding energies, and Zn/O atomic ratios determined from the fitted data and are presented in Table 2. Carbon and oxygen contamination were present on the surface of all specimens due to handling in air. Crystal structure and the degree of crystallinity were determined by analysis of Raman spectra and glancing angle x-ray diffraction (GAXRD) which are shown in Figure 1 and Table 3.

Table 2: XPS data from the different films

	O 1s eV	Zn 2p <sub>3/2</sub> eV	Zn LMM eV	O/Zn
ZnO target	531.28	1023.46	987.30	1.0
RT, vac	531.31	1022.48	987.60	0.75
RT, O <sub>2</sub>	531.30	1023.60	987.76	0.95
300°C, vac	531.25	1023.44	987.14	0.90
300°C, O <sub>2</sub>	531.26	1023.45	987.40	0.95

binding energies  $\pm .04$  eV; atomic ratios  $\pm 0.03$

A high resolution SEM micrograph of the RT, vac film is shown in Figure 2a. The film is extremely smooth and no grain boundaries could be seen even at very high magnification. By comparison, the RT, O<sub>2</sub> films begin to reveal some structure (Figure 2b). Introduction of oxygen has resulted in the formation of nanophase clusters. Also, compared with the films grown in vacuum, the ones grown in partial oxygen appear to be rough. Figure 2c is a typical high resolution SEM micrograph of 300°C, vac films. Unlike the previous ones, the topography of the 300°C, vac film appears to be granular with nanocrystalline grains. A typical scanning electron micrograph of 300°C, O<sub>2</sub> films is shown in Figure 2d. Here the clusters grew into sub micron particles, and the film has a well developed two-phase structure.

The steady state coefficient of friction (COF) for the polished surface of the hot pressed ZnO (stoichiometric, hexagonal) is rather high, 0.65. Friction coefficients for the different films are reported in Table 4. The RT, O<sub>2</sub> film performed the best so it was further evaluated by performing a long duration tribo test. The wear life of the film was nearly a million cycles, and for most of the test, the COF was less than 0.2. There were several peaks in the 300°C, O<sub>2</sub> friction trace, and the COF varied between 0.2 and 0.4.

Table 3: XRD data from the different films

ZnO d(Å)	powder I/I <sub>0</sub>	plane (hkl)	RT, vac d(Å)	I/I <sub>0</sub>	RT, O <sub>2</sub> d(Å)	I/I <sub>0</sub>	300°C, vac d(Å)	I/I <sub>0</sub>	300°C, O <sub>2</sub> d(Å)	I/I <sub>0</sub>
2.816	71	100	2.780	3	2.784	3	2.781	2	2.785	4
2.602	56	002	2.576	100	2.569	100	2.572	100	2.576	100
2.476	100	101	2.449	6	2.446	4	2.451	3	2.455	18
1.911	29	102	-	-	-	-	1.899	1	1.898	3
1.626	40	110	-	-	-	-	1.616	1	1.617	10
1.477	35	103	1.469	9	1.471	10	1.469	16	1.469	21



Table 4: Friction coefficients for ZnO films

	$\mu$ initial	$\mu$ SS
RT, vac	0.6	0.34
RT, O <sub>2</sub>	0.1	0.16
300°C, vac	0.1	0.18
300°C, O <sub>2</sub>	0.2	0.3

SS = steady state after 10,000 cycles

### 3.4 Discussion

XPS, Raman, and XRD data were used to study the film chemistry and crystallinity. All films were slightly oxygen deficient. Sputter etching the films for 10 sec, 5 min., and 15 min. did not significantly change their stoichiometries demonstrating that they did not suffer post-deposition oxidation. All peaks in the XRD scans were accounted for by hexagonal ZnO and the 440C substrate.

The RT,vac films were most oxygen deficient; the stoichiometry, determined using XPS data, was ZnO<sub>0.75</sub>. The oxygen deficiency is likely caused by recombination of oxygen atoms in the plasma or at the film surface and subsequent removal of the O<sub>2</sub> molecule through the pumping system. Raman spectra shown in Figure 1 demonstrate that the film was not fully crystalline, as compared to the ZnO target. Only one broad peak at 430 cm<sup>-1</sup> representative of ZnO was present. Another broad peak centered at 570 cm<sup>-1</sup> was observed, but it was shifted 10 cm<sup>-1</sup> to lower wave number compared to the target material. Unambiguous identification of the origin of this peak has not been made, although it is likely related to the crystal size and the substantial oxygen deficiency in the film. The dominance of the (002) line in the XRD scans suggests a texture with the c-axis preferentially aligned perpendicular to the substrate. The topography of the film is smooth, and the high resolution SEM micrographs did not show any grain boundaries.

To increase the oxygen content of the film, the deposition chamber was backfilled with O<sub>2</sub> to a pressure of  $6.7 \times 10^{-1}$  while keeping the substrate at room temperature. Background oxygen only slightly increased oxygen content (ZnO<sub>0.95</sub>) compared to the films grown in vacuum (ZnO<sub>0.75</sub>). Raman spectra indicate that these films are somewhat more similar to the target material because the main peak at 430 cm<sup>-1</sup> was somewhat sharper. The relative peak intensities in XRD scans did not significantly change indicating a similar texture to the RT,vac film. However, high resolution SEM examination revealed the presence of nanoscale clusters in the RT,O<sub>2</sub> films (Figure 2b).

To increase the grain growth and the oxygen content further, the substrate temperature was raised to 300°C while maintaining the vacuum. XPS data indicated that the film was quite similar to the ones grown at room temperature and were ZnO<sub>0.90</sub>. The main Raman peak at 430 cm<sup>-1</sup> was somewhat more pronounced and sharper for the 300°C,vac film than for

the previous films suggesting it is similar to the crystalline target material. The (002) peak in the XRD scan was dominant; however, the relative peak intensities changed somewhat indicating a change in film texture. It is worth noting that the topography of the 300°C,vac film is granular with nanocrystalline grains.

The films grown in an oxygen background (i.e.,  $6.7 \times 10^{-1}$  Pa) at 300°C were ZnO<sub>0.95</sub>. XRD peak intensity ratios changed significantly with the (103) and (101) peaks becoming relatively more intense indicating a change in the texture. Among the various films grown under four sets of conditions, Raman spectra from the 300°C,O<sub>2</sub> films best match with that of the target material. However, the microstructure of the 300°C,O<sub>2</sub> films is of dual-phase with submicron sized dark particles evenly dispersed in a matrix. The shape of the second phase reveals that it is not due to particles often generated by "splashing" during PLD [26,27]. Splashed particles are spherical if molten material ejected from the target solidifies before it reaches the target or they are elongated and flattened if they reach the substrate in the molten state. Each phase in the 300°C,O<sub>2</sub> films may have a different chemistry and crystal structure but XPS, Raman, XRD, or energy dispersive x-ray spectroscopy can not be used to probe them separately because the probing radiation is large compared to the size of the dark particles.

In summary, the films are all crystalline based on XRD data but Raman data best show their degree of similarity (perfection) to the target material: RT,vac < RT,O<sub>2</sub> < 300°C,vac < 300°C,O<sub>2</sub>. The films are oxygen deficient with the RT,vac film having the lowest oxygen concentration. SEM data clearly show nanophases in the RT,O<sub>2</sub> and 300°C,vac films.

The results of the current study clearly demonstrate that the friction coefficients of pulsed laser deposited ZnO films, particularly RT,O<sub>2</sub> and 300°C,vac are comparable to that of commonly used solid lubricants like graphite. It is noted that the friction coefficient of hot pressed ZnO is rather high, 0.65. Zinc oxide, either in powder form or as a disk, does not provide a lubricious surface, whereas nanophase PLD ZnO films provide lubricious surfaces with friction coefficients of less than 0.2 and wear lives as high as a million cycles.

Among the various PLD ZnO films, the RT,O<sub>2</sub> and at 300°C,vac films had the lowest friction. Interestingly, these two films had nanoscale microstructural features. For instance, the RT,O<sub>2</sub> film had clusters which are of 50 to 60 nm in size, and the 300°C,vac film had a granular structure with an extremely fine grain size. By contrast, the RT,vac film is almost featureless even at a magnification of 50K. Finally, the 300°C,O<sub>2</sub> film showed dual-phase microstructure with submicron particles. The Raman spectrum of this film most closely resembles that of the target indicating the onset of a microstructure with a sufficiently large target-like phase. Adjusting the microstructure further toward that of the target is clearly undesirable. It is worth noting that the friction

coefficient of these latter two films is not as low as those containing nanoscale features.

It is well established that the plastic deformation of crystalline solids occurs by the movement of lattice dislocations and/or by diffusional creep. In the case of oxides the lattice dislocations are usually immobile, and plastic deformation by diffusional creep is significant only at temperatures close to the melting point. That is why the friction coefficient of ZnO powder and the hot pressed ZnO disk were found to be high. However, reducing the grain size of ceramics to nanometer levels may allow plastic flow by diffusional creep even at room temperature (20). SEM examination of the wear scars revealed RT, O<sub>2</sub> films show a significant amount of plastic deformation. A typical micrograph showing heavy deformation is given in Figure 2e. Although a contribution to low friction from oxygen substoichiometry can not be ruled out, the results described in this study indicate that the lubricious nature of the two ZnO films (RT, O<sub>2</sub> and 300°C, vac) at room temperature is due to plastic deformation induced by small grain size. Thus there is significant potential for ZnO to be useful as a high temperature solid lubricant.

#### 4 ADAPTIVE LUBRICANT FILMS

##### 4.1 Background

As discussed earlier, there is no solid lubricant that provides good tribological properties from subambient to >700°C. One potential concept, nanophase lubricious oxides, is being evaluated for this purpose as discussed in the previous section. Alternate materials being explored are adaptive lubricants. Adaptive lubricant materials are selected by considering the different reactions among materials comprising the lubricant and components of the environment (e.g., O<sub>2</sub>, H<sub>2</sub>O in air). Thermodynamics and the available data base of solid lubricants are used to guide the selection of materials. A successful adaptive lubricant would provide a low friction surface at room temperature to its oxidation point. Components in the environment would then react with the solid components to form the high temperature lubricant. Since oxidation reactions are usually irreversible, adaptive lubricants must be engineered so that they can be cycled between low and high temperatures. The engineering challenge arises at this point. The exposed lubricant surface must be lubricious at all times, so materials in the bulk cannot react with each other to form high temperature lubricants. The reaction must be dependent on the presence of atmospheric components interacting at the surface. Even when this criteria is met, oxygen can diffuse through the top layers and eventually convert the entire film to high temperature lubricant. Concepts are under evaluation to overcome these limitations. Layering the adaptive lubricant components between diffusion barriers is one approach. Another concept is to include the adaptive components in a diffusion barrier support matrix [18]. In such a system, the solid components would not react with each other or with the atmosphere until they were shear activated. This means that encapsulated materials exposed during wear provide low friction at low temperature. As temperature increases, they

react to form high temperature lubricant (generally poor low temperature lubricant). As temperature decreases, the high temperature material would be worn off causing high friction and wear. As the matrix wears, unreacted low temperature lubricant buried in the matrix is released.

The purpose of this research is to investigate the synthesis-structure-property relationships of some potential adaptive lubricants grown by pulsed laser deposition. PLD was selected for film deposition because it permits precise control of chemical and physical properties of lubricant materials [18]. PbO-MoS<sub>2</sub> mixtures were selected for evaluation because they react with air to form PbMoO<sub>4</sub> [28]. MoS<sub>2</sub> based films have good tribological properties at room temperature and PbMoO<sub>4</sub> thin films have been demonstrated to have good tribological properties at 700°C [23]. ZnO-WS<sub>2</sub>, and ZnO-MoS<sub>2</sub> were also selected for investigation because they form oxythiomolybdates, molybdates, oxythiotungstates, and tungstates which have been demonstrated to have good potential for high temperature applications [2,6,29]. Substrate temperature and the relative fraction of components were varied to control film crystallinity and chemistry. The reactions leading to adaptive behavior were evaluated by heating the samples in air.

##### 4.2 Experimental Details

The major objective of this research was to grow adaptive lubricant films with different component fractions and varying degrees of crystallinity. In order to achieve this objective, a number of different deposition conditions were employed as listed in Table 5.

A pressed disk of the adaptive components was used as the target. The crystal structures of the materials were: WS<sub>2</sub>, MoS<sub>2</sub> - hexagonal, PbO - orthorhombic, and ZnO - hexagonal. Substrates were fabricated from 440C stainless steel coupons that were polished to 0.01 μm and washed in soap and water and then cleaned ultrasonically in hexane, acetone and methanol. Prior to deposition, the specimens were degassed at 573K for 1 h and allowed to cool to room temperature. The duration of each deposition was adjusted to provide films that were about 200.0 nm thick.

Friction measurements were made as before except a constant rotation speed of 200 RPM was used. Tests were run in dry N<sub>2</sub> and 50% RH air; measurements were made at room temperature. Wear life was defined as the number of revolutions before the friction coefficient reaches 0.4; film failure was always catastrophic.

##### 4.3 Results

Surface chemistry and stoichiometry were determined from analyses of the Zn 2p<sub>1/2-3/2</sub>, Mo 2p<sub>1/2-3/2</sub>, W 4f<sub>5/2-7/2</sub>, S 2p<sub>1/2-3/2</sub>, and O 1s XPS spectra. Binding energies, spectral areas, and peak full-width-half-maximums (FWHM) were

Table 5: Target and film compositions of adaptive lubricants

	Temp. (°C)	M1/M2	% MoS <sub>2</sub> , WS <sub>2</sub>	S <sub>n</sub>	% oxide	Balance
PbO-MoS <sub>2</sub>	RT	0.25	38	49	1	12 - PbMo <sub>0.76</sub> S <sub>1.7</sub> O <sub>1.4</sub>
PbO-MoS <sub>2</sub>	RT	0.5	34	16	3	47 - PbMo <sub>0.24</sub> S <sub>1.3</sub> O <sub>2.5</sub>
PbO-MoS <sub>2</sub>	RT	1	23	7	2	68 - PbMo <sub>0.23</sub> S <sub>1.4</sub> O <sub>0.5</sub>
PbO-MoS <sub>2</sub>	300	0.25	74	-	5	21 - PbMo <sub>0.54</sub> S <sub>0.62</sub> O <sub>0.87</sub>
PbO-MoS <sub>2</sub>	300	0.5	58	-	4	38 - PbMo <sub>0.14</sub> S <sub>0.96</sub> O <sub>0.81</sub>
PbO-MoS <sub>2</sub>	300	1	23	-	5	72 - PbMo <sub>0.15</sub> S <sub>1.0</sub> O <sub>0.3</sub>
ZnO-WS <sub>2</sub>	RT	1	11	-	7	50 - Zn(O+S) <sub>1.0</sub>
ZnO-WS <sub>2</sub>	300	1	9	-	9	65 - Zn(O+S) <sub>0.8</sub>
ZnO-MoS <sub>2</sub>	RT	1	50	-	-	50 - Zn(O+S) <sub>1.1</sub>
ZnO-MoS <sub>2</sub>	300	1	26	-	9	65 - Zn(O+S) <sub>1.1</sub>

RT = room temperature; M1/M2 = ratio of (Pb or Zn)/(Mo or W); oxide includes trioxides, tungstates, and molybdates

determined by fitting XPS spectra to Voight functions. Measured spectral areas from XPS data and sensitivity factors from SSI were used to determine the relative mole fractions of components near film surfaces. Table 5 lists film components and relative mole fractions.

Table 6. Friction coefficients and wear lives, in dry N<sub>2</sub>

	300K		573K	
	μ	1000 cycles	μ	1000 cycles
1/1 PbO - MoS <sub>2</sub>	0.04	369	0.04	390
0.5/1 PbO - MoS <sub>2</sub>	0.03	395	0.05	375
0.25/1 PbO - MoS <sub>2</sub>	0.04	285	0.03	311
ZnO-WS <sub>2</sub>	0.03	>800	0.03	7
ZnO-MoS <sub>2</sub>	0.03	>800	0.04	500
100% WS <sub>2</sub>	0.04	80	0.04	250
100% MoS <sub>2</sub>	0.03	70	0.04	290

<sup>1</sup> Composite film thickness was half as thick as 100% MoS<sub>2</sub>, WS<sub>2</sub> films to limit the length of tribo-testing.

#### 4.3.1 PbO-MoS<sub>2</sub>

The PbO-MoS<sub>2</sub> (0.25/1, 0.5/1 and 1/1) films deposited at 300K provided featureless Raman spectra. This indicates that film components were not Raman active or that crystalline domains were less than about 25Å in diameter. Raman spectra of (1) room temperature films annealed in 248 nm laser radiation and (2) the 1/1 PbO-MoS<sub>2</sub> film annealed at 773K in air for 0.5 h shown in Figure 3a are crystalline. Films deposited on substrates at 573K using the 0.25/1, 0.5/1 and 1/1 PbO-MoS<sub>2</sub> targets provided Raman spectra (not shown) that revealed the films contained a fraction of crystalline MoS<sub>2</sub>. The friction coefficients and the wear lives of the films are listed in Table 6. Raman spectra of wear debris and transfer films from some of the composite coatings are presented in Figure 3b. Formation of MoO<sub>3</sub> and PbMoO<sub>4</sub> was observed.

#### 4.3.2 ZnO-MoS<sub>2</sub> and ZnO-WS<sub>2</sub>

The relative atomic fractions of the different components in the films are shown in Table 5. Crystal structure was determined by analysis of the Raman spectra shown in Figures 4a and 4b.

The Raman data collected from the different films after having been annealed at 500 - 800°C in 100°C steps are displayed in Figure 4. Crystalline WS<sub>2</sub> was observed in films grown at 300°C. MoS<sub>2</sub> films grown at 300°C were amorphous. The difference in ablation rates for WS<sub>2</sub> and MoS<sub>2</sub> accounts for the difference in concentrations between films. Friction and wear data collected from the different films are presented in Table 6.

## 4.4 DISCUSSION

### 4.4.1 PbO-MoS<sub>2</sub>

**Composition and Chemistry.** The mole fractions of Pb, Mo and S listed in Table 5 show that film surfaces have greater proportions of Pb and S than expected from target compositions and are O deficient. The level of S enrichment at the surface agrees with earlier studies of PLD MoS<sub>2</sub> films [18] where: (1) XPS demonstrated that film surfaces were S rich (elemental S) and (2) RBS showed that the bulk films were nearly stoichiometric, supporting assignment of excess sulfur to the surface. The increased concentration of Pb at film surfaces is understood by considering that PbO targets are ablated at a higher rate than MoS<sub>2</sub> targets. Oxygen deficiencies are likely caused by O atom recombination in the plasma and at film surfaces whereupon it leaves the growing film/plasma interface.

Raman spectra of RT, amorphous films, show the presence of crystalline MoS<sub>2</sub> after laser annealing at 38 mJ/cm<sup>2</sup>. Based on the results of earlier studies, it is likely that amorphous MoS<sub>2</sub> was present before annealing and that laser irradiation merely served to nucleate crystals that were large enough for detection by Raman spectroscopy. Films grown at 300°C contained a fraction of crystalline MoS<sub>2</sub>. The fraction of MoS<sub>2</sub> in the different films increased with the fraction of MoS<sub>2</sub> in the targets. No other components were observed in the Raman spectra. This suggests that PbO is not present in significant quantity because deposition of PbO from a single component target provided a well defined Raman fingerprint. The presence of PbS cannot be ruled out since PbS has no first order Raman modes. XPS spectra were quite complex and it is noted that assignments made by deconvolution of complex spectra may

not be unique. The components assigned to the different films are listed in Table 5 and include:  $\text{MoS}_2$ ,  $\text{PbMoO}_4$ ,  $\text{MoO}_3$ , elemental S, and Pb-Mo-S-O compounds that were not formally identified. Most importantly,  $\text{MoS}_2$  and Pb-Mo-S-O compounds were dominant and the oxides were present in small (i.e., <7%) fractions.

Raman spectra of the transfer film or wear debris from the 1/1 RT film (tested in 50% RH air) are shown in Figure 3b and demonstrate that mechanical stressing and/or frictional heating (1) induce crystallinity in the  $\text{MoS}_2$  phase, and (2) provide energy to promote reactions between the film and air to produce  $\text{PbMoO}_4$  and  $\text{MoO}_3$ . After mechanical stressing, the 0.25/1 and 0.5/1 PbO- $\text{MoS}_2$  films provide similar Raman spectra, so they are not shown. Raman spectra of wear debris from pure  $\text{MoS}_2$  films demonstrate that mechanical stressing induces crystallinity and produces  $\text{MoO}_3$ . Figure 3b shows Raman spectra of the transfer film or wear debris from the 1/1 film deposited at 573K and tested in air. This data demonstrates that tribomechanical stress and frictional heating induce crystallinity in  $\text{MoS}_2$ .  $\text{PbMoO}_4$  and  $\text{MoO}_3$  were not observed as with the films deposited at 300K. The amorphous Pb-Mo-S-O phase appears to be more thermodynamically stable toward oxidation than in the 300K films. The "adaptive" composite films may have provided superior wear lives compared to  $\text{MoS}_2$  due to increased oxidation resistance and/or by forming lubricant species during reaction with air (i.e.,  $\text{PbMoO}_4$ ).

**Friction and Wear Results.** An important result of this study is that PbO- $\text{MoS}_2$  films have significantly longer wear lives than  $\text{MoS}_2$  or PbO single component films. Films deposited in this study last about 5 times longer than pure  $\text{MoS}_2$  films deposited at room temperature. It should be noted that the films employed in the present study were only 1/2 as thick as films employed in PLD  $\text{MoS}_2$  studies. For thin  $\text{MoS}_2$  films, it is generally observed that wear life increases almost linearly with thickness. Indeed, a 1/1 film of equal thickness to the earlier  $\text{MoS}_2$  films provided a wear life in excess of 600,000 cycles (the test was terminated before the film failed). Thinner films were deposited for this study so that they could be tested in shorter times.

#### 4.4.2 ZnO- $\text{MoS}_2$ and ZnO- $\text{WS}_2$

The objective of this study was to evaluate the potential of ZnO- $\text{MoS}_2$  and ZnO- $\text{WS}_2$  to behave as adaptive lubricants. First, the as-deposited film chemistry and crystal structure were characterized and then their tribological behavior was established at RT. The second step was to heat the films in air at 500-800°C in 100°C intervals and recharacterize them to determine if the predicted high temperature lubricants were formed.

**Composition and Chemistry.** The films grown at room temperature were amorphous or their crystalline domains were too small to be detected by Raman spectroscopy or XRD.

XPS data showed the presence of  $\text{MoS}_2$  and  $\text{WS}_2$  bonding. Zn was oxidized; it was bonded to sulfur, oxygen or both elements. Since the binding energy of the Zn 2p peaks for ZnO and ZnS are close and the peaks were broad, no attempt was made to discriminate between the two. In fact, when the oxygen and sulfur not bonded to Mo or W were added together and compared to zinc:  $\text{Zn}/(\text{O}+\text{S})$  was approximately equal to one. This suggests that both elements are bonded to Zn in a substituted compound.

There was no significant quantity of  $\text{MoO}_3$  or  $\text{Mo}^{+6}$  present in the RT films. About 38% of the available W was in the +6 oxidation state. The binding energies of the W 4f and O 1s peaks suggest  $\text{WO}_3$ . However, the presence of Zn oxythiotungstates or Zn tungstates cannot be ruled out. Formation of complex chemistries would seem unlikely due to the fast arrival rate of material, low temperature, and high thermodynamic stability of the two element oxides and sulfides. Since  $\text{WO}_3$  is a stable compound, the  $\text{W}^{+6}$  was assigned to it. It should be noted here that the targets were mixed to provide a 1/1 molar ratio of W and Mo to Zn. The Mo films reflect this ratio almost exactly, while the surface of the W films are quite rich in Zn (i.e.,  $\text{Zn}/\text{Mo} = 4.5$ ). Differences in ablation rates are likely responsible for the observed concentrations. The corresponding larger fraction of O in the plume contributed to the high fraction of W+6 in the ZnO- $\text{WS}_2$  films.

The ZnO- $\text{WS}_2$  films grown on substrates held at 300°C contained a fraction of crystalline  $\text{WS}_2$ . The ZnO- $\text{MoS}_2$  films had very small crystallites or were amorphous. XPS data showed the presence of  $\text{MoS}_2$  and  $\text{WS}_2$  bonding in the films. Zn had approximately the same binding energy as in the RT films and the  $\text{Zn}/(\text{O}+\text{S})$  ratio was very close to one. Therefore, the substituted compound is again suggested. Of the Mo present, about 26% was  $\text{MoO}_3$ . Fifty percent of the W was  $\text{WO}_3$ . The presence of Zn/Mo oxythiotungstates or Zn/Mo tungstates cannot be ruled out, but for the same reasons as discussed for the RT films, the high binding energy states were assigned to trioxides. Mo containing films grown at RT had a 1/1 Mo/Zn ratio while the ratio was less than one for the 300°C films. At higher temperature and with energy added to the surface by the plume, the  $\text{MoO}_3$  ( $T_{\text{sublime}} = 600^\circ\text{C}$ ) was likely more volatile, decreasing the fraction of Mo in the film. There was no difference in the relative fraction of W in the RT and 300°C films. The fact that  $\text{WO}_3$  does not sublime and has a melting temperature of 1770°C supports the argument for the loss of Mo.

**Friction and Wear Results.** All of the films provided low friction coefficients (i.e., < 0.04). The Mo films grown at RT provided the longest wear life. Mo films grown at 300°C had shorter wear lives and slightly higher friction. This is likely due to their increased  $\text{MoO}_3$  content. The W films grown at RT performed nearly as well as the Mo films. This is somewhat surprising because they had a significant fraction of  $\text{WO}_3$  present and the fraction of lubricant on the surface was small (i.e., 11% was lubricant). The W containing films

grown at 300°C failed almost immediately. It is tempting to presume that the cause of the failure is the high trioxide content, but the reason for early failure has not been pursued. Wear debris and/or transfer films of coatings rubbed in air contained  $\text{MoO}_3/\text{ZnMoO}_4$  and  $\text{WO}_3/\text{ZnWO}_4$ . Films rubbed in air had shorter wear lives than those rubbed in  $\text{N}_2$ . Rubbing also induced crystallinity of amorphous  $\text{WS}_2$  and  $\text{MoS}_2$ .

**Anneals in air.** After the 500°C anneal, the Mo films showed Raman bands for crystalline  $\text{MoS}_2$ ; no other crystalline material was observed. For pure  $\text{MoS}_2$  films, anneals to 500°C cause film oxidation and  $\text{MoO}_3$  bands are observed in the Raman spectra. A possible explanation for the difference is that the  $\text{Zn}(\text{O}+\text{S})$  may be forming a diffusion barrier and limiting the oxidation to the surface region.  $\text{WS}_2$  and  $\text{WO}_3$  were observed at 500°C. At temperatures above 700°C, high temperature lubricants were observed (i.e.,  $\text{ZnMoO}_4$  and  $\text{ZnWO}_4$ ). It is noted that the Mo containing films lost Mo as the temperature was increased. This is likely due to the volatility of  $\text{MoO}_3$  intermediate.  $\text{ZnO-WS}_2$  films appear to have the greatest potential because they do not lose lubricant metal as did the  $\text{ZnO-MoS}_2$  films. In addition, they do not contain Pb which is becoming increasingly unacceptable because of environmental concerns.

$\text{PbO-MoS}_2$ ,  $\text{ZnO-WS}_2$ , and  $\text{ZnO-MoS}_2$  films deposited by PLD at 300 and 573K provide significantly longer wear lives than single component  $\text{WS}_2$  or  $\text{MoS}_2$  films. The chemistry of the films is controlled by (1) the relative fraction of target components, (2) the temperature of the substrate during deposition, (3) the level of post deposition anneals and (4) the kinetics and thermodynamics of plasma recombination during deposition. Thermal annealing and tribomechanical stressing provide energy for crystallizing  $\text{MoS}_2$  and  $\text{WS}_2$  and for promoting reactions with air to form  $\text{PbMoO}_4$ ,  $\text{ZnWO}_4$ ,  $\text{ZnMoO}_4$ ,  $\text{WO}_3$ , and  $\text{MoO}_3$ . Composite films therefore act as "adaptive" lubricants by changing with the environment to alternate lubricious states.

## 5 CONCLUSIONS

There is significant potential to produce low friction, low wear coatings using the nanophase oxides and adaptive lubricants concepts. PLD is an effective process to grow the new types of films and has been used to produce: (1) nanophase  $\text{ZnO}$ , and (2)  $\text{PbO-MoS}_2$ ,  $\text{ZnO-MoS}_2$ , and  $\text{ZnO-WS}_2$  adaptive lubricants. To fully explore the potential of the new materials, high temperature tribo-tests must be completed and is the subject of continuing research.

## 6 REFERENCES

1. E.L. McMurtrey, NASA TM-86556 (1985).
2. J.P. King and N.H. Forster, AIAA Paper 90-2044, presented at AIAA, SAE, ASME, and ASEE Joint Propulsion Conference, 26th Orlando, July 16-18, 1990.
3. M.N. Gardos, Tribol. Trans., 31 (1988) 427.
4. M.N. Gardos, Tribol. Trans., 33 (1990) 209.

5. M.B. Peterson and R.L. Johnson, Lubrication Eng., 13 (4) (1957) 203.
6. M.B. Peterson, S.F. Murray, and J.J. Florek, ASLE Transactions, 2 (1960) 225.
7. V. Buck, Thin Solid Films, 139 (1986) 157.
8. V. Buck, Wear, 114 (1987) 263.
9. Jeffrey S. Lince, J. Mater. Res., 5(1) (1990) 218.
10. J.R. Lince and P.D. Fleischauer, J. Mater. Res., 2 (1987) 827.
11. P.D. Fleischauer, ASLE Trans., 27 (1984) 82.
12. M. Matsunaga, T. Homma, and A. Tanaka, ASLE Trans., 25 (1982) 323.
13. T. Spalvins, J. Vac. Sci. Technol. A, 5(2) (1987) 212.
14. C. Muller, C. Menoud, M. Maillat, and H.E. Hintermann, Surf. and Coatings Technol., 36 (1988) 351.
15. R.N. Bolster, I.L. Singer, J.C. Wegand, S. Fayeulle and C.R. Gosset, presented at the ICMCTF-90, San Diego, CA 1990.
16. Hiroki Kuwano and Kazutoshi Nagai, J. Vac. Sci. and Technol. A, 4(6) (1986) 2993.
17. Hiroki Kuwano and Kazutoshi Nagai, J. Vac. Sci. and Technol. A, 3(4) (1985) 1809.
18. "Tribological Materials", by M.S. Donley and J.S. Zabinski in Pulsed Laser Deposition of Thin Films, edited by D.B. Chrisey and G.K. Hubler, John Wiley and Sons, New York (1994), pp. 431-453.
19. S.J.P. Laube, Hierarchical Control of Pulsed Laser Deposition Processes for Manufacture, Dissertation, Division of Research and Advanced Studies for the University of Cincinnati, Cincinnati OH, 15 Feb 1994.
20. R. Birringer, H. Gleiter, H-P. Klein and P. Marquardt, Phys. Lett. 102A (1984) 365.
21. J. Karch, R. Birringer and H. Gleiter, Nature, 330 (1987) 556.
22. J. S. Zabinski, M. S. Donley, V. J. Dyhouse, N. T. McDevitt, in Photons and Low Energy Particles in Surface Processing, edited by C.I.H. Ashby, J.H. Brannon, and S.W. Pang, (MRS Symposium Proceedings - 236), Materials Research Society (1992), Pittsburgh, PA, pp 437-442.
23. J.S. Zabinski, A.E. Day, M.S. Donley, C. DellaCorte, and N.T. McDevitt, J. of Mater. Sci., 29 (1994) 5875.
24. N.J. Ianno, L. McConville, N. Shaikh, S. Pittal, and P.G. Snyder, Thin Solid Films, 220 (1992) 92-99.
25. V.S. Ban and D.A. Kramer, J. Mater. Sci., 5 (1970) 978-982.
26. J.F. Ready, Appl. Phys. Lett., 3(1) (1963) 11-13.
27. see for example chapters by, Li-Chyong Chen and J.T. Cheung in Pulsed Laser Deposition of Thin Films, eds. D.B. Chrisey and G.K. Hubler, John Wiley and Sons, New York (1994).
28. J.S. Zabinski, M.S. Donley, V.J. Dyhouse, and N.T. McDevitt, Thin Solid Films, 214 (1992) 156-163.
29. S.D. Walck, N.T. McDevitt, J.E. Bultman, and J.S. Zabinski, Characterization of Pulsed Laser Deposited  $\text{ZnO-WS}_2$  Thin Solid Film Lubricants, Proc. of the 53rd Annual Meeting of the Electron Microscopy Society of America, San Francisco Press, Kansas City (1995).

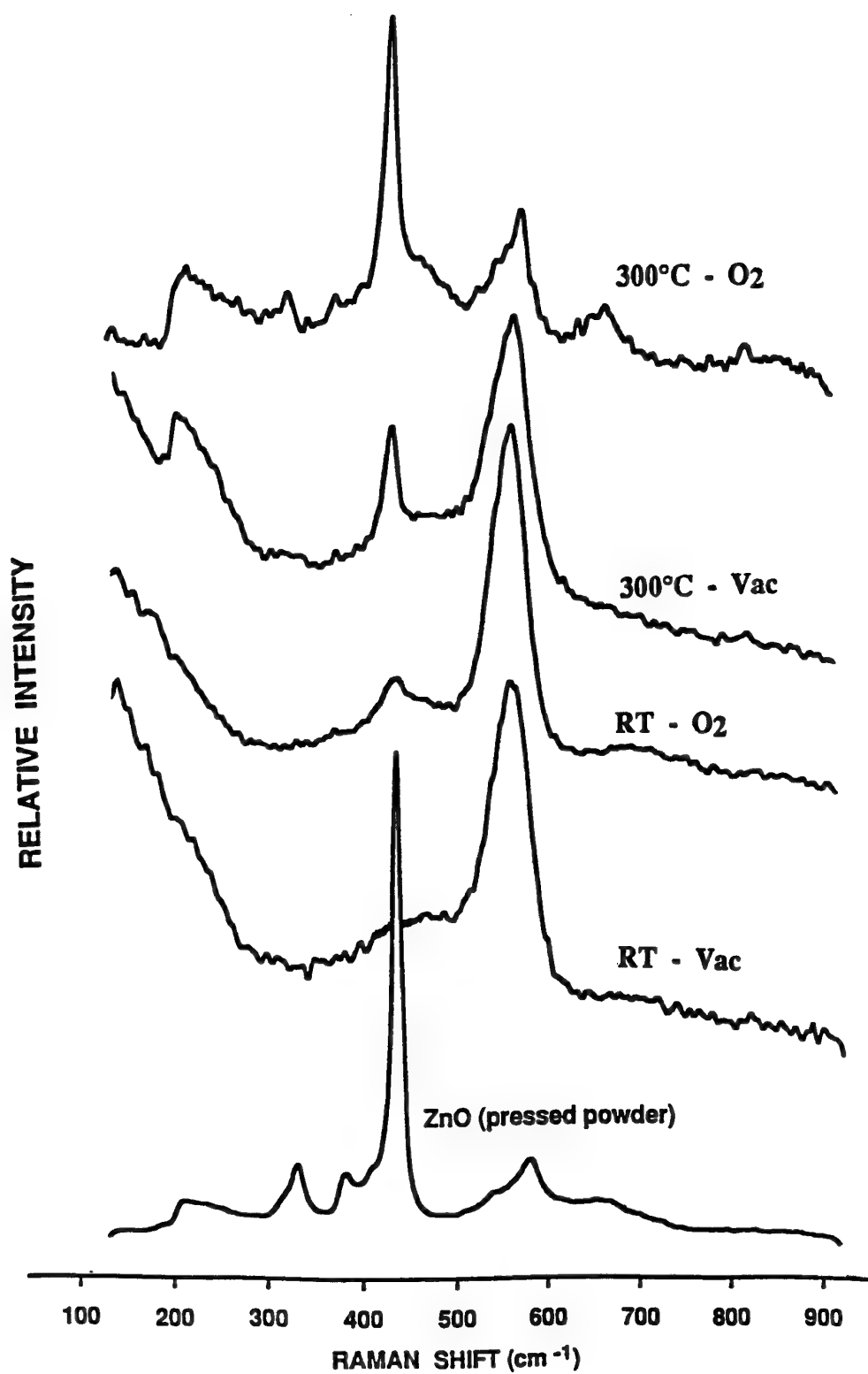


Figure 1: Raman spectra from ZnO powder and the different films.

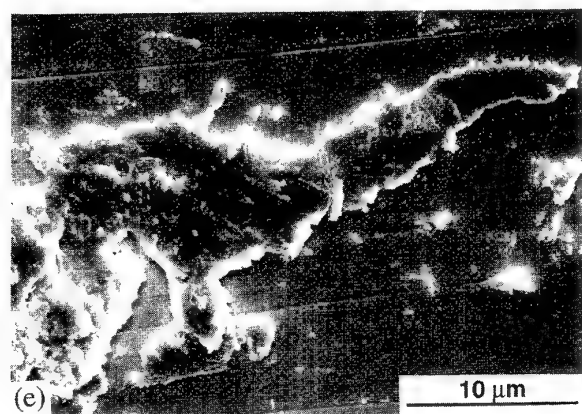
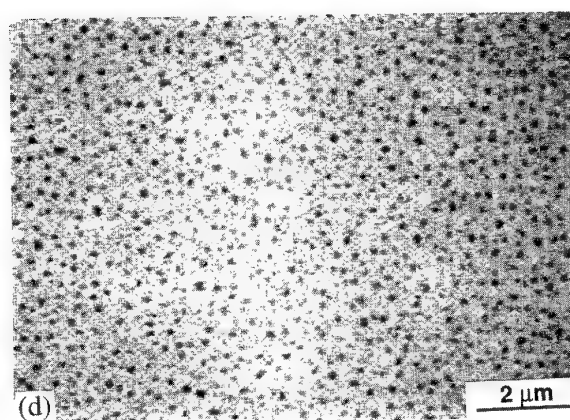
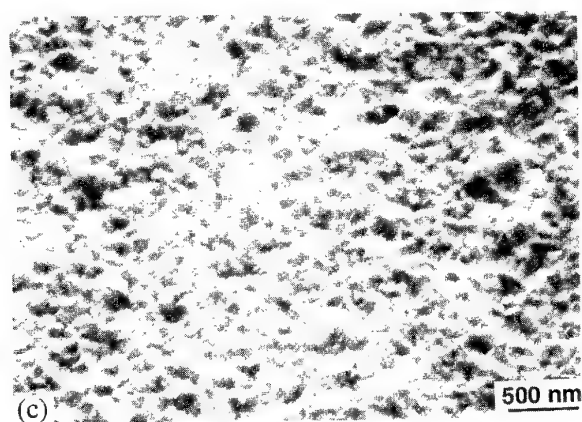
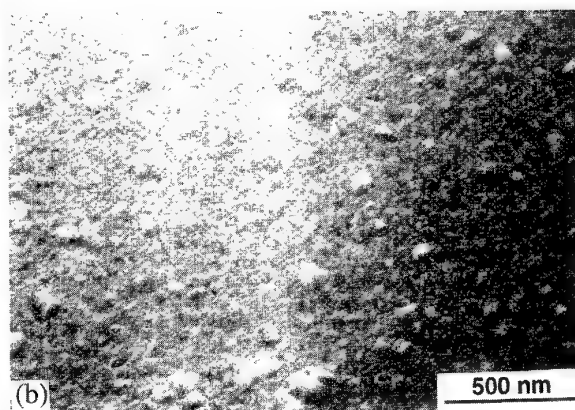
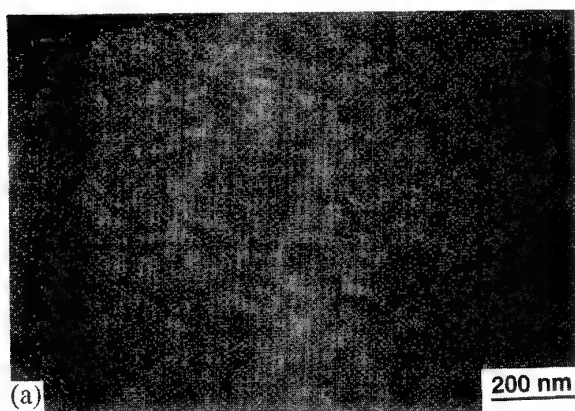


Figure 2: Scanning electron micrographs of PLD ZnO films: (a) RT,vac; (b) RT,O<sub>2</sub>; (c) 300°C,vac; (d) 300°C,O<sub>2</sub>; and (e) a typical wear scar showing deformation of ZnO.

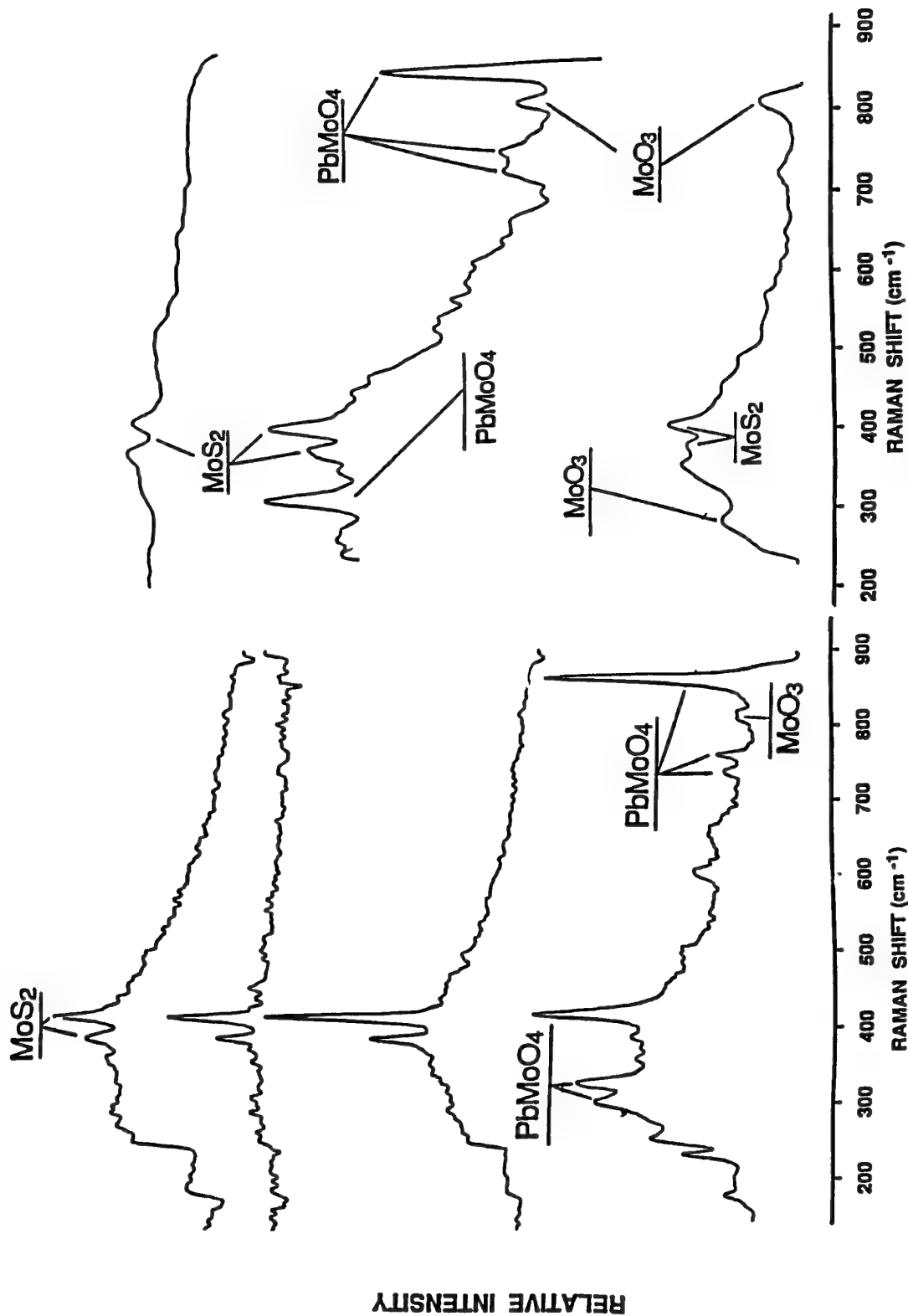


Figure 3a: Raman spectra of (from top to bottom); 0.25/1, 0.5/1, and 1/1 PbO-MoS<sub>2</sub> films annealed in 248 nm laser radiation at 38 mJ/cm<sup>2</sup>, and the 1/1 PbO-MoS<sub>2</sub> film after heating in air at 773K.

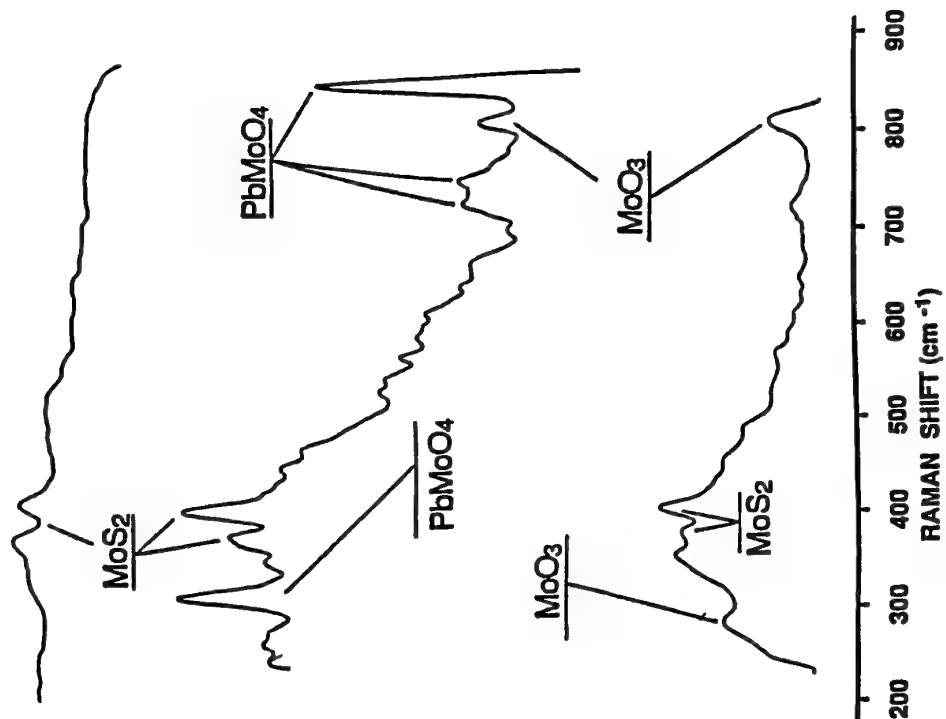


Figure 3b: Raman spectra of wear tracks (from top to bottom); MoS<sub>2</sub>, 1/1 PbO-MoS<sub>2</sub> deposited at 300°C, and 1/1 PbO-MoS<sub>2</sub> deposited at 573°C.



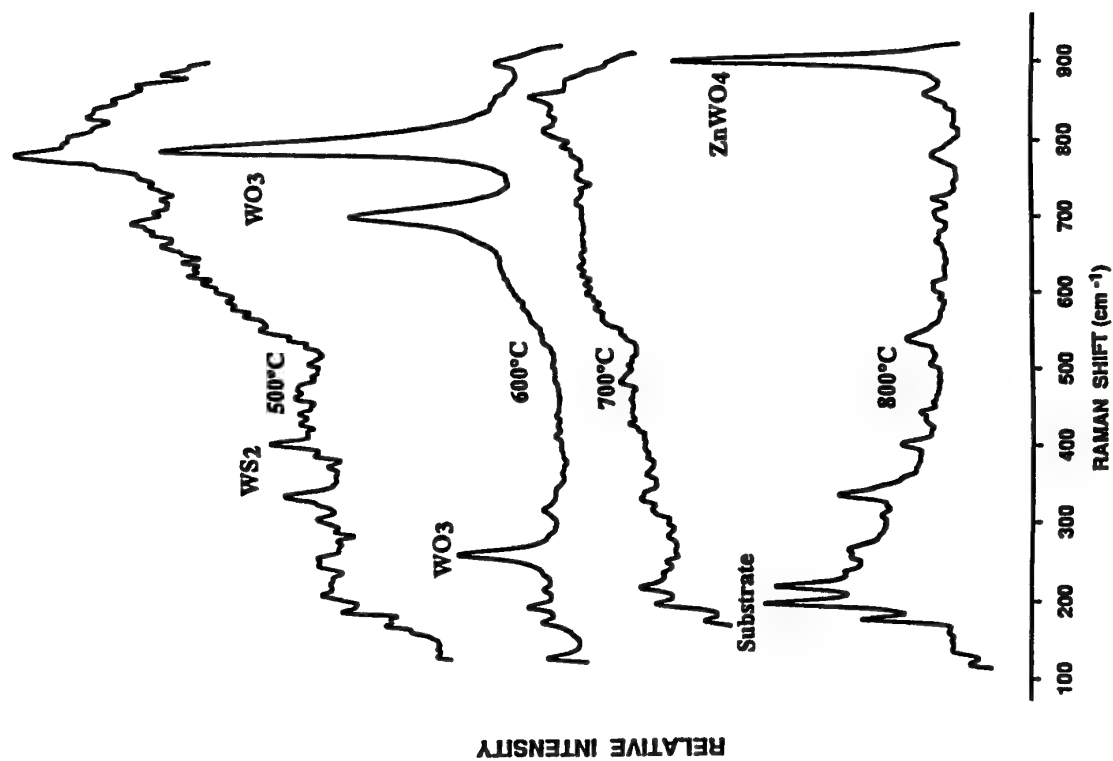


Figure 4a: Raman spectra of  $\text{WS}_2$ - $\text{ZnO}$  films after heating to different temperatures for 0.5 hours.

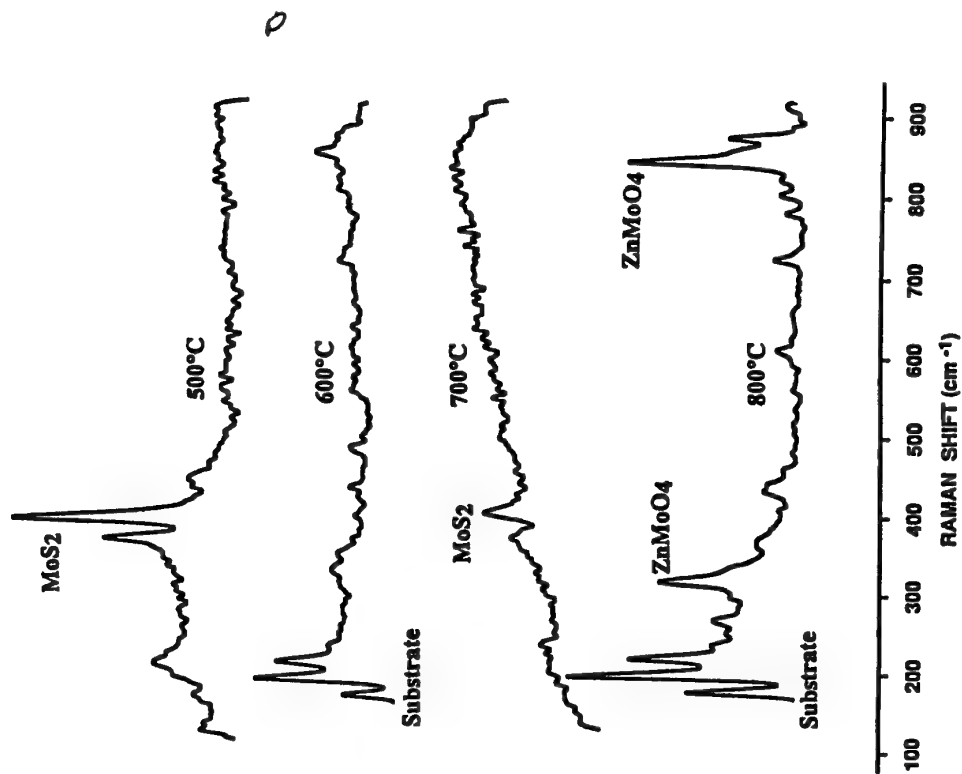


Figure 4b: Raman spectra of  $\text{MoS}_2$ - $\text{ZnO}$  films after heating to different temperatures for 0.5 hours.

## ADVANCED HARD COATINGS AND WEAR RESISTANT MATERIALS FOR AEROSPACE

J.S. Zabinski, A.A. Voevodin, and M.A. Capano, WL/MLBT Materials Directorate  
WPAFB, OH 45433

### SUMMARY

Increasing demands placed on aerospace systems with respect to performance, lifetime, and operational environment have pushed lubrication and coatings technology to its limit. To meet increased demands, a number of hard, wear resistant coating materials and deposition processes are being developed. Discussion in this paper includes transition metal nitrides/carbides and diamond-like carbon (DLC). In particular, the use of these materials in multilayer and functionally gradient architectures and as corrosion resistant, boundary lubricants for candidate high temperature turbine engine oils is highlighted. To effectively use new coating materials, processes that permit the growth of coatings at low temperature are required. This prevents loss of dimensional tolerance and loss of mechanical properties of precision components. Several low temperature deposition processes are discussed, including a combined pulsed laser deposition - sputter source that permits the growth of infinitely variable gradients and sharp interfaces.

### 1 INTRODUCTION

Advances in hard coating technology are required for aerospace systems operating in extreme environments. Targeted operational temperature and lifetime requirements are beyond current capabilities. For example, to increase the thrust to weight ratio in turbine engines, fluids are under development for operation at temperatures above 340°C. Corrosion resistant coatings that have low friction surfaces have significant potential for advancing this high temperature fluid technology. Other advanced coatings applications include fuel pumps, turbine engines, sleeves, actuators, gears, splines, optics, magnetically levitated bearings, and bearings in momentum control devices for space systems. A particularly difficult challenge is to provide a wear and corrosion resistant coating that also has a low friction surface. Perhaps equally as challenging is to develop a coating process that can be used to apply good coatings at low temperature. Technological advancements may be achieved through development of coating materials, processes, and coatings strategies. Materials discussed in this report are diamond-like carbon, transition metal carbides/nitrides and carbo-nitrides. While sputter deposition was used to grow some films, the technique is not discussed since it is widely utilized and has been extensively studied. Instead, the processes that this report focuses on are pulsed laser deposition (PLD) and a combined PLD-magnetron technique that has the capability to precisely layer and functionally grade hard coatings. Using these processes, multilayer and functionally gradient coating strategies that have been evaluated are discussed.

There are a number of excellent reviews of hard coating, multilayers, and thin film deposition technologies that have been published recently [1-6]. Because they are available, it is not the intention here to review hard coatings and hard coating technology. Coating research on-going at the Materials Directorate, Wright Laboratory will be presented. Materials that are discussed can be grouped into two categories. The first category is known or existing coatings. Here, evaluation of the behavior of well characterized TiN in hot, candidate high temperature turbine engine oil is presented. The candidate fluid is a perfluoropolyalkylether (PFPAE). It holds great promise, but has two shortcomings: (1) they are poor boundary and elastohydrodynamic lubricants, and (2) they can chemically react with steel surfaces [7]. Indeed, iron is one of the more reactive metals with PFPAE's. In earlier reports, coatings have been evaluated at room temperature [8-10]. This paper reports on the evaluation of TiN and electroless nickel at temperatures to 370°C.

The second category is new or emerging materials. This includes materials grown by new or emerging processes at low temperature and materials with new structures (e.g., multilayer and functionally gradient). Here, research has been directed toward growing hard, tough coatings with low friction surfaces. An additional requirement was that the coatings be applied at low temperature. TiC and diamond-like carbon (DLC) are candidate materials. TiC is a transition metal carbide that has a rigid framework of tightly bonded atoms. It is a refractory material that has a high melting point and high hardness. However, the friction coefficient is only modest (ca. 0.2-0.5) [2] and conventional deposition technologies can require substrate temperatures in the range of 500-1000°C to grow a dense, adherent film [11-14]. High processing temperatures introduce high levels of stress at the film-substrate interface in materials with different thermal expansion coefficients and can reverse the beneficial microstructural effects of heat treatment. DLC coatings grown by PLD are super-hard, approaching the hardness of natural diamond, and they have a low coefficient of friction [15]. In fact, it is as low as many of the well known solid lubricants such as MoS<sub>2</sub> and graphite. PLD can be used to grow both TiC and DLC films at low temperature [3,6,15-17]. However, both TiC and DLC tend to be brittle. To toughen the films, duplex, multilayer, and functionally gradient structures may be employed [2,4,5,18]. For TiC coatings, nitrogen can be incorporated into the crystal structure to both toughen and harden the coating [2,18,19]. This paper reports on: (i) the properties of TiC and DLC films grown at low temperature using PLD, (ii) a new magnetron-PLD technique to grow multilayer and functionally gradient coatings, (iii) the use of multilayer and functionally gradient architectures to provide tough /lubricious Ti/TiC/DLC based coatings, and (iv) the effects of adding nitrogen to PLD grown TiC (i.e., TiCN) coatings.

## 2. EXPERIMENTAL

### 2.1 Pulsed Laser Deposition

The system used for coating deposition is constructed from a stainless steel vacuum chamber that was specially instrumented for pulsed laser deposition and magnetron sputtering. A schematic of the system illustrating the components and the essential features of the technique are shown in Figure 1. There are five key components: (1) a laser, (2) optical beam steering and focusing, (3) an instrumented chamber, (4) a magnetron sputter gun and (5) a computer data collection and process control system. For the experiments discussed in this manuscript, a Lambda Physik LPX 110i excimer laser was filled with a Ne, KrF mixture to provide a beam of UV radiation at 248 nm. The beam was pulsed at a rate between 1 and 100 Hz (17 ns pulse width) and it was focused to a 1.0x1.5 or 2.0 by 4.0 mm rectangle on the target face providing a fluence of between 1 and 5.0 J/cm<sup>2</sup>, depending on the laser power setting. Beam steering was accomplished using a computer controlled raster mirror. An unbalanced magnetron that accepts 30 mm diameter targets was directed such that a perpendicular line originating from the center of the target intersects the center of the substrate. The laser target is positioned in the same fashion so that the laser plume is directed toward the center of the substrate. Using this arrangement, multilayer/functionally gradient materials were produced by varying laser pulse rate and/or magnetron power.

The base pressure in the chamber was  $9 \times 10^{-7}$  Pa for laser depositions. When the magnetron was used, the chamber was backfilled with Ar to 0.2 Pa. The target voltage was usually about 500V and the sputtering was performed at a constant power of 100W; this provided a Ti flux at the substrate to grow 10 nm/min. A calibrated quartz crystal oscillator was used to measure film thickness. Resistive heating was employed to degas and/or anneal the specimens; temperature was measured using an alumel-chromel thermocouple or infrared pyrometer. System parameters were monitored using a computer and include: film thickness, growth rate, system pressure, laser power, laser pulse rate, magnetron voltage, magnetron power, sample bias and residual gas concentrations.

TiN coatings were obtained from a commercial source that employed the cathodic arc method. The deposition chamber was backfilled with 8 mTorr of Ar and N was bled into the background as a reactive gas at several pressures. Substrate bias was used to vary the microstructure of the coatings.

### 2.2 Sample Preparation and Analysis

Substrates for tribo-tests were fabricated from 440C stainless steel (SS) coupons that were polished to 0.01  $\mu$ m; others were polished to 1  $\mu$ m. Materials were cleaned in soap and water and then ultrasonically washed in acetone and methanol. Glow discharge cleaning was employed to provide a clean metal surface immediately prior to deposition.

Surface chemistry of the coatings was studied with a Surface Science Instruments (SSI) M-probe XPS instrument operated at a base pressure of  $3 \times 10^{-7}$  Pa. Using an Al anode, a 400 X 1000 mm line spot, and a 25 eV pass energy, the full width at half maximum (FWHM) of the Au 4f<sub>7/2</sub> peak was 0.71 eV. Binding energy positions were calibrated against the Au 4f<sub>7/2</sub> peak and energy separations were calibrated using the Cu 3s and Cu 2p<sub>3/2</sub> peaks at 122.39 and 932.47 eV, respectively. Bulk chemistry and film crystallinity were investigated by Raman spectroscopy using a SPEX 1877 spectrometer and the incident light of a 514.5 nm Ar<sup>+</sup> laser. An intensified 1024 element, diode array detector was used to collect the Raman signal. Crystal structures were determined using data acquired by a Rigaku D/max -1B diffractometer equipped with a thin film attachment and a monochromator. High resolution scanning electron microscopy (SEM) was performed on the films using a Leica 360 field emission SEM equipped with an energy dispersive x-ray analyzer.

Room temperature friction and wear data were collected using a ball-on-flat tribometer. The ball was held in a lever arm, and the friction force was measured using strain gauge circuitry. The normal load was computed from the dead weight hung in the cantilever assembly. In order to maintain a constant humidity level in the test environment, the ball-disk assembly was enclosed in a chamber. Flow rates of dry air and saturated humid air were adjusted to control relative humidity from near zero to almost 100%. The percentage relative humidity was measured by a sensor inserted in the chamber. The tests reported here were run in dry air and moist air. Hardness and Young's moduli were measured using a Nanoindenter II. A Berkovich indenter was loaded in the range of 1-10 mN to cause a penetration of about 1/10 of the film thickness. Loading in this fashion and following procedures by Oliver and Farr, substrate effects and indentation size effects were minimized [20]. Hardness values were taken at the maximum penetration depth and moduli were calculated from the upper unloading portion of the load displacement curve. Adhesion measurements were made using a CSEM Revetester. Acoustic signal and friction were monitored to provide the critical load for decohesion/delamination and film breakthrough. Visual inspection of the scratches provided information about the toughness of the films. Optical micrographs were used to record images.

## 3 PROTECTIVE COATINGS FOR PFPAE's

### 3.1 Background

Aircraft engines can be made more efficient by operating at higher temperatures. Polyphenylether based MIL-L-87100, the most thermo-oxidatively stable gas turbine engine oil to date, can operate to about 288°C. The Air Force has been investigating perfluoropolyalkylethers (PFPAE) as candidate lubricants for use at temperatures to 370°C [21]. These fluids are thermodynamically stable and have acceptable viscosities

over a broad temperature range. They hold great promise but have two shortcomings (1) they are poor boundary and elastohydrodynamic lubricants, and (2) they can chemically react with steel surfaces [7]. Indeed, iron is one of the more reactive metals with PFPAE's. One approach to overcome these problems is to formulate additive packages to improve lubricity and to protect against fluid/metal degradation [22]. An alternative approach is reported in this paper whereby bearing steel surfaces are coated with protective material [23]. 440C steel was selected as a representative bearing steel and TiN was used as a protective coating.

TiN is resistant to corrosion. For example, Agarwal et. al have shown that TiN is effective in preventing corrosion in simulated aircraft engine tests [10]. Carre has demonstrated that it protects steel against degradation by PFPAE in bearing tests conducted at room temperature [9]. Finally, it is noted that coatings are used with PFPAE fluids in the space industry [8]. However, the temperature of the fluid is low in these applications. Titanium metal has been reported to be relatively inert towards PFPAE fluid at high temperature [24]. The reports cited suggest that TiN has a good probability of success for resisting corrosion in PFPAE at high temperature. The nature of the coating is extremely important for determining its protective capability. A porous coating with columnar microstructure would provide little protection; fluid could penetrate to the steel surface and cause corrosion. A fully dense coating with fine grained microstructure would be best for prevention of fluid penetration. It has been shown that in sputter deposition pressure and bias can be used to control TiN microstructure [25]. For this research, the zone T type microstructure was targeted [26]. The substrate biases and pressures used in this study were selected in a range around the values that the commercial vendor considered optimum, and they are discussed in the next section.

### 3.2 Experimental Details

The major objective of this research was to grow TiN coatings with different microstructures to determine the best corrosion resistant coating. In order to achieve this objective, six different deposition conditions were employed as listed in Table 1 below:

Table 1: Deposition parameters for TiN films

Coating	Pressure N <sub>2</sub> (mTorr)	Bias V
1.7/75	1.7	75
1.7/125	1.7	125
6/75	6.0	75
6/125	6.0	125
11/75	11.0	75
11/125	11.0	125

Washers made of 440C steel were used as the corrosion test coupons. The test was conducted as follows: (1) four washers separated by glass spacers were immersed in 6 ml of Fomblin Z (a linear perfluoropolyalkylether -CF<sub>3</sub>O[CF<sub>2</sub>CF<sub>2</sub>O]<sub>n</sub>-

[CF<sub>2</sub>O]<sub>m</sub>-CF<sub>3</sub>; n/m=1.5) with 1 % perfluoroalkyldiphenylether additive (2) 1.0 l/hour of air was bubbled through the fluid and then vented, and (3) washers were visually inspected and weighed [27]. Failure was defined as a weight loss of 0.2 mg/cm<sup>2</sup>; when severe corrosion occurred, buildup of corrosion product and "flaking" was observed. XPS, XRD, and hardness measurements were made on the 25 mm 440C steel disks discussed earlier.

### 3.3 Results

Surface chemistry and stoichiometry were determined from analyses of the Ti 2p<sub>1/2-3/2</sub>, N 1s, and O 1s XPS spectra. Peaks were fitted to Voigt functions by minimizing the Chi-squared value; N/Ti atomic ratios were determined from the fitted data. Carbon and oxygen contamination were present on the surface of all specimens due to handling in air. Specimens were sputter etched to remove surface contamination. Crystal structure and texture were determined from glancing angle x-ray diffraction (GAXRD) scans collected at several values of constant theta from 0.5-10.0 degrees. This permitted the evaluation of microstructural evolution through the coating thickness since increasingly glancing angles enhanced surface sensitivity. An example of the GAXRD data is shown in Figure 2. The hardness of the different coatings was 33±3 GPa except for the coatings grown at 11.0 mTorr which were slightly softer (i.e., 29±5 GPa).

The weight losses from the different specimens after treatment in PFPAE at different temperatures are listed in Table 2. Photographs of some of the washers are shown in Figure 3.

### 3.4 Discussion

#### 3.4.1 Coating chemistry

XPS was used to determine film chemistry and stoichiometry. Surfaces had an overlayer of TiO<sub>2</sub> and TiO<sub>x</sub> on them. Argon ion sputtering was used to remove the oxidized layers so that a more accurate N/Ti ratio could be measured. The remaining Ti 2p, N 1s, C 1s, and O 1s XPS peaks demonstrated that all of the films were mostly TiN with 1-8% oxygen and 3-8% carbon. The oxygen comes from 3 sources: (1) water vapor and O<sub>2</sub> contamination in the deposition chamber, (2) recontamination of clean surfaces by H<sub>2</sub>O and O<sub>2</sub> in the XPS during the course of analysis (e.g., about 2 hours), and (3) oxidized grain boundaries that are difficult to sputter etch and persist well below the surface. A mixture of graphitic and carbide carbon was present in the films. The stoichiometry of the different films remained relatively constant with N/Ti = 1.1 ± 0.03. This ratio was calculated using all available N and Ti. The XPS data demonstrated that Ti was bonded as TiO<sub>x</sub>, TiO<sub>2</sub>, TiN, TiO<sub>x</sub>N<sub>y</sub>, and Ti-C. It is an over simplification to calculate the ratio as reported, but it is useful for the purpose of this paper. The N/Ti ratio reported reveals that the deposition conditions did not cause significant changes in film chemistry and stoichiometry; more variability

Table 2: Weight loss (in mg/cm<sup>2</sup>) of coated 440C metal washers as a function of temperature.

Temp. °C	1.7/75 mTorr/V	1.7/125 mTorr/V	6.0/75 mTorr/V	6.0/125 mTorr/V	11.0/75 mTorr/V	11.0/125 mTorr/V	e-Ni e-Ni	e-Ni Heat Treat	TiN/e-Ni
300	0.0	0.0	0.0	0.0	0.0	-0.04	0.0	0.0	-0.06
315	0.0	0.0	-0.01	-0.01	-0.02	-0.03	-0.02	0.0	-0.01
330	-0.06	-0.24	-0.10	-0.03	-0.07	-0.17	0.00	-0.01	-0.04
345	-0.21	-0.25	-0.19	-0.07	-0.53	-0.43	-0.02	-0.02	-0.02
360	-4.05	-1.83	-1.68	13.78	-0.67		-0.03	-0.06	-0.04
370							-0.08	-0.19	-0.13

in chemistry was likely caused by variations in the contaminant levels.

#### 3.4.2 Coating microstructure

GAXRD showed that the coatings had the cubic crystal structure. As observed in Figure 2, the bias voltage has a significant effect on microstructure. The N<sub>2</sub> partial pressure does not cause significant changes in the GAXRD scans so only an example spectral series is shown (i.e., the 6.0 x 10<sup>-3</sup> Torr at 75 and 125V series). At the higher bias voltage, there is a more rapid and complete change from a [111] texture to a [220] texture at the surface (i.e., as theta is reduced and surface sensitivity enhanced). In general, at higher bias voltages, the zone T microstructure can be produced at lower temperature and/or higher pressure. However, it is noted that at too high a bias voltage, coating stress can cause loss of adhesion and can even result in a porous structure due to resputtering. In cathodic arc deposition, increasing the N<sub>2</sub> partial pressure too high can cause particulates to form which, when incorporated in the coating, increase the potential for fluid penetration. There is an optimum, therefore, between bias voltage and N<sub>2</sub> pressure for achieving the best properties. The hardness of the films provides some indication of their bonding and density. It is noted that all films have similar hardness with the 11.0 x 10<sup>-3</sup> Torr coatings beginning to lose some hardness. This suggests that 6.0 x 10<sup>-3</sup> Torr may be approaching the optimum.

#### 3.4.3 Coating resistance to corrosion

Table 2 shows that the different coatings behave about the same after treatment in PFP AE fluid to about 330°C. At 345°C, the coatings deposited at 1.7 and 6.0 x 10<sup>-3</sup> Torr, were significantly less corroded than those deposited at 11.0 mTorr. This behavior may be related to a more porous microstructure and/or more particles in the films. Figure 3a shows that the TiN protects the steel surface up to at least 330°C. Failure started with the appearance of brown spots. On closer inspection (see Figure 3b), the spots were actually pits with corrosion product in the pit and on the coating surface in the near vicinity. XPS sputter depth profiles revealed that the corrosion product on the coating could be removed by light sputtering. The pit itself was filled with Fe fluoride and Fe oxide compounds that could not be removed after prolonged sputtering. This behavior demonstrates that coating failure

started with fluid penetration and corrosion of the underlying steel. The corrosion product, having a higher specific volume, contributed to coating fracture and loss. The fluid was then able to penetrate at the edges and continue the degradation cycle. Cathodic arc sputtering has been noted to suffer from particles and occasional pin-holes which supports the assessment of the failure mechanism. Nickel alloy has been noted to be resistant to degradation by PFP AE's [24]. Therefore, electroless Ni (e-Ni) coatings were tested in hot fluid to determine if the pit forming mechanism is valid and the results are shown in Table 2. Three coatings were tested in fluid: (1) e-Ni as deposited, (2) e-Ni heat treated to about 350°C, and (3) TiN coated, heat treated e-Ni. The heated e-Ni was included because it is phosphide precipitate hardened and is a good support layer for TiN. The data shows that e-Ni is resistant to the maximum useful temperature of the fluid (i.e., 370°C). It is also noted that e-Ni/TiN did suffer from fluid penetration/corrosion failure at 370°C. This demonstrates that TiN is relatively inert toward the fluid and that pin holes in the TiN coatings are responsible for its failure.

TiN and e-Ni do not undergo significant degradation in PFP AE fluid to 370°C. The failure mode for the TiN coatings evaluated was porosity or pin holes which allowed fluid penetration. The results of this study suggest that alternate types of coating methods that result in fewer particles (e.g., reactive ion plating) should be evaluated. In addition, other inter layers will be evaluated; including a Ti layer since it is known that Ti is relatively inert to PFP AE's. These results suggests that TiN has significant potential for bearing applications and that e-Ni may be useful as a inexpensive, easily applied coating for engine components in contact with high temperature oil.

### 4 TiC/DLC/Gradient Hard Coatings

#### 4.1 Background

TiC and diamond-like carbon (DLC) coatings have relatively low friction surfaces. PLD has been used successfully to grow TiC at low temperature [6,16-17,28]. For example, Rist and Murray [28] reported growth of stoichiometric TiC films on Si (100) substrates using the frequency doubled Nd:YAG ( $\lambda=532$  nm, 15 ns duration). Films grown at substrate temperatures between RT and 600°C were near stoichiometric TiC. For

films grown above 600°C, film/substrate interdiffusion and different chemistries were observed.

In the authors laboratory, additional synthesis-triboproperty research was undertaken on TiC coatings grown by a 248 nm excimer laser [16,17]. Further, nitrogen was incorporated into the TiC coatings by introducing N<sub>2</sub> into the background during deposition. Of the many hard coatings available, TiC, TiN, and TiCN have been used extensively [1-5]. TiCN has been reported to have superior properties to the binary nitrides. It is chemically resistant and has superior hardness and wear resistance properties. Deposition of TiC and TiCN by PVD has involved using a hydrocarbon to provide carbon. Using CVD techniques, Ti containing vapors have been used (e.g., TiCl<sub>4</sub>). Precise control of the partial pressures and handling of the different gases (some of which are flammable) complicates traditional PVD and CVD techniques. The technique presented here is comparatively simple; a commercial hot-pressed TiC disk supplies Ti and C, and N<sub>2</sub> (i.e., inert and relatively safe) is made available as a reactive gas in the background [19].

#### 4.2 Experimental Details

TiC films were grown at room temperature and at 300°C by using about  $2 \times 10^8$  W/cm<sup>2</sup> of 248 nm-wavelength laser radiation to ablate a commercial hot pressed TiC target in vacuum. TiCN films were grown by ablating the TiC targets in a N<sub>2</sub> gas background. Coatings were grown at 400°C onto 440C stainless steel substrates, with N<sub>2</sub> background pressures of 5 mtorr and 20 mtorr. These conditions were considered as upper processing extremes in both temperature and pressure, because higher deposition temperatures alter the phase distributions within the substrate, and higher pressures severely reduce the kinetic energies of the condensing species which are known to provide beneficial characteristics to the deposited materials [6]. For comparison, coatings were also grown at room temperature in 5 mtorr N<sub>2</sub>. The nominal thickness of the different coatings was 800 nm.

The second approach to growing a hard, wear resistant coating at low temperature was to use multilayering and functionally gradient architectures. The PLD-magnetron system described earlier was used for these studies. The magnetron target-substrate distance was 15 cm, and the PLD target-substrate distance was 6 cm, which is the optimal distance for producing DLC. The laser energy was focused onto the graphite target to achieve  $\sim 10^9$  W/cm<sup>2</sup> power density. Carbon plumes formed under these conditions expanded in a direction normal to the target towards the substrate.

#### 4.3 Results/Discussion

##### 4.3.1 TiC

Titanium carbide coatings were grown at RT and 300°C onto 440C stainless steel substrates. The films were near stoichiometric and nanocrystalline. The grain size from TEM analysis was in the range of 2-10 nm. The tribological behavior of coatings on annealed 440C (HRC 23) showed that

plastic deformation of the substrate lead to shortened wear lives of the coatings. Tests run against 440C steel balls showed initially low friction,  $\mu=0.2$ , which increased to about 0.6 within 200 revolutions. Stick slip behavior was observed and micrographs of the wear track showed patches of transferred steel. Essentially, a steel on steel couple with high friction was produced. Friction tests against sapphire balls displayed low friction ( $\mu$  about 0.2) throughout the 2000 revolution test. However, micrographs of the track reveal that some of the film is being removed after only 200 revolutions. The friction is maintained by the transfer film on the ball and the remaining film in the track.

Friction tests on the tempered (HRC 57) 440C substrates show that the RT coatings have a longer wear life than 300°C coatings. They are also harder than the 300°C coatings and cause more ball wear. Coatings grown at RT and 300°C onto tempered substrates dramatically lower the wear of the 440C ball compared to coatings grown onto the annealed (23 HRC) and uncoated (annealed and tempered) substrates. The most important observations from this study are that: (1) the load capability of the substrate has a significant effect on coating friction and wear, and (2) the tribological properties of the coatings are dependent on deposition temperature. To improve the toughness of the coatings, N was incorporated to create TiCN, which as discussed earlier, is reported to have better tribological properties.

##### 4.3.2 TiCN

Coatings were transferred from the deposition system to the XPS system in air so the surfaces were oxidized and contaminated with carbon and hydroxyl species. By sputtering coating surfaces for 10 minutes with 4 kV Ar ions, the contamination and oxide layers were removed without significantly changing chemistry and stoichiometries. All XPS data reported are from sputter cleaned specimens. Table 3 lists the atomic fractions of the different elements in the coatings. The areas of the Ti 2p doublet, N 1s, C 1s, and O 1s peaks, corrected for cross section, were used to calculate these values.

Table 3: Atomic percentages of elements in the coatings

	Ti %	C %	N %	O %
5 mTorr, 400°C	50.5	23.9	17.0	8.6
20 mTorr, 400°C	36.2	15.6	37.9	10.2
5 mTorr, RT	41.4	16.7	22.6	19.3
TiC, target	48.3	49.6		2.1

As shown in Table 3, increasing the N<sub>2</sub> pressure in the deposition chamber causes significant increases of N in the coatings. Figure 4a shows that increasing the fraction of N in the coatings causes increases in the Ti 2p<sub>3/2</sub> binding energy (5 mTorr = 455.0 eV and 20 mTorr = 455.2 eV) compared to the TiC target (454.8 eV). A shift to higher binding energy is expected as more nitrogen participates in the bonding of the TiCN lattice because of the larger electronegativity of nitrogen compared to carbon. The Ti 2p<sub>3/2</sub> electron binding energy

observed in the TiCN film grown in 20 mtorr  $N_2$  is nearly equivalent to that observed in TiN films (data not shown). Lattice oxygen was present in all the coatings which is likely due to contaminants in the deposition chamber. As shown in Figure 4b, two nitrogen peaks are observed. The most intense peak is due to Ti bonded to C and N; the small peak to higher binding energy is assigned to excess nitrogen at grain boundaries [31]. The C 1s spectra in Figure 4c show the intense carbide carbon peak at low binding energy and the graphitic carbon peak at higher binding energy. Graphitic carbon is believed to arise from the binder phase in the target [16]. The XPS data demonstrate that nitrogen is readily incorporated into the coatings forming TiCN, and that the nitrogen concentration scales with  $N_2$  pressure.

X-ray diffractometry data were collected using the Bragg-Brentano geometry. Diffractograms from the 5 mTorr, 400°C and 20 mTorr, 400°C TiCN films, and TiC films are presented in Figure 4d. The TiC(111) peak is centered at  $35.69^\circ 2\theta$ , which is  $0.21^\circ$  less than published in the JCPDS powder diffraction database [32]. The positions of the TiCN(111) peaks shift to larger angles with increasing nitrogen concentration. Both TiC and TiN have atomic structures similar to NaCl (space group: Fm3m), with lattice parameters of 4.3274 Å and 4.2417 Å, respectively. If the ternary solution is formed by substitution of nitrogen on the carbon lattice sites in TiC, a contraction of the lattice would occur. Such a contraction is consistent with the peak shifts to larger Bragg angles observed in this data. The vertical, dashed line in Figure 4d represents the (111) peak position of strain-free TiC, and the dot-dashed line represents the (111) peak position of strain-free TiN. The TiC(111) peak from the coating is at a lower scattering angle than for the stress free reference indicating the presence of a compressive stress in the plane of the film resulting from laser deposition. The position of the TiCN(111) peak for the film grown in 5 mtorr  $N_2$  also appears on the low-angle side of the strain-free TiC(111) peak. It is reasonable to conclude that an in-plane compressive stress is present in the TiCN coating. As the nitrogen content in the coating increases, it becomes more TiN-like and the (111) peak moves further toward that for pure TiN(111). The peak resides between the angles for the pure, stress free binary compounds (i.e., TiC and TiN). It is difficult, therefore, to determine how much of the peak position is due to stress and how much is due to the relative fractions of carbon and nitrogen in the 20 mTorr coating. Based on the data for the other coatings, it is likely that the coating has some in-plane compressive stress. The cause of the changing peak intensity ratios with increasing nitrogen concentration is believed to be related to texturing of the TiCN grains.

Hardness data were collected in the controlled displacement mode, where total displacements of 40 nm to 100 nm are chosen as appropriate for the 800 nm thick coatings considered. For each displacement, ten indentations are performed to improve the statistics of the experiments. TiC coatings grown at RT have hardness values between 35 and 40 GPa. Coatings grown in 5mTorr  $N_2$  have a significantly higher hardness - 60 GPa. This is surprisingly high and falls

in the range of good DLC coatings [15]. When the nitrogen concentration is increased to 20 mTorr, the TiCN film hardness decreases to 23 GPa, which is similar to that observed from TiN [33]. Similar trends in the elastic moduli with nitrogen concentration are observed, where the moduli for the 5 mtorr  $N_2$  and 20 mtorr  $N_2$  films are 452 GPa and 278 GPa, respectively. Previous reports suggest the enhanced mechanical properties are related to compressive stresses in the film, and that the optimum nitrogen concentration in TiCN is approximately ten-percent [34].

For the film grown at RT, 5 mTorr  $N_2$  the nitrogen concentration is 17.6%, comparable to that measured in the film grown at 673 K. This similarity in nitrogen concentration implies that temperature is not a strong factor in controlling nitrogen concentrations. Nitrogen partial pressure during deposition appears to control the atomic fraction of N in the coating.

Ablation of a pure TiC target in a backfill of  $N_2$  gas is shown to produce crystalline TiCN films at 400°C. Mechanical properties are shown to be closely related to the nitrogen concentration. Pulsed laser deposition is shown to be well suited for the growth of TiCN films, and additional work focuses on understanding the processing-structure-property relationships necessary for performance optimization, and on understanding the mechanisms for nitrogen incorporation into the films. Preliminary scratch tests demonstrate that TiC, 5 mTorr, and 20 mTorr coatings have low adhesion, (e.g., about 10 GPa critical load compared to 30-40 GPa for sputter coatings). This is attributed to two factors: (1) no bond layer was used to improve adhesion, and (2) the substrate provided insufficient mechanical support. A process and coating strategy to overcome both problems has been developed and is discussed in the next section.

#### 4.3.3 Magnetron Sputtering-PLD (MSPLD) Method for Producing Multilayers and Functionally Gradient Coatings

The experimental configuration for growing multilayers and functionally gradient coatings described earlier was evaluated using the Ti - TiC - DLC system [30,35]. It has been established that hard coating performance can be improved by proper selection of materials used in the assembly of functional layers (interface bonding, diffusion resistance, mechanical support, toughness, low friction and transitions between layers). The MSPLD technique was designed to permit infinite variability of composition across a thickness as well as to permit growth of discrete, sharp interfaces.

Of particular concern in combining PLD and magnetron sputtering, was the potential loss of high energy species generated during ablation due to thermalization of plume species in the high pressure (e.g.,  $2 \times 10^{-1}$  Pa) environment required for sputtering. The high energy species are necessary for production of good adherent films [6], and for producing ultra hard DLC coatings [15]. Calculations of the collision frequency of atomic species in the MSPLD environment



demonstrate that a high fraction of the energetic species should be available [30]. In this study, film composition was controlled by varying the carbon deposition rate, while the Ti deposition rate was held constant at 10 nm/min. When films containing no titanium were required, the magnetron was switched off. Deposition rate of carbon was varied by changing the frequency of laser pulses, exploiting the linear dependence between deposition rate and the laser pulse frequency. Figure 5a illustrates this dependence as measured experimentally using a quartz crystal thickness monitor calibrated for DLC.

The deposition rate of carbon is 0.016 nm/pulse as calculated from the slope of line a in Figure 5a. Thus, the variation of  $Ti_xC_y$  composition can be predicted from the pulse frequency using Figure 5a. Detailed equations have been developed to predict composition based on PLD and magnetron parameters and this work is reported elsewhere [30,35]. Good agreement between the predicted and actual film stoichiometries shown in Figure 5a, measured with x-ray photoelectron spectroscopy, validates the predictive equations.

It is important to emphasize that the energy of deposited Ti and C atoms stays constant in the range of  $Ti_{1-x}C_x$  compositions evaluated, since magnetron power, energy of a laser pulse and background pressure remain the same. This facilitates studies of film structure as a function of only compositional changes.

The capabilities of the MSPLD system were tested by designing and growing a multilayer functionally gradient coating using the Ti-C system [35]. An optimized hard coating requires adhesion, load support, and low friction layers. Each of these layers must be joined through appropriate transition regions. The first part of the study was to determine the chemistry, structure, and mechanical properties of  $Ti_{1-x}C_x$  coatings, where x was varied from 0 ( $\alpha$ Ti) to 1 (DLC). Using this data, the optimum bond, load support, low friction, and transition layer compositions were identified.

The values of x selected in  $Ti_{1-x}C_x$  were: 0.0, 0.11, 0.31, 0.54, 0.68, 0.75, 0.85, 0.93, and 1.0. Figure 5b shows the XPS peaks for C 1s. The spectra shown were collected after sputter removal of the oxide and C contamination layers. Oxygen 1s spectra were also collected but are not shown. XRD data shown in Figure 5c, reveal the presence of the TiC (111),  $\alpha$ Ti (100), and TiC (200) peaks. These data show that for x = 0, the film is  $\alpha$ Ti with about 14% lattice oxygen. For x = 0.11 and 0.31, data suggests the presence of two phases: an  $\alpha$ Ti matrix and TiC inclusions. The TiC fraction increases with increasing x. Coatings with x = 0.54 and 0.68 are fcc TiC. XRD scans of these compositions show that the excess carbon (i.e., x > 0.5) is likely in the TiC interstices because the (111) and (200) peaks are shifted to lower angles indicating stress. The  $\alpha$ Ti (100) peak in all scans beyond x = 0.31 is due to the Ti bond layer as determined from measurements made with the bond layer removed.

When the carbon concentration was increased to x = 0.75, 0.85, and 0.93, a two phase system was observed; the matrix was amorphous carbon and the inclusions were TiC. Raman data (not shown) were used to characterize the carbon phase. These data demonstrated that the C  $sp^3/sp^2$  ratio increased with increasing x. For x = 1.0, the coating had the highest  $sp^3/sp^2$  ratio which is supported by hardness data discussed later. The highest  $sp^3$  content is obtained by growing in vacuum where the C kinetic energy is highest [30].

The hardnesses of the different coatings are shown in Figure 5d. The hardness increases with increasing TiC content to x = 0.54; a local hardness maximum occurs at x = 0.68. This is consistent with the compressive stresses suggested by the XRD data, which can lead to higher values of hardness in thin film systems [34].

Using the data presented above, the multilayer functionally gradient coating shown in Figure 6a was designed and fabricated. The essential features of the design are as follows: (1) an  $\alpha$ Ti layer was deposited to enhance adhesion to the substrate, (2) an x = 0.1 transition layer was deposited to grade into TiC support layers where x = 0.3, 0.5 and 0.7, (3) two thin transition layers where x = 0.75 and 0.9 were deposited to prepare for the first DLC support layer, and finally (4) a super-hard, vacuum grown DLC layer was deposited as the topcoat. The transitions between the layers shown in Figure 6a were graded over 10 nm to further enhance adhesion. It should be noted that coating hardness continually increases toward the surface which had a hardness of 60-70 GPa.

The mechanical properties of the coating were excellent. The friction coefficient was < 0.1 for over  $10^5$  cycles under a load of 1.4 GPa. Under the same conditions a single layer DLC coating failed immediately. A scratch test of the functionally gradient coating is compared to that from a single layer DLC coating in Figure 6b. The single layer coating failed at about 9 N whereas the functionally gradient coating survived to about 50 N load, which is where the stylus penetrated the coating. In addition peripheral cracking and adhesion failure were not observed on the functionally gradient coating until penetration.

The MSPLD technique is shown to permit the fabrication of functionally gradient coatings with superior mechanical and tribological properties. Future research will continue with the incorporation of the TiCN system into graded structures. The addition of multilayers into the coating design will also be investigated as this approach has shown tremendous potential.

## 5.0 CONCLUSIONS

There is significant potential to use TiC, TiCN, and Ti-TiC-DLC coatings in aerospace systems. TiN and e-Ni coatings are resistant to attack by perfluoropolyalkylether candidate high temperature fluids. They may, therefore, be used to accelerate the application of the fluids in high temperature turbine engines. The MSPLD technique has been shown to be a powerful tool for growing functionally gradient and multilayer

coatings. Coatings grown using this technique can be used to determination composition-structure-property relationships which can in turn be used to design superior coatings with low friction and long wear lives.

## 6.0 REFERENCES

1. B. Bhushan and B.K. Gupta, eds., "Handbook of Tribology : Materials, Coatings, and Surface Treatments", New York, McGraw-Hill, Inc., 1991 (ISBN 0-07-005289-2).
2. K. Holmberg and A. Mathews in "Coatings Tribology: Properties, Techniques, and Applications in Surface Engineering", Tribology Series, 28, ed. D. Dowson, Amsterdam, Elsevier, 1994 (ISBN 0-444-88870-5).
3. A.A. Voevodin and M.S. Donley, *Surf. Coat. and Technol.*, in press.
4. H. Holleck, *J. Vac. Sci. and Technol. A*4(6) (1986) 2661.
5. C. Subramanian and K.N. Strafford, *Wear*, 165 (1993) 85.
6. M.S. Donley and J.S. Zabinski in "Pulsed Laser Deposition of Thin Films", edited by D.B. Chrisey and G.K. Hubler, New York, John Wiley and Sons (1994) 431; and other chapters therein.
7. D.J. Carré, *ASLE Trans.*, 29, 121 (1986).
8. R.A. Rowntree and M.J. Todd, in "New Materials Approaches to Tribology: Theory and Applications", eds. L.E. Pope, L.L. Fehrenbacher, and W.O. Winer, Pittsburg, PA, Materials Research Society, MRS Symposium Series - 140, 1989 (ISBN 1-55899-013-5) 21.
9. D.J. Carre, *Surf. Coat. and Technol.*, 43/44 (1990) 609.
10. P. Agarwal, P. Nath, H.J. Doerr, R.F. Bunshaw, G. Kuhlman, and A.J. Koury, *Thin Solid Films* 83 (1981) 37.
11. T. Spalvins, *Wear of Materials 1977*, ASME, 1977.
12. G. Georgiev, N. Feschiev, D. Popov, and Z. Uzuov, *Vacuum*, 36 (1986) 595.
13. M. Eizenberg and S.P. Murarka, *J. Appl. Phys.*, 54 (1983) 385.
14. J.E. Sundgren, B.-O. Johansson, H.T.G. Hentzell, and S.-E. Karlsson, *Thin Solid Films*, 36 (1988) 329.
15. A.A. Voevodin, M.S. Donley, J.S. Zabinski and J.E. Bultman, *Surf. Coat. Technol.*, 77 (1995) 534.
16. M.S. Donley, J.S. Zabinski, W.J. Sessler, V.J. Dyhouse, S.D. Walck, and N.T. McDevitt, in *Photons and Low Energy Particles in Surface Processing*, edited by C.I.H. Ashby, J.H. Brannon, and S.W. Pang, (MRS Symposium Proceedings - 236), Materials Research Society (1992), Pittsburgh, PA, pp 461-466.
17. W.J. Sessler, M.S. Donley, J.S. Zabinski, S.D. Walck, and V.J. Dyhouse, *Surface and Coatings Technology*, 56 (1993) 125.
18. A.A. Voevodin, C. Rebholz, J.M. Schneider, P. Stevenson, and A. Mathews, *Surf. Coat. and Technol.*, 73 (1995) 185; A.A. Voevodin, R. Bantle, and A. Mathews, *Wear*, 185 (1995) 151.
19. M.A. Capano, A.A. Voevodin, J.E. Bultman, and J.S. Zabinski, *Scripta Mat.*, submitted.
20. W.C. Oliver and G.M. Pharr, *J. Mater. Res.* 7, 1564 (1992).
21. C.E. Snyder, Jr. and L.J. Gschwender, *I&EC Product Research and Development*, 22 (1983) 383.
22. L.J. Gschwender, C.E. Snyder, Jr., and G.W. Fultz, *Lub. Eng.*, 49/9 (1993) 702.
23. J.S. Zabinski, L. Gschwender, M.S. Donley, and P. John, *Proc. of the 50th Annual Meeting of the Society of Tribologists and Lubrication Engineers*, STLE Publications, Chicago, May 1995.
24. W.L. Chandler, L.B. Lloyd, M.M. Farrow, R.K. Burnaham, and E.M. Eyring, *Corrosion NACE*, 36(3) (1980) 152.
25. For example, J.E. Sundgren, *Thin Solid Films*, 128 (1985) 21.
26. J.A. Thorton, *J. Vac. Sci. and Technol.*, A11(4) (1974) 666.
27. L. Gschwender, C.E. Snyder, G.W. Fultz, D.A. Hahn, J.R. Demers, *Tribol. Trans.*, 38/3 (1995) 618.
28. O. Rist and P.T. Murray, *Mtls. Lett.*, 10/7,8 (1991) 323.
29. K. Narasimhan, S.P. Boppana, and D.G. Bhat, *Wear*, 188 (1995) 123.
30. A.A. Voevodin, M.A. Capano, A.J. Safriet, M.S. Donley, and J.S. Zabinski, *J. Appl. Phys.*, submitted.
31. A. Ermolieff, and P. Bernard, *J. of Less Com. Met.*, 120 (1986) 9.
32. Joint Congress on Powder Diffraction Spectra (JCPDS): Card 6-0614 for TiC and card 38-1420 for TiN. International Centre for Diffraction Data, 12 Campus Boulevard, Newtown Square, PA 19073-3273.
33. M.B. Karamis, *Thin Solid Films*, 217 (1992) 38.
34. J.M. Schneider, A.A. Voevodin, C. Rebholz, and A. Matthews, *J Vac. Sci. Technol. A*, 13, 2189 (1995); J.M. Schneider, A.A. Voevodin, C. Rebholz, A. Matthews, J.H.C. Hogg, D.B. Lewis, and M. Ives, *Surf. Coat. Tech.*, 74/75, 312 (1995).
35. A.A. Voevodin, M.A. Capano, S.J.P., Laube, M.S. Donley, and J.S. Zabinski, *Thin Solid Films*, submitted.

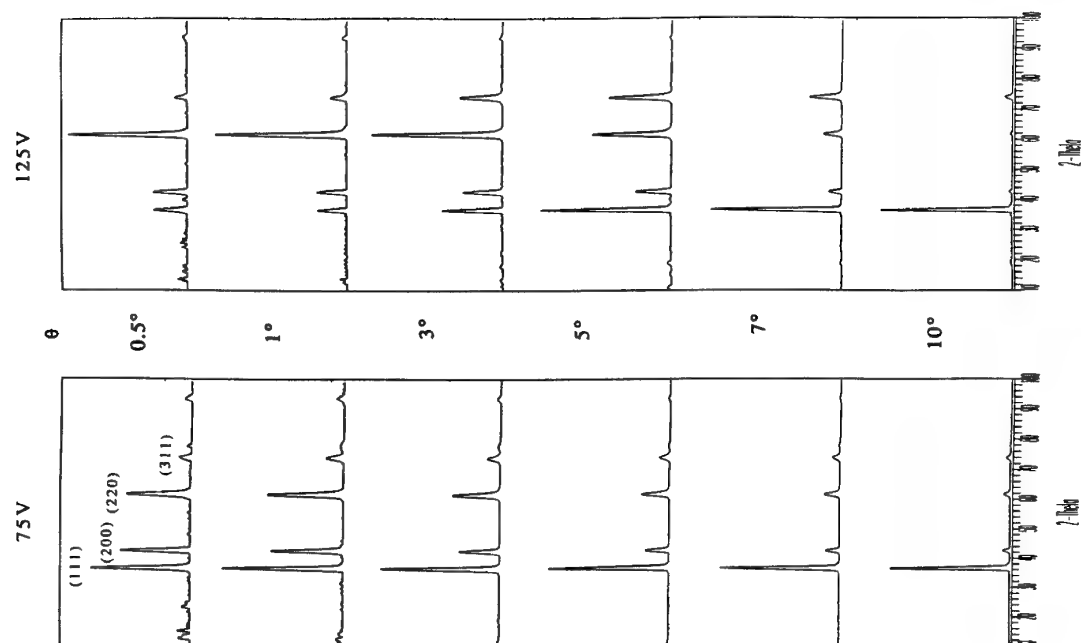


Figure 2: Glancing angle x-ray diffraction data from the coatings grown at  $6 \times 10^{-3}$  torr, 75 V and  $6 \times 10^{-3}$  torr, 125 V.

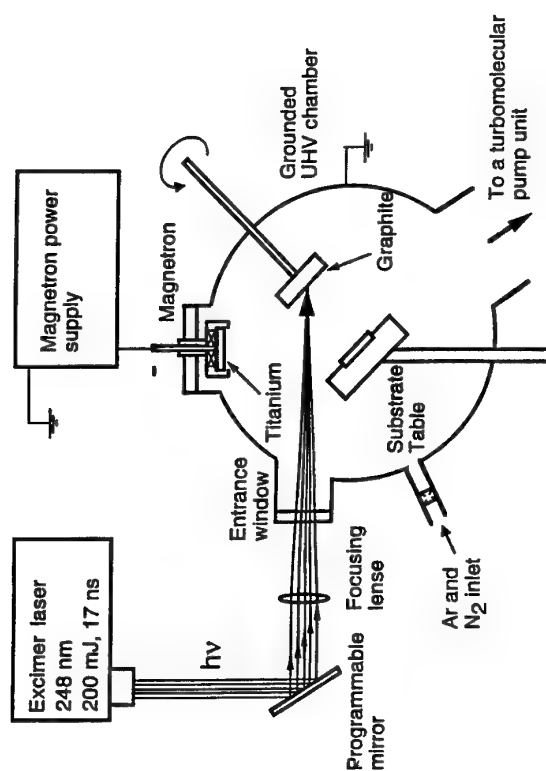


Figure 1: Schematic of the Magnetron Sputtering Pulsed Laser Deposition System (MSPLD)

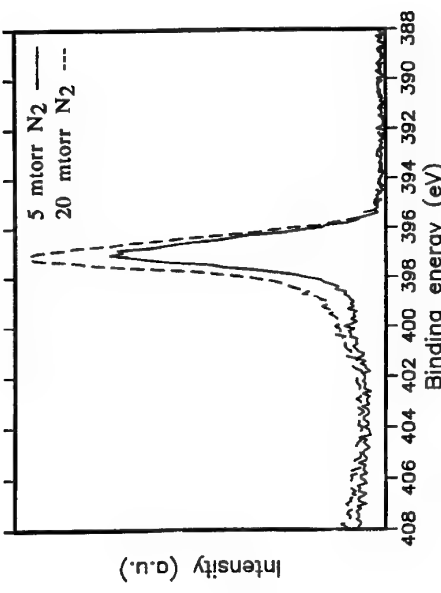
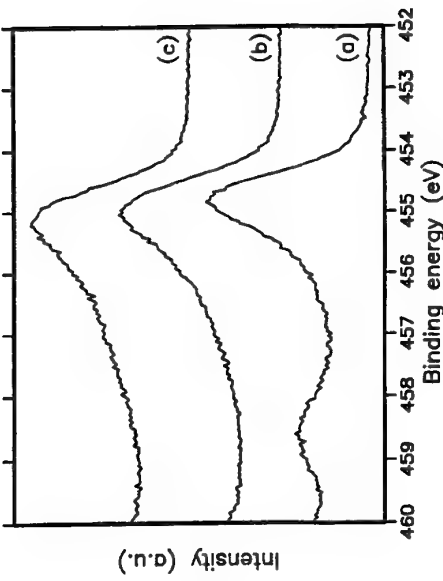


Figure 4: a. (upper) Ti 2p<sub>3/2</sub> XPS spectra. "a", TiC hot pressed target; "b", Coating grown in 5 mtorr N<sub>2</sub>; and "c", Coating grown in 20 mtorr N<sub>2</sub>.  
b. (lower) N 1s XPS spectra from the coatings grown in 5 and 20 mtorr N<sub>2</sub>.

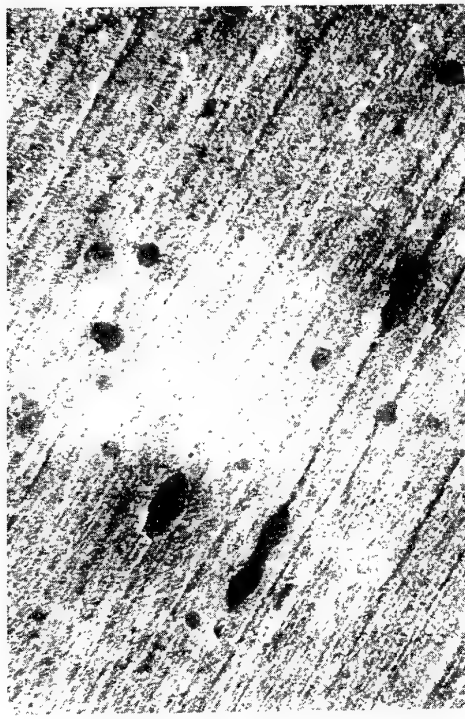
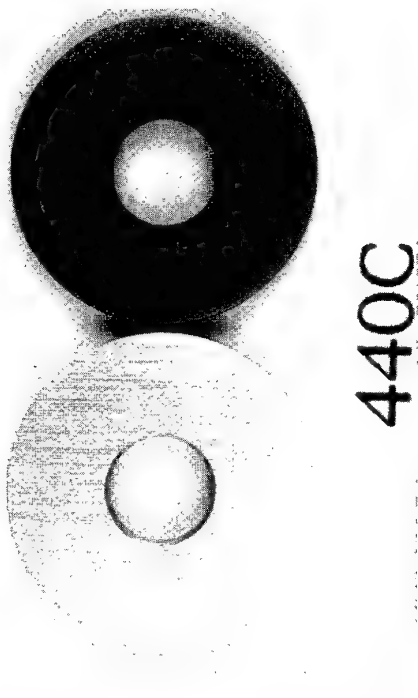


Figure 3: a. (upper) Photograph comparing a TiN coated 440C washer on the left to an uncoated washer on the right after they were heated in PFPAC fluid for 24 hours at 330° C.  
b. (lower) Photograph showing pits formed on TiN coated washer after heating for 24 hours at 345° C. XPS showed that the brown stains were mostly corroded iron.

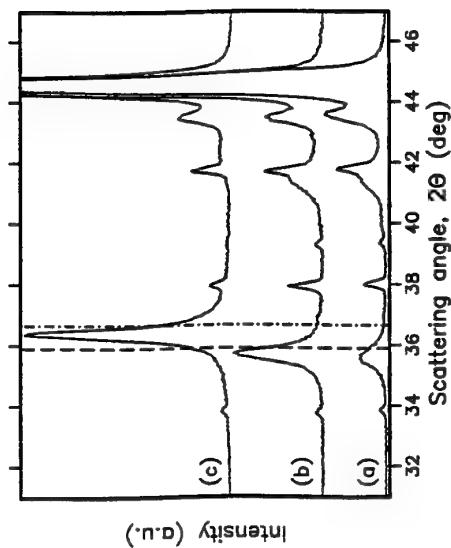
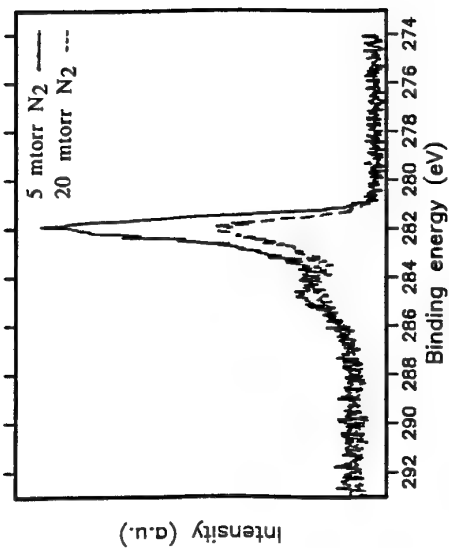


Figure 4: c. (upper) C 1s XPS spectra from the coatings grown in 5 and 20 mtorr N<sub>2</sub>.  
d. (lower) XRD scans from "a" TiC coating, "b" 5 mtorr N<sub>2</sub> coating, and "c" 20 mtorr N<sub>2</sub> coating.

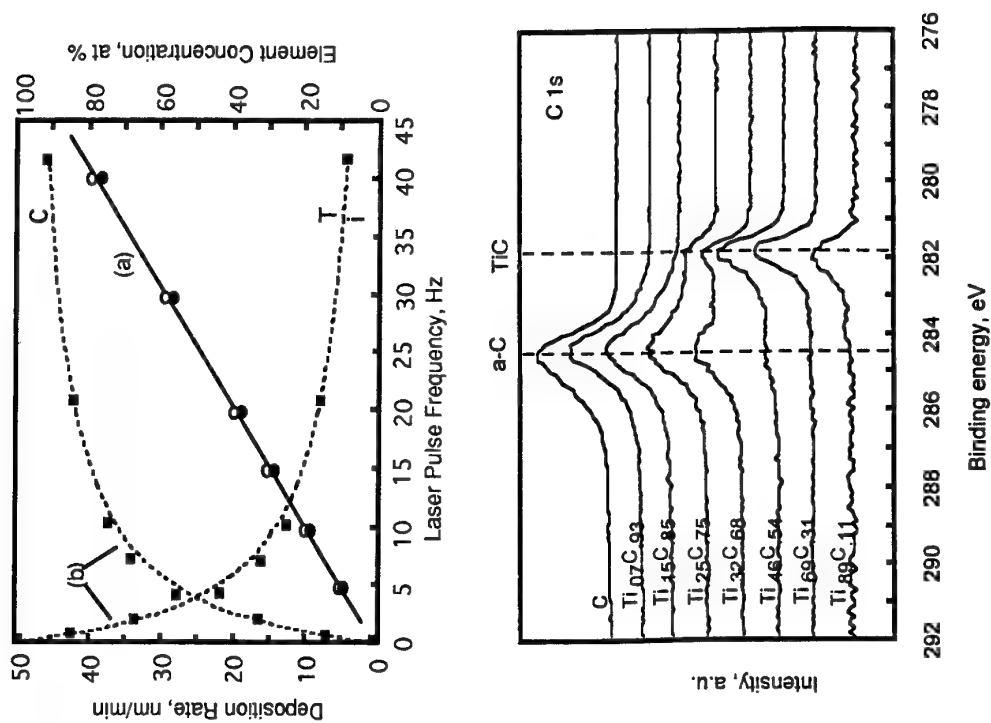


Figure 5: a. (upper) Deposition rate and elemental concentration of carbon and titanium as a function of laser pulse rate where "a" is deposition rate of carbon and "b" is elemental compositions of Ti and C.  
b. (lower) C 1s XPS spectra of the Ti<sub>1-x</sub>C<sub>x</sub> coatings.

Material	Hardness	Elastic modulus	Thickness
DLC at $10^{-5}$ Pa	70 GPa	650 GPa	400 nm
DLC at $2 \times 10^{-1}$ Pa	43 GPa	450 GPa	100 nm
Ti <sub>10</sub> C <sub>90</sub>	25 GPa	290 GPa	25 nm
Ti <sub>25</sub> C <sub>75</sub>	27 GPa	350 GPa	25 nm
Ti <sub>30</sub> C <sub>70</sub>	29 GPa	370 GPa	100 nm
Ti <sub>50</sub> C <sub>50</sub>	20 GPa	290 GPa	100 nm
Ti <sub>70</sub> C <sub>30</sub>	14 GPa	230 GPa	100 nm
Ti <sub>90</sub> C <sub>10</sub>	6 GPa	150 GPa	50 nm
$\alpha$ -Ti	4 GPa	140 GPa	50 nm
440C steel	11 GPa	220 GPa	

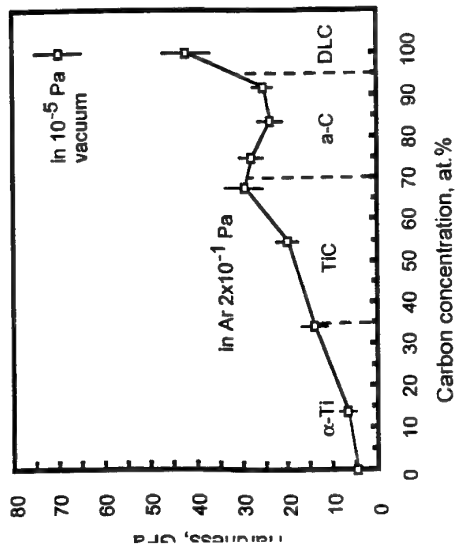
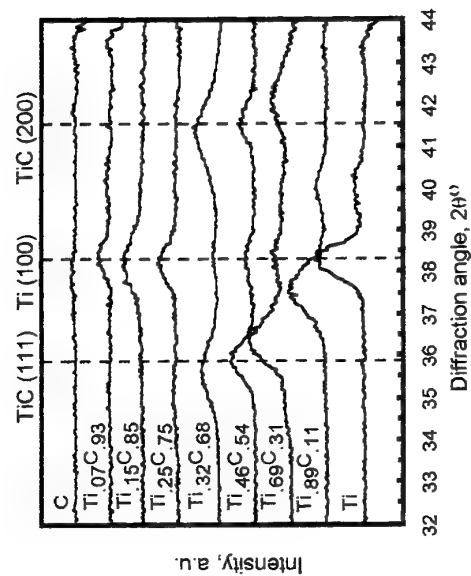


Figure 5: c. (upper) XRD scan of the Ti<sub>1-x</sub>C<sub>x</sub> coatings.  
d. (lower) Plot of the hardness of the Ti<sub>1-x</sub>C<sub>x</sub> coatings as a function of x.

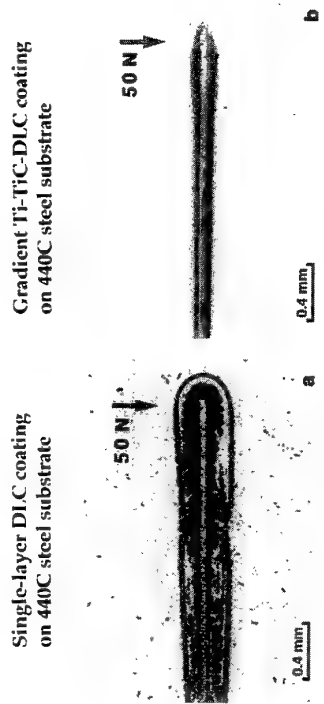


Figure 6: a. (upper) Schematic of the functionally gradient coating showing the thickness, composition, and mechanical properties of the different regions.  
b. (lower) Comparison of scratches made of single layer and functionally gradient coatings.

## AN INVESTIGATION ON SURFACE TREATMENTS FOR IMPROVING THE FRETTING FATIGUE RESISTANCE OF TITANIUM ALLOYS

A.K.Koul<sup>1</sup>, L.Xue<sup>1</sup>, W.Wallace<sup>1</sup>, M.Bibby<sup>2</sup>,  
S.Chakravarty<sup>3</sup>, R.G.Andrews<sup>3</sup>, P.C.Patnaik<sup>3</sup>

<sup>1</sup>The Institute for Aerospace Research, National Research Council of Canada, Ottawa, Canada, K1A 0R6.

<sup>2</sup>The Department of Mechanical and Aerospace Engineering, Carleton University, Ottawa, Canada, K1S 5B6.

<sup>3</sup>Hawker Siddeley Canada Inc, Orenda Division, Ottawa, Canada, K1J 9L8.

### ABSTRACT

The effects of different surface modification treatments (shot peening, carbon and nitrogen ion implantation, CuNiIn soft coating, MoS<sub>2</sub> solid lubricant and various combinations thereof) on the fretting fatigue resistance of Ti-6Al-4V and Ti-17 alloys have been investigated.

Shot peening produces work hardening and compressive residual stresses in the surface layers, and shows the best improvement in the fretting fatigue life of both Ti-6Al-4V alloy at room temperature and Ti-17 alloy at 278°C.

The application of a CuNiIn soft coating plus an overlay of MoS<sub>2</sub> solid lubricant increases the fretting fatigue resistance of baseline Ti-6Al-4V and Ti-17 materials at room temperature and 278°C, respectively, by providing surface lubrication. However, the fretting fatigue life of shot peened plus CuNiIn and MoS<sub>2</sub> coated Ti-6Al-4V material appears to be vendor dependent and, in some cases, the fretting fatigue life is dramatically reduced after the application of a CuNiIn soft coating. This reduction in life may be attributed to the relaxation of compressive residual stresses in the shot peened layers by the plasma spraying process.

Both carbon and nitrogen ion implantation improve the fretting fatigue life of baseline Ti-6Al-4V at room temperature. However, the application of carbon or nitrogen ion implantation significantly reduces the fretting fatigue resistance of shot peened specimens.

### 1. INTRODUCTION

Fretting is a type of surface wear damage caused by small amplitude oscillating slip of the order of 15~75  $\mu$ m between two surfaces in contact under a normal pressure. During fretting, wear debris is formed and the combined effects of galling, seizing, and delamination produce surface stress raisers. Under cyclic loading conditions, fretting fatigue cracks can initiate in the damaged area, which can dramatically reduce the fatigue life of the components [1-4].

Fretting fatigue problems are frequently observed in some aero gas turbine engines in the blade/disc dovetail regions of fan and compressor components made from titanium alloys [5]. In general, there are two loading conditions which are involved in fretting fatigue damage accumulation along the dovetail contact surfaces. The first condition results from substantial changes in disc rotating speeds due to engine start-up or shut-down. This causes changes in centrifugal loading which in turn causes the disc rim slots to open up or close down slightly, and allows the blades to slip outward or inward. Fretting occurs on the blade dovetail/disc slot contact regions as they repeatedly slip against one another during start-up and shut-down cycles. The second condition is associated with the high frequency vibration of the blade. Aerodynamic excitation in the gas turbine may induce blade flutter, which in turn produces fretting action between the contact surfaces of the blade dovetail and the disc slot.

Titanium alloys, because of their inferior wear resistance, are especially prone to fretting damage. The fretting at the blade/disc dovetail contact region induces early crack initiation either in the dovetail region of the titanium alloy blade or in the rim slot surface of the titanium alloy disc, which can drastically reduce the fatigue life of the affected components.

A number of workers have documented that some surface modification treatments can improve the fretting fatigue resistance of titanium alloys [6-9]. Shot peening has been established as a standard process for improving the fatigue and fretting fatigue life of fan and compressor blades and discs made of titanium alloys. Application of soft coatings (such as CuNiIn coating), or lubricants (such as MoS<sub>2</sub> solid lubricant), carbon and nitrogen ion implantation have also been identified as promising surface modification techniques for improving the fretting fatigue resistance of Ti-alloys. However, the combined effects of these different surface modification treatments on fretting fatigue are not clearly understood. For example, the combination of above-mentioned treatments with shot peening may not necessarily have an additive effect on the fretting fatigue life improvement. In some cases, it may instead impair the fretting fatigue resistance [10].

It is well known that the magnitude of surface compressive residual stresses is an important factor in improving the fretting fatigue resistance of a component [11]. Surface modification treatments of the type mentioned above may produce different residual stress levels, which, in turn, can affect the fretting fatigue life. However, there is little information available on the stress states produced by these surface modification treatments or the relationship between the residual stresses and the fretting fatigue life of titanium alloys.

A pair of fretting bridges is invariably used in fretting fatigue test rigs to apply a normal pressure on cyclically stressed specimen surfaces and to produce fretting action between the specimen and the bridges (Fig.1). It has been observed that the bridge geometry can have a significant effect on the fretting fatigue life. Results [12] indicate that, when a pair of square edge bridges are used, intense peak stresses occur at those locations on sample surfaces which correspond to the outer edges of the bridge legs. This, in turn, can decrease the fretting fatigue life of a surface modified test-piece considerably. When the geometry of a bridge is changed from square to round edges, these peak stresses are reduced significantly. However, there is no quantitative information available on the effect of bridge geometry on the fretting fatigue life of titanium alloys.

This paper summarizes recent work on the surface modification treatments for improving fretting fatigue resistance of Ti-6Al-4V and Ti-17 at room and elevated temperatures respectively. Some of these results have been discussed in detail elsewhere [10,13,14]. Emphasis in this paper is on revealing the combined effects of various surface treatments on the fretting fatigue life of shot peened titanium alloys. The effects of surface residual stresses and fretting bridge geometry on the fretting fatigue of surface modified Ti-6Al-4V are also addressed. Finally, some promising new technologies for improving the fretting fatigue resistance of Ti-alloys are also identified.

## 2. EXPERIMENTAL MATERIALS AND METHODS

Two separate cases of fan blade/disc configurations were addressed during this investigation. The blade material in both cases was Ti-6Al-4V, while the disc material was Ti-17 (Ti-5Al-2Sn-2Zr-4Mo-4Cr). Both materials were processed as per manufacturer's material specifications for gas turbine blades and discs. Two temperature levels were selected for fretting fatigue testing. The first stage fan blade problem was addressed through room temperature tests. Bridges were made of Ti-17 disc material without any surface treatments. Various surface treatments and their combinations thereof were applied to specimens made of blade material (Ti-6Al-4V) to investigate their effects on the fretting fatigue life of the blade material. The third stage fan disc problem, on the other hand, was addressed through elevated temperature (278°C) tests. Specimens were made of Ti-17 fan disc material and some specimens were shot peened. Different surface treatments were applied to the surface of bridges made of blade material (Ti-6Al-4V) to evaluate the effects of surface modified blades on the fretting fatigue life of the baseline and shot peened disc materials. All surfaces were polished to 600 grit finish prior to subjecting them to surface

modification treatments in order to provide a consistent surface finish.

The following surface modification treatments were applied individually as well as in various combinations:

- (a) shot peening,
- (b) CuNiIn soft coating,
- (c) MoS<sub>2</sub> solid lubricant,
- (d) carbon ion implantation,
- (e) nitrogen ion implantation;

Shot peening was conducted with MI 110 steel shot at an Almen intensity of 0.006" to 0.008" (type A test strip) with 125% coverage. The CuNiIn soft coating was applied with a plasma spraying process, while the MoS<sub>2</sub> solid lubricant film was simply brushed. Both processes were performed as per manufacturer's specifications for the production of gas turbine blades and discs. The CuNiIn coating and/or MoS<sub>2</sub> solid lubricant were applied by two separate vendors, Vendor #1 and Vendor #2, on Ti-6Al-4V specimens. Their processing quality in terms of effect on the fretting fatigue life was to be compared. The ion implantation parameters used are proprietary.

Residual stresses were measured using the conventional  $\sin^2\psi$  method [15] with a Rigaku x-ray diffractometer. Results from these measurements were then correlated with the fretting fatigue measurements.

All fretting fatigue tests were conducted with a servo-hydraulic fatigue machine. For the first stage fan blade room temperature tests, a maximum cyclic stress of 553 MPa was used with an R ratio (minimum stress over maximum stress) of 0.25 and a sine wave load form at a frequency of 5 Hz. A normal pressure of 338 MPa was applied on opposite sides of the specimen by the four bridge legs using two bridges to produce the fretting effect (Fig.1).

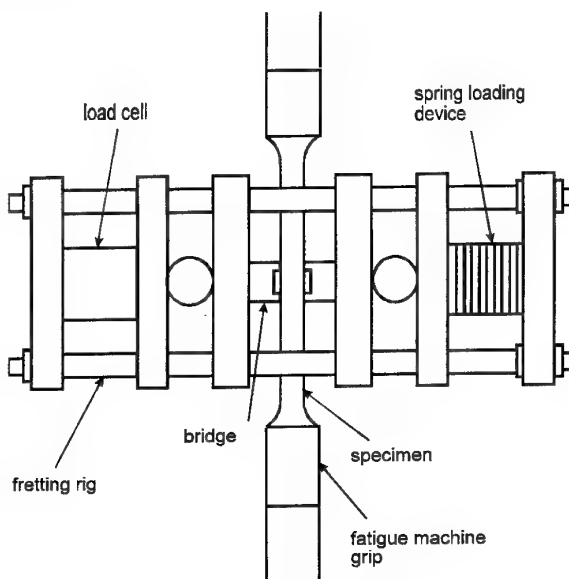


Figure.1 Schematic demonstration of fretting fatigue test facility.



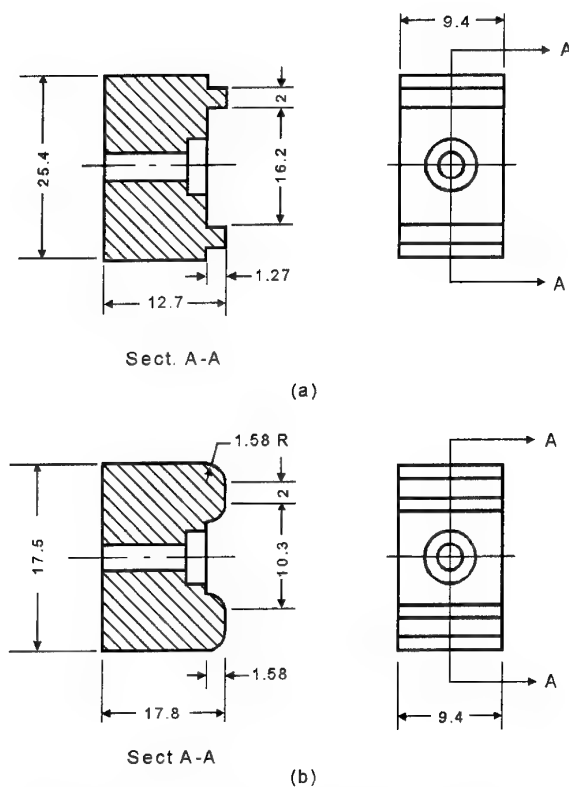


Figure 2. Bridge geometries used in the fretting fatigue tests: (a) square edge bridge, and (b) round edge bridge; all measurements in mm.

Two bridge geometries were used, i.e. the square and the round edge configurations (Fig.2). For the fan disc tests conducted at 278°C, a maximum cyclic stress of 600 MPa and a normal pressure of 414 MPa were used, while other parameters were kept the same. Only round edge bridges were used in elevated temperature tests.

### 3. RESULTS AND DISCUSSION

#### 3.1 Fretting Fatigue Testing of Ti-6Al-4V Material at Room Temperature

##### 3.1.1 CuNiIn coating and MoS<sub>2</sub> solid lubricant

The effects of CuNiIn coating and/or MoS<sub>2</sub> solid lubricant (both applied by Vendor #1) on the fretting fatigue life of baseline (unpeened) and shot peened Ti-6Al-4V materials are shown in Fig.3. All tests were conducted with round edge fretting bridges. For baseline Ti-6Al-4V material, without any surface treatment, the fretting fatigue life of four samples varied from 57,750 to 79,230 cycles with an average value of 67,100 cycles. All specimens failed at a fretting boundary, a position corresponding to the outer side edge of the bridge. The application of CuNiIn coating and MoS<sub>2</sub> lubricant on baseline Ti-6Al-4V showed significant and consistent improvement in the fretting fatigue life presumably by reducing friction between the contact surfaces. The fretting fatigue life ranged from 146,670 to 387,240 cycles. The average life of the three coated specimens was 245,600 cycles, which represented an increase by a factor of 4 relative to the baseline results.

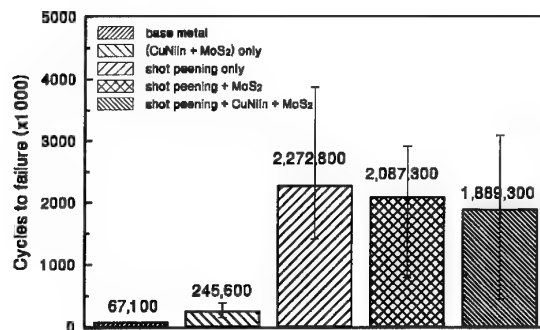


Figure 3. Effects of CuNiIn coating and MoS<sub>2</sub> lubricant on the fretting fatigue life of Ti-6Al-4V (round edge bridges). The coating and lubricant were applied by Vendor #1.

Shot peening dramatically improved the fretting fatigue resistance of Ti-6Al-4V, although the scatter in the fretting fatigue data was relatively large. The fretting fatigue life of four shot peened samples varied from 1,416,030 to 3,864,240 cycles with an average value of 2,272,800 cycles, which was some 34 times longer than the life for the baseline Ti-6Al-4V material. Shot peening produced work hardened layers on the specimen surface with a high compressive residual stress level (about - 500 MPa) and an increased surface hardness (about HV 600). Both factors contributed towards improvement in the fretting fatigue resistance of the Ti-6Al-4V material.

The fretting fatigue life of three shot peened Ti-6Al-4V specimens coated with CuNiIn and MoS<sub>2</sub> lubricant applied by Vendor #1 exhibited a very large scatter. Two specimens failed after 2,129,140 and 3,092,670 cycles, whereas the third specimen only lasted for 446,190 cycles. The application of MoS<sub>2</sub> lubricant on its own on shot peened specimens also produced similar results where two specimens lasted 2,558,990 and 2,909,900 cycles, and whereas the third specimen only lasted for 793,100 cycles. These results indicate that the application of CuNiIn coating and/or MoS<sub>2</sub> lubricant does not improve the fretting fatigue life of shot peened Ti-6Al-4V specimens.

The effects of CuNiIn coating and/or MoS<sub>2</sub> lubricant, applied by Vendor #2, on the fretting fatigue life of shot peened and/or carbon ion implanted Ti-6Al-4V material are shown in Fig.4. All tests were conducted with round edge fretting bridges. Four shot peened Ti-6Al-4V specimens with CuNiIn coating again showed a large scatter in fretting fatigue life which ranged from 409,350 to 1,391,720 cycles, all of which were lower than the uncoated shot peened specimen lives. The average life of shot peened Ti-6Al-4V material was reduced by 65% as a result of CuNiIn coating application. The residual stress measurement on the shot peened surface was -500 MPa, while the stress measured on the shot peened plus CuNiIn coated surface changed to +130 MPa. The fretting fatigue life of shot peened Ti-6Al-4V coated with CuNiIn and MoS<sub>2</sub> was also low. All four specimens failed between 57,630 and 286,840 cycles. The average life was 151,000 cycles, which is only 7% of the average life for shot

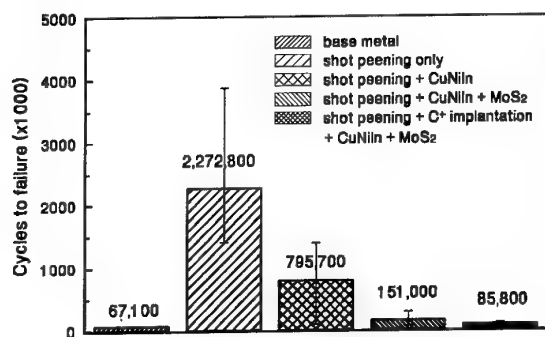


Figure 4. Effects of CuNiIn coating and MoS<sub>2</sub> lubricant on the fretting fatigue life of Ti-6Al-4V (round edge bridge). The coating and lubricant were applied by Vendor #2.

peened specimens. The application of CuNiIn coating and MoS<sub>2</sub> lubricant on four shot peened and carbon ion implanted Ti-6Al-4V specimens produced a further decrease in fretting fatigue life which ranged from 64,050 to 109,720 cycles, with an average value of 85,800 cycles. This value is close to the fretting fatigue life of the baseline Ti-6Al-4V without any surface modification treatment (67,100 cycles).

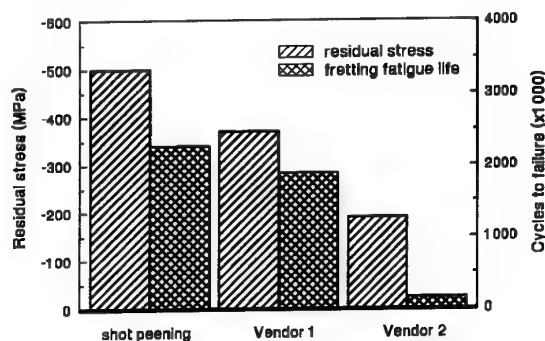


Figure 5. Comparison of residual stress and fretting fatigue life of shot peened Ti-6Al-4V with CuNiIn and MoS<sub>2</sub> coated by two different vendors.

A comparison of the residual stress levels and fretting fatigue lives of the two sets of coated shot peened Ti-6Al-4V specimens supplied by two different coating vendors is presented in Fig.5. Four shot peened specimens coated by Vendor #2 with CuNiIn and MoS<sub>2</sub> showed consistently lower fretting fatigue life than the specimens coated by Vendor #1. The average life of the specimens with two coatings supplied by Vendor #2 was 151,000 cycles, which was only about 8% of that provided by Vendor #1 (1,889,300 cycles). The difference of one order of magnitude in fretting fatigue lives was totally unexpected because both vendors were required to follow the same processing specifications. The difference of this magnitude in fretting fatigue life of the two sets of coated shot peened specimens may be related to the difference in their residual stress states, considering that CuNiIn coating is plasma sprayed onto the shot peened surfaces. Test results show that the application of the coating by Vendor #2 reduced the compressive residual stress level of the shot peened

surface from -500 MPa to -190 MPa, whereas the application of the coating by Vendor #1 only led to a decrease in the compressive residual stress from -500 MPa to -370 MPa. The reduction in the beneficial compressive residual stresses offsets the lubrication effect provided by the coating and significantly reduces the fretting fatigue resistance of the test-pieces. The relaxation of compressive residual stresses in the shot peened surface is directly related to control of the plasma spraying coating process, which in turn can vary with different coating vendors.

### 3.1.2 Ion implantation

The effect of carbon and nitrogen ion implantation on the fretting fatigue life of baseline and shot peened Ti-6Al-4V specimens is shown in Fig.6. This set of fretting fatigue tests was conducted with square edge fretting bridges (the effect of bridge geometry will be presented and discussed in section 3.1.4). For baseline Ti-6Al-4V without any surface treatment, the fretting fatigue life of three samples ranged from 37,870 to 49,320 cycles with an average life of 44,900 cycles. All specimens failed at the fretting boundary.

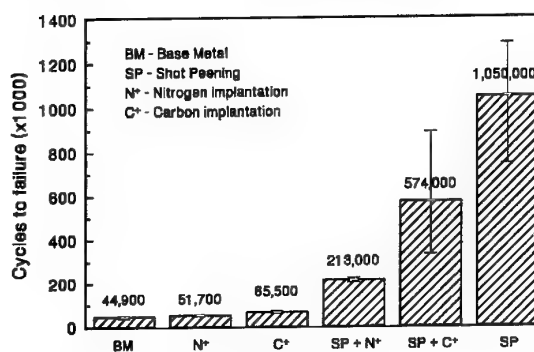


Figure 6. Effects of ion implantation and/or shot peening on the fretting fatigue life of Ti-6Al-4V (square edge bridges).

Carbon or nitrogen ion implantation improved the fretting fatigue resistance of baseline Ti-6Al-4V to some extent. For nitrogen implantation, the fretting fatigue life of three specimens ranged from 47,890 to 55,670 cycles and, on an average, the fretting fatigue life of 51,700 cycles was 15% higher than that of the baseline material life. For carbon implantation, the improvement in fretting fatigue life was more significant. Three carbon implanted samples failed between 59,140 to 71,190 cycles with an average fretting fatigue life of 65,500 cycles. This represented an average increase of 46% compared to that of the baseline material. The improvement in fretting fatigue resistance of baseline Ti-6Al-4V by ion implantation may be attributed to the increased surface hardness. After nitrogen or carbon implantation, the surface hardness of Ti-6Al-4V increased from HK<sub>50</sub> 420 (baseline material) to HK<sub>50</sub> 490 and HK<sub>50</sub> 550 respectively. With an increase in surface hardness, the fretting wear mechanism may be partly changed from seizing and adhesion to sliding wear. As a result, the fretting fatigue life is improved.

Similar to the results obtained with round edge bridges, shot peening dramatically improved the fretting fatigue resistance of Ti-6Al-4V in all tests conducted using square edge bridges, although the scatter in the data was relatively large. The fretting fatigue life of three shot peened samples varied from 747,110 to 1,287,590 cycles with an average value of 1,050,000 cycles, which was some 23 times longer than that of the baseline Ti-6Al-4V specimens.

Although both shot peening and ion implantation (carbon or nitrogen) on their own increase the fretting fatigue life of Ti-6Al-4V, the application of carbon or nitrogen ion implantation on shot peened specimens significantly reduced the fretting fatigue resistance. For shot peened specimens followed by carbon implantation, the fretting fatigue life of four samples varied from 331,530 to 891,460 cycles. The average fretting fatigue life was 574,000 cycles, which was 45% lower than the average shot peened Ti-6Al-4V life. Nitrogen implantation reduced the fretting fatigue life of shot peened Ti-6Al-4V more dramatically than carbon implantation. The fretting fatigue life of three shot peened plus nitrogen implanted samples ranged between 200,670 and 224,460 cycles. The average fretting fatigue life was 213,000 cycles, which accounts for a reduction of about 80% in the shot peened Ti-6Al-4V life.

The reduction in fretting fatigue life of shot peened plus ion implanted Ti-6Al-4V may be attributed to a combination of the rough surface finish and the creation of a shallow hardened layer by ion implantation. Due to plastic deformation, shot peening significantly increases surface hardness and roughness of Ti-6Al-4V samples. The mean of the maximum peak-to-valley (R<sub>tm</sub>) value increases from 1.16  $\mu\text{m}$  (600 grit polished surface) to 13.0  $\mu\text{m}$  after shot peening. Carbon or nitrogen ion implantation on the other hand produce titanium carbide or titanium nitride layers respectively. These phases are very hard but also brittle. Because of the shallow effective depth of the implanted layer (usually less than 1000 Å), ion implantation does not form a uniform hardened layer on the shot peened surface. Instead, only the peaks of the rough surface are hardened. Under cyclic loading conditions coupled with high normal pressures, the relatively brittle and nonuniform hardened layer could be easily broken at weak sites within the fretting region to form hard fretting debris and early cracks, which may result in a reduction of fretting fatigue life of the shot peened samples.

### 3.1.3 Residual stress effects

In the case of both baseline and shot peened Ti-6Al-4V, carbon ion implantation showed higher fretting fatigue life than that produced by nitrogen ion implantation, which may be attributed to its high level of compressive residual stress. Figure 7 shows that a general correlation usually exists between the average surface residual stress and average fretting fatigue life for ion implanted and/or shot peened Ti-6Al-4V. Carbon ion implanted test-pieces have a higher magnitude of surface compressive residual stress (-320 MPa on average) than nitrogen ion implanted test-pieces (-150 MPa on average), and the figure shows that in relative terms this correlates well with the fretting fatigue

life of 65,500 cycles for carbon implanted samples and 51,700 cycles for nitrogen ion implanted samples.

A similar tendency is apparent for test-pieces that were subjected to combined shot peening and ion implantation treatments. The shot peened plus carbon ion implanted Ti-6Al-4V test-pieces have a higher average fretting fatigue life (574,000 cycles) than the shot peened plus nitrogen ion implanted specimens (213,000 cycles). This in turn correlates well with respective compressive residual stress levels. The carbon ion implanted test-pieces have an average compressive residual stress of -510 MPa while the nitrogen ion implanted test-pieces have an average residual stress level of only -310 MPa.

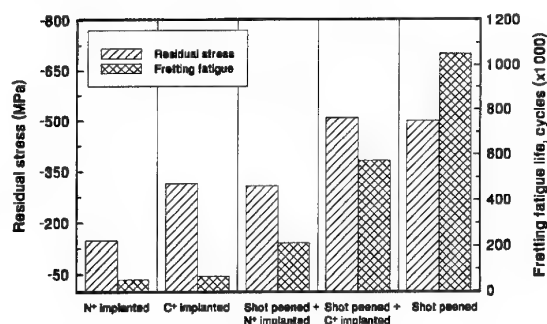


Figure 7. Fretting fatigue life and residual stress of Ti-6Al-4V with different surface modification treatments.

Figure 7 shows that the average fretting fatigue life increases in the following order: nitrogen ion implantation, carbon ion implantation, shot peening plus nitrogen ion implantation, shot peening plus carbon ion implantation, and finally shot peening only. Generally, fretting fatigue life increases with an increase in the magnitude of compressive residual stress level. However, the results also indicate that the fretting fatigue life does not depend solely on the surface residual stress level but that other factors are also involved. This is because the fretting fatigue life dependence on residual stress does not always exhibit a one on one relationship. It is, nevertheless, reasonable to state that surface compressive residual stress level plays a dominant role. Other factors such as surface hardness, brittle surface phases and surface roughness may also contribute to fretting fatigue.

### 3.1.4 Bridge geometry effects

The effects of fretting bridge geometry on the fretting fatigue life of Ti-6Al-4V with different surface treatments are shown in Fig.8. Four baseline Ti-6Al-4V specimens were tested with round edge bridges and they failed between 57,750 and 79,230 cycles with an average life of 67,100 cycles. With square edge bridges, the fretting fatigue life of the three baseline Ti-6Al-4V samples ranged between 37,900 and 49,300 cycles with an average value of 44,900 cycles, which was only about 67% of the round edge bridge life.

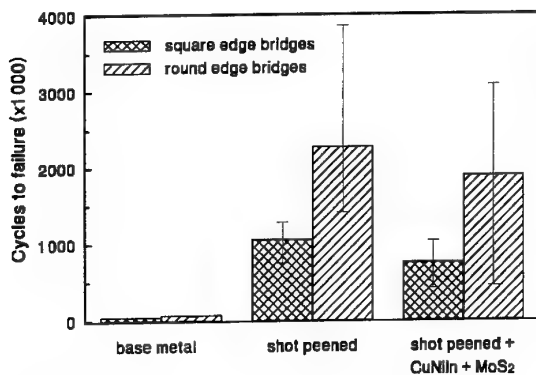


Figure 8. Comparison of the effect of bridge geometry on the fretting fatigue life of Ti-6Al-4V with different surface treatments. The CuNiIn and MoS<sub>2</sub> coatings were applied by same vendor (Vendor #1).

After shot peening, four Ti-6Al-4V specimens were tested with round edge bridges. Their fretting fatigue life ranged between 1,416,030 and 3,864,240 cycles with an average value of 2,272,800 cycles, which represented an increase of more than 38 times the baseline Ti-6Al-4V fretting fatigue life tested using the same bridge geometry. The fretting fatigue life of the three shot peened Ti-6Al-4V samples tested using square edge bridges varied between 747,110 and 1,287,590 cycles. The average life of these samples was 1,050,200 cycles, which is only 41% of the life obtained with the round edge bridges.

Another surface treatment tested was a combination of shot peening and CuNiIn and MoS<sub>2</sub> coatings (applied by Vendor #1). With round edge bridges, the fretting fatigue life of three treated specimens ranged from 446,190 to 3,092,670 cycles with an average value of 1,889,300 cycles. Four fretting fatigue specimens, subjected to the same treatments by the same vendor but tested with square edge bridges, lasted between 410,170 to 1,035,420 cycles revealing an average fretting fatigue life of 752,200 cycles, which was only 40% of the life obtained with round edge bridges.

The above results confirm that the fretting fatigue lives of specimens tested with square edge bridges are significantly lower than those tested using round edge bridges. It also seems that the edge effect is more significant for surface modified test-pieces than it is for the baseline material. For round edge bridges, the life improvement afforded by shot peening is some 38 times better than for the baseline Ti-6Al-4V, while the improvement is only 23 times for the square edge geometry. The same tendency has been observed for shot peened plus CuNiIn and MoS<sub>2</sub> coated specimens. These results indicate that if fretting fatigue tests are conducted with square edge bridges, a common practice for fretting fatigue testing [16], the improvement due to a surface modification treatment on fretting fatigue life can be underestimated. In addition, the sharp stress concentration produced by the square edge geometry is rarely tolerated in gas turbine engine component designs.

### 3.2 Fretting Fatigue Testing of Ti-17 Material at 278°C

For fretting fatigue tests conducted at elevated temperature (278°C), specimens were made of Ti-17 (the disc material), whereas round edge bridges were made of Ti-6Al-4V (the blade material). Different surface treatments were applied to the Ti-6Al-4V bridges to evaluate the effects of surface modified blades on the fretting fatigue life of the baseline (unpeened) and shot peened disc material.

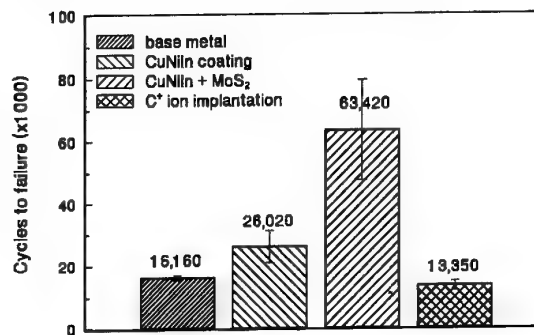


Figure 9. Effects of different surface treatments of Ti-6Al-4V bridges (round edge) on the fretting fatigue life of baseline Ti-17 specimens. Tests were conducted at 278°C.

The effects of various surface treatments on the fretting fatigue resistance of baseline Ti-17 are shown in Fig.9. The average fretting fatigue life of baseline Ti-17 specimens was 16,160 cycles. The application of CuNiIn soft coating on the Ti-6Al-4V bridges increased the fretting fatigue life by about 60% to 26,020 cycles. This improvement is attributed to the reduction in friction on the specimen caused by the soft coating on the bridges. The solid MoS<sub>2</sub> film applied on the CuNiIn coating further reduced the friction. As a result, the fretting fatigue life of baseline Ti-17 was improved by a factor of 4 to 63,420 cycles. These results are consistent with the results observed in room temperature fretting fatigue tests. They confirm that the application of CuNiIn coating plus MoS<sub>2</sub> lubricant on Ti-alloys improves fretting fatigue life of unpeened blade and disc materials over a range of temperatures.

Carbon ion implantation of Ti-6Al-4V bridges slightly reduced the fretting fatigue life of baseline Ti-17 to about 13,350 cycles. This may be attributed to the increased fretting damage on the relatively soft specimen surface when it frets against the hardened bridge surfaces produced by carbon ion implantation.

Figure 10 shows the effects of several surface treatments, applied to Ti-6Al-4V bridges, on the fretting fatigue life of shot peened Ti-17 specimens. When shot peened specimens were fretted against shot peened bridges, the average fretting fatigue life was about 88,100 cycles, which was about 5 times longer than the baseline fretting fatigue life using both untreated specimens and bridges.

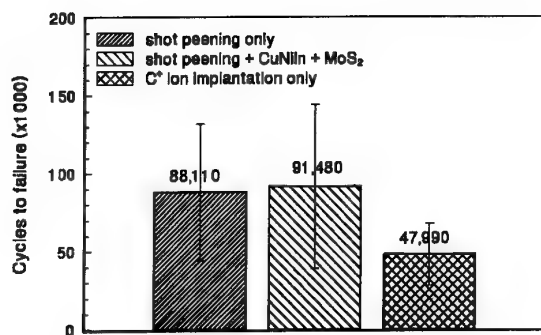


Figure 10. Effects of different surface treatments of Ti-6Al-4V bridges (round edge) on the fretting fatigue life of shot peen Ti-17 specimens. Tests were conducted at 278°C.

This improvement may be attributed to the high level of compressive residual stresses and the increased surface hardness produced by shot peening. The former increases the resistance to fretting fatigue damage accumulation, while the latter reduces the frictional forces on the specimen.

For shot peened Ti-17 specimens, the application of CuNiIn coating plus MoS<sub>2</sub> lubricant (provided by Vendor #1) on the shot peened Ti-6Al-4V bridges produced an average fretting fatigue life of 91,500 cycles, which is similar to the result obtained without the application of these lubricant coatings if the large scatter in the data are taken into consideration. This result indicates that increased lubrication between both the shot peened specimen and the bridges does not produce much benefit. Furthermore, since the CuNiIn coating was plasma sprayed on the shot peened Ti-6Al-4V bridges, the shot peened Ti-17 specimen itself was not directly affected by the coating process. As a result, no negative effects are observed on the fretting fatigue life of the Ti-17 material.

When unpeened fretting bridges were carbon ion implanted, the average fretting fatigue life of shot peened Ti-17 specimens was reduced to 48,000 cycles, which is only about 54% of the life obtained with shot peened bridges. The hardened layer produced by carbon ion implantation is relatively thin and brittle. When it frets against a rough shot peened surface under high normal pressure, the implanted layer might break and form some hard debris which is believed to accelerate the fretting fatigue process. As a result, the fretting fatigue life was reduced.

### 3.3 Surface Treatments and Fretting Fatigue Damage Mechanisms

A surface treatment improves certain surface properties of a material but it also affects the substrate itself (such as surface finish and stress state). The effectiveness of a particular surface treatment in improving the fretting fatigue life of a titanium alloy will depend upon the operative fretting fatigue mechanism. For different fretting fatigue mechanisms, these two effects may act differently as explained below.

Baseline Ti-6Al-4V material is relatively soft, and during fretting fatigue, under high normal pressures and cyclic loadings, significant plastic deformation occurs on specimen surfaces at the contact regions with the fretting bridge legs to form fretting debris and eventually a fretting scar (Fig11). In addition, slip bands formed through plastic deformation move towards the outer edges of the four fretted regions, i.e. the fretting boundaries, and accumulate there to form fretting grooves. Cracks simultaneously initiate at these four fretting boundaries and final fracture develops as one of these propagating cracks exceeds the critical size. Therefore, sub-critical cracks are often observed in failed test-pieces at fretting boundaries other than the fracture location. In the baseline material, the fretting fatigue mechanism is, therefore, fretting-damage-dominated. The application of CuNiIn and MoS<sub>2</sub> coatings improves lubrication between the fretting bridges and the specimen. The rate of build up of slip bands at the fretting boundaries is reduced due to decreased friction and the fretting life improves.

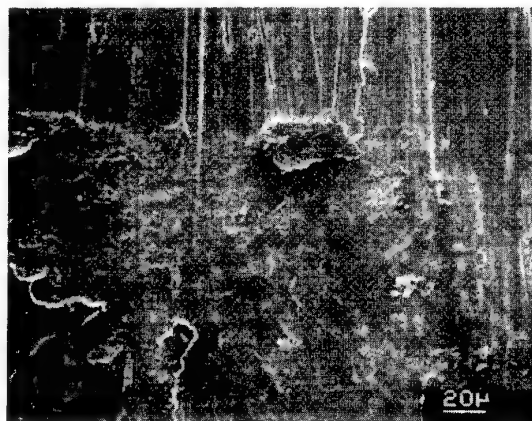


Figure 11. Fretting scar on the surface of baseline Ti-6Al-4V specimen; debris found at the edge of the fretted area.

The fretting fatigue crack initiation mechanism in shot peened Ti-6Al-4V is different from that of the unpeened material, and plasma sprayed coating produces a negative impact on peened material. Shot peening changes the surface conditions of titanium alloys by work hardening. The most beneficial effect created by this process is the surface compressive residual stresses (about -500 MPa for Ti-6Al-4V). Surface hardness also increases due to the work hardening effect. The shot peening process removes oxides and produces a fresh surface. The presence of the high level of compressive residual stresses and the increased hardness in the shot peened Ti-6Al-4V surface prevents significant plastic deformation. There is little fretting damage observed on the shot peened surface. Grooves do not form at the fretting boundaries. Fretting fatigue cracks initiate at the stress concentration site and, usually, only one crack initiates and propagates to cause final fracture. Under this fatigue-dominated fretting fatigue mechanism, the lubrication provided by CuNiIn coating has little impact on the crack initiation. Instead, the plasma spraying process may reduce compressive residual stress and impair the improvement provided by shot peening.



Shot peening significantly increases the fatigue as well as the fretting fatigue lives of titanium alloys, and this is why it has been selected by many gas turbine manufacturers as a standard surface treatment for a number of fan, compressor and turbine components. Any other surface treatment intended to improve the fretting fatigue life of these components will have to be used in combination with shot peening. Our test results show that several surface treatments (such as  $C^+$  or  $N^+$  ion implantation, CuNiIn coating and  $MoS_2$ ) improve the fretting fatigue resistance of baseline Ti-6Al-4V. However, in many cases, they show negative effects on the life of shot peened material. Therefore, the effects of various surface treatments on the shot peened material must always be assessed for gas turbine applications.

Nitrogen ion implantation significantly reduces the compressive residual stresses of shot peened Ti-6Al-4V material and dramatically reduces its fretting fatigue life (compared to carbon ion implantation). In the case of CuNiIn coating, the plasma spraying process can change the surface residual stress state from compressive to tensile, and, therefore, seriously reduce the fretting fatigue life of shot peened Ti-6Al-4V material. In addition, the control of the plasma coating process, which will in turn affect the residual stress level, may also be important in controlling the fretting fatigue life. For example, the same type of coating applied by different vendors can result in more than one order of magnitude difference in the fretting fatigue life.

The surface roughness of shot peened surfaces is another factor which cannot be ignored when considering additional surface treatments for shot peened test-pieces. Many stress concentration sites exist in the rough shot peened surface. If a surface treated layer is very hard but very thin and does not cover the entire rough surface, it can easily break at stress concentration sites to produce early crack initiation from debris entrapment. Therefore the fretting fatigue life is reduced, as in the case of ion implantation of shot peened Ti-6Al-4V. An effective surface coating for further improving the fretting fatigue life of shot peened materials should be thick enough to cover the rough surface and it should have some ductility.

### 3.4 Some Promising Emerging Technologies for Improving Fretting Fatigue Life of Ti-Alloys

From the above results and discussion, it is clear that a potential research direction for improving the fretting fatigue life of Ti-alloys may involve new technologies that can produce a relatively smooth surface with considerable level of compressive residual stress to replace the shot peening process. Ultrasonic shot peening and laser shock treatment are two such technologies that appear very promising.

Ultrasonic shot peening is based on the vibration of balls using high power ultrasound. The entire surface of the treated work piece is peened with a very high number of impacts during a very short time. It has been shown that this newly emerging technique can produce a higher magnitude of compressive residual stress and smoother surface finish on Ti-6Al-4V than conventional shot peening. The ultrasonic shot peening can increase the low

cycle fatigue life of HP310 steel relative to the conventional shot peening life. It also improves the high cycle fatigue strength of AISI 431 steel and of alloy Ti-7Al-4Mo [17].

Laser shock treatment utilizes a mechanical phenomenon based on the generation of a shock wave created by an explosion of laser irradiated material. This process can produce considerable levels of compressive residual stress as well as hardening in surface layers. Compared with shot peening, it is possible to produce a smoother surface with a deeper penetration of compressive residual stresses with the laser shock treatment, even though the surface stress magnitude and the surface hardness may not be as high [17,18]. Test results also indicate that the laser shock treatment can improve the fatigue life of 7075 aluminium alloy more significantly than the shot peening process [17].

The potential for combining these processes with other treatments is high because of the relatively smooth surface finish produced by these treatments. The ultrasonic shot peening may be applied on the entire surface, while the laser shock treatment may be considered as a special process for localized treatments.

## 4. CONCLUDING REMARKS

- (1) Shot peening significantly increases the fretting fatigue life of titanium alloys because it produces compressive residual stresses and increases surface hardness. However, for gas turbine engine components, if other surface treatments are considered for improving their fretting fatigue resistance, it is necessary to study the effects of these surface treatments on the shot peened titanium alloy specimens.
- (2) Application of CuNiIn coating and ion implantation (carbon or nitrogen) increases the fretting fatigue life of baseline titanium alloys. However, these treatments reduce the fretting fatigue life of shot peened titanium alloy specimens due to a combination of reducing the compressive residual stress and producing uneven hardening on shot peened surfaces.
- (3) Ultrasonic shot peening and laser shock treatment appear to be two promising technologies for substantially improving the fretting fatigue life of titanium alloys.

## ACKNOWLEDGEMENT

This work was conducted under the NRC Institute for Aerospace Research project JHM01 with financial support provided by the Department of National Defence Canada under CRAD FA220791NRC51.

## REFERENCES

1. Waterhouse, R.B., "Fretting Fatigue", *International Materials Review*, 37, 1992, pp 77-97.
2. Broszeit, E., Kloos, K.H. and Schweighofar, B., "The Fretting Fatigue Behaviour of the Titanium Alloy Ti-6Al-4V", in "Titanium Science & Technology", 1984, pp 2171-2178.
3. Harris, W.J., "The Influence of Fretting on Fatigue, Part III", AGARD-AR-45, 1972.
4. Hoepfner, D.W., "Mechanisms of Fretting-Fatigue and Their Impact on Test Methods Development", in "Standardization of Fretting Fatigue Test Methods and Equipment", ASTM STP 1159, 1992, pp 23-32.
5. Elder, J.E., Patnaik, P. and Thamburaj, R., "Life Extension of Titanium Alloy Gas Turbine Components by Ion Implantation", in "Tribological Mechanisms & Wear Problems in Materials", 1987, pp 11-21.
6. Waterhouse, R.B., "The Effect of Surface Treatment on the Fatigue and Fretting Fatigue of Metallic Materials", in "Metal Treatments against Wear, Corrosion, Fretting and Fatigue", 1988, pp 31-40.
7. Burman, G., "Fretting Tests of Titanium Alloy Ti-6Al-4V with Shot-Peened and Solid Lubricant Coated Surface", FFV Maintenance Division, Laboratory Report, 1979.
8. Vardiman, R.G., Creighton, D., Salivar, G., Effatian, A. and Rath, B.B., "Effect of Ion Implantation on Fretting Fatigue in Ti-6Al-4V Alloy", in "Materials Evaluation Under Fretting Conditions", ASTM STP 780, 1982, pp 138-149.
9. Saritas, S., Procter, R.P.M. and Grant, W.A., "Effect of Ion Implantation on Fatigue, Fretting and Fretting-Corrosion of Ti-6Al-4V", *Materials Science and Engineering*, A115, 1989, pp 307-314.
10. Xue, L., Koul, A.K., Bibby, M., Wallace, W. and Islam, M., "A Survey of Surface Treatments to Improve the Fretting Fatigue Resistance of Ti-6Al-4V", in "Computer Methods and Experimental Measurements for Surface Treatment Effects II", 1995, pp 265-272.
11. Waterhouse, R.B. and Trowsdale, A.J., "Residual Stress and Surface Roughness in Fretting Fatigue", *Journal of Physics D: Applied Physics*, 25, 1A, 1992, pp A236-A239.
12. O'Connor, J.J., "The Role of Elastic Stress Analysis in the Interpretation of Fretting Fatigue Failures", in *Fretting Fatigue*, 1981, pp 23-66.
13. Xue, L., Koul, A.K., Bibby, M., Wallace, W., Andrews, R. and Islam, M., "The Effects of Residual Stress and Fretting Bridge Geometry on the Fretting Fatigue", *Canadian Aeronautics and Space Journal*, 41, 2, 1995, pp 78-85.
14. Chakravarty, S., Andrews, R.G., Patnaik, P.C. and Koul, A.K., "The Effect of Surface Modification on Fretting Fatigue in Ti Alloy Turbine Components", *Journal of Metals*, 47, 4, 1995, pp 31-35.
15. Cullity, B.D., "Elements of X-Ray Diffraction", 1956, pp 431-453.
16. Nakazawa, K., Sumita, M. and Maruyama, N., "Effect of Contact Pressure on Fretting Fatigue of High Strength Steel and Titanium Alloy", in "Standardization of Fretting Fatigue Test Methods and Equipment", ASTM STP 1159, 1992, pp 115-125.
17. Lu, J., Peyre, P., Omam Nonga, C., Benamar, A. and Flavenot, J.F., "Mechanical Surface Treatments, Current Trends, and Future Prospects", in "Surface Modification Technologies VIII", 1995, pp. 589-602.
18. Peyre, P. and Fabbro, R., "Laser Shock Processing: A Review of the Physics and Applications", *Optical and Quantum Electronics*, 27, 12, 1995, pp.1213-1229.

# Thin Film Lubrication of Non-Smooth Surfaces

Bo Jacobson

SKF Engineering & Research Centre B.V.  
Postbus 2350, 3430 DT Nieuwegein, The Netherlands

## ABSTRACT

The reliable performance of heavily-loaded mechanical contacts can only be sustained over long periods when a lubricant film fully separates the two bodies and asperities do not interact. Engineering surfaces do have a certain degree of roughness and this would then determine the required thickness of the lubricant film. Unfortunately, thick lubricant films have disadvantages such as high power losses (oil churning) or they may not be attainable because of prescribed lubricants or high operating temperatures.

In order to optimize the quality of the surface against these conflicting requirements, or in order to design specific surfaces for extreme operating conditions, a thorough understanding of the mechanisms of micro EHL or asperity lubrication is needed. This required level of understanding goes beyond the current one which employs  $\Lambda$ , the ratio between calculated film thickness and combined surface roughness. When detailed analysis of the behaviour of surface asperities in heavily-loaded elastohydrodynamic contacts includes non-Newtonian effects, two phenomena become evident. One phenomenon is the possibility to describe theoretically the collapse of an oil film and to determine when a lubricated rough surface in contact with another surface can come into solid contact through the lubricant film. The other phenomenon, which is closely related to the first one, is the explanation of the well-known fact that the oil film thickness needed to separate two elastohydrodynamically lubricated surfaces is strongly dependent on the structure of the surface roughness and not only on the values of the different surface roughness parameters. Both of these phenomena can only be explained if the pressure distribution in the lubricant film has such high frequency variation that local asperities in the lubricant film become elastically deformed by the pressure distribution, making the contact surfaces conform much more than in the unstressed state outside the high pressure contact zone.

## 1. LUBRICATION OF NON-SMOOTH SURFACES

Recently, when computer modelling of EHL films and dry contacts was made possible, all the way down to the level of single surface roughness asperities, using powerful hardware and modern numerical techniques, it became evident that, just as for dry contacts, the Newtonian lubricant models produced very spiky pressure distributions. In fact, the variation in pressure became almost a mirror image of the local roughness pattern, magnified some orders of magnitude ( $6 \times 10^{10}$  Pa rad<sup>-1</sup>). The resulting surface roughness on the deformed lubricated surfaces became only a few percent of the oil film thickness, reflecting the variation in the compression of the lubricant in the high pressure region. For oils compressed into the glassy state, the compressibility is only 3-5% GPa<sup>-1</sup>, giving a variation in the oil film thickness in the order of  $\pm 4\%$  for a pressure variation of  $\pm 1$  GPa superimposed on the normal elastohydrodynamic pressure distribution.

Such a spiky pressure distribution induces shear stresses in the lubricant which are proportional to the pressure gradients and proportional to the local oil film thicknesses for pure rolling contacts. When some sliding motion is superimposed on the rolling, such as the kinematic sliding in deep groove ball bearings and spherical roller bearings, high stresses in the lubricant are also introduced in the direction of slip.

## 2. NEWTONIAN VERSUS NON-NEWTONIAN LUBRICANTS

Applying the Newtonian rheological model, the shear stress that a fluid can sustain is unlimited. Consequently, this model is not suited for a theoretical prediction of the friction in the contact. However, in the past the Newtonian fluid model has led to accurate film thickness predictions for smooth surfaces, which were confirmed by experiments.

For heavily-loaded lubricated contacts the total shear deformation of the oil in the high pressure region gives stresses well above the limit for Newtonian behaviour of the lubricant. This means that stresses and lubricant flows in two perpendicular directions in the oil film will be coupled to each other via the limited shear strength of the oil. A pressure gradient in one direction will also influence the flow in the perpendicular direction, much the same as for dry friction between solid bodies.

### 2.1 Experimental Evidence

As early as 1941, Bridgeman [1] showed experimentally that liquids of the same type as lubricating oils converted to solids at pressures much below those found in lubricant films between the load-carrying parts of a ball bearing. Bridgeman's experiments were all static, and as the high viscosity/solid behaviour at high pressures inside an EHL contact is only present for a millisecond or a fraction of a millisecond, the behaviour on that time scale is even more like that of a solid. This type of behaviour for the oil in the central high pressure part of an elastohydrodynamically lubricated point contact was used by Jacobson [2] in his calculation of the oil film thickness distribution in a circular contact. To obtain input data for the computer calculations, Jacobson measured the shear strength of the solidified oil and the pressure at which it solidified. Later, more accurate measurements were published [3] which show that typical liquid lubricants convert to glassy solids at pressures ranging from 0.5 GPa to above 2.2 GPa, depending on the temperature and molecular structure of the lubricant. As soon as the lubricant is compressed into the solid state, even very slow sliding speeds superimposed on the rolling speed will introduce high shear stresses in the direction of surface sliding. These stresses superimposed on the stresses emanating from the pressure distribution in the contact drive the lubricant into a strongly non-Newtonian state. When the limiting shear strength of the lubricant is approached, a



motion of the surfaces in one direction will directly influence the lubricant flow perpendicular to it.

This had already been experimentally shown in [4] when high-speed photography was used to study the behaviour of an oil film in a sapphire disc machine where a sliding vibration perpendicular to the rolling entrainment velocity had a major influence on the formation of the oil film. For a Newtonian lubricant the small sideways vibration of  $\pm 0.1$  mm should not have any influence on the oil film build-up, but experiments showed that the central oil film thickness in

the inlet decreased almost to the same level as the film thickness on the side lobes of the elastohydrodynamic contacts; see Figure 1. The oil was already clearly non-Newtonian far out in the inlet region, causing a back-flow to take place when the sideways sliding was introduced. This means that not only the stresses but also the flow of lubricant inside the high pressure region of the EHL contact are strongly affected by the non-Newtonian behaviour of the lubricant. Therefore, the asperity behaviour in a heavily-loaded lubricated contact will be quite dependent on the presence or absence of a sliding motion

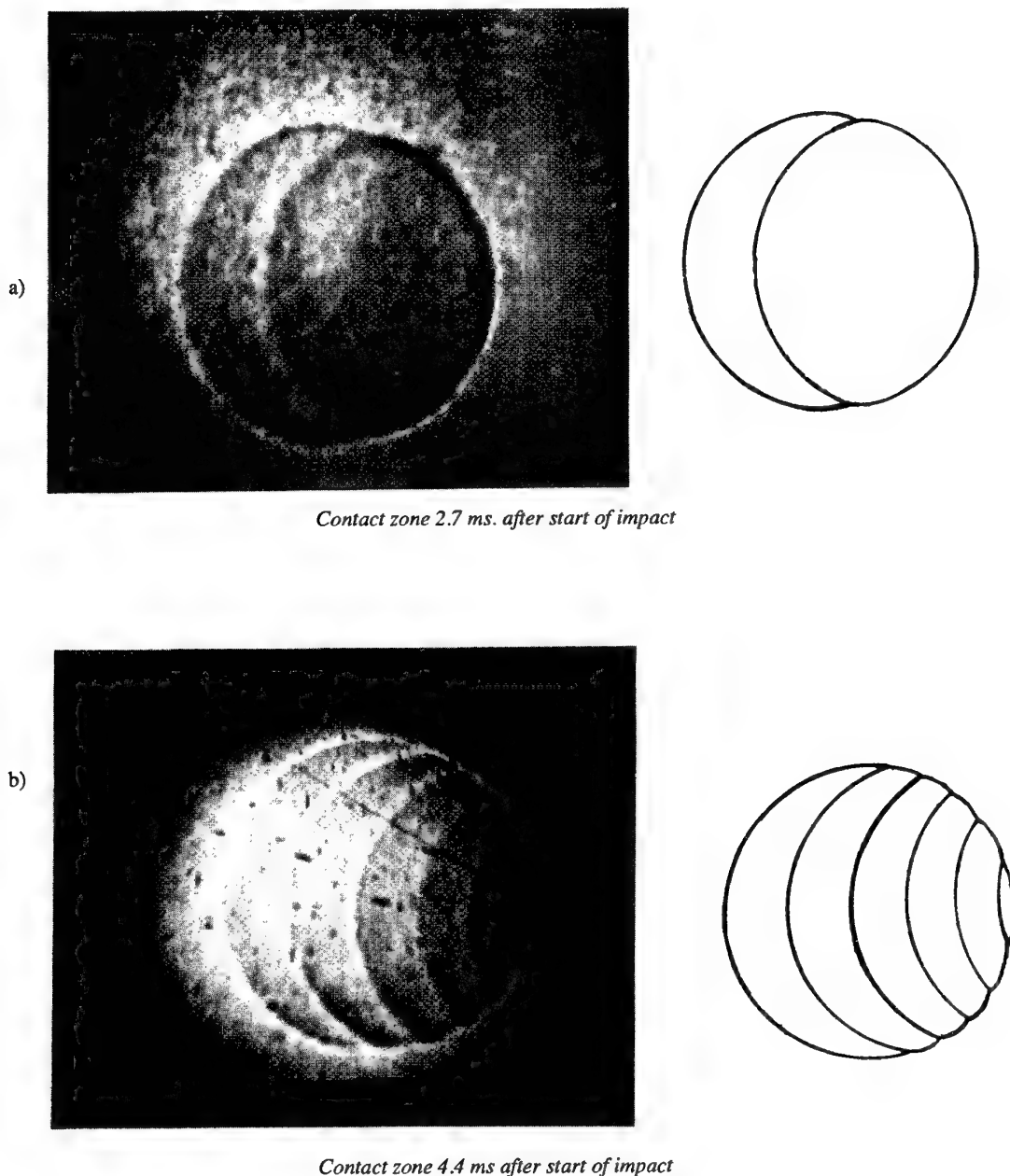


Figure 1: Disturbed oil film build-up due to slight sideways vibration.

component superimposed on the main rolling velocity component. If no sliding is present, the oil can behave like a Newtonian liquid, building up high local pressures on the asperity tops by squeeze motion which pushes them down and makes the lubricated surfaces conform much more than outside the Hertzian contact. The composite surface roughness of the two contacting surfaces becomes almost zero and the  $\Lambda$  values become large.

This ideal condition is quickly destroyed if some sliding is introduced between the loaded surfaces. The sliding motion in one direction uses all of the available strength of the oil in that direction which makes it very easy for local pressure variations within the contact to push the oil down into the valleys of the surface structure, allowing the asperity tops to reach through the oil film and collide. The interaction between the surface asperity behaviour and the lubricant rheology determines the state of lubrication.

## 2.2 Mixed Lubrication

Depending on the local rheology of the lubricant in the EHL contact and the surface structure of the contacting surfaces, the asperities will be more or less elastically deformed in the high pressure zone by the local pressure variations. For pure squeeze or rolling motion, the shear strength of the oil is high enough to deform the surfaces elastically so that they become totally conformal and thus need only a very thin oil film to avoid metallic contact. For pure sliding motion on the other hand, the shear stresses in the high pressure zone of the contact reach the lubricant shear strength and thus no strength is left to keep the oil from flowing out sideways from the asperity contacts, and a mean oil film thickness large enough to prevent the high tops of the asperities from colliding is necessary.

Thus, depending on the details of the surface structures of the co-operating surfaces and the kinematics of the contact, a very large variation can be found in the  $\Lambda$  value needed to  $\Lambda_n$  the contact without breaking through the oil film. values as high as 20 can give occasional metallic contact, while for well run-in surfaces,  $\Lambda$  as low as 0.3 can stop all metallic contact. It all depends on the lubrication of the asperities and on whether local pressure hills can elastically make the contacting surfaces more conformable inside the Hertzian contact area compared with the roughness they have outside the contact.

As shown in [5,6,7], the lubricated asperity behaviour inside the Hertzian contact zone is mainly a function of the surface roughness slope, wavelength, contact pressure, rolling and sliding velocity and the time it takes for an asperity to move through the Hertzian contact.

Numerical calculations of the oil film thickness over an asperity top in an elastohydrodynamic contact [7] showed that even when the asperity was 10 times higher than the central oil film thickness in the contact, virtually no trace could be seen of it in the converged numerical solution. The asperity built up its own pressure spike so it was almost totally flattened and pushed into the surface; see Figure 2. For a non-Newtonian lubricant model in sliding, the asperity was scraping away the lubricant and left a zero oil film thickness trace behind it; see Figure 3.

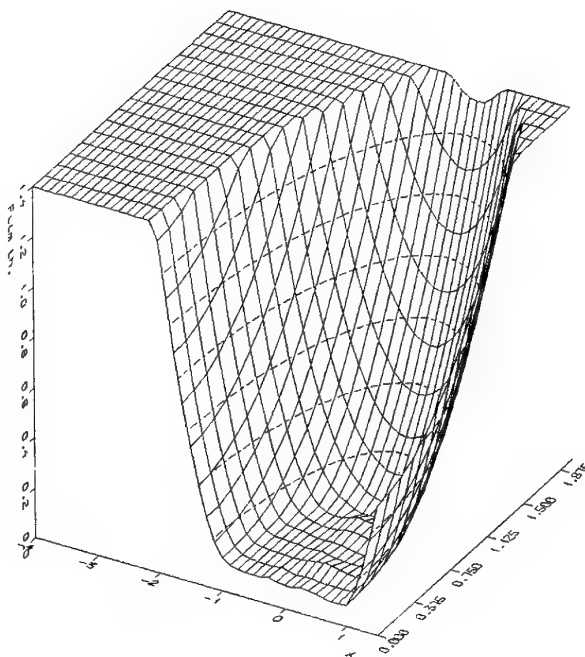


Figure 2: Asperity lubricated with Newtonian oil.

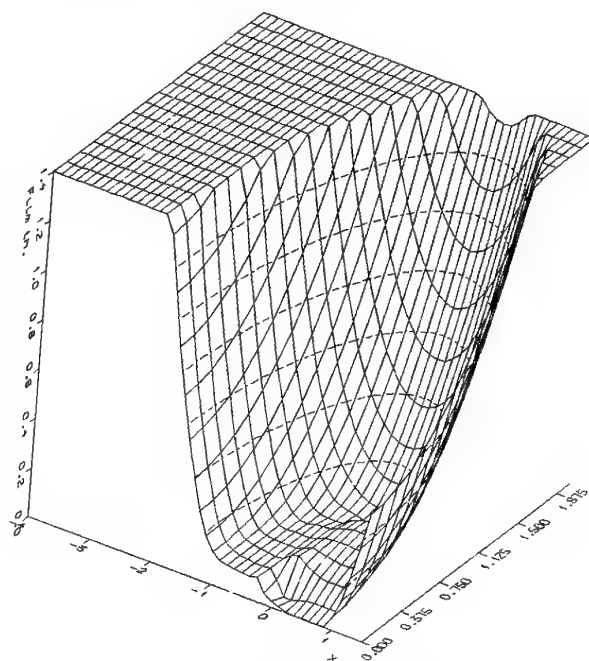


Figure 3: Asperity lubricated with non-Newtonian oil.

A simple steady-state calculation of the minimum oil film thickness above an asperity top showed that if a rough surface is stationary and a smooth, lubricated surface is rolling and sliding over it with local contact pressures above the glass transition pressure for the lubricant, the oil film thickness will fall to zero at each asperity top if enough time

is available. A simple model of the lubricant in the glassy state is in the form of a solid with a given shear strength  $\tau_L$  which varies with pressure and temperature. If then the smooth surface slides over the asperity, the film thickness will fall to

$$h_{\min} = \frac{2\tau_L \left| \frac{\partial \phi}{\partial x} \right|}{\left( \frac{\partial \phi}{\partial x} \right)^2 + \left( \frac{\partial \phi}{\partial y} \right)^2}$$

if enough time is available. this leads to oil film collapse on all the asperity tops with contact pressures above the glass transition pressure. The dynamic analysis of the compression of the asperities in the inlet zone and their reappearance during the transport through the contact showed that the important parameters determining whether metallic contact takes place or not are, in addition to the contact pressure, the surface roughness, the number of asperities inside the Hertzian contact area, the sliding speed, the transport time for an asperity through the lubricated contact, and the mean oil film thickness.

It could be summarized in the equation

$$n \frac{U_1 - U_2}{U_2} \bullet h_{\min} < \Delta h \quad \text{to avoid film collapse}$$

where

$n$  is the number of asperities from the inlet to the outlet of the lubricated contact

$U_1$  and  $U_2$  are the surface speeds

$h_{\min}$  is the mean oil film thickness

$\Delta h$  is the elastic springback of the asperity during its passage through the contact.

This means that a surface with 5 wavelengths within the Hertzian contact can have the relative sliding speed

$$\frac{U_1 - U_2}{U_1} = 0.44 = 44\%$$

for a given asperity springback, while a surface with 36 asperities needs less than 10% slip for the same springback.

The analysis of these parameters shows that using the ratio between the calculated oil film thickness and the composite surface roughness as a measure of how well the surfaces are separated by an oil film will underestimate how well smooth surfaces are lubricated compared with rough surfaces. Smooth surfaces need not only proportionally thinner oil films for good lubrication but also the ratio of oil film thickness to surface roughness can be decreased.

### 3. RHEOLOGY

The non-Newtonian behaviour of the oil, manifested by a limiting shear strength, can lead to oil film collapse, as discussed above. This collapse can be studied by considering the solidified oil as a plastic solid and applying the extrusion theory [8]. As expected, increasing sliding speeds and decreasing asperity wavelengths increase the likelihood of film collapse. Figure 4 shows the minimum film thickness reduction with time for different asperity wavelengths. Clearly, in these circumstances the simple measure of the film thickness ratio,  $\Lambda$ , is inadequate in explaining the risk of asperity metallic contact.

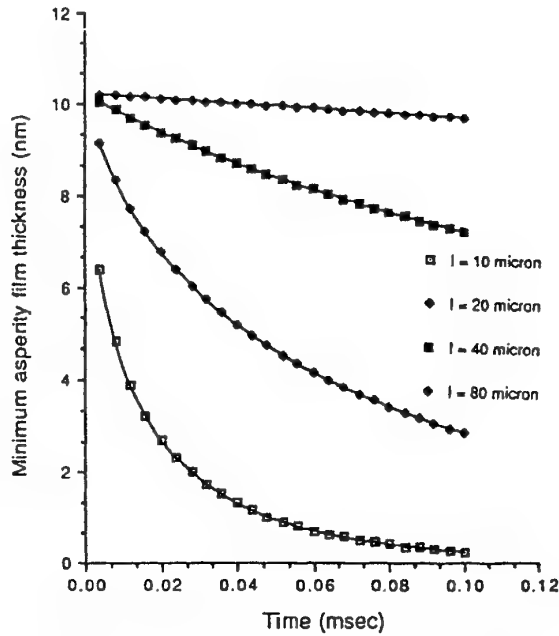


Figure 4: Plot of minimum film thicknesses during collapse for different asperity wavelengths [14].

### 4. STARVATION

Lubrication analysis generally assumes a sufficient supply of lubricant to ensure that the inlet to the conjunction is fully flooded. If this condition is not met and the contact is operating in the starved lubrication regime, then significant deviation from the predicted film thickness will occur. EHD film thickness can drop to 50% of its fully flooded value under moderately starved conditions, effectively invalidating the  $\Lambda$  criterion. Many machine elements operate in the starved regime; the condition is particularly severe for grease-lubricated bearings, and the accurate prediction of lubricating film thicknesses under these conditions is almost impossible.

In the starved condition there is insufficient lubricant to fill the inlet and, as a result it does not experience the full hydrodynamic pressure build-up required to generate the high viscosity necessary to maintain contact separation. This inevitably leads to lower film thicknesses than in the fully flooded condition. It is the inlet lubricant supply condition that determines the degree of film reduction, and it is not possible to predict this for many practical applications.

In early experimental studies [9], starved film thicknesses were measured using optical interferometry. As starvation increases and the inlet meniscus approaches the Hertzian radius, then film thickness drops below the lower detection limit of 100 nm and it is impossible to quantify the fully starved condition. More recent experimental studies [10,11] of the fully starved or parched regime have shown that a thin film does persist, maintaining contact separation, also when the meniscus reaches the Hertzian contact edge.

The regime of parched lubrication was first proposed by Kingsbury [10] to denote the fully starved condition where there is no inlet meniscus. In the parched regime no free oil

is present and only a thin film of oil remains on the surface. It was shown that instrument bearings could run successfully for several hours with only thin films (80-200 nm) of deposited oil as lubricant. This would not be predicted by the  $\Lambda$ evaluation. More direct evidence of residual film separation in the parched regime has been obtained with thin film optical interferometry measurements of heavily starved contacts [11].

Starvation-controlled lubrication is seen in many different applications, one example being lubrication by oil-in-water emulsions where EHD film formation is determined by the ability of the oil phase to maintain an inlet reservoir around the contact [12]. It is in grease lubrication, however, that the severest effects are seen.

It is very difficult to predict EHD film thicknesses for a grease-lubricated contact with any degree of confidence. The problem stems from a lack of understanding, at a detailed level, of the mechanism of grease lubrication. It is still not possible to establish the nature of the separating film, to identify the film formation and supply mechanism, nor to predict bearing lubrication performance from fundamental properties.

Experimental studies of film formation by greases in a model contact [13] have shown that, unless an external supply is used to replenish grease constantly within the raceway, it is rapidly pushed to either side of the raceway, thus starving the contact. Grease lubrication can therefore be considered to be a starvation phenomenon where the development of the EHD film is governed by the supply of

lubricant from the surrounding grease reservoir. This is seen in Figure 5 where EHD film thickness is plotted against increasing rolling speed [14]. Initially, the film increases with speed and then drops rapidly as the system passes through the speed/viscosity starvation boundary. The final speed-independent film thickness for the fully starved condition is approximately 40 nm. This behaviour is characteristic of greases although the starvation speed and final film thickness level vary greatly with different types of grease and operating conditions. The grease lubricating film has two components: a residual film of deposited gellant particles and a speed-dependent EHD contribution. Both components show a speed and time dependence making prediction of film thicknesses in rolling contacts for a grease very difficult. This can be seen in Figure 6 where film thickness is monitored at constant rolling speed over a period of 30 minutes [14]. The usual characteristics of grease lubrication in this type of test are seen in this result: rapid loss of film thickness in the first few minutes due to increasing starvation, gradually stabilizing to give a constant separating film. In all cases the film thickness is dependent on test history, and isolated results need to be interpreted with care.

The ability of a grease to form an EHD film is often considered only in relation to its base oil viscosity. The ability of a grease to form and maintain a residual film that continues to separate bearing surfaces once the normal EHD component has failed has considerable implications when applying the  $\Lambda$ criterion. Such a film is not predicted by consideration of the base oil contribution alone.

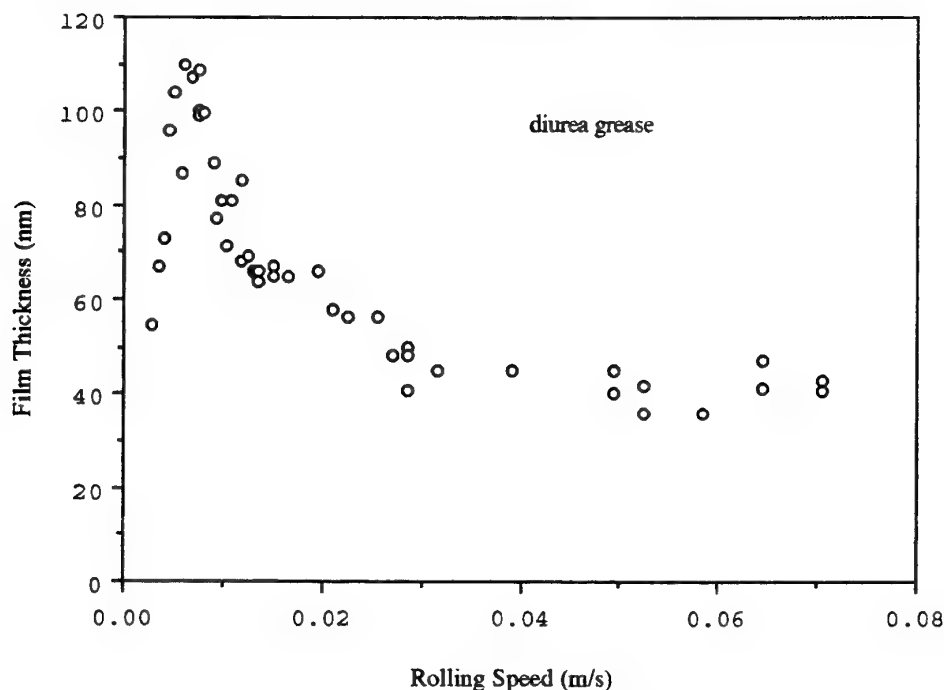


Figure 5: EHD starvation curve for a grease [14].

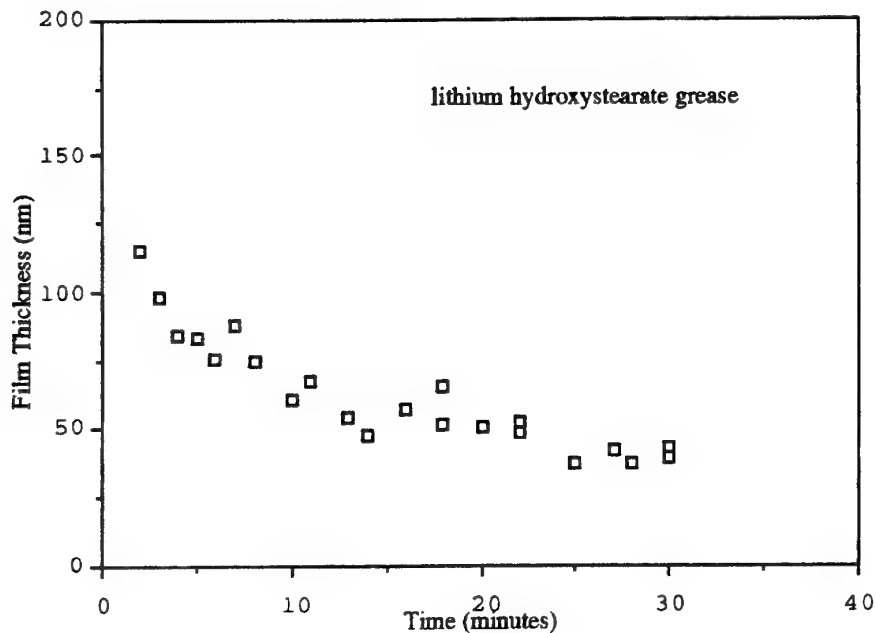


Figure 6: Film thickness decay with time for a grease [14].

## 5. THIN FILM LUBRICATION

The Acriterion provides a broad guide to the safe/unsafe operating limits for a lubricated contact. It cannot be used to assess operation at low  $\Lambda$  values; here the criterion is invalid. Under these conditions the  $\Lambda$  ratio is far too crude a tool as paradoxically many systems are known to run successfully at low  $\Lambda$  ratios [10]. This is particularly true for thin film lubrication where the estimated film thickness is less than the (undeformed) surface roughness parameter. Again the problem lies in being unable to predict with confidence the separating film thickness arising from the local contact conditions.

It is with formulated lubricants, where the effects of including additive packages are ignored, that the greatest difficulties arise. One example is the addition of polymers as dispersant/viscosity index improvers. Such solutions are known to be strongly non-Newtonian and it is difficult to quantify their rheological response to the high strain rates and increases in temperature associated with an EHD inlet. The chemical response of anti-wear or boundary additives can also significantly alter the nature and thickness of the separating film.

The above analyses show that using the basic bulk properties of the lubricant, such as viscosity and viscosity pressure coefficients, and the surface roughness properties as measured outside the heavily-loaded contacts and comparing the measured roughness with the theoretically calculated lubricant film thickness, cannot predict the contact behaviour for low  $\Lambda$  applications. Only when the calculated oil film thickness is large compared with the surface roughness, and no starvation effects are present, can the smooth surface approximation be used to predict the lubricant film thickness. As soon as the lubricated surfaces are not

mathematically smooth and the roughness heights are not negligible compared with the mean oil film thickness, the local pressure fluctuations caused by the asperities will have an influence on the elastic deformations of the surfaces. This leads to sensitivity for roughness structure and directionality by the lubricated contact, as well as sensitivity to the amount of oil available for lubrication.

If the contact is starved because too little active lubricant is present, the normal EHL theory overestimates the oil film thickness if fully flooded results are used, but at the same time the local asperity pressure variations within the heavily-loaded contact can partly flatten the roughness asperities, leading to smoother surfaces in the contact area.

For very smooth surfaces, the elastic deformations lead to an almost total conformity within the EHL contact and thus a very high ratio of oil film thickness to roughness, even for very thin lubricant films. Thus, the calculated oil film thickness compared with the measured roughness of the surfaces cannot directly determine if a separating oil film is present in the contact. It depends both on the details of the surface structure and on the amount of lubricant available.

## ACKNOWLEDGEMENT

The author wishes to thank Dr. H.H. Wittmeyer, Managing Director of SKF Engineering & Research Centre B.V., for his kind permission to publish this paper.

## REFERENCES

- 1 Bridgeman, P.W., Proc. Am. Acad. Arts Sci., 74 (12) (1942) pp 399-424.
- 2 Jacobson, B., "On the Lubrication of Heavily Loaded Spherical Surfaces Considering Surface Deformations and Solidification of the Lubricant", Acta Polytech. Scand., Mech. Eng. Ser., No. 54 (1970).

- 3 Höglund, E. and Jacobson, B., "Experimental Investigation of the Shear Strength of Lubricants Subjected to High Pressure and Temperature", *J. Tribol.*, 108 (1986), pp 571-578.
- 4 Jacobson, B., "Solid Oil in Rolling Contacts", *Intertribo* (1981), pp 92-98.
- 5 Jacobson, B. Ioannides, E. and Tripp, J.H., "Redistribution of Solidified Films in Rough Hertzian Contacts, Part I: Theory, Proc. 14th Leeds-Lyon Symp., Lyon (1987). In *Interface Dynamics, Tribology Series 12*, Elsevier, Amsterdam (1988), pp 51-57.
- 6 Jacobson, B., "Redistribution of Solidified Films in Rough Hertzian Contacts, Part II: Experimental, Proc. 14th Leeds-Lyon Symp., Lyon (1987). In *Interface Dynamics, Tribology Series 12*, Elsevier, Amsterdam (1988), pp 59-63.
- 7 Jacobson, B. "Mixed Lubrication", *Wear*, 136 (1) (1990), pp 99-116.
- 8 Hamer, J.C., Sayles, R.S. and Ioannides, E., "The Collapse of Sliding Micro-EHL Films by Plastic Extrusion", *Proc. Joint ASME/STLE Tribology Conf.*, Toronto, Canada (1990), paper 90-Trib-47.
- 9 Wedeven, L.D., Evans, D. and Cameron, A. "Optical Analysis of Ball Bearing Starvation", *J. Lubr. Technol.* 93, (1971), p 349.
- 10 Kingsbury, E., "Parched Elastohydrodynamic Lubrication", *J. Tribol.* 107 (1985) p 229.
- 11 Guangteng, G., Cann, P. and Spikes, H.A., "A Study of Parched Lubrication", *Wear* 153 (1992), p 91.
- 12 Barker, D.C., Johnston, G.J., Spikes, H.A. and Bunemann, T.F., "EHD Film Formation and Starvation of Oil-in-Water Emulsions", *STLE preprint* 92-TC-18-1, (1992).
- 13 Cann, P.M. and Spikes, H.A., "Film Thickness Measurements of Lubricating Greases under Normally Starved Conditions", *NLGI Spokesman*, 56 (1992), p 21.
- 14 Cann, P.M., Ioannides, E., Jacobson, B. and Lubrecht, A.A., "The Lambda Ratio - A Critical Re-Examination", *Wear*, 175 (1994), pp 177-188.

# Machining and Slip-Rolling of Ceramics

M. Woydt and U. Effner

*Federal Institute for Materials Research and Testing (BAM)*

*Unter den Eichen 44-46, 12200 Berlin, Germany*

## Abstract

The slip-rolling test of friction and wear was done in a twin disc tribometer of the Amsler-type at 3 GPa. As lubricant water and paraffin oil without any additives was used. The surfaces of the ceramics were machined with different processes, resulting in different surface roughnesses (i.e. rough and fine honed, rough and fine grounded, rough and fine lapped and rough and fine polished). Ceramic materials like HIP-Si<sub>3</sub>N<sub>4</sub> (NBD 200), SiC (EKasic D) and Si<sub>3</sub>N<sub>4</sub>-TiN (EDM) were investigated.

HIP-Si<sub>3</sub>N<sub>4</sub> and Si<sub>3</sub>N<sub>4</sub>-TiN shows in paraffin oil generally a small wear coefficient in range of 10<sup>-9</sup> mm<sup>3</sup>/Nm. In paraffinic oil, the wear coefficient of Si<sub>3</sub>N<sub>4</sub> and Si<sub>3</sub>N<sub>4</sub>-TiN correlates to the initial surface roughness and the material removal rate. The wear coefficient in water is for both materials higher two orders of magnitude. The surface of the SiC components shows Pitting after the tribological tests independent from the ambient.

## Key Words

Ceramics, HIP-Si<sub>3</sub>N<sub>4</sub>, SiC, Si<sub>3</sub>N<sub>4</sub>-TiN, slip-rolling test friction and wear, water, unadditivated paraffinic oil, machining

## 1 Introduction

Ceramic ball bearing, particularly hybrid bearing, are commercially available products<sup>1,2,3,4,5</sup>. All-ceramic bearings have prove to be effective in dry high-temperature conditions, while hybrid bearings (with ceramic rolling elements and metallic rings) have been used in low-temperature, high-speed applications. Promising commercial applications includes use in a high-speed machine tool spindles, instrument bearings, turbomolecular pumps, and other appli-

cations where high rotational speeds and/ or lubrication deprivation may occur. Both all-ceramic and hybrid bearings have been successfully tested under high-acceleration and ultra-precision conditions. Additionally, ceramic bearing materials are ideal in corrosive environments.

Today high manufacturing costs hinder, although a wider application of Si<sub>3</sub>N<sub>4</sub> in slip-rolling stresses tribosystem.

components	share of machining costs
Si <sub>3</sub> N <sub>4</sub> automobile valve	~ 55 %
Si <sub>3</sub> N <sub>4</sub> ball bearing	~ 70 %
SiC standard sliding seal	15 - 30 %
Al <sub>2</sub> O <sub>3</sub> washer seals	~ 35 %
cutting tool inserts	~ 30 %
SiC special sliding seal	60 - 80 %
SiC sliding bearing	~ 70 %

**Table 1:** Share of machining costs for commercial ceramic components.

The machining process and the powder prices contribute both mainly to the manufacturing costs. In order to minimise fatigue and increase strength, the surface

were finished according to the philosophy "best-as-possible". Table 1 illustrates the share of machining costs to the final price. Therefor, investigation to reduce the

machining costs show the greatest cost reduction potential.

In this test program, the work was focused on the correlation between slip-rolling wear coefficient, machining process (e.g. honed, grounded, lapped and polished) and the resulting surface roughnesses. As lubrication was used water or paraffin oil without any additives.

## 2 Experimental

The tribological tests were performed in a twin disc wear tester, where two cylindrical

samples were mounted on two shafts. The rotational speed between both shafts differed by 10 %. Also the influence of geometry was investigated through, cylindrical sample with a simple shape and a round sample with two radii and represents a significant advantage of this wear tester. All tests were performed with a initial hertzian pressure of 3 GPa, so due to the different elastic moduli, the normal force was adapted to the materials. The operation conditions are shown in Table 2.

Operation conditions	HIP-Si <sub>3</sub> N <sub>4</sub> (NBD 200)	SiC (EKasic D)	Si <sub>3</sub> N <sub>4</sub> -TiN (EDM)
Type of motion	slip-rolling with 10% slip	slip-rolling with 10% slip	slip-rolling with 10% slip
Normal force $F_N$	1005 N	665 N	1150 N
Hertzian pressure $P_0$	3000 N/mm <sup>2</sup>	3000 N/mm <sup>2</sup>	3000 N/mm <sup>2</sup>
Rotational speed	386 rpm/ 347 rpm	386 rpm/ 347 rpm	386 rpm/ 347 rpm
Sliding speed $v_{diff}$	0.085 m/s	0.085 m/s	0.085 m/s
Test duration $n_{ges}$	$2 * 10^6$ cycles	$2 * 10^6$ cycles	$2 * 10^6$ cycles
Sliding distance $s$	26.390 m	26.390 m	26.390 m
Ambient temperature $T$	RT ( $\approx 22^\circ\text{C}$ )	RT ( $\approx 22^\circ\text{C}$ )	RT ( $\approx 22^\circ\text{C}$ )
Lubrication	paraffin oil or water	paraffin oil or water	paraffin oil or water

**Table 2:** Operation conditions of the twin disc tribometer for the different materials under mixed lubrication.

Tribological quantities were the friction coefficient  $f$  and the wear coefficient  $k_V = W_V / F_N s$  [mm<sup>3</sup>/Nm], with  $W_V$  [mm<sup>3</sup>] the

wear volume,  $F_N$  [N] the normal force and  $s$  [m] the sliding distance.

Mechanical properties of	HIP-Si <sub>3</sub> N <sub>4</sub> (NBD 200)	SiC (EKasic D)	Si <sub>3</sub> N <sub>4</sub> -TiN (EDM)
Density $\rho$	3.16 g/cm <sup>3</sup>	3.10 g/cm <sup>3</sup>	3.86 g/cm <sup>3</sup>
Elastic Modulus $E$	320 GPa	410 GPa	300 GPa
Poisson Ratio $\nu$	0.26	0.17	0.26
Hardness, Vickers	16.6 GPa [HV 10]	28 GPa [HV 0.5]	17 GPa [HV 0.5]
Fracture toughness $K_{IC}$	4.1 MPa*m <sup>1/2</sup>	3.2 MPa*m <sup>1/2</sup>	7.5 MPa*m <sup>1/2</sup>
Flexural strength $\sigma_{4B}$	800 MPa	410 MPa	700 MPa

**Table 3:** Mechanical Properties of the tested materials HIP-Si<sub>3</sub>N<sub>4</sub><sup>6</sup>, SiC<sup>7</sup> and Si<sub>3</sub>N<sub>4</sub>-TiN<sup>7</sup>.

Before the wear testing, ceramic-surfaces were finished with different machining processes. The sample, which were tested with water and oil, were rough (D 30) or fine

(D 7) honed, rough (D 64) or fine (D 15) grounded, rough (PWB 30) or fine (PWB 7) lapped or rough (D 3) or fine (D 1) polished.



The basic mechanical properties of the tested couples are shown in Table 3.

### 3 Results

#### Friction

The friction coefficient under conditions of slip-rolling in water or oil for the ceramic-couples at room temperature depends on the ambient media. For the HIP-Si<sub>3</sub>N<sub>4</sub> the higher friction coefficient ( $f=0.25$ ) for water lubrication at the beginning of the test decreases to lower values around 0.05 for all machining processes. The frictional behaviour in paraffin oil is different, since the friction

coefficient is nearly unchanged throughout the test. A similar course shows the friction coefficient of SiC. Under water lubrication the friction coefficient starts at  $f=0.18$  and decrease to  $f=0.15$ , under paraffin oil lubrication the friction coefficient was by  $f=0.09$  and is nearly unchanged throughout the test for all machining processes. Also for Si<sub>3</sub>N<sub>4</sub>-TiN under paraffin oil lubrication the course of the friction coefficient shows unchanged values during the tribological test, it starts around  $f=0.1$  and ends around  $f=0.09$ . The friction level correlates to the ambient media, but not to the machining process or to the initial surface roughness.

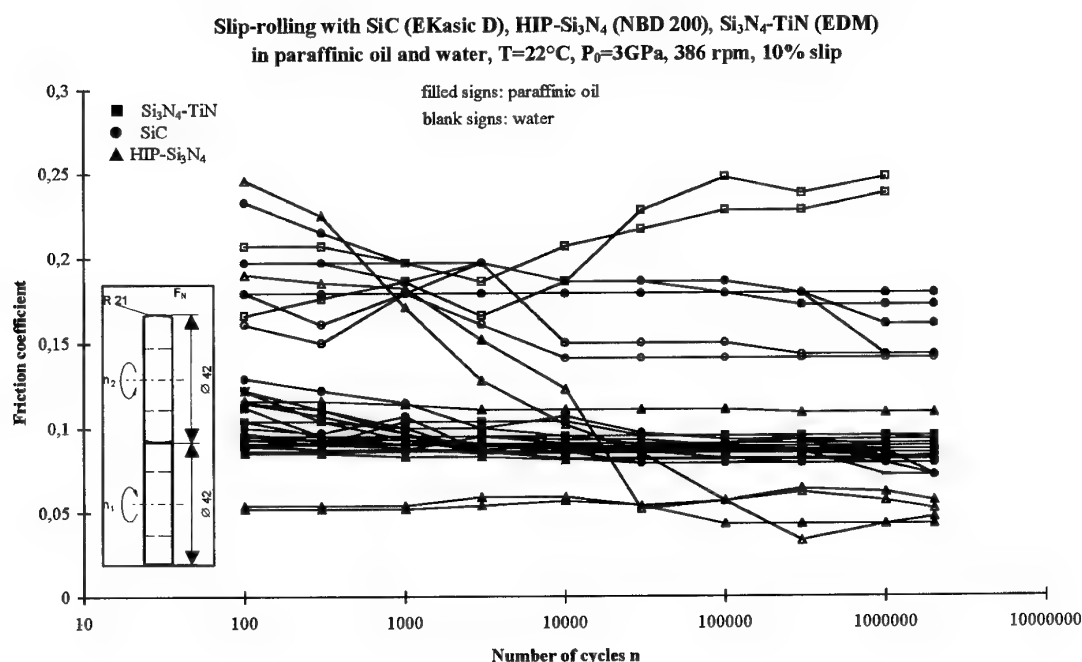


**Figure 1:** Friction coefficient under slip-rolling for different ceramics as a function of the number of cycles.

#### Wear

The wear coefficient depends on the surface geometry, the ambient media and the surface roughness and consequently, on the machining process. The wear coefficients lie for SiC in the  $10^{-7}$ -range and for HIP-Si<sub>3</sub>N<sub>4</sub> and Si<sub>3</sub>N<sub>4</sub>-TiN in the  $10^{-9}$ -range.

The wear coefficient for the materials HIP-Si<sub>3</sub>N<sub>4</sub> and Si<sub>3</sub>N<sub>4</sub>-TiN depends on the material removal rate proportional (s. Figure 2). Smaller material removal rate conducts to

much lower wear coefficients. For SSiC, the material removal rate influences the slip-rolling wear coefficient in a completely different way. Smaller material removal rate generates surprisingly below  $Q_w=0.005\text{mm}^3/\text{s}$  an increase in wear rates. To understand this, TEM and ESCA analysis are underway. After  $n=2 \cdot 10^6$  cycles the SSiC-discs exhibit pitting and conical cracks. The material SSiC fail due to fatigue (s. Figure 3).

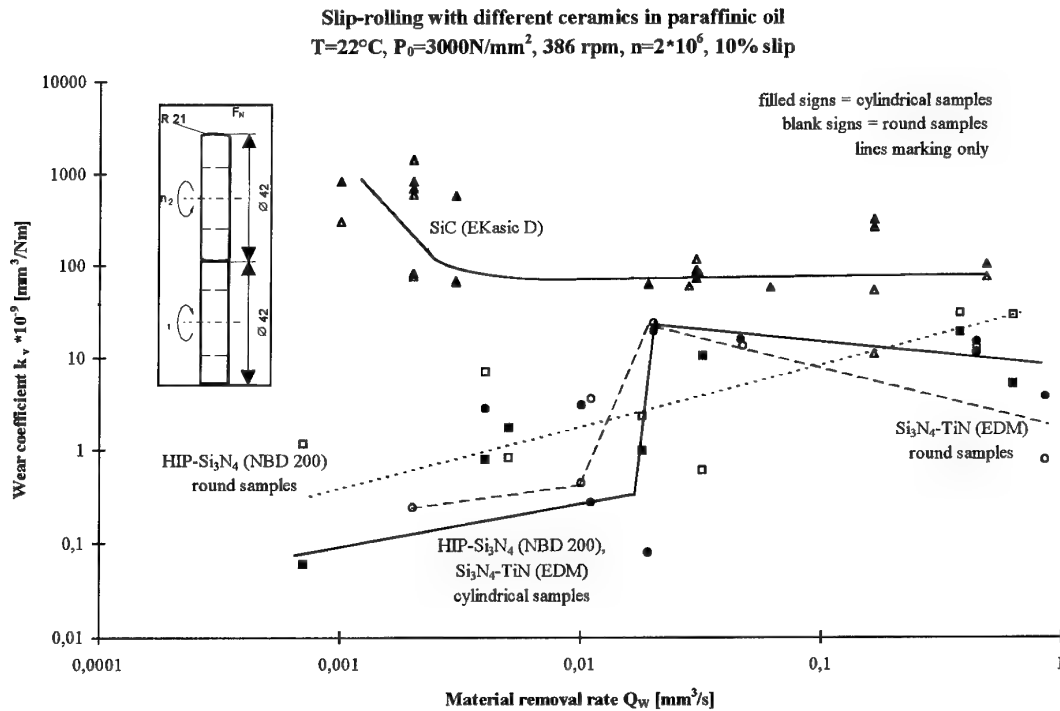


**Figure 2:** Slip-rolling wear coefficient for different ceramics as a function of the material removal rate.

The materials SSiC and Si<sub>3</sub>N<sub>4</sub>-TiN are not suitable for water lubrication, because for SSiC the generation of Pitting is accelerated and the TiN-phase of the Si<sub>3</sub>N<sub>4</sub>-TiN dissolves in water. Thus, the wear coefficient

is in the range  $10^{-7}$  to  $10^{-6} \text{ mm}^3/\text{Nm}$  or the materials fail by cracking. Only HIP-Si<sub>3</sub>N<sub>4</sub> can be used for water lubrication, even the wear coefficient in water lubrication is 10 times higher than in paraffin oil lubrication.

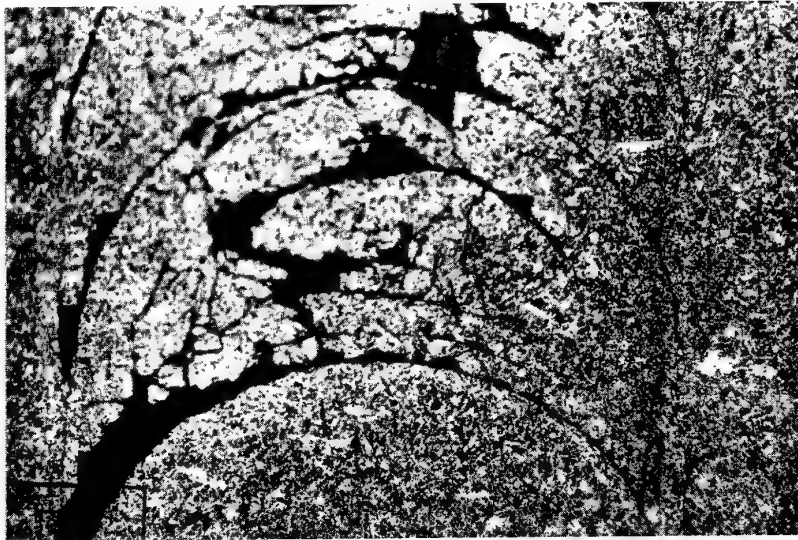


**Figure 3:** SiC sample after  $n=2\cdot 10^6$  cycles with pitting and conical cracks (100:1).

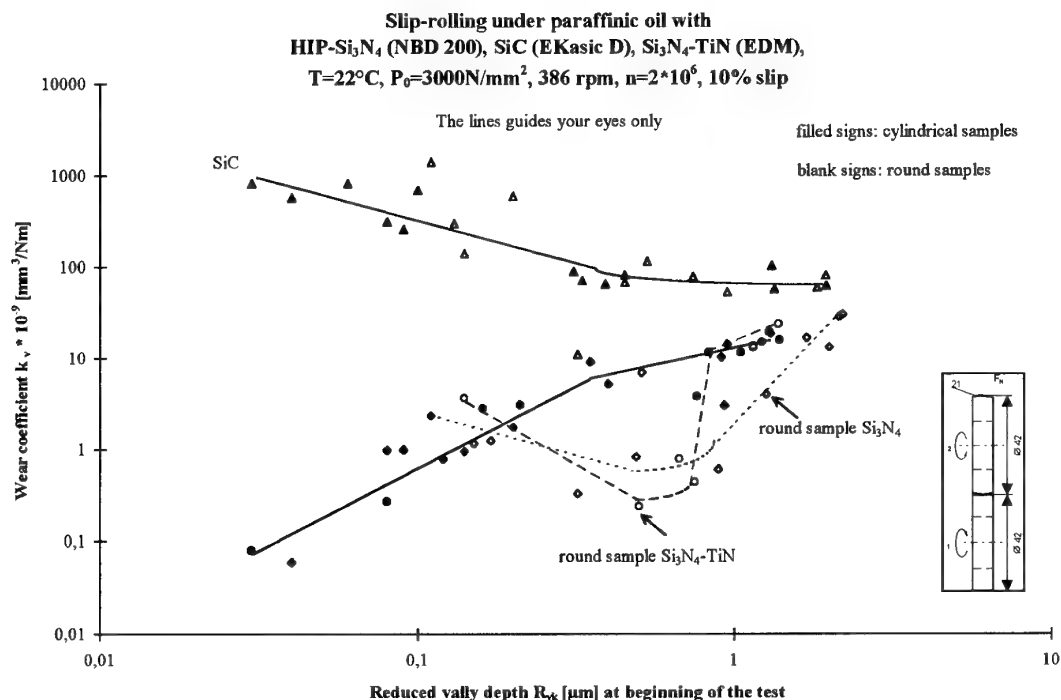


**Figure 4:** Wear coefficient for different ceramics as a function of the roughness value  $R_{vk}$  ( $R_{vk}$  = reduced valley depth<sup>8</sup>).

As pointed out in Figure 4, the wear coefficient is not only related to the removal rate (s. Figure 2), but also to the initial surface roughness.

Machining processes, which finishes on SiC the surface with a roughness  $R_{vk} \leq 0.3 \mu\text{m}$ , increases the wear coefficient and on Si<sub>3</sub>N<sub>4</sub> or Si<sub>3</sub>N<sub>4</sub>-TiN, roughnesses lower than  $R_{vk} \leq 0.3 \mu\text{m}$  exhibits considerable wear reductions in paraffinic oil.

The round samples of the materials HIP-Si<sub>3</sub>N<sub>4</sub> and Si<sub>3</sub>N<sub>4</sub>-TiN show a minimum in the wear coefficient in the range of  $0.5 \mu\text{m} \leq R_{vk} \leq 0.9 \mu\text{m}$ . Such roughness values can be produce by machining processes like grinding, honing or lapping. By cylindrical samples the wear coefficient is proportional to the roughness. If a certain amount of running-in wear can be accepted, polished surfaces can be replaced by grinded, honed or lapped HIP-Si<sub>3</sub>N<sub>4</sub> and Si<sub>3</sub>N<sub>4</sub>-TiN surfaces with shortenend machining time and reduced costs.

For HIP-Si<sub>3</sub>N<sub>4</sub> and Si<sub>3</sub>N<sub>4</sub>-TiN in general, running-in can act as further, cost-free "surface finishing" process, i.e. for cams and

gears. The roughness ( $R_z$  and C.L.A.) of the sample surfaces before and after the tribological tests exhibits a smooth initial surface roughness was not significantly reduced by running-in, but rough surfaces were made smoother to one order of magnitude. Is the roughness  $R_z \leq 0.5 \mu\text{m}$  and C.L.A.  $\leq 0.2 \mu\text{m}$  no significant variation of the roughness could detected after the wear test<sup>9</sup>.

A machining process with a higher material removal rate can be used from the tribological point of view. This can reduce the shares of machining costs of ceramic components. The results presented here does not consequently support the philosophy "best as possible".

#### 4 Conclusion

The slip-rolling wear coefficient is for SiC in the range of  $10^{-7} \text{ mm}^3/\text{Nm}$  and for HIP-Si<sub>3</sub>N<sub>4</sub> and Si<sub>3</sub>N<sub>4</sub>-TiN in the range of  $10^{-9} \text{ mm}^3/\text{Nm}$  and it depends on the surface geometry, the ambient media and the surface roughness and consequently on the machining process and the material removal rate.

If it is possible to accept a running-in wear in the range of  $0.5\mu\text{m}$  to  $3\mu\text{m}$ , polishing with long machining times can be avoided for HIP- $\text{Si}_3\text{N}_4$  and  $\text{Si}_3\text{N}_4$ -TiN and be replaced by grinding, honing or lapping. These two materials exhibits their best slip-rolling wear resistance for round surfaces in the range of  $0.5\mu\text{m} \leq R_{vk} \leq 0.9\mu\text{m}$ .

Very smooth machining processes (e.g. polishing) for SiC are not economical, because they increases wear.

Slip-rolling in water is critical for the tested materials. In this ambient media the ceramics exhibits cracks, pitting, fatigue and higher wear rates.

In the future the achieved results have clearly demonstrated, that through the appropriate machining process the machining costs can be further reduce.

#### Acknowledgement

The authors are very gratefull acknowledge from J. Schwenzien in profilometry, S. Binkowski and R. Pahl for preparation samples and microscopic observations. The surface finishing of the samples was done at the Institute for Machining Tools and Production Technology (IWF) at the Technical University in Braunschweig (Prof. Dr. E. Westkämper), 38106 Braunschweig, Germany. This work was supported by a grant from the German Research Foundation (DFG), 53170 Bonn, Germany, under contract Wo 521/1-1 to -3.

- <sup>1</sup> Anon  
*Precision angular contact ball bearings with ceramic balls*,  
SKF Publication 4041E, 1989, Reg. 47115.5000.  
1989-08
- <sup>2</sup> J.F. Chudecki  
*Ceramic bearings - Application and performance advantages in industrial applications*,  
SAE-TP-891904
- <sup>3</sup> Anon  
*Angular Contact Ball Bearings with Ceramic Balls*,  
NTN Toyo Bearing Co., Ltd, CAT No. 2643
- <sup>4</sup> Anon  
*Ceramic- angular Contact Ball Bearings*,  
Company documentation of Nippon Seiko NSK
- <sup>5</sup> Anon,  
*EXSEV-Bearing Series, Extreme special environment*,  
KOYO Seiko Co., Ltd, Cat.No. 281E, July '95,  
OSAKA 542
- <sup>6</sup> Technical Data Sheet  
*Normalide NBD 200 Silicon Nitride*,  
CERBEC Ceramic Bearing Company,  
Conneticut, USA
- <sup>7</sup> Technical Data Sheet  
*Engineered Ceramics - General Characteristics*,  
Elektroschmelzwerk Kempten GmbH (ESK),  
87405 Kempten, Germany
- <sup>8</sup> DIN 4776  
*Parameters  $R_b$ ,  $R_{pb}$ ,  $R_{vk}$ ,  $M_{r1}$ ,  $M_{r2}$  for the description of the material portion (profile bearing length ratio) in the roughness profile*  
May 1990, Normenausschuß Länge und Gestalt (NLG) im DIN Deutsches Institut für Normung e.V., Burggrafenstr. 6, 10787 Berlin, Germany
- <sup>9</sup> U. Effner, M. Woydt  
*Bearbeitung und Wälzreibung von Ingenieur-Keramiken in Wasser und Öl*  
(*Machining and slip-rolling of ceramic materials in water and oil*)  
VDI Berichte No. 1207, (1995), 223-233

# SPUTTER-DEPOSITED LUBRICANT THIN FILMS OPERATING AT ELEVATED TEMPERATURES IN AIR

C. ZIMMERMANN  
Materials and Technologies

DASSAULT AVIATION  
78, Quai Marcel Dassault CEDEX 300  
92552 SAINT CLOUD FRANCE

and  
Yves PAULEAU  
CEA / Grenoble, CEREM 38054 GRENOBLE CEDEX 9 FRANCE

## 2 - INTRODUCTION.

## 1 - SUMMARY

For the lubrication of sliding contacts operating in hostile environments (vacuum, high temperatures, corrosive ambient,...), for which liquid lubricants are ineffective or undesirable, the solid lubricant coatings are needed to reduce friction and wear in order to prevent damage.

Many solutions such as soft metals (Ag,Pb), lamellar compounds (MoS<sub>2</sub>), polymers, and graphite fluoride have been proposed in the last decade. The Plasma-Sprayed composite PS212 developed by NASA<sup>1</sup> is known as a reference. This thick coating (about 150  $\mu\text{m}$ ) is a matrix of metal-bonded chromium carbide (Cr<sub>3</sub>C<sub>2</sub>) for wear control at high temperatures (800°C) mixed with silver and alkaline earth metal fluorides for the lubrication at respectively low and high temperature.

However major drawbacks of these thick coatings are essentially related to their thickness and their roughness; a diamond grinding operation is necessary to adjust the thickness and to improve the surface quality required for a sliding contact. This operation is not easy in small size parts and in ball bearings.

The high level of temperature (up to 700°C) required by the spherical bearings of the space shuttle HERMES control surfaces associated with a low friction coefficient (less than 0,3) has needed a specific development.

DASSAULT in collaboration with the CENG<sup>2</sup> and ISMCM<sup>3</sup> has developed and tested an innovative thin coating, based on the same compounds as those of the PS212, deposited by radio frequency sputtering process. A specific test mean, able to conduct tests on spherical bearings under representative conditions of a reentry (temperature, pressure, high load and oscillatory motion...) has also been developed.

The concept of thin layers lubrication is quite different to thick coatings and lies on the tribological model developed by Halling<sup>4,5</sup> which shows that a soft layer of solid lubricant (CaF<sub>2</sub>) deposited on a hard material (substrate + Cr<sub>3</sub>C<sub>2</sub>) plays a very efficient role for an optimum thickness magnitude close to the standard deviation value of the distribution of the asperity heights acting in the contact. This effect has been widely reported, essentially for thin metallic coatings (Ag, Pb, and In); for instance by Sherbiny and al<sup>6</sup>, who observed a minimum friction coefficient for a lubricant layer thickness twice thicker than the surface roughness, or by Arnell and al<sup>7</sup>. It is thus foreseen that accurate optimisation in number and size of thin layers will improve the friction behaviour.

In this work, chromium carbide (Cr<sub>3</sub>C<sub>2</sub>), calcium fluoride (CaF<sub>2</sub>) and silver (Ag) thin films have been deposited on Cobalt based superalloy substrates (Alacrite - AFNOR KC20WN) by standard RF sputtering. The CaF<sub>2</sub> has been preferred to the eutectic BaF<sub>2</sub> - CaF<sub>2</sub> (used for the PS212) because of the non stability observed in a preliminary test. After a preliminary investigation of the tribological properties of the basic layers, the aim of this study has been to define the best combination.

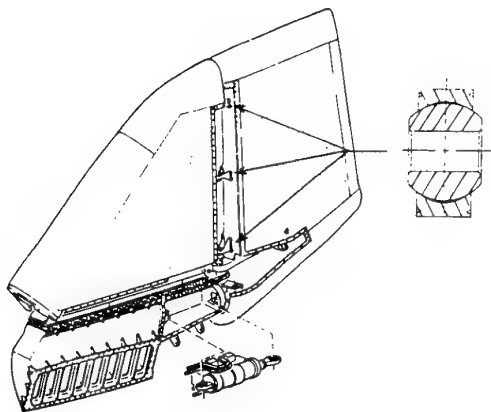
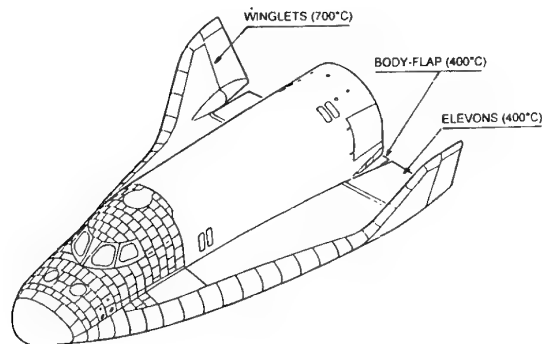
The following basic coatings have been prepared :

- substrate / 3  $\mu\text{m}$  Cr<sub>3</sub>C<sub>2</sub> + 0,6  $\mu\text{m}$  CaF<sub>2</sub> (Sa)
- substrate / 3  $\mu\text{m}$  Cr<sub>3</sub>C<sub>2</sub> + 3  $\mu\text{m}$  CaF<sub>2</sub> (Sb)
- substrate / various thickness of Ag

For comparison Plasma Sprayed PS212 coatings have been deposited on similar alacrite substrates by Advanced Materials Products Inc. (Ohio, USA) at the request of DASSAULT.

### 3 - SPACE SHUTTLE HERMES APPLICATIONS

For the HERMES project, DASSAULT was in charge of the development of the thermal protection system (TPS). One of the technologies needed by the TPS was the tribology used for the flight control surfaces such as elevons, body-flap and winglets. These last parts were the hottest (up to 700°C on the hinges) and has required, after an investigation of the 'on the shelf products', a specific development.



## 4 - TEST MEANS USED FOR THIS WORKS

### 4.1 - Pin on Disk Apparatus (Fig 1)

This tribological tests were performed in CENG by standard ball-on-disk measurements. The 10 mm thick alacrite disk specimen was rotated about the vertical axis and the dia.8 mm alumina ball specimen with an average surface roughness  $R_a$  of about  $0,03 \mu\text{m}$  was held firmly in a fixed position. The test were conducted in ambient air, at room temperature and at 500°C, with a sliding velocity of 0,02 m/s, under various loads.

This type of tests, conducted during development, will provide a first approximation of the friction

behaviour and thus allow the deposition parameters to be adjusted.

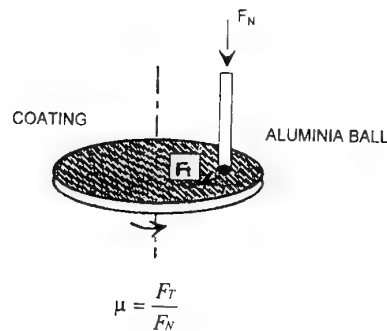


Figure 1: Pin on disk friction test rig.

### 4.2 - Flat to Flat rig (Fig 2)

Tribological tests of coatings were conducted at ISMCM, with a flat to flat contact apparatus in air at 500 and 700°C. The experimental test rig is schematically presented on figure 2. Coated faces of two coaxial cylinders ( $\varnothing = 40 \text{ mm}$ ,  $th = 13,5 \text{ mm}$ ) were rubbed together, in an electrical furnace able to reach a maximum temperature of 1000°C.

The static and the kinetic friction coefficients were deduced from the tangential friction force continuously recorded during the tests performed at a sliding velocity of 0,3 cm/s and under a contact pressure of 25 Mpa.

The wear volume was estimated either from the mass loss of samples measured with a microbalance (accuracy of 0,1 mg) or by profilometry measurements.

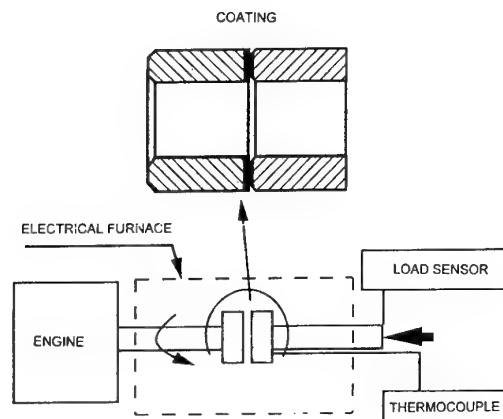


Figure 2: flat to flat test rig.

#### 4.3 - Spherical bearing test mean (fig 3)

Upon completion of all investigations on the friction properties by use of relatively simple means (flat to flat tests), the study were pursued by an évaluation, on parts being more representative of utilization, of the performance capabilities of the technology.

The HERMES tribology test facility dedicated to the development and the qualification of spherical bearings used in flight control surfaces is installed at National Institute of Aerospace Technology (INTA) in Madrid. This test mean funded by the European Space Agency and developed under the responsibility of DASSAULT is able to simulate the real conditions encountered during the reentry phase.

The main characteristics are the following :

- Mechanical loads  $\Rightarrow$  250 KN
- Tilt angle simulation  $\Rightarrow \pm 5^\circ$
- Shaft angular rotation  $\Rightarrow \pm 25^\circ$  at 40°/s
- Reentry pressure simulation  $\Rightarrow$  10 Pa to 1bar.
- Spherical bearing size  $\Rightarrow \varnothing 25$  mm at 700°C.  
(limited by the oven capacity)

All parameters can vary simultaneous in function of time with a great precision in the regulation and quick response. the system is provided with a control panel for automatic operation, and a computer including the adequate software to program the cycles needed by the Hermes applications.

Because of the cancellation of the HERMES project this test mean has not be used, but his acceptance test, conducted on a spherical bearing under representatives conditions, has shown he is in accordance with the HERMES requirements. The figure 3 show the architecture of the HTTF (High Temperature Test Facility).

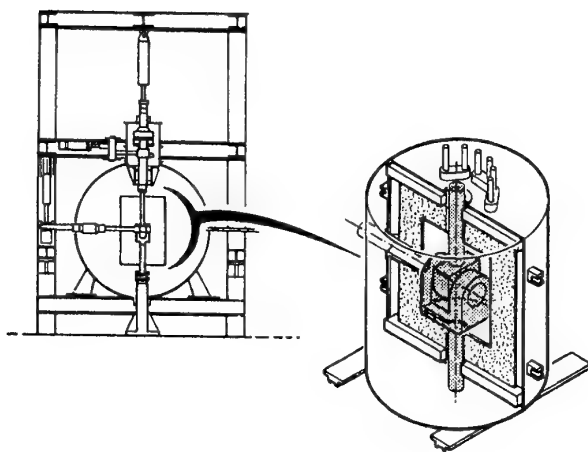


Figure 3. HERMES Test Facility.

## 5 - RESULTS OF THE STUDY

### 5.1 - Silver film

The deposition parameters of silver films were selected on the basis of data collected during a previous work and recently published<sup>8-9-10</sup> by the CENG.

Under the experimental conditions investigated, the deposition rate of 80 nm/min (at an argon pressure of 2 Pa and a sputtering power of 200 W) was suitable to produce 0,4 to 20  $\mu$ m thick films for a reasonable deposition duration. The silver films exhibited a crystallographic structure preferentially oriented in the (111) direction with grain sizes of around 150 nm. the morphological structure of films examined by scanning electron microscopy was found to be fully dense and the compressive residual stresses in the film determined by X-ray diffraction were as low as 0,05 Gpa, the silver films were tightly adherent to alacrite substrates.

The friction coefficient of alacrite disks coated with 1,3  $\mu$ m of Ag sliding against an alumina ball was determined<sup>11</sup> at room temperature as a function of the number of cycles under loads of 1-2,9 and 9,8 N. The results, given on the curve Fig 4, showed that the initial friction coefficient is equal to 0,25 but increased progressively up to values given in table 1 after 5000 cycles.

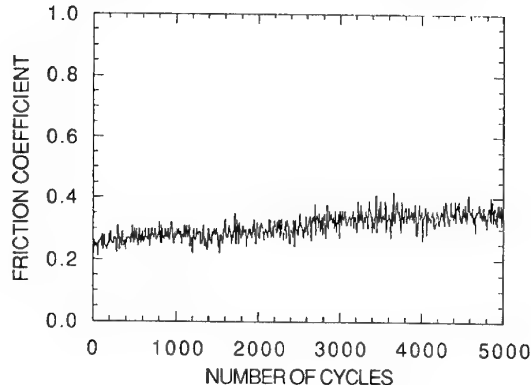


Figure 4. Friction coefficient vs  $n^b$  of cycles for 1,3  $\mu$ m Ag under a load of 1 N at RT.

LOAD (N)	AVERAGE FRICTION COEFFICIENT
1	0,31
2,9	0,38
9,8	0,39

Table 1. Tribological tests of 1,3  $\mu$ m Ag at RT.

The value of 0,35 can be considered as a characteristic friction coefficient value for these sample.

The friction coefficient of alacrite sample coated with various thicknesses (0,4 to 20  $\mu\text{m}$ ) of Ag was also determined as a function of the number of cycles under a load of 1 N at room temperature and 500°C. The typical curve presented in fig 5 showed that after an initial stage of 1000 to 1500 cycles, the friction coefficient remained essentially constant and its value determined for various film thicknesses was obtained with a small standard deviation (table 2).

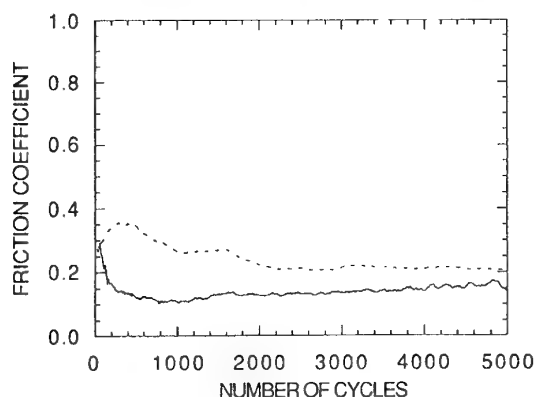


Figure 5. Friction coefficient vs. Nb of cycles for 4,8 $\mu\text{m}$  Ag under 1 N at RT (—) and 500°C (---).

FILM THICKNESS ( $\mu\text{m}$ )	AVERAGE Cf at RT and 500°C
0,4	0,42 - 0,30
0,7	- 0,22
1,3	0,31 - 0,21
1,7	0,37 - 0,20
4,8	0,14 - 0,24
20	0,25 - 0,37

Table 2. Tribological tests of silver films of various thicknesses at RT and 500°C.

The disks covered with Ag films thinner than 2  $\mu\text{m}$  exhibited a friction coefficient lower at room temperature than at 500°C; the reverse situation prevailed when the film thickness was greater than 2  $\mu\text{m}$ . The average friction coefficient value was dependent on the film thickness (fig 6).

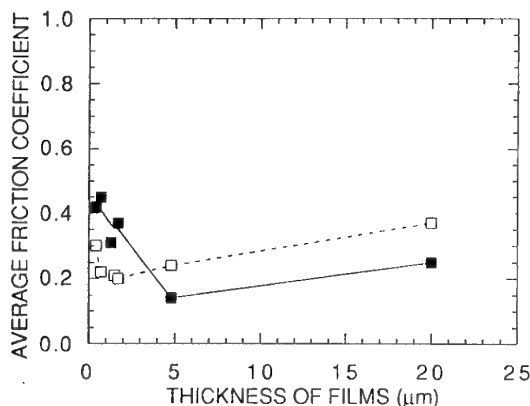


Figure 6. Average friction coefficient vs. thickness under a load of 1 N at RT (■) and 500°C (□).

This value decrease sharply with increasing film thickness. The minimum value of 0,15 to 0,20 was obtained from 4,8  $\mu\text{m}$  thick at room temperature and 1 to 2  $\mu\text{m}$  thick at 500°C.

## 5.2 - Calcium fluoride films

The alkaline earth metal fluoride exhibit a fragile-ductile transition at high temperatures, in particular  $\text{CaF}_2$  crystals show appreciable ductility above 400°C<sup>12-13</sup>. Therefore this material is an attractive candidate for the lubrication at high temperatures. Films of calcium fluoride, 0,2 to 4  $\mu\text{m}$  thick, were produced with a deposition rate of 2nm / min corresponding at an argon pressure of 1 Pa and at a sputtering power of 100 W.

The friction coefficient of this compound was investigated as a function of the film thickness in air at 500°C under a load of 1 N by pin on disk test. (table 3).

FILM THICKNESS ( $\mu\text{m}$ )	AVERAGE FRICTION COEFFICIENT
0,2	0,63
0,7	0,53
1,2	0,41
2	0,41
4	0,44

Table 3. Tribological tests of calcium fluoride films at 500°C

The average friction coefficient after 5000 cycles was relatively high (0,6 to 0,7) for the thinnest films and decreased progressively down to 0,4 as the film thickness increased (figure 7). The critical thickness corresponding to this minimum friction coefficient was about 1  $\mu\text{m}$ .



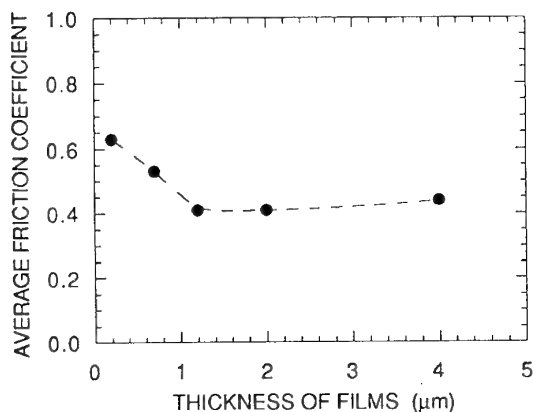


Figure 7. Average friction coefficient vs. thickness of  $\text{CaF}_2$  films under a load of 1 N at 500°C.

### 5.3 - Chromium carbide/calcium fluoride bilayer comparison with PS212

Sputter deposited  $\text{Cr}_3\text{C}_2/\text{CaF}_2$  films were found to be dense, adherent and isotropic. Scratch test and 3 points bending test were performed on small scale special samples in order to qualitatively estimate the adhesion of the coatings to superalloy substrates. SEM examination showed very dense structure of the films, as classically observed for low pressure sputtering experiments.

The friction coefficients at 500 and 700°C were determined and compared to those of PS212 as shown on figures 8 (500°C) and 9 (700°C).

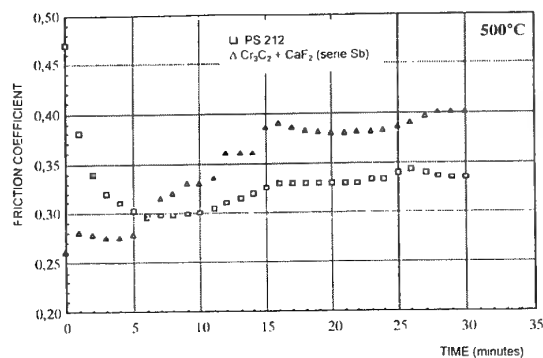


Figure 8. Comparison of Cf at 500°C of  $\text{Cr}_3\text{C}_2$  3μm/ $\text{CaF}_2$  3μm and PS212 coatings.

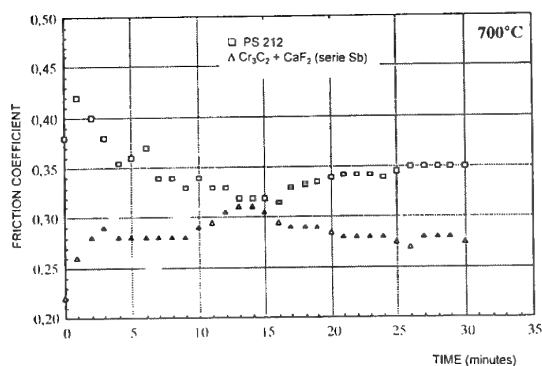


Figure 9. Comparison of Cf at 700°C of  $\text{Cr}_3\text{C}_2$  3μm/ $\text{CaF}_2$  3μm and PS212 coatings.

The values of friction coefficients for each series of samples (Sa-Sb-defined in introduction) are given on figures 10 to 12.

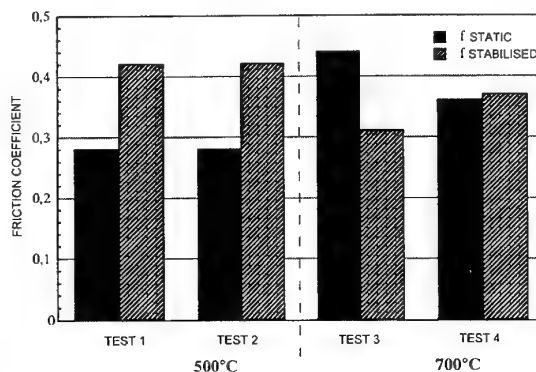


Figure 10. Comparison of static and stabilised friction coefficient of 'Sa' series of coating.

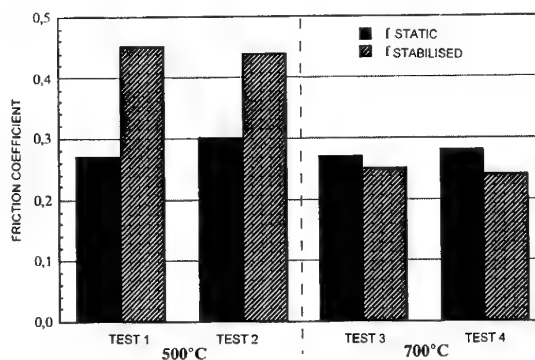


Figure 11. Comparison of static and stabilised friction coefficient of 'Sb' series of coating.

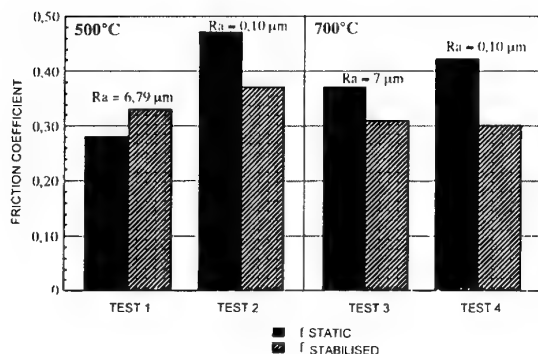


Figure 12. Comparison of static and stabilised friction coefficient of PS 212.

The prime stabilized friction coefficient, at the lowest temperature, is roughly the same for all series, close to 0,42, higher than PS212 value, 0,36. This result is probably due to the fragile-ductile transition of  $\text{CaF}_2$  occurring at about 500°C. At low temperature solid lubricant such as silver is mandatory to get 'allowable' values about 0,3 or less at this working temperature.

The presence of silver in PS212 can explain the lower friction coefficient value observed after stabilisation. Tribological tests performed at high temperature (700°C) show that the behaviour of series 'Sa' is again not satisfactory, although a decrease of the friction coefficient is observed, but the performance of series 'Sb' and PS212 samples is now reverse.

The static and the dynamic friction coefficients of  $\text{CaF}_2$  'Sb' decreased down to 0,28 and 0,25 respectively, and are appreciably better than those of PS212. This result may be explained by the high ductility of calcium fluoride at 700°C, far away from the fragile-ductile transition temperature of  $\text{CaF}_2$ , while the  $\text{Cr}_3\text{C}_2$  matrix of PS212 is now limiting its effect (all components are mixed into PS212 and are continuously in sliding contact). In this temperature range,  $\text{CaF}_2$  'Sb' is the best candidate for the Hermes applications.

The main results of the wear rates, classically defined as the ratio of the measured wear volume to the applied load and the total sliding length, are presented on figure 13. It is shown that the thin  $\text{CaF}_2$  'Sb' coating may efficiently replace the thick PS212; infact its wear rates are 15 times lower at 500°C and 25-30 times lower at 700°C.

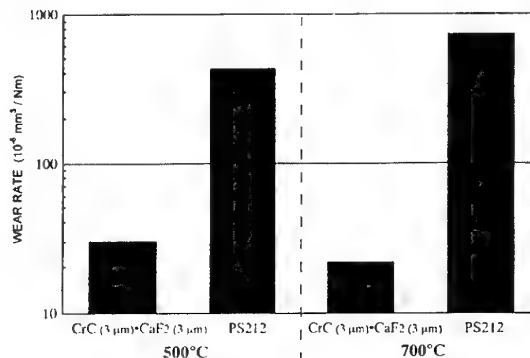


Figure 13. Comparison of wear rates of 'Sb' serie coating and PS 212.

## 6 - CONCLUSIONS

The development of this coatings contribute to the improvement of the performance capabilities of the materials used for tribology applications for space or aircraft applications and for other industrial applications as bearings for rolling mills (700°C), dynamic seals for lock-gates of turbopumps (500 to 700°C), sliding gates for blast furnaces (600 to 1000°C), hot gas extractor (200 to 700°C) etc...

The different examples listed above are part of the potential European tribology application market which represented, in 1985, 196 M\$ and which, since then, has been steadily increasing by 6% per year.

This study showed that dense thin layers of solid lubricants deposited by RF sputtering can be an interesting solution for high temperatures applications and especially for the Hermes control surfaces bearings.

## 7 - ACKNOWLEDGEMENTS

The financial support for this study by the European Space Agency is gratefully acknowledged.

## 8 - REFERENCES

- 1 C. Dellacorte, H. E. Sliney and D. L. Deadmore, Tribol. Trans., 31 (1988) 329.
- 2 CENG, Centre d'Etudes Nucleaires de Grenoble 85 X - 38041 Grenoble Cedex (FRANCE) - Yves PAULEAU.
- 3 ISMCM, Institut Supérieur des Matériaux et de la Construction Mécanique, Laboratoire de Tribologie

- 4 J.Halling; Thin Solid Films, 108, 1983, 103.
- 5 J.Halling; Tribology International, 10, 1979, 203.
- 6 M.El Sherbiny and F.Salem; ASLE Transactions, 29(2), 1985, 223.
- 7 R.D.Arnell and F.Soliman; Thin Solid Films, 53, 1978, 333.
- 8 N.Marechal, E.Quesnel and Y.Pauleau, J.Vac.Sci. Technol. A, (in the press)
- 9 N.Marechal, E.Quesnel, P.Juliet and Y.Pauleau, J. Appl. Phys., 74(8), (1993) 5203.
- 10 N.Marechal, E.Quesnel and Y.Pauleau, Thin Solid Films, (1994) in press.
- 11 C. Tribological Properties of Silver Thin Films Sputter-Deposited on Superalloy Substrates, N.Marechal, E.Quesnel, P.Juliet, Y.Pauleau and C. Zimmermann, Thin Solid Films 249(1994) 70-77
- 12 R. Burn and G.T.Murray, J.Am.Ceram.soc.,45(5) (1962)251
- 13 W.L.Phillips, Jr.,J.Am. Ceram. Soc.,44(10)(1961) 499.



## TRIBOLOGICAL PROBLEMS IN SPACECRAFTS

A. Borrien

CNES

18 Avenue Edouard Belin  
31055 TOULOUSE CEDEX  
FRANCE

### ABSTRACT

Spacecrafts are very specific vehicles, which have to work over a long period of time after experiencing severe mechanical stresses, without any maintenance and in a harsh environment, quite difficult to reproduce on ground. Economical constraints leading to the mass minimization and the low power availability complete the quick description of a situation propitious to mechanisms failures. The tribological problems are then the crucial point to assess in order to control in orbit mechanisms behaviour, and this will ask for a good knowledge of kinematics, materials, relative velocities and contact pressure.

Increasing complexity of payloads, especially in the field of optical instruments, microvibration requirements needed for satellite attitude stability, fifteen years life time now expected for telecommunications satellites, deployment and pointing of very large appendages as for radar missions, point out the wide range of satellite mechanism's applications.

The aim of this paper is to present the space environment specificity, the tribological solutions achieved on current programs, and the limits of these technologies. The surface adhesion due to ultra vacuum, the materials outgassing, the problem of thermal regulation and the difficulties to control fluid lubricants migration under micro-gravity will be discussed. We will show that the necessity of ground tests and the constraints brought by the launch vibrations could highly influence the chosen solution. The main on board functions calling for a mechanism will be briefly described and will be taken as actual examples for the description of the family of dry and wet space lubricants.

Some general recommendations for space tribology will be given in the last part and we will mention the Research and Technology program performed in Europe under CNES\* and ESA\* fundings.

Keywords: Tribology - Satellite - Spacecraft -  
Mechanism - Lubrication - Friction -

### \*Acronyms :

CNES : Centre National d'Etudes Spatiales

ESA : European Space Agency

ESTL : European Space Tribology Laboratory

LMC : Laboratoire de Mécanique des contacts

INSA : Institut National des Sciences Appliquées

### 1. INTRODUCTION

A lot of functions on board satellites are provided by mechanisms using tribology for motion transmission, guiding and positioning of appendages or parts of equipments. Tribology is in the heart of several subsystems such as the power subsystem unit, the attitude control system, and the radio frequency link with ground stations. Just to give an idea, it is interesting to notice that there are more than 200 bearings on the SPOT 4 satellite and about 12 locking devices using friction interfaces to transfer the loads during launch vibrations.

The most common need of tribology on spacecrafts is relative to the deployment of solar arrays and antennas after launch. These elements are very light but they are bulky as they often passed several square meters. The required angular accuracy and stiffness after deployment ask for a locking device to ensure a stable behaviour of the satellite attitude control system. In the stowed configuration, these appendages have to be stiffly bolted to withstand the launch vibrations without mechanical resonances at low frequency.

Mechanisms are also used to drive the solar array towards the sun at a rotational speed depending on the orbit period. These mechanisms have to permanently rotate at a very low speed and to transfer the electrical power to the satellite through sliprings up to 15 years for the geostationary orbit. The motion has to be very smooth to avoid the low frequency oscillations of the large inertia panels.

The satellite attitude reference is generally obtained thanks to a sun sensor and a scanning Earth sensor equipped with a rotating mirror to reflect on a bolometer the infrared transition between the Earth and the deep space. In this case, the sensor resolution is affected by the mechanical friction noise in the mirror bearings. The attitude stability is obtained by the mean of a servo loop with gyrometers and reaction wheels or kinetic momentum wheels. These mechanisms, whose rotation speed is very high, are generally put in a hermetically sealed box to allow ground tests without aerodynamic disturbances, and to implement a lubricant with no outgassing properties.

Satellite payloads are more and more sophisticated and they need many mechanisms to perform missions such as Earth observation or environment monitoring as well as planetary discovery or deep space exploration. These kind of missions often need pointing systems, scanning mirrors, interferometers, refocussing mechanisms, flip-flop mechanisms for covers or filters, and so on.

The design and the performances of all these mechanical functions are highly determined by the internal contacts friction behaviour. Unfortunately, space environment is quite specific and the designers cannot take any benefit from what has been already done in other industrial frames such as aeronautics.

## 2. PROBLEMATICS OF TRIBOLOGY ON SPACECRAFTS

A satellite is a small isolated world with a very low available electric power compared with other vehicles. It has to be very reliable because there is no opportunity to correct any malfunction until the end of its life. Thus, every technological choice must be validated through extensive ground tests to reproduce the whole in orbit environment, and redundancy is installed whenever it is feasible.

### 2.1. Tribology and ultra-vacuum

The residual pressure inside a satellite is about  $10^{-7}$  Torr and  $10^{-10}$  Torr outside. The remaining molecules are mainly long chain organic molecules coming from the outgassing of the satellite components. Each material has a specific vapour pressure which corresponds to the equilibrium between the liquid and gaseous phases at a known temperature, and for fluid lubricants this increases very quickly and non linearly with temperature. Thus, all space lubricants must provide a very low vapour pressure over a wide temperature range to limit the pollution of cold surfaces such as mirrors and lens. Standard requirements have been defined to check the lubricants properties under vacuum by measuring the percentage weight loss of a heated sample as well as the amount of volatile material which condenses on a cooled plate of specific dimensions. These screening tests are called "Total Mass Loss (TML)" and "Collected Volatile Condensable Materials (CVCN)" [1].

Some friction problems under vacuum are related to the adhesion forces existing between atomically cleaned surfaces. In the absence of oxygen, the oxide films which normally act as a shield between surfaces, cannot be regenerated and the surfaces are no more protected [2]. So it is recommended to avoid the use of similar metallic materials on two pieces in sliding contact.

In ultra-vacuum, the physical adsorption of the atmosphere gas by the materials is no more possible and the properties of some dry lubricants could be widely affected. This has been already observed for graphite dry lubricant which is considered as a very good solution under atmosphere and becomes defective at low atmospheric pressure.

For atmospheric pressure lower than  $10^{-3}$  Torr, it is known that convecting thermal exchange is neglectable. The consequence is the increase of the contact temperature which could provide vaporization or

structural transformation and lubrication failure. This effect is observable on high speed mechanisms.

### 2.2. Tribology and microgravity

The microgravity environment leads to hazardous migration of the fluid lubricants and binds the designer to implement seals and anti-migration barriers to concentrate the lubricant on the contacting surfaces. Moreover, this migration is very sensitive to thermal gradients and surfaces wettability. To overpass this difficulty, low mobility fluids are chosen. Nevertheless, It is very difficult to test the efficiency of such a solution on ground because of the disturbance coming from the Earth gravity. For these reasons, the fluid lubricants were not commonly used in space applications in the past, despite their high lubrication performance.

In the case where dry lubricants are used, some solid particles are created between the worn surfaces and could float in the mechanism in the absence of gravity. These particles are very difficult to catch and may produce some disturbances inside the mechanisms and some pollution on sensitive parts of the satellite especially on optical components. This is the case for example of filamentous particles generated by PTFE coatings.

### 2.3. Tribology and launch vibrations

The launch vibrations induce high alternate stresses and micro-movements in the mechanical interfaces. The moving mechanical parts are always preloaded to eliminate plays. Nevertheless, fretting problems are frequently observed between surfaces and the friction noise systematically increases after launch.

A lot of mechanisms are locked to survive the vibrations and the loads are deviated to go through a locking device. In this case, contact pressure is required to withstand the loads, and materials in contact have to ensure simultaneously a high friction coefficient and a low residual adherence force after release.

The dry lubrication solutions give a limitation for the allowable contact pressure whereas wet lubrication authorizes to increase the pressure up to the substrate limit. It is usually considered that the 440C stainless steel ball bearings could support a  $4000\text{N/mm}^2$  contact pressure with wet lubrication and only about  $2000\text{N/mm}^2$  in case of MoS<sub>2</sub> lubrication.

### 2.4. Tribology and thermal environment

Inside the thermal blanket of the satellite, the thermal environment is generally limited between  $-20^\circ\text{C}$  and  $+60^\circ\text{C}$  that is compatible with most of fluid lubricants. However there is a requirement that the change in viscosity be as small as possible over this temperature range because of the weak torque margin of the motorization unit.

On the other hand, all the appendages located outside the satellite could roughly see a temperature range of  $-100^{\circ}\text{C}$  to  $+100^{\circ}\text{C}$ . In this case, solid lubricant, whose properties are not temperature dependant, are generally preferred.

Some scientific satellites are dedicated to cryogenic experiments and tribological solutions have been found to work at a few Kelvin. This is the case of the Infrared Space Observatory (ISO) satellite that has been launched on november 1995, and on which the focal instruments are cooled down to 3 K. The mechanisms of the ISO camera are working in that environment [3].

## 2.5. Tribology and life-time

Space lubricants must provide a very low wear rate in order to comply with the expected life-time which is about 5 years for low Earth orbit and 15 years for geostationary orbit. Their chemical stability must be high and they have to be insensitive to radiation effects up to 100 krad in the worst case when the orbit crosses the Van Allen belts where corpuscular radiation are geomagnetically trapped. [4] In the case of low Earth orbit, the total dose inside the satellite after 5 years is less than 10 krad.

In many mechanisms, the friction torque noise is of great importance to ensure a motion linearity or a dynamic angular accuracy. That means for the lubricant, a stable behaviour over a wide period of time. For a dry lubricant, it is rather easy to reproduce an extensive ground life test with an increase of the motion frequency because the wear is mainly dependant of the number of cycles. For wet lubrication, the contact behaviour is a function of the relative velocity and a life test could be as long as the satellite life-time. This is the case for momentum wheels and gyroscopes. The quantity of oil must be small to limit the friction torque and there is a need for an oil replenishment coming either from the retainer either from a reservoir located nearby the contact.

## 2.6. Ground tests and storage

The mechanisms are generally mounted under filtered laminar air flow and people use gloves to avoid oxydization and pollution. It is quite often necessary to test the mechanisms in air when mounted on the payload or on the satellite for acceptance or calibration purpose. These tests add a constraint on the lubricants because the effect of the gravity cannot be always compensated and the humidity is unavoidable for human safety.

The ground storage could be specified as long as 9 years because the next satellite has to be ready to launch in case of a launcher failure of the previous one. During this period, the satellite is put in a container filled with dry nitrogen at a regulated temperature. These conditions ask for a good knowledge of the gravity effect on the fluid lubricant and of the ageing on the adherence forces between contact pieces. Some critical equipments could be stored alone to allow periodic working sequences. This is the case for the tape magnetic recorders.

As an example, we can mention the SPOT 3 satellite which has been stored for 3 years before launch.

## 3. THE SPACE LUBRICANT FAMILY

A very large amount of tests have been performed in tribology laboratories on a wide range of materials but only a few of them revealed good lubrication properties under ultra vacuum. The two main difficulties were to extrapolate the results obtained on a tribometer to a real application on one hand, and to ensure a stable quality of the lubrication process especially for coatings which are generally dependant on the geometry, the size, the surface roughness and the setting of the machine, on the other hand.

### 3.1. Dry lubricants

Dry lubrication is used in Europe since the beginning of the sixties, thanks to its relative insensitivity to ultra vacuum and temperature variation. The main solutions are based on molybdenum disulfide ( $\text{MoS}_2$ ), polytetrafluorethylen (PTFE), self lubricating composites and lead.

$\text{MoS}_2$  has a lamellar structure with a very low shear strength and shows a low wear rate and a low friction coefficient under vacuum. It can be used in a wide temperature range up to  $300^{\circ}\text{C}$ . The main drawback is its wide sensitivity to humidity leading to a great friction coefficient increase. Ground tests in humid air are then forbidden. The  $\text{MoS}_2$  coatings are deposited thanks to sputtered, bonded or burnished processes.

Sputtered coatings are a Physic Vapour Deposition (PVD) process brought about by applying Radio Frequency power between a target made from high purity  $\text{MoS}_2$  and a substrate in a low pressure Argon environment. An Argon ion plasma is formed and accelerated towards the target. Molybdenum and sulphur atoms are then pulled out the target and transferred to the substrate. The other method is a Magnetron reactive pulverization in which a molybdenum target is bombarded by argon ions in the presence of a  $\text{H}_2\text{S}$  flow. In this method, the tuning of the  $\text{H}_2\text{S}$  rate will change the percentage of sulphur in the coating. Thus,  $\text{MoS}_{1.6}$  could be obtained to improve the tribo properties. An other difference with the first process is the kinetic of deposition which is ten times faster. Extensive tests have been performed by CNES on this coating and show that the decrease in performance in humid air is less sensitive than the one observed with other processes [7].

Bonded coatings are a mixture of solvent, resin, and  $\text{MoS}_2$  particles. This mixture is sprayed on the surfaces and the solvent is removed by baking. The main disadvantages of this method is the difficulty to provide a regular film thickness and the insufficient adhesion quality which may require extensive pre-treatment such as sand blasting.

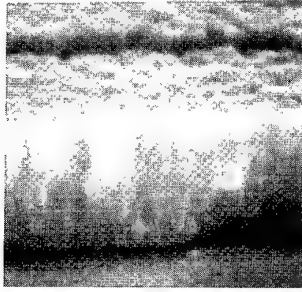


**Figure 1 - Structure of the MoS<sub>1.6</sub> PVD coating**

Burnished coatings are obtained through the rubbing of MoS<sub>2</sub> powder on to the surfaces. This method is widely used to coat the bearing balls by putting them in a small rotating barrel. The bearing rings are coated with an impregnated tissue polished on the raceways. A running in period is necessary to stabilize the friction torque.

PTFE is a polymer with a very low friction coefficient (0.05) and its tribo properties are the same under vacuum and air. Unfortunately, the outgassing behaviour is not as good as the MoS<sub>2</sub> one. PTFE coatings are obtained by mechanical projection on cleaned and tarnished pieces followed by a baking sequence between 300°C and 400°C. The film thickness is generally high (4 to 8 μm) and it is compulsory to run in the mechanism to remove the coating excess. PTFE is often used on gears where it can withstand an hertzian pressure up to 450 MPa. The drawback is the pollution brought on sensitive parts by detachable filamentous or lumpy particles.

Lead is able to act as a dry lubricant when it is laid down in thin films. The film thickness is about 1 μm in order to achieve a low friction coefficient. The most commonly used process is ion-plating. It is based on an electric field applied between a lead filament and the specimen to be coated is placed in a vacuum chamber in an argon ion plasma environment. Atoms of lead are thermally evaporated from the filament, then become ionised, and are accelerated towards the specimen. The main difficulty with lead is its sensitivity to oxidization in air which deteriorate its properties and requires for nitrogen use whenever the mechanism is on ground operated. The other drawbacks are the unsuitability when the velocity becomes high and the wear debris which can lead to a noisy torque. It is then recommended to implement elastic preload of the bearings to limit the quick fluctuation of the friction torque.

Duroid is a commercial name used by DUPONT for a composite material made of glassfiber, PTFE, and MoS<sub>2</sub>. This material is used to manufacture self lubricating bearing cages. Solid particles remove from the cage to the balls and then are spread on to the raceways. This solution allows a very long life time because the lubricant is always regenerated by the movement. It is not applicable to oscillating bearings and the main problem is relative to the friction torque which shows a

succession of quiet and noisy periods due to the wear particles cut off from the retainer.

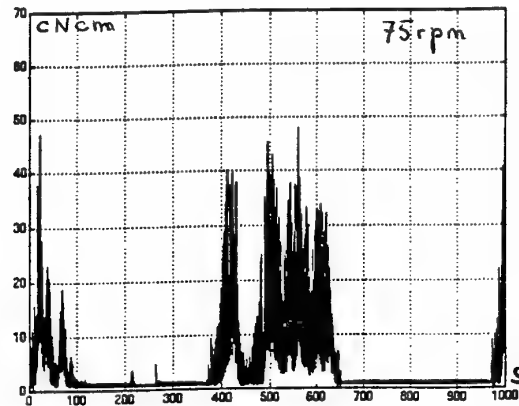


**Figure 2 - Duroid lubricated bearing friction torque**

Before closing this chapter on dry lubricants it is important to say a few words on ceramic coatings which could not be considered as lubricants but only as a neutral barrier between two metallic pieces to forbid any molecular diffusion and to protect the lubricant from metallic atoms contact. The main application of a ceramic coating is the titanium carbide (TiC) chemical vapour deposited on balls with a 3 to 4 microns thickness. This coating has to be polished before use in a ball bearing and leads to a substantial increase in the life time of fluid PFPE lubricants ( see 3.2) [6].

### 3.2. Fluid lubricants

The first use of fluid lubricants in space was relative to pressurized equipments. In this case, the ultra-vacuum requirements disappear and the remaining problem concerns the replenishment of the contact for a long time in microgravity. However, it has to be noticed that the subsequent critical problem is the sealing of the equipment to obtain an acceptable leakage rate. Momentum wheels, gyroscopes and magnetic tape recorder are in that category. Because of their excellent lubrication power, mineral oils are therefore generally used. A very large number of additives can be added to these products and many kinds of greases are formulated with available thickeners. As good examples of such lubricants, we can mention the Andok C grease made by Exxon and the KG80 and SG60 oils manufactured by Kendal Refining Company.

The oils compatible with outgassing requirements are only a few. The first family used in the space conquest was the silicon oils. We can mention the Versilube F50 and F44 from General Electric with a high viscosity index, a good thermal stability but only a poor lubricating property. Fluorosilicon oils were employed later and brought a better lubricating performance. Nowadays, the main family of vacuum space fluid lubricant is the perfluorinated lubricants. However, one



synthetic hydrocarbon oil is also widely used because of its very good outgassing behaviour.

The perfluorinated lubricants often called PFPE are long chain polymers build up from carbon, oxygen and fluorine atoms. Their qualities are a very high chemical stability, a very low evolution of viscosity versus temperature and, above all, a very low vapour tension which can reach  $10^{-12}$  Torr at  $20^{\circ}\text{C}$ . As examples of this family, we can mention the wellknown Fomblin Z 25 oil manufactured by Montedison [6] which thermal stability is quite outstanding between  $-40^{\circ}\text{C}$  and  $100^{\circ}\text{C}$  and the derived Braycote greases elaborated by Castrol. The Krytox 143 oil and its derived Krytox 240 greases made by DuPont are also used but they present a worst thermal stability.

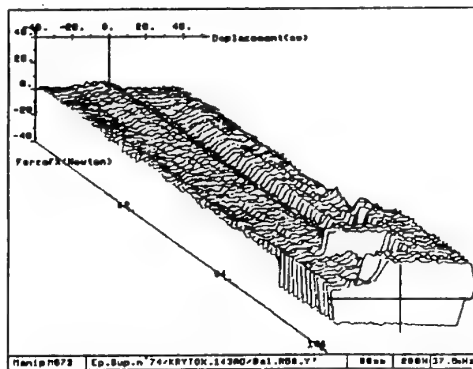


Figure 3 - Friction force time perspective with KRYTOX 143 AD lubricant

The problem comes with these lubricants when the elastohydrodynamic film cannot be ensured, that is often the case in spacecrafts because of low speed and wide temperature range. In this case called boundary lubrication condition, there are metal to metal contacts and the fluor contained in the oil chemically reacts with the iron contained in the steel and produces acids that transform the lubricant into lumpy particles which are called "brown sugar" [5].

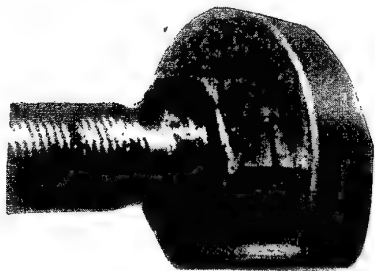


Figure 4 - Degradation of Braycote 601 grease on a roller screw

This phenomenon appears quicker when the relative sliding velocity is high, that is to say the number of cycles achieved with a ball bearing will be higher than

those obtained with a gear or a screw transmission. In any case, the use of this kind of lubrication is not suitable when the expected life time is very long.

The Pennzane SHFX 2000 oil is a synthetic hydrocarbon fluid manufactured by the Pennzoil company in USA. Its outgassing properties are quite good and there is no chemical reaction with metals but its relative poor thermal stability will limit the use between  $-20^{\circ}\text{C}$  and  $60^{\circ}\text{C}$ . CNES has performed a lot of work with the LMC\* laboratory of INSA\* in Lyon to manufacture new greases using Pennzane oil with PTFE and  $\text{MoS}_2$  thickeners [8]. These products show a good tribological behaviour and they are considered as full of promise for space use. Their commercial availability will be obtain soon in 1996.

#### 4. MAIN KINDS OF APPLICATIONS AND ASSOCIATED SOLUTIONS

After this quick overview of the space lubricant candidates, we are going to take some examples of mechanical functions and to present in each case the appropriate lubrication solution.

##### 4.1. Locking and latching devices

As described in the first part, all the appendages of a satellite have to be stowed and locked during launch in order to withstand the low frequency sine acceleration below 100 Hz with a level of about 15g to 25g, and the random vibrations up to 2000 Hz with a RMS value between 12 and 20g. All the bearings are thus axially preloaded to support the load transfer without shocks. When it is not enough because of the weakness of the moving part, this one is stiffly pressed against a rigid clamping zone of the satellite. It is generally preferred to select a polymer to metal contact when the contact area can be wide enough to comply with the limited allowable pressure of such a material. In other cases, a plane metal to metal contact is implemented with a specific high friction surface treatment such as tungsten carbide in order to avoid sliding micro-movements. The residual adhesion force between the surfaces after unlocking has to be carefully determined and measured in worst case conditions to ensure the release of the appendage. Solar panels, solar array drives, and most of antennas are stowed in such a way and released by the mean of a pyrotechnic device or a thermal knife and, even now, a shape memory alloy actuator to cut a pretension rod or bolt. Magnetic suspended rotors, as for the SPOT reaction wheels, are also clamped with this kind of system to prevent any motion of the rotor in the magnetic gap.

These tribological functions are always very sensitive to the local dynamic behaviour and to the evolution of the surface characteristics after several ground vibration tests (generally three or four) which are required for the flight models.

#### 4.2. Deployment mechanisms

The deployment of multi-panels solar arrays and large antennas requires a reliable and sophisticated mechanism. One of the difficulty is to estimate the residual friction forces after vibration and over a wide temperature range. The motor torque margin is then calculated as a compromise between the worst friction torque case and the worst shock valuation at the end of the deployment.

A good example to illustrate this kind of mechanisms is the TELECOM 2 deployable antennas, whose mass and size are about 20 kg and 2.2 m in diameter. The deployment mechanism is composed of two joints to guide the angular motion, an helical spring for motorization, a speed regulating system and an adjustable thrust to keep the right positioning for the mission.

The ball-socket joints make the self alignment of the antenna easier and are lubricated with MoS<sub>2</sub> to be efficient over a wide temperature range. The speed regulating system is composed of a two stages gearbox and a centrifugal brake made with two eccentric polymers blocks pushed against a metallic raceway by the centrifugal force. The corresponding friction torque is proportional to the square of the angular velocity that will limit the kinetic energy of the antenna at the end of the deployment. The motion transmission is obtained thanks to a pinion meshing with a gear sector and carrying a pulley. A wire cable attached to the centrifugal brake is winding around this pulley. At the final position, a rolling cam releases a pawl and a bolt is pushed into a slot by a linear spring to clamp the antenna. The pawl and the bolt are MoS<sub>2</sub> PVD lubricated.

The specificity of this kind of mechanism is a short life time, severe thermal conditions, the capability of performing air ground tests using a gravity compensation system, and the need of a reproducible constant friction torque, whatever conditions happen. To satisfy these conditions, the MoS<sub>2</sub> dry lubricant is often considered as the best arrangement despite its poor behaviour in humid air.

#### 4.3. Solar array drives

The satellite electric power is produced by photovoltaic cells laid on solar panels and permanently faced towards the sun. The satellite itself is generally stabilized to point its antennas towards the Earth, and it becomes mandatory to rotate the solar panels to keep the efficiency of the solar cells. In addition, the power has to go through the rotating system to reach the storage batteries and the converters. We will describe this kind of mechanism named "Solar Array Drive Mechanism" (SADM), taking the example of the geostationary EUTELSAT telecommunications satellites equipped with two solar array wings.

There are two mechanisms, one for each wing, that are build around a main rotating shaft mounted on large ball

bearings with an elastic preload to comply with high temperature gradients due to wires internal heating. This shaft is fixed on the solar wing yoke and is equipped with a series of power slip-rings designed for use in vacuum [10]. The shaft rotation is given by a stepper motor through a spur gear transmission with a ratio of 15. The angular backlash of the gear transmission has not to be temperature dependent. This is obtained with a specific pinion mounting, that follows the gear wheel thermal expansion. The number of revolutions of the wheel is about 6000 over the life time. The hertzian pressure on the gear box teeth is not very high and is compliant with a mechanical PTFE coating called "Nuflon". This process has been qualified by CNES through a technological program in 1986 and found as the best solution for gears dry lubrication [11]. The thickness of this coating is about 5 to 8 microns that is acceptable for a gear transmission and the maximum allowable pressure is about 450N/mm<sup>2</sup> to ensure 10<sup>6</sup> revolutions. The large angular contact ball bearings of the main shaft are lead lubricated. This solution is suitable when the angular velocity is low. However, the mechanism must be put in dry nitrogen to perform ground tests. The motor and pinion bearings are lubricated with MoS<sub>2</sub>.

The solar array drive mechanisms have to work outside the satellite body in a harsh thermal environment and to support high loads during apogee transfer manoeuvre. As the number of revolutions is not so high, the dry lubrication solution is well suited and limits the risk of slip-rings contamination.

#### 4.4. Attitude control mechanisms

The geostationary satellites generally use a scanning Earth sensor to know their attitude and they control it by the mean of momentum and reaction wheels. The Earth sensor is composed of a rotating head equipped with a flat mirror, while two other mirrors are fixed to the sensor housing. The optical beam scans the space and crosses the Earth surface four times per revolution. A bolometer sense the thermal transitions between Earth and deep space, and the calculation of the four corresponding angles gives the attitude of the satellite. The rotating head is mounted on two ball bearings axially preloaded with elastic springs, lubricated with "Duroid" cages and motorized with a dc brushless motor in a servo loop way to get a constant angular rate. The rate is about one revolution per second and the life time is fifteen years, that leads to 5.10<sup>8</sup> revolutions. The Duroid solution ensures a permanent transfer of lubricant from the cage to the balls and then the raceways, to achieve an extended life time. This transfer occurs because of the permanent rotation of the bearings and it requires at the beginning, a running in sequence to establish the lubricant film. The main drawback of this solution is the irregular torque noise due to the Duroid particles removal which are progressively flattened between balls and raceways. This rough increase of the torque noise appears from time to time and may disturb

the bolometer sensitivity because of the conversion of the mechanical noise into an electric noise by a microphone effect.

This kind of mechanism seems to be a good candidate for a wet lubricant solution in order to decrease the torque noise. However, this requires a good know-how of the retainer impregnation process and to get the replenishment mechanism of the film under control. Another difficulty is the increase of the mean friction torque due to a viscous resistance that will lead to a higher power consumption.

#### 4.5. Pointing mechanisms

Pointing mechanisms are the largest space mechanism family because of the various payloads applications and requirements. The technical split between these categories is given by the accuracy, the reachable angular domain, and the bandwidth.

The first family is a wide angle open loop mode positioning of a mirror or a telescope without any tracking requirements. This is the case of most of antennas pointing systems (TELECOM 2) and entrance mirror for Earth observation to allow lateral viewing (SPOT). The use of an hybrid stepper motor with a high steps number per revolution and sometimes, the use of a backlash free speed reducer such as harmonic drives [12] are enough to comply with the requirements. The wide angular displacement and the bending stiffness is given by a pair of low mass annular ball bearings. If a harmonic drive reducer is implemented, the sliding friction in the flexspline contacts asks for a wet lubrication in any case. Up to now, the most commonly used lubricant is Braycote 601 grease.

The SPOT instrument entrance flat mirror is machined in a zerodur blank and is mounted on two pairs of angular MoS<sub>2</sub> lubricated ball bearings. The chosen process coating, qualified for 800.000 motions is a burnished one. In this large thin bearings, a classical cage would be too brittle and is replaced by PTFE ball spacers. Extensive tests have been made at CNES to understand the influence of such spacers on the stabilization behaviour of the rotating mirror [13].

The second family gathers the wide angle closed loop dynamic pointing systems for which a target acquisition and tracking is specified. In this case, the association of a d.c. brushless motor and an optical encoder increases the bandwidth and the accuracy of the line of sight. The preferred bearing lubrication is wet despite the boundary conditions because of the large hysteretic start-stop behaviour of the dry lubrication often called "Dahl" friction [14]. An example of this family is given by the coarse pointing mechanism of the SILEX experiment which is related to inter-orbital optical communications and should be tested between the french low orbit SPOT 4 and the geostationary ESA ARTEMIS satellites.

The third family is composed of small angle mechanisms (a few degrees) to point accurately a telescope or a mirror in a servo loop mode with either external inertial sensors or internal displacement

sensors. In this case, the non linearity and the friction noise brought by the tribological contacts is avoided as much as possible and the guiding is generally obtained with flexural pivots [15] or elastic deformation of a supporting part, instead of bearings. The GOMOS pointing ahead mechanism, a payload of the ENVISAT satellite dedicated to the atmosphere ozone monitoring is a typical example of this family.

The last family is related to high bandwidth small mechanisms, which action is to stabilize an optical beam by the compensation of the satellite high frequency local movements (up to 200 Hz). They are energized with piezoelectric actuators without any tribological contact.

#### 4.6. Scientific instruments mechanisms

Many mechanisms are located inside the scientific instruments such as aperture mechanisms, optical filters mechanisms, scanning mechanisms, interferometers mechanisms, refocussing mechanisms, pumps, Stirling cryocoolers, gates and so on. To illustrate some specificities of this class of mechanism, we will get the example of a telescope refocussing mechanism which main interest is the need of a few millimeters precise linear motion.

The aim of a refocussing mechanism is to compensate the in orbit change of the optical length between mirrors to maintain the focal plane on to the detectors. This change is the consequence of the launch vibrations, the humidity desorption of composite structures, and the thermoelastic deformations. The compensation mechanism has to provide a precise linear displacement of lens with a few microns accuracy. The main parts of the mechanism are a stepper motor, a roller screw transmission and flexural blades to guide the lens. The wet lubrication is sometimes forbidden because of the risk of pollution and the dry lubrication solution leads to a limited life time because of the complex kinematic of the recirculating rollers and the high internal pressure between rollers and the screw. A solution based on a MoS<sub>2</sub> and silver coating has been qualified for a few thousands motor drives in the frame of Earth observation programs. Nevertheless, the best way to reach a higher number of cycles is to use a grease and to prevent the pollution of optical parts with bellows or seals. The great interest of the roller screw transmission for a refocussing mechanism is the high potential axial load, the high machining accuracy and the irreversible motion even in case of power cut.

### 5. GENERAL RECOMMENDATIONS FOR DESIGNERS

The mechanisms are often single point failure on board satellites. Although it is always difficult to understand the key reason of a satellite failure due to the lack of information, we can say that most of mechanical failures at the beginning of the life are the consequence of a human mistake during the assembly or screening acceptance tests operations. After this period, most of

failures are related to design unsuitability and tribology is frequently the heart of the problem. The first key for success is to put the reliability and simplicity criterias ever before the mass and the power consumption. The optimization of mass and power consumption have to be studied on the critical components in the field of specific research programs without severe delivery constraints. The reliability aspect has to be kept in mind everytime and the ground life tests must be carefully prepared and instrumented.

The second important point is to understand how the mechanism performance budget has been shared with other contributors to check if it is well-balanced. A too stringent requirement may lead to a risky solution and the designer has to decline any change in the qualified technologies if it is not mandatory. This is important especially if the people who write the mechanism requirements is not a tribology specialist.

The third key point is to consider the tribology not as a specific point to be chosen and added on an existing design but to build all the mechanism: sealing, corrosion protection, contamination by debris, thermal conductivity and heaters, electrical continuity, fretting problems and so on, taking into account the chosen lubricant.

The choice of the lubricant is mainly led by the kinematics, the load, the life time and the thermal environment. A complex kinematics with a high specific sliding and high loads steers the designer to a wet solution whereas a wide temperature range asks for a dry solution and a long life time requires a lubricant replenishment system such as "duroid" or oil reservoirs.

The choice of materials is also an essential condition for a successful design. Corrosion is an ever present problem and materials have to be protected from this degradation. The most commonly used materials are stainless steels, bronze, and thermoplastic polymers such as "Vespe", a polyimide, "Delrin", a polyacetal and "Hostafion", a P.T.F.E.

Finally, we can recommend to designers, whatever solution they use, to take care of the whole process, especially the cleaning process, to check the quality of the coating on specific additive test specimen, and to define, if necessary, a lot acceptance test.

## 6. EUROPEAN RESEARCH AND TECHNOLOGY PROGRAM

Research and technology activities in the field of space tribology are still going on in Europe under CNES and ESA fundings. We will briefly present some of the topics under study at the present time.

- Since 1995, the composite "duroid" material is no more manufactured and there is no qualified alternative solution. Extensive tests are done at ESTL\* to select

another material with the same properties and with a good mechanical resistance for the bearing cages machining. Several composites materials such as "Salox M" from Allegheny Plastics, "Rulon" from Dixon Industries and "Vespe SP3" from Du Pont are candidates for this matter.

- As mentioned previously, the PFPE fluid lubricants will chemically react with the metals and works are done to propose alternative solutions. New greases made from Pennzane oil and thickeners additives have been formulated under CNES fundings and are tested on bearings, gears and roller-screws. These new products will be commercially available in 1996.

- A new MoSx coating obtained with a sputtered PVD process with a 1,6 rate of sulphur has been developed and gives promising results, especially for the humidity sensitivity and the homogeneity of the coating structure. A qualification procedure is initiated.

- The behaviour of compressed contact surfaces during launch vibrations is a critical point to evaluate the risk of micro-sliding and the residual adherence force after release. A selection based on high friction coefficient materials and surface roughness adaptation is done at present time and the aim is to find a couple of materials with a high resistance to pressure, a low adherence force under ultra-vacuum and a friction coefficient greater than 0.6.

- The need for reliable electric slip-rings in space is essential but, unfortunately, the design of such contact materials is a compromise between tribo and electric properties which cannot be easily improved simultaneously. CNES has developed a specific test bench to analyse the in vacuo influence of various parameters on the life time: material, geometry, contact pressure, current density, angular rate, temperature and first conclusions are available for power slip-rings with 20000 revolutions. A similar work is planned for signal slip-rings with more than one million revolutions.

## 7. CONCLUSION

Tribology in space is a wide domain related to almost platforms and payloads. This technology is in the heart of mechanisms and is always a single point failure. People involved in the mechanisms design have always to keep in mind that a meticulous care is required at all stages of the definition, the manufacture, the qualification program and the acceptance tests.

This kind of symposium is a good opportunity to open discussion with specialists coming from outside the space community and to learn about their experience.

## Bibliography :

- [1] ESA PSS 01-702 : "A thermal vacuum test for the screening of space materials".
- [2] "Solutions tribologiques pour frottement sous vide". Ph Reynaud . Y. Berthier L. Flamand M. Godet LMC INSA Lyon A.Borrien CNES Toulouse
- [3] "Cryogenic mechanism of ISO camera" G. Luciano (Aérospatiale) Third European Space Mechanisms

- and Tribology Symposium, Madrid, Spain, October 1987.
- [4] "Techniques et technologies des véhicules spatiaux". Cépadués Editions 1994
- [5] "Perfluoropolyalkylether Oil degradation".  
"Inference of FeF<sub>3</sub> formation on steel surfaces under boundary conditions". David J. CARRE  
The Aerospace Corporation El Segundo  
California 90245
- [6] "In vacuum performance of Fomblin Z25 lubricated 52100 steel bearings with TiC coated balls."  
S. Gill, W. Price, R. Rowntree European Space  
Tribology Laboratory (ESTL), H. Bowing,  
H. Hintermann. Centre Suisse  
d'Electronique et de Microtechnique (CSEM)
- [7] "Qualification of a new molybdenum sulfide coating". J. Sicre (CNES) A. Aubert - A. Ginet  
(CEA/CEREM) Y. Berthier (INSA) Sixth European  
Space Mechanisms and Tribology Symposium,  
Zurich Switzerland, October 1995
- [8] "New considerations on fluid lubricants for spacecrafts applications" J. Sicre (CNES)  
P. Vergne - P. Prat (INSA) M. Pochard  
(SODERN) Sixth European Space Mechanisms and  
Tribology Symposium, Zurich Switzerland,  
October 1995.
- [9] "Noise analysis of dry lubricated ball bearings for a scanning Earth mechanism" L. Nicollet - M.  
Pochard (SODERN) J. Sicre (CNES). Sixth  
European Space Mechanisms and Tribology  
Symposium, Zurich Switzerland, October 1995.
- [10] "Long life, elevated velocity slip-ring contacts investigation" P. Mausli - A. Gisiger (MECANEX)  
J.M. Gavira (ESA/ESTEC) Sixth European Space  
Mechanisms and Tribology Symposium, Zurich,  
Switzerland, October 1995.
- [11] "Définition et essais d'engrenages dans le domaine de la robotique spatiale". L. Petitjean et A. Borrien  
CNES Toulouse. Snd European Space Mechanims  
and Tribology Symposium, Meersburg Germany  
1985.
- [12] "Application of Harmonic drive in space".  
E. Schaeffer. International Harmonic Drive  
Symposium. Matsumoto, Japan - 1991.
- [13] "Friction energy loss in annular ball bearings oscillations". A. Borrien - E. Condé - J. Sicre.  
CNES, Sixth European Space Mechanisms and  
Tribology Symposium. Zurich. Switzerland -  
October 1995.
- [14] "A solid friction model". Dahl . AFO 4695 -67C -  
D158 - Aerospace Corp. - 1968.
- [15] "Flexural pivots for space application".  
F. A. Seelig. The BENDIX Corporation Fluid  
Power Division. Utica - New-York. Third  
Aerospace Mechanism Symposium NASA.

# METALLIC AND NON-METALLIC PROTECTION SYSTEMS FOR REDUCTION OF TRIBOLOGIC INFLUENCES IN SEVERAL AREAS ON TORNADO AIRCRAFT

by  
C. D. Hamm  
K. Blomeier \*

Daimler-Benz Aerospace AG, Military Aircraft, D-81663 München, Postfach 801160

\* Daimler-Benz Aerospace AG, Airbus, D-28199 Bremen, Hünefeldstr. 1-5  
GERMANY

## 1. Introduction

The TORNADO multi-role combat aircraft was designed in the 70ties and went into service at the beginning of 1980. From this time up to now several aircraft have achieved approximately 3000 flight hours.

With respect to its operational role the TORNADO has been designed as a swept wing aircraft. This type of aircraft with variable wing sweep capability includes in principle more areas which are subjected to sliding and wear than a fixed wing aircraft. Due to this design the affected interfaces of different structural materials have been protected with adequate coatings or materials to maintain the operability of the aircraft. Depending on the function of the moveable joints on the aircraft structure, metallic and non-metallic coatings/ materials with adequate hardness and wear resistance have been adopted. The range of applied antiwear coatings comprises silver plating against fretting corrosion, abrasion resistant polymers etc..

This paper describes the application of adequate protection methods in view of their functional integrity in the aircraft structure. Longterm experiences during service life and repairability aspects.

Protection methods of leading edges against rain erosion are not subject of this presentation.

## 2. Identification of tribologic areas on TORNADO aircraft.

The main areas subjected to sliding and wear on the TORNADO structure are:

- \* Attachment of the wings to the wing carry through box. This attachment consists of the wing pivot pin, the wing bearing and the shear bearing device.
- \* Contact area of the wing fairing panels on the upper and lower side of the wings.
- \* Roller bearings on the wing nib.
- \* Flap track trails.

Figure 1 shows the location of these areas on the aircraft structure.

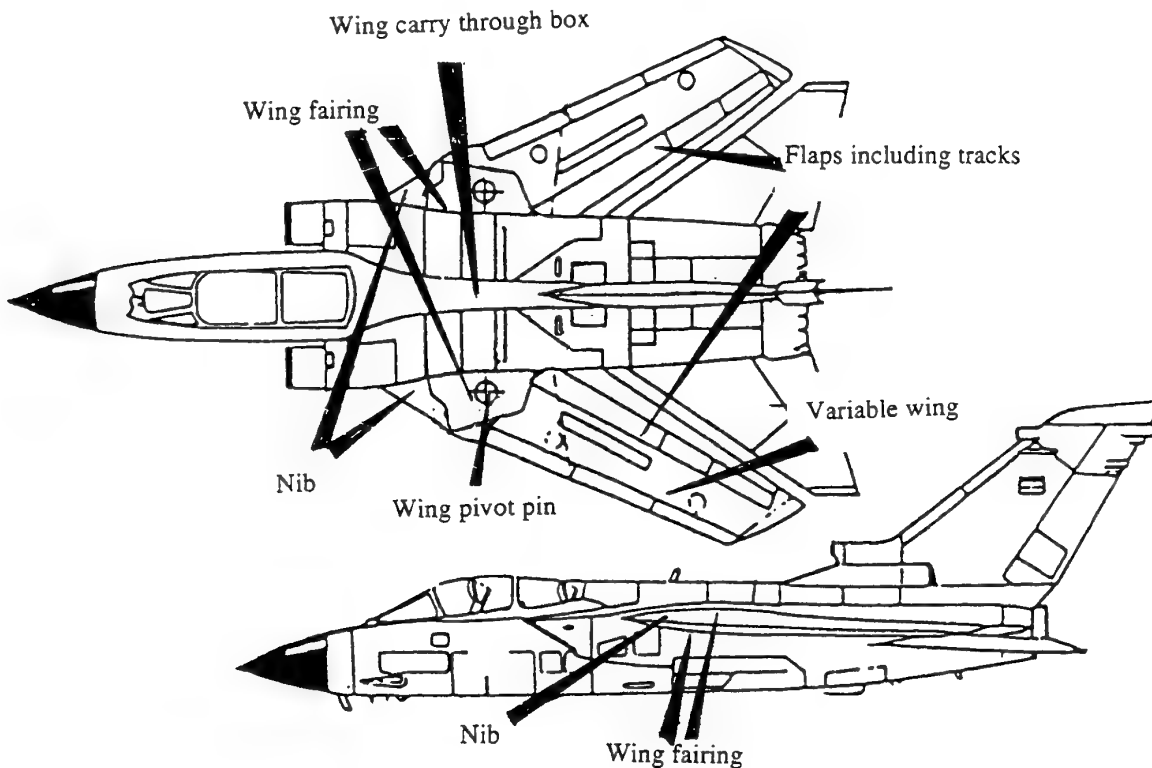


Fig. 1 Location of tribologic areas on TORNADO aircraft

### 3. Structural analysis of tribologic areas

The following paragraphs contain a brief description of the principle design of the affected areas, the typical load spectra, the tribologic aspect, the substrate materials and wear reducing materials involved in the moveable and static joint.

#### 3.1 Attachment of the wings

##### 3.1.1 Design aspects and structural materials

The moveable wings are attached to the wing carry through box by the following design:

- a) Wing pivot pin, consisting of a forging from titanium alloy, with the following overall dimensions:  
Diameter: appr. 180 mm, length: appr. 310 mm
- b) Upper and lower wing bearing, consisting of spherical and cylindrical elements made from corrosion resistant steel
- c) Upper and lower shear bearing device with spherical interface to the face wall of the wing box and made of corrosion resistant steel.
- d) Wing section for introduction of shear loads, made from titanium alloy.

### 3.1.2 Applied coatings and materials

Titanium and steel parts of the wing bearing system, which have interfaces to the centre fuselage structure and hence subjected to wear, are protected with the following coatings and materials:

#### 3.1.2.1 Silver plating

For reduction of fretting during installation of bushes and bearings, using the shrinking method, silver plating has been adopted. The following process has been used for titanium parts:

\* Cleaning and activation of the titanium surface using the ion etching process.

\* Vapor deposition of titanium with a coating thickness of appr. 90 nm.

\* Vapor deposition of silver with a coating thickness of appr. 750 nm.

After application of these coatings in the vacuum chamber the thickness of silver plating is increased up to 30  $\mu\text{m}$  using a galvanic coating process.

For steel parts a galvanic silver plating process is adopted.

#### 3.1.2.2 Application of TEFLON-liners

The elements of the bearing which are affected by the wing sweep operation are protected with a TEFLON liner.

#### 3.1.3 Protection of tribologically affected areas of the wing bearing elements

Table 1 gives an survey of the bearing elements and the areas on which the specific coatings/materials are applied.

Table 1: Bearing elements and coatings/materials

Bearing element	Affected area of the bearing element	Protection method
Wing pivot pin	Complete outer area which has interfaces to the upper and lower wing bearings	Silver plating acc. to para. 3.1.2.1
Wing bearing consisting of the functional elements: Sleeve, ball and race	<b>Sleeve:</b> Joining area to wing pivot pin	Silver plating acc. to para. 3.1.2.1
	<b>Ball:</b> Interface area to the sleeve	Teflon liner acc. to para. 3.1.2.2
	<b>Race:</b> Spherical interface to the ball element and shrink bush in the wing*	Teflon liner acc. to para. 3.1.2.2, *Silver plating acc. to para. 3.1.2.1
Shear bearing device	Interface of the spherical area to wing box face wall (shear device) and to the wing	Teflon liner acc. to para. 3.1.2.2
Wing area for shear load introduction	Interface to the shear bearing device	Strip from titanium alloy



### 3.1.4 Assembly of the wing attachment

The bearing elements of the wing attachment which are affected by the wing sweep operation are fitted with a teflon liner. This interface material reduces sliding and protects the bearings against fretting. Parts which are subjected to the wing movement are the upper and lower wing bearings and the shear bearing device. Figure 2 and 3 identify the bearing elements and show an approximate installation sequence.

Silver plating has only been applied on static bearing elements for protection against fretting during the installation process. Although shrinking by means of liquid nitrogen is adopted, relatively high installation loads are applied. Consequently, this coating became necessary due to the very close tolerances of the joint and materials being susceptible to fretting corrosion, if not protected.

### 3.1.5 Loads induced on the moveable joints

The load reaction of the wing bending moments through the wing bearings depends mainly on the position of the wing. The bending moments are reacted by the upper and lower lugs.

Typical bending moments for wing sweep positions of  $25^\circ$  are appr. 700 KNm and for  $45^\circ$  appr. 500 KNm.

The shear forces are reacted at the pivot pin and shear device.

Approximately 20% of the load is reacted by the pivot pin and 80% by the shear device.

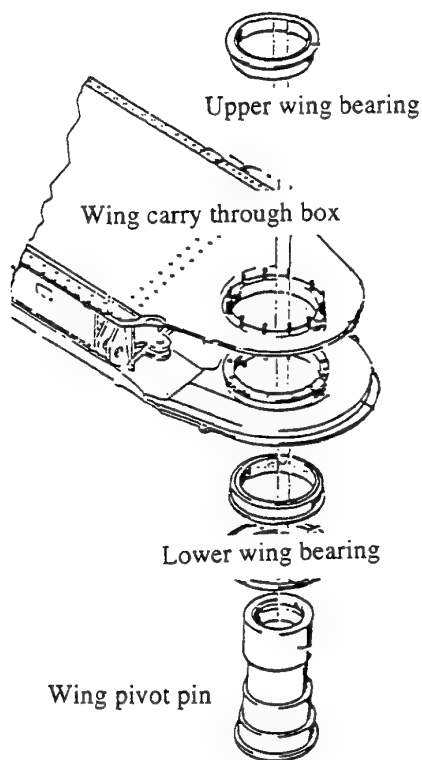


Fig. 2 Installation of the wing bearing and associated elements

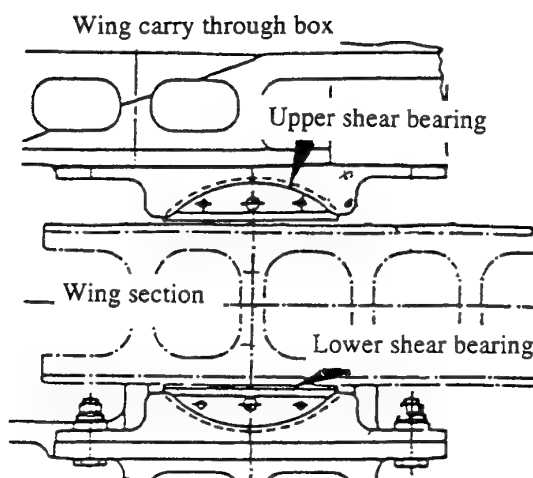


Fig. 3 Upper and lower shear bearing

### 3.1.6 Damage behaviour of the wing bearing during service

The wings normally will be removed during the major structural maintenance interval between 2000 and 2500 flight hours (FH).

For this reason the wing pivot pin is cooled down with liquid nitrogen and pull out of the wing bearing using a special device. The wing bearings are also removed, but not the shear bearings.

In general the wing pivot pin is designated as a static element of the wing attachment but the practice shows that micro movements can occur. Damage to the silver coating and the pivot pin, caused by fretting, can be caused in very specific areas. Experience obtained by the major airframe fatigue test (MAFT) , regarding wear effects on the wing pivot pin, exceed the current requirement of 4000FH. Because no scatter factor is applied for wear test hours are comparable to FH. Depending on the findings during the major structural maintenance interval a decision has been made for implementation of repair measures. The German Airforce has established a structural maintenance program for inspection of aircraft with a high number of FH. This program covers all critical areas of the air frame obtained from the MAFT. The findings will be assessed with respect to MAFT results and adequate measures will be established.

Part of this program is the wing pivot pin assembly so that service experience will be obtained in addition to the MAFT results.

### 3.1.7 Inspection and repairability of the coating

Acceptance criteria have therefore to be introduced for reinstallation or repair. Pivot pins which show a silver coating in good condition, e.g. no adhesion loss or serious damage of the coating, are reinstalled in a 90° displaced position. Damaged silver coatings and signs of fretting on the substrate material require the removal of the silver coating for non destructive testing and inspection of the depth of fretting.

Provided that the tolerance of the bush is within drawing limits after mechanical reworking, replating with silver is performed using the process shown in para. 3.1.2.1.

Bushes with serious fretting and out of drawing tolerance are phased out until an adequate repair procedure is qualified.

The moveable elements of the wing attachment, such as the wing bearings, are inspected for bearing tolerances. Replacement of the complete bearing is conducted if the clearance fit is out of tolerance, due to a back lash requirement.

No damage has been observed on the shear bearing device within this maintenance interval.

### 3.2 Roller bearings on the nib

**3.2.1 General function of the nib**  
The nib consists of an aerodynamic fairing with integrated kruger flap and the internally located moveable element, which is attached to the fuselage. Rollers of the moveable element follow tracks on the wing during sweep operation and induce vertical movement of the aerodynamic fairing. Figure 4 shows the nib fairing.

**3.2.2 Design aspects and materials**  
The moveable element consists of a special bracket design with an integrated roller assembled with wear reducing bushes and a bearing pin. Figure 5 shows the moveable element. The involved materials are:

- \* Bracket made from titanium alloy
- \* Roller made from corrosion resistant PH-steel
- \* Bush consisting of steel coated with a self lubricating low friction material (Teflon)
- \* Bearing pin made from corrosion resistant PH-steel

The overall dimensions of the roller, with a spherically shaped circumferential area, are: Diameter: appr. 32 mm, width: appr. 17 mm. The pin diameter is appr. 12 mm.

#### 3.2.3 Protection of moveable elements against tribologic effects

On the basic design no special protection was applied on the affected moveable elements, such as the roller and the bearing pin. To reduce friction between the roller and the bearing pin a bush fitted with a Teflon liner was installed.

Interfaces on the wing with contact to the rollers have been protected with titanium strips.

#### 3.2.4 Loads induced on the moveable elements

The maximum load at the roller is appr. 23 KN and the max. rolling speed appr. 90mm/sec. During mission flight appr. 10 wing sweep cycles are performed per hour.

#### 3.2.5 Damage behaviour during service

Damage of the moveable element was mainly caused by failure of the Teflon liner which led to extensive fretting of the bearing pin.

During service the life of this item was unacceptable short so that an alternative wear protection system was investigated.

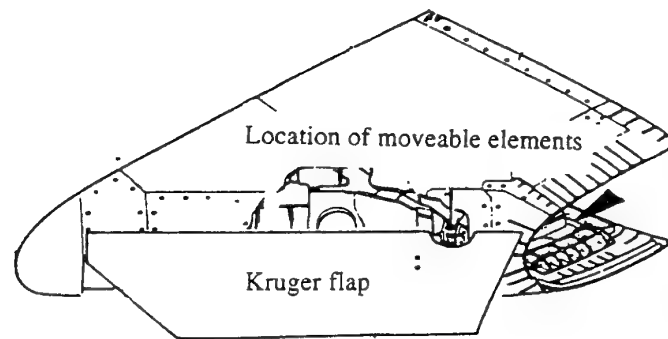


Fig.4 Wing nib

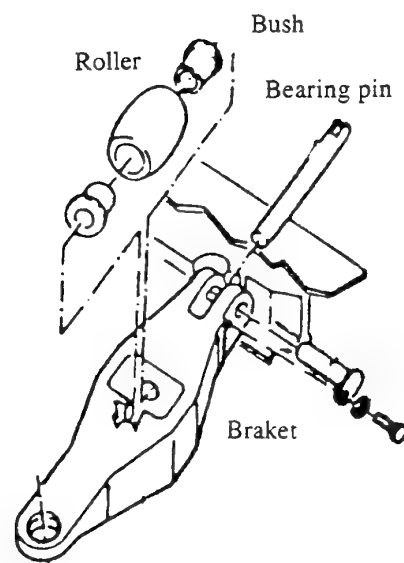


Fig. 5 Moveable element

### 3.2.6 Investigation of alternative wear protection

To solve the problem of premature failure of the antifriction liner, investigations with several antiwear coatings on the interface roller and bearing pin were performed.

For application of realistic service conditions a special device was constructed simulating loads, velocity and wing sweep cycles as shown in para. 3.2.4. Additional environmental media have been applied for realistic test simulation.

### 3.2.7 Test equipment and requirements

For simulation of the length of the track for roller movement a special test apparatus was constructed with a length of appr. 400 mm. A complete wing sweep follows a track length of about 800 mm, which is defined as 1 cycle containing 2 load cycles.

With respect to the number of wing sweep cycles per hour (see para. 3.2.4) and the service life of 4000 FH, appr. 80.000 load cycles have been simulated on the test apparatus.

The test apparatus was equipped with a thermal element which interrupted the test when temperatures of more than 55°C were achieved on the bearing surface.

### 3.2.8 Environmental exposure

The complete moveable element was statically exposed to the following environmental media for 8 days at R.T. :

- \* Appr. 10mg dust acc. to MIL-STD-810
- \* 1 part water
- \* 1 part deicing fluid isopropanol acc. to NATO S-737

During exposure the test fluid was stirred to avoid sedimentation of the

dust.

After the static exposure the interface between bracket and roller was wetted with this fluid every hour, but not at night.

### 3.2.9 Coatings and materials tested

For protection of the roller and the bearing pin the following polymeric and metallic coatings were used:

- \* KARON V polymeric coating containing PTFE, application e.g. by spray equipment, thickness appr. 0,3 mm
- \* LDT-400C Co/Mo/Cr coating, applied by D-gun, hardness appr. 700 HV, thickness appr. 0.3 mm
- \* LC-1C Chromium oxid particles embedded in chromium/nickel matrix, applied by D-gun, hardness appr. 700 HV, thickness appr. 0.3 mm
- \* LW-5 tungsten carbide applied by D-gun, hardness appr. 700 HV, thickness appr. 0.3 mm
- \* GLACIER composite bearing material consisting of a steel bush coated with a thin layer of tin bronze and an antiwear coating of PTFE and lead.

Table 2 shows the materials and coatings involved in this test program and the achieved load cycles.

### 3.2.10 Interpretation of test results

After completion of the test the following result has been achieved with respect to the investigated materials according to table 2:

- 1) Extensive wear both on the TEFLON bush and the bearing pin.
- 2) Slight wear on the KARON coating without any effect to the bearing pin.
- 3) Fretting of the bearing
- 4) Slight wear on the KARON coating without any effect to the bearing pin.
- 5) Fretting of the bearing.
- 6) Fretting both on the roller and the bearing pin.

Table 2 Materials and coatings

Item No.	Materials/coatings		Achieved load cycles	Service life (hours)	Test criteria acc. to para. achieved/not achieved
	Roller (PH-steel)	Bearing pin (PH-steel)			
1	Fitted with TEFLON bush 1)2)	Without treatment 1)2)	4000	200	not achieved
2	Without treatment	KARON V coated	80.000	4000	achieved
3	Bush, high strength steel, surface hardened (700HV)	LW5-coated, lubricated with grease NATO S-722	200	10	test interrupted, not achieved
4	KARON V coated	LDT-400C coated	80.000	4000	achieved
5	GLACIER bush	LC-1C coated	20.000	970	not achieved
6	KARON V coated	LW5-coated	70.000	3600	not achieved

- 1) Tested under environmental exposure, all other tests were performed under dry conditions.  
 2) Basic design

### 3.2.11 Introduction of the improved wear coating

Due to the achieved test results the variant KARON V coating of the bearing pin assembled with the non treated roller has been introduced on the TORNADO nib.

## 3.3 Wing fairing

### 3.3.1 General function of the wing fairing

The wing fairing is in general an aerodynamic aid which covers the wing attachment. It is fixed on the upper and lower side of the wing carry through box. The wing fairing has a tribologic interface to the upper and lower wing skins.

### 3.3.2 Design aspects and materials

The wing fairing consists of a glass fibre reinforced composite structure with a syntactic core material. Integrated spring elements consisting of steel slide on the wing skins and compensate structural bending. The moving element of this tribologic component are the wings during sweep operation. Fig. 6 shows a wing fairing component.

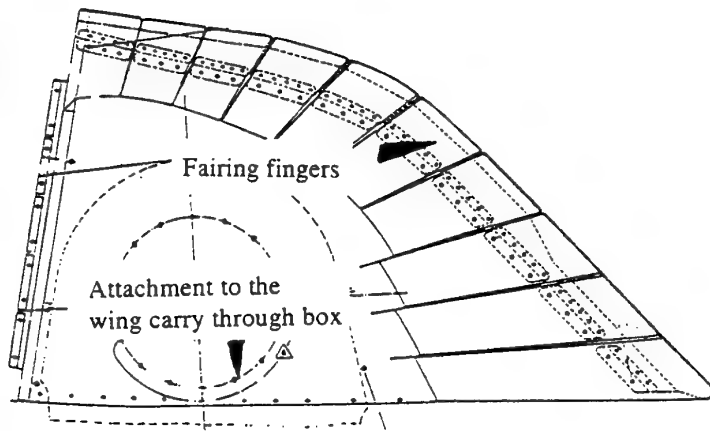


Fig. 6 Wing fairing

### 3.3.3 Protection methods

The area on the wing skin which is subjected to sliding of the spring elements is protected with a polymeric abrasion resistant coating. The coating consists of a polyurethane based material which is filled with TEFLON particles. Application is done using conventional spray equipment applying a coating thickness of appr. 300  $\mu\text{m}$ . For an adequate adhesion of this coating on the aluminium substrate

material a pretreatment with chromic acid anodising and subsequent painting with epoxy primer has been conducted. Adequate abrasion resistant coatings are e.g. AERODUR ARC or LAMINAR X500, both from AKZO/DEXTER.

### 3.3.4 Loads induced on wing skin area

This specific area on the wing is mainly affected by the surface pressure of the spring elements. Depending on the angle of the wing sweep the surface pressure varies within a certain range. In view of an average contact area of appr. 135  $\text{mm}^2$  per spring element the surface pressure is 4,5  $\text{N/mm}^2$  at a sweep position of 25° and 6,9  $\text{N/mm}^2$  at 68°.

### 3.3.5 Damage behaviour of the coating during service

The abrasion resistant coating was in good condition over an average service life of appr. 2000 FH. Failure occurs mostly on gaps and fastener holes which results in peeling off.

Repairability is ensured by partial removing of damaged coatings, abrading of overlapping areas of the remaining paint and recoating with the original paint until the required thickness is achieved.

## 3.4 Flap track

### 3.4.1 General function of the flap tracks

The flap track elements attached to the wing structure and flaps and rollers fitted to the flap tracks allow continuous movement of the flaps during flight operation.

### 3.4.2 Design aspects and materials

The flap track elements are bolted to the flap and wing structure while the roller follows the track during operation. The wear affected part of this assembly

consists of the following materials:

- \* Flap track consisting of titanium alloy
- \* Roller consisting of steel
- \* TEFLON liner (anti-wear-strip) attached to the face wall of the flap track.

### 3.4.3 Protection systems

The track on which the roller is moving during flap settings has no protection. An anti-wear-strip is adhesive bonded to the flap track area subjected to sliding by the end buttons of the roller during certain load cases. Figure 7 shows the flap track and the location of the wear protection.

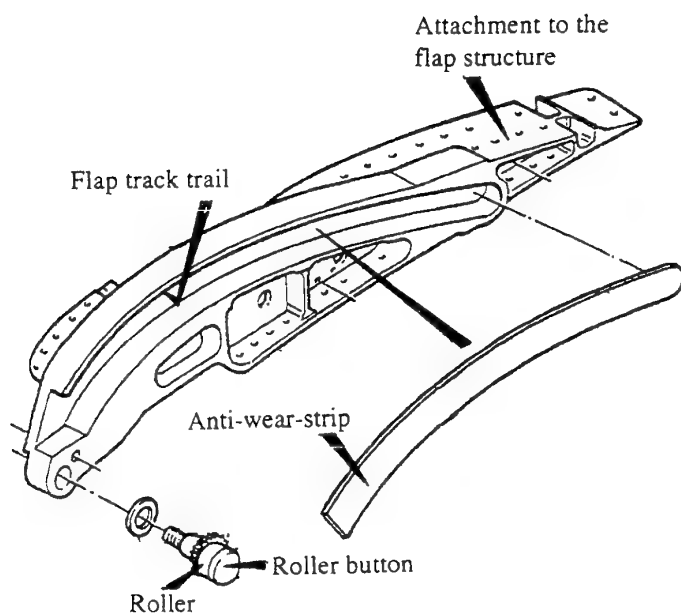


Fig. 7 Flap track

### 3.4.4 Induced loads

The max. pressure on the main flap is appr. 20 KPa. This depends in general on the flap setting and the air speed.

### 3.4.5 Damage behaviour

The flap track is subjected to slight deformation in the contact area of the roller in completely extended position of the flap. Deformation of this specific area is mainly caused through aircraft taxiing and during landing.

Severe problems are caused by the anti-wear-strip which is the protection against contact of the roller end button with the flap track material.

In the past loss of the adhesive bonded anti-wear-strip or damage of this protection caused fretting on the flap track. Damage mostly occurred within less than 300 FH. Introduction of a new adhesive system reduced the loss of the anti-wear-strip, but significant improvement of the reliability could not be achieved.

### 3.4.6 Further investigations

To improve this unacceptable situation related to fretting, subsequent loss or damage of the anti-wear-strip, alternative protection systems were investigated. Coating of the roller end buttons with KARON V and replacement of the TEFLON strip was proposed for testing. Test rig simulation with this protection scheme experienced good results so that flight tests have been conducted with several aircraft. More than 300 FH have been achieved in the meantime without serious signs of wear both on the flap track and the roller buttons.

## 4. Summary

This presentation shows the most affected tribologic areas on the TORNADO aircraft structure. Since TORNADO is designed as a swept wing aircraft the attachment for the variable wings, the related components and the flap tracks are subjected most to tribologic influences.

With respect to the loads induced on affected areas adequate wear protection has been selected.

Most of the adopted protection methods showed good results over the in-service time.

Especially the protection systems and bearings on the wing attachment and the wing fairing area show adequate endurance during service.

In several cases, e.g. for the roller bearings in the nib, the original design was replaced due to unacceptably short service life. Similar problems occurred on the flap tracks which requires improved wear protection.



## IMPROVING SOLID LUBRICATED AEROSPACE BEARINGS

B. Mortimer  
S. Mason  
Structural Materials Centre  
Defence Research Agency  
Farnborough, Hants, UK  
GU14 6TD

### SUMMARY

Plastics-based liners, 0.3-0.4 mm thick, containing polytetrafluoroethylene are usually mated against steel counterfaces in dry bearings used extensively in aircraft and helicopters. Wear experiments have been made on a number of these liners, using a tri-pin on disc apparatus, to examine the effect of decreasing the roughness of the steel and other counterfaces manufactured from harder materials and coatings. For some hard materials, WC-Co and alumina, the primary importance of hardness and surface roughness on liner wear is confirmed; the smoother the surface the lower the wear. Other materials, and in particular physical vapour deposited titanium nitride, do not lead to lower liner wear rates. The very low liner wear obtained against cermet and alumina counterfaces suggest that bearing lives could be extended considerably, perhaps by an order of magnitude, by using harder counterfaces than the hardened AISI 440C stainless steel which is currently used.

### 1 INTRODUCTION

Dry-bearings, containing polytetrafluoroethylene (PTFE) as a solid lubricant, are now widely used for a wide variety of flight control applications in airframes. The reduction in maintenance effort compared with the more conventional, grease lubricated, bronze-steel bearings, has been the main impetus for their introduction. These bearings consist of a thin layer of a plastics-based composite, typically 0.3-0.4 mm thick, bonded to a substantially thicker steel backing. This combination gives high load-carrying-capacity despite the low strength of major constituents of the plastic composite. The supported liner is usually mated against a polished steel counterface, typically AISI 440C hardened to around 700 Vickers Pyramidal Hardness (VPN). Over the last few years a wide ranging research programme has studied the friction and wear of such bearing materials and investigated the main factors influencing performance and its relationship to structure and composition (1-4). The present work is part of this general endeavour and is concerned mainly with the influence of counterface topography on the liner friction and wear.

A previous investigation (5) has shown that the counterface roughness during sliding is one of the most important parameters affecting liner wear. The state of the counterface surface is influenced by its hardness and initial roughness, and by the formation of transfer films. Very hard counterfaces remain essentially undamaged during sliding and liner wear rates then decrease monotonically as the initial surface is decreased. Counterfaces of lower hardness, but even as high as 1000 VPN, can still be damaged by some composites containing glass fibre, resulting in a limiting value of the surface roughness generated during operation and hence a limiting value of liner wear. For AISI 440C steel, hardened to around 700 VPN, this roughness is approximately 0.05  $\mu\text{m}$  Ra. (This roughness is approximately that obtained on such a steel ground on the finest grade of SiC paper.) Counterfaces initially smoother than this undergo rapid,

if slight, roughening and give no further reduction in liner wear. With the exception of four tests in ref. 5 all previous work has been carried out with interfaces of roughness 0.05  $\mu\text{m}$  Ra or higher. The aim of the present investigation has been to extend these studies to a wider range of very smooth, hard surfaces.

### 2 MATERIALS

Plastic, composite, dry-bearing liners can have structures built up in a number of ways: those used in this investigation are shown schematically in Figure 1. Both types are widely used in commercially-available bearings. Liner K, in Figure 1a, consists of an interwoven, double-layer fabric of PTFE and glass fiber in a phenolic resin matrix. In a variant of this, liner L, a small proportion of the upper PTFE layer is replaced with glass. It is the latter structure, with  $\approx 94\%$  PTFE-6% glass in the upper 100  $\mu\text{m}$  of the liner, which has primarily been used in the present work. Other variants, L1 and L2, with 3% and 12% glass respectively in the upper woven layer, have also been used, along with liners K and L, to assess the influence of the proportion of glass at the sliding interface on the friction and wear. The surface of liner L is shown in the scanning electron micrograph in Figure 2. The glass can be seen as the lighter coloured strands made up from  $\approx 10 \mu\text{m}$  diameter glass fibers. The remainder of the woven structure consists of strands of  $\approx 30 \mu\text{m}$  diameter PTFE fiber. Phenolic resin fills the spaces in the weave structure and to a substantial extent impregnates through the fiber in the strands and bonds them together.

The second type of liner, D in Figure 1b, is constructed from a single-layer, fabric-reinforced, vinyl-phenolic resin containing a dispersion of PTFE short fiber ('flock').

The usual counterface material in aerospace dry-bearings is AISI 440C steel. This martensitic stainless steel has the composition (wt %): 17.3Cr, 1C, 0.5Mo, 0.5Mn, 0.4Si, 0.17V, balance Fe. Specifications (6) require that the steel be hardened to at least 55Rc ( $\approx 600$  VPN) and subsequently ground and polished to better than 0.2  $\mu\text{m}$  Ra. In practice, the hardness usually lies between 600-740 VPN and the surface finish is around 0.05  $\mu\text{m}$  Ra. Results obtained from experiments against this counterface are used for comparison throughout this paper.

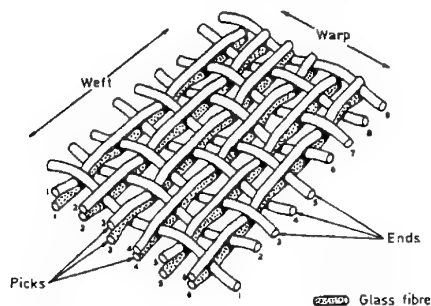
Details of all the hard counterfaces examined are listed in Table 1. Different surface roughnesses down to 0.05  $\mu\text{m}$  Ra, were obtained on the hardened 440C by random abrasion on various grades of silicon carbide paper. Roughnesses lower than this were achieved by diamond polishing after grinding.

### 3 WEAR MEASUREMENTS

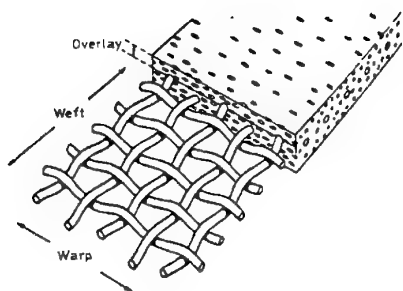
The wear apparatus is shown in Figure 3. A conventional four-ball lubricant-testing machine was modified to provide a lower, stationary, flat counterface against which was mated an upper, rotating specimen holder. Three, plane-ended,

cylindrical pins, equally spaced around a circle of 32 mm diameter, protruded from the holder. Discs punched from the liner were adhesively bonded to the ends of each of these 5 mm diameter pins.

For the liner containing interwoven PTFE fiber (Fig 1a), an epoxy resin was used as the adhesive, whereas for that containing PTFE flock (Fig 1b), the adhesive was the same vinyl-phenolic as that which impregnated the liner. The upper specimen holder aligned itself against the lower counterface by means of a spherical bearing ball. It was driven by a peg which also acted as a shear pin in the event of seizure.



a



b

Figure 1 Plastic composite liner structures. (a) Liner K - woven PTFE/glass fabric impregnated with phenolic resin, (b) Liner D - PTFE chopped fiber in a reinforced resin.

The rate of rotation was 12 rev/min, which corresponds to a speed of 0.02 m/s at the pin/disc interface. The counterface was mounted on a base supported by a rolling-element, thrust bearing and loaded against the three pins by a lever arm and weights. In all the experiments, the load applied was 800 kg, which corresponds to a mean stress of 133 MPa (19,300 psi) on the pins. Movement of the lower disc, due to friction, was restrained by a cantilever beam, the deflection of which was sensed by an inductive transducer to determine the frictional force.

Wear depth, frictional force and counterface temperature were all monitored during the tests. The frictional force was recorded continuously, but the temperature was only measured intermittently with a surface contact thermometer touching the side of the lower stationary disc.

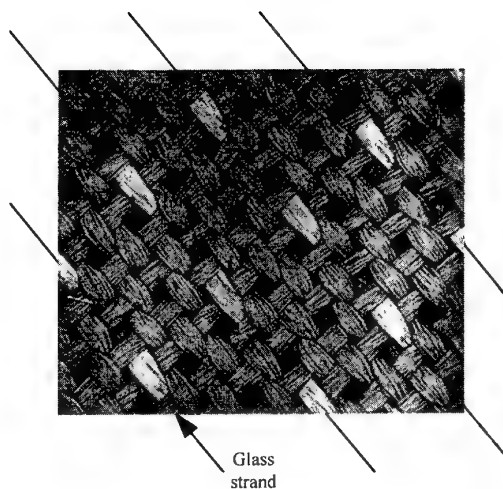


Figure 2 Backscattered electron micrograph showing PTFE and glass fabric impregnated with phenolic resin : Liner L

The upper specimen was periodically removed to determine wear. The change in the liner thickness on each pin was measured in two ways; by a double inductive transducers system, using the specimen holder base as a reference plane, and by an electronic micrometer sensitive to  $\pm 1\mu\text{m}$ . Measurements were made on each pin using these methods and the final depth of wear recorded is thus an average of these six values. Previous work (5) has shown that any deformation which occurs on first applying the load is substantially complete after about 2 hrs. The surfaces were thus always loaded together statically for several hours, prior to the wear experiment, to obtain an appropriate datum for the subsequent measurements.

#### 4 SURFACE EXAMINATION

The surface topography was examined using a profilometer to give the centre-line-average roughness ( $R_a$ ). The surfaces of the counterfaces and the liners were also examined optically and by scanning electron

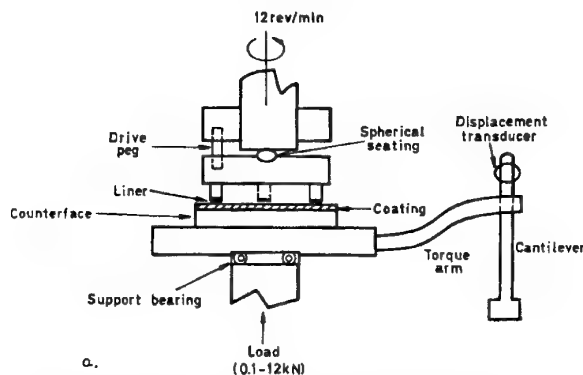


Figure 3 Schematic of the friction and wear apparatus

	Substrate	Treatment	Microhardness (VPN)	Comments
A	440C Steel	Hardened	780	
B	Nitrided 440C Steel	Gas nitrided	1140	
C	Borided 440C Steel	Pack borided	940	
D	WC-10 wt% Co cermet		1670	Special fine-grained WC powder used
E	Alumina		2080	Single crystal
F	440C Steel	Physical vapour deposited TiN coating	~2100	Arc plasma source

Table 1 - Substrate and Coating Details

Counterface					Linear specific wear rate (mm <sup>3</sup> N <sup>-1</sup> m <sup>-1</sup> )	Counterface temperature during steady wear (°C)
	Material	Hardness (VPN)	Initial Roughness (µm Ra)	Final Roughness (µm Ra)		
G	WC-Co cermet	1670	0.002	0.002 *	5.2 x 10 <sup>-9</sup>	47-52
			0.016	0.014 *	32 x 10 <sup>-9</sup>	70-75
			0.076	0.065	26 x 10 <sup>-9</sup>	50-55
H	440C Steel †	780	0.02	0.06	160 x 10 <sup>-9</sup>	62-75
			0.05	0.07	150 x 10 <sup>-9</sup>	70-75
			0.10	0.10	410 x 10 <sup>-9</sup>	68-73
			0.14	0.12	6000 x 10 <sup>-9</sup>	-

\* any PTFE transferred to counterface carefully removed

† data from reference 5

Table 2 - Specific Wear Rates of Liner L Against WC-Co Cermet and 440C Steel

microscopy (SEM). Hardness measurements were made with a microhardness tester on an optical microscope, generally with 100g or 200g loads. In the case of the thin, physical vapour deposited (PVD) TiN coatings only very low loads (5g or 10g) could be used.

## 5 WEAR RESULTS

### 5.1 Counterface Roughness

The variation of composite wear depth with time for the liner L sliding against hardened 440C stainless steel of various initial roughnesses is presented in Figure 4a (from ref. 5). In each case there is an initial running-in period followed by a linear or near-linear increase of wear. The steady-state specific wear rates, counterface temperatures and the initial and final surface roughnesses are all given in Table 2. These results may be compared with those shown in Figure 5a and Table 2 for wear against a tungsten carbide - 10 wt% cobalt cermet. The wear rate on the steel is not reduced for the smoothest counterface, 0.02 µm Ra, because this smoother surface increases in roughness during the early stages of sliding to around the 0.05 µm Ra level. However, the much harder cermet surfaces, 1670 VPN, are not roughened in this manner and the reduction in wear rate as the initial surface roughness decreases can thus continue monotonically down to the lowest level examined - 0.002 µm Ra.

The improvement in performance achieved with the smoothest WC-Co counterface is more easily seen when compared with the best result for 440C stainless steel on the same scale (Fig 6). This marked reduction in liner wear when sliding against a very smooth hard

surface was further confirmed by using a single crystal alumina counterface: 0.002 µm Ra. VPN = 2080. The results of two experiments are shown in Figure 7. The surface of the alumina was not damaged in any way and its roughness remained at the initial level, 0.002 µm Ra throughout. In one of these experiments water was introduced as a contaminant after a long period of dry sliding and Figure 7 shows that this leads to a considerable increase in the wear rate. On returning to dry conditions the rate of wear decreases to its original, lower value. In both these experiments against smooth alumina surfaces the friction coefficient was initially 0.04 and gradually increased to a value between 0.06 and 0.07, i.e. the trend was virtually identical to that on the WC cermet of comparable roughness (Figure 5).

### 5.2 Type of Liner

A comparison of the wear of liners L and D, against a very smooth WC-Co counterface (0.002 µm Ra), is presented in Figure 8. The specific wear rates are given in Table 3. Both liners have similar low wear rates and friction levels. Because liner D does not contain glass and is thus unlikely to produce significant damage on 440C stainless steel, it was therefore considered of interest to see whether the wear rate of this liner was also low when mated against very smooth (0.004 µm Ra) steel. Curve 3 in Figure 8 shows that this is indeed so. Only a few, light scratches were produced on the steel and these led to only a small increase in surface roughness (from 0.004 to 0.006 µm Ra). Although the steady-state wear rate is not as low as that against the cermet surface, it is still the lowest wear rate which has ever been observed for any liner sliding against a 440C steel counterface.

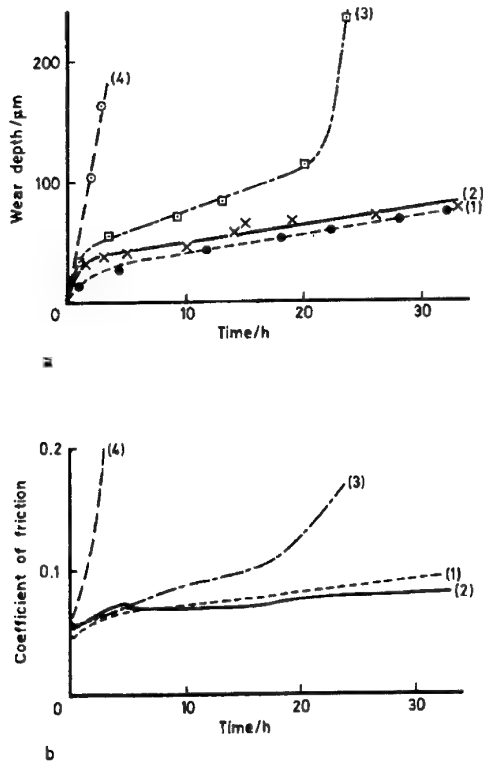


Figure 4 Variation of wear depth (a) and coefficient of friction (b) during sliding on hardened 440C steel of initial roughness (1) 0.02  $\mu\text{m}$  Ra, (2) 0.05  $\mu\text{m}$  Ra, (3) 0.10  $\mu\text{m}$  Ra, (4) 0.14  $\mu\text{m}$  Ra.

### 5.3 Influence of Surface Glass Content on Wear

It follows from the results above that that the surface glass content in a liner is likely to be a major factor influencing counterface damage during sliding and, in turn, the rate of liner wear. Further experiments were therefore carried out in which the glass content was varied in liners shown in Fig 1a. The wear of the four liners K, L, L1 and L2 was determined during sliding against very smooth WC-Co counterfaces. The results are given in Figure 9 and Table 3. Again the wear is low compared to results for liners against stainless steel of conventional surface roughness. Liner L, with 6% surface glass, gives the lowest steady-state wear rate and this liner, together with K, also has the lowest friction level. The higher initial wear and variable friction of liner L1 can not be explained. The poor performance of liner L2 however, could well be due to some form of 'lubricant starvation' i.e. insufficient PTFE can be mobilised at the interface to prevent a significant proportion of glass-cermet interactions.

### 5.4 Other, Hard Smooth Counterfaces

Figure 10 shows the results of a series of experiments in which the friction and wear of liner L was determined against other hard surfaces. These counterfaces were all polished to as smooth a surface finish as possible. Roughness values approaching those achieved with the WC-Co and alumina were obtained for the nitrided and borided 440C steel (Table 4) and the wear rates against these counterfaces are about half the lowest values obtained with untreated, hardened 440C.

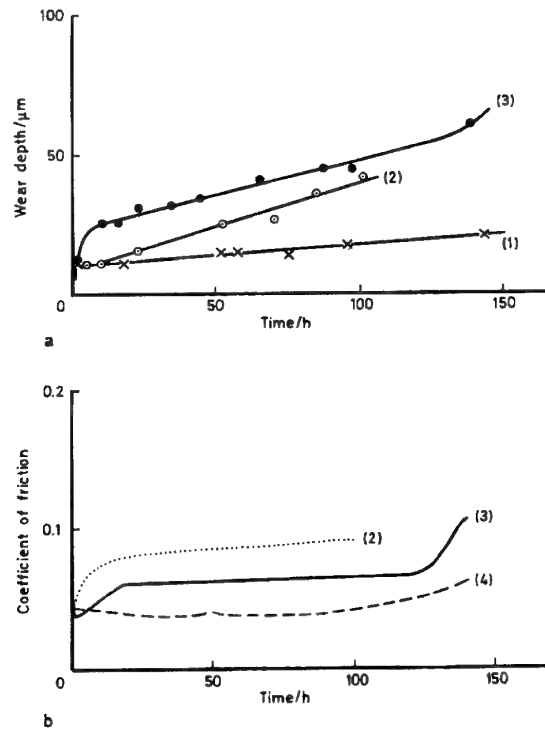


Figure 5 Variation of wear depth (a) and coefficient of friction (b) for Liner L sliding against WC-Co cermet of initial roughness (1) 0.002  $\mu\text{m}$  Ra, (2) 0.016  $\mu\text{m}$  Ra, (3) 0.076  $\mu\text{m}$  Ra

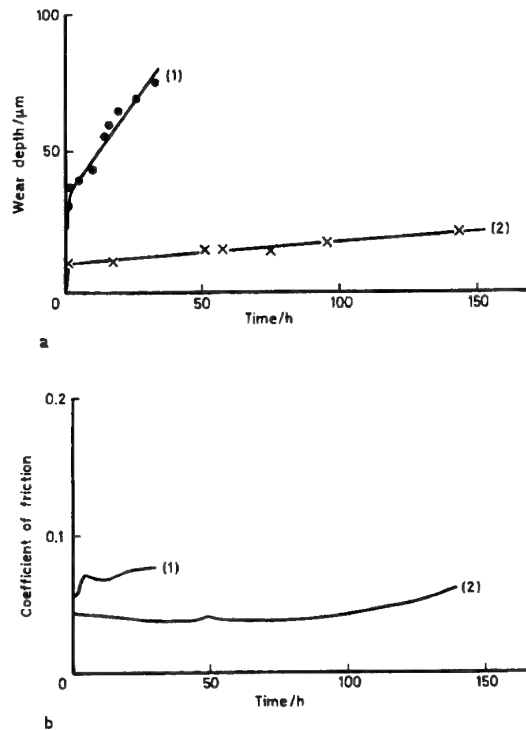


Figure 6 Variation of wear depth (a) and coefficient of friction (b) for Liner L sliding against (1) hardened 440C steel: 0.02  $\mu\text{m}$  Ra and (2) WC-Co cermet: 0.002  $\mu\text{m}$  Ra

	Counterface			Liner Type (% glass)	Linear specific wear rate (mm <sup>3</sup> N <sup>-1</sup> m <sup>-1</sup> )	Counterface temperature during steady wear (°C)
	Material	Hardness (VPN)	Initial and Final Roughness (μm Ra)			
I	440C Steel	780	0.004/0.006	D-Chopped PTFE Fiber (Fig 1b)	17 x 10 <sup>-9</sup>	45-65
	WC-Co cermet	1670	0.002	"	3.1 x 10 <sup>-9</sup>	47-52
J	WC-Co cermet	1670	0.003	Woven PTFE (Fig 1a)	15 x 10 <sup>-9</sup>	45-50
	"	"	0.002	K 0%	7.3 x 10 <sup>-9</sup>	50-70
	"	"	0.002	L1 3%	5.2 x 10 <sup>-9</sup>	47-52
	"	"	0.002	L 6%	110 x 10 <sup>-9</sup>	50-85
	"	"	0.003	L2 12%		

Table 3 - Specific wear rates for various liners against smooth counterfaces

The physical vapour deposited titanium nitride coating could not be prepared to a roughness lower than 0.036 μm Ra. The as-received specimen surface contained both pits and protruding 'spikes' and although diamond polishing eliminated most of the latter, the limited coating thickness, 4 μm, did not permit complete obliteration of the original topography. Although one would not expect the pits to play any significant role in the wear of the liner, the wear rate against this surface was nevertheless some 50 times higher than that against the smooth cermet or alumina. After 20 hours sliding the counterface roughness had increased greatly to around 0.6 μm Ra. In comparison with experiments on other surfaces, the coefficient of friction against TiN was also abnormally high (0.09-0.11).

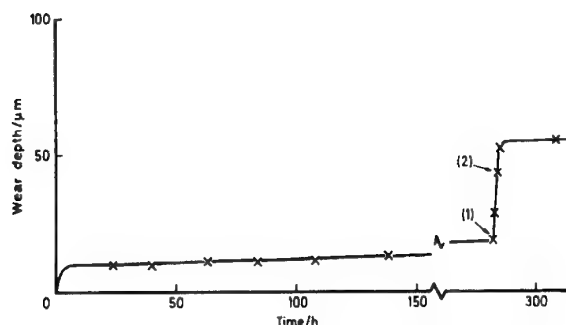


Figure 7 Variation of wear depth during sliding against an alumina single crystal (0.002 μm Ra) under dry conditions and immersed in water between points (1) and (2).

## 6 EVALUATION AND DISCUSSION

The criterion of failure in most dry-bearing applications is unacceptable backlash and therefore the depth of liner wear is the most relevant parameter. The depth which can be tolerated in practise may vary from 0.02 to 0.2 mm, depending on the application, and both the initial wear depth and the rate of steady-state wear are important. The initial wear of composite bearing liners depends primarily on their structure (4) and in particular on the type of reinforcing fiber. The present work shows that counterface roughness can also be very important and this is consistent with work on other types of composites (7). In contrast, the steady-state wear rate of composite liners has been found to be more

dependent on composition than on structure, and particularly on the PTFE content (8). The interpretation previously given has been that the low friction and wear during the linear, steady-state period is associated with the formation of transfer films on the counterface and third-body films on the liner. The presence of these films is believed to reduce wear by reducing the effective roughness of the counterface, thus lowering the localised contact stresses, and to reduce friction by ensuring that the majority of localised contacts involve PTFE-covered asperities. At roughness levels around 0.02 μm Ra however, some ambiguity arises and there have been reports (9-12) of increased polymer wear against very smooth surfaces. No really satisfactory explanation has ever been given to account for this increase, although one suggestion (10) has been that it might be attributed to an increased real contact area, associated with very smooth surfaces, which leads to the removal and transfer of relatively large 'lumps'. It is very clear in the present work, with PTFE composite liners under relatively high loads, that there is no such increase in wear rate against very smooth surfaces. It was therefore considered of interest to examine in some detail what changes occurred to the wear surfaces after sliding against hard, smooth counterfaces.

As a basis for comparison, Figure 11 shows the appearance of the wear track on WC-Co of 0.076 μm Ra of similar roughness to that expected for 440C counterfaces in service. The scratches are filled with PTFE and the relatively flat, bright areas between scratches appear to be partially, and sometimes wholly, covered with PTFE. The corresponding liner shows the tops of the PTFE strands worn down and a film of debris covers both glass and PTFE fibers and also, to some extent, the square-shaped phenolic lands between the strands. In contrast, on very smooth WC-Co surfaces, 0.002 μm Ra, no scratches could be seen and there was little transfer except for occasional patches or streaks of very thin PTFE films. In a few areas, very light wear of the cermet was visible - Figure 12 - and appeared to result from the 'plucking out' of tungsten carbide particles. On the liner surface, there is no obvious third-body film in contrast to the results obtained against rougher counterfaces.

The smooth, single crystal alumina counterfaces nearing the ultimate that can be achieved in terms of uniformity of composition and topography. As on the smooth cermet, occasional patches of transferred very thin PTFE film could be observed and Figure 13 shows an example. On the liner surface, after wear against the alumina, there is little or no formation of a third-body film - Figure 13b - and this result is again similar

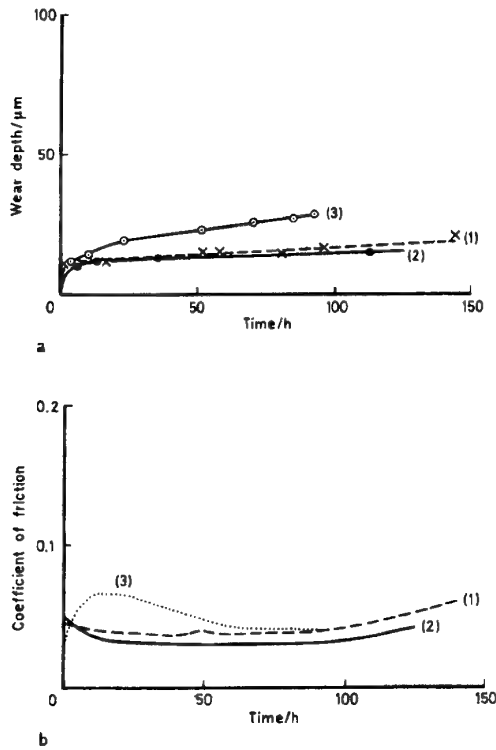


Figure 8 Variation of wear depth (a) and coefficient of friction (b) during sliding against WC-Co cermet of initial roughness 0.002  $\mu\text{m}$  Ra, (1) Liner L, (2) Liner D and (3) Liner D against 440C steel 0.004  $\mu\text{m}$  Ra

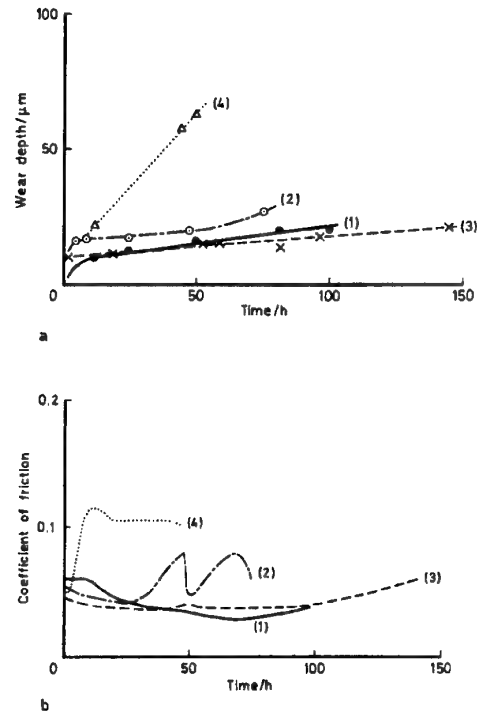


Figure 10 Variation of wear depth (a) and coefficient of friction (b) for Liner L against (1) nitrided 440C steel, (2) borided 440C steel, (3) physical vapour deposited titanium nitride, and (4) hardened 440C steel.

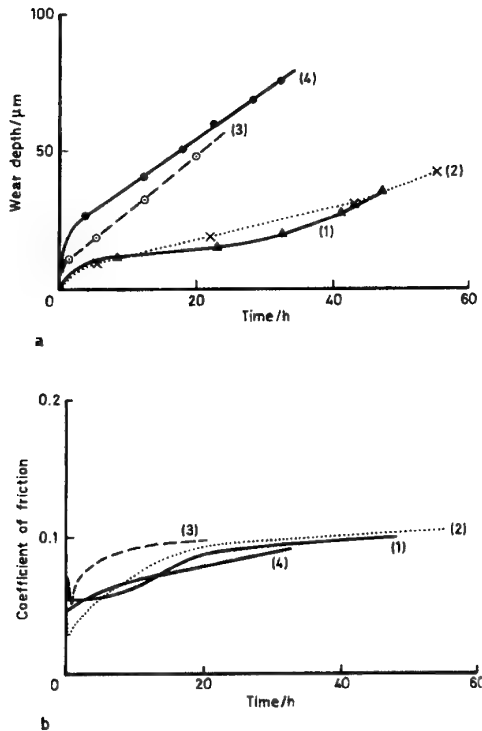


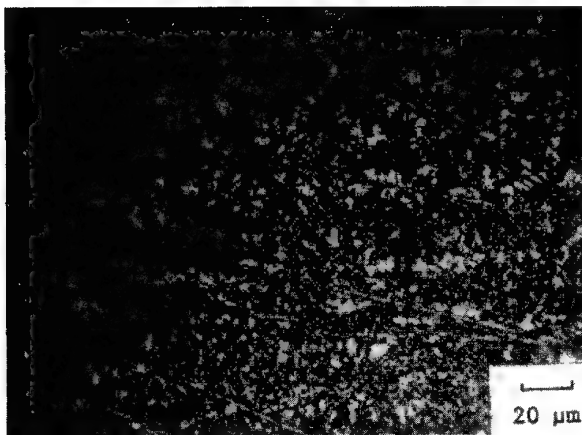
Figure 9 Variation of wear depth (a) and coefficient of friction (b) for Liner L sliding against (1) hardened 440C steel - 0.02  $\mu\text{m}$  Ra, and (2) WC-Co cermet - 0.002  $\mu\text{m}$  Ra

to that obtained against the smooth WC-Co. The essential feature thus emerging is that against very smooth counterfaces low liner wear is associated with greatly reduced transfer film formation and third-body debris films on the liner itself. At first this seems contrary to the conventional wisdom developed for rougher surfaces where consolidated PTFE debris produces smoother surfaces, reduces contact stresses and thus reduces wear. However, the extremely low friction obtained against smooth, hard counterfaces suggests that a oriented PTFE film must still be present on one or both of the surfaces and the results may thus be different from previous work only in scale rather than in kind. Since SEM examination cannot reveal the presence of this PTFE film directly, further work is needed to provide positive identification e.g. by ESCA or Auger analysis. The absence of any 'lumpy' transfer of PTFE, as observed in previous studies on monolithic materials (13), may well be due to the fact that in this case gross extrusion of the PTFE is prevented because of its fibrous nature within a complex composite structure and because of the much higher loads involved (14).

The deleterious effects of fluid contamination on the wear of composite dry bearing liners are now well known (15), and two main reasons have been proposed. Firstly, the fluid disrupts the transfer and third-body films exposing the underlying, rougher topography and secondly the fluid may penetrate into cracks within the composite structure, facilitating disruption via hydrostatic stresses. However, the relative importance of these two processes has not been established. The present results, obtained when adding water to a very smooth alumina counterface - Figure 7 - support the idea that the hydrostatic effect

	Counterface					Linear specific wear rate (mm <sup>3</sup> N <sup>-1</sup> m <sup>-1</sup> )	Counterface temperature during steady wear (°C)
	Material	Hardness (VPN)	Initial Roughness (μm Ra)	Final Roughness (μm Ra)			
				with PTFE	without PTFE		
J	Single crystal alumina	2080	0.002	-	0.002	3.2 x 10 <sup>-9</sup>	50-60
	Nitrided 440C	1140	0.004	0.018	0.011	49 x 10 <sup>-9</sup>	68-73
	Borided 440C	940	0.005	0.139	0.163	59 x 10 <sup>-9</sup>	70-75
	Physical vapour deposited TiN	~2100	0.036	0.7-0.9	0.6	190 x 10 <sup>-9</sup>	60-76

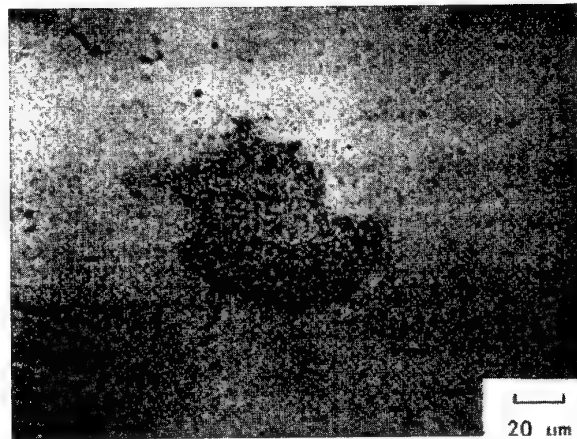
Table 4 - Specific wear rates of liner L against other hard composites

Figure 11 Wear track with PTFE transfer film on WC-Co counterface after 23 hours testing. Initial roughness  $0.076\mu\text{m}$ 

is the most important. Although very thin PTFE films may well be present during dry sliding, the underlying counterface surface is extremely smooth and it does not seem plausible to envisage that the disruption of these films in water could lead directly to such marked increases in wear as observed. Regrettably, therefore, the use of a hard, smooth counterface does not provide a solution to the fluid-contamination problem. The only practical possibility remaining is to prevent the fluid from reaching the contact surfaces by some form of sealing arrangement.

Figure 14 summarises all the experimental results for liner L and clearly shows the substantial reductions in wear rate below that found with 440C that can be achieved with ceramics and cermets as their counterface roughness is decreased. The poor performance of the titanium nitride coating is somewhat surprising considering its notable success in improving the wear lives of drills and extrusion dies. However, these applications do not require the maintenance of such perfection in surface finish as required in PTFE bearings. It may well be that PVD TiN coatings can microcrack during diamond polishing or under the severe asperity forces present during the wear process and even a small number of TiN wear particles released would score the remaining coating. Figure 15 shows a selection of the previous wear measurements replotted against the counterface hardness. The data points relate to an approximately constant initial roughness, except for those substrates

softer than 800 VPN which are, in any case, damaged during sliding. There is a general increase in the composite wear rate as the counterface hardness decreases. It seems reasonable to assume that the wear rate will not be substantially reduced further by using even harder materials than the alumina because this counterface remains essentially unaffected by the liner. At the other extreme for counterfaces of hardness in the range 200-600 VPN, specific wear rates between  $10^{-6}$  and  $10^{-7} \text{mm}^3\text{N}^{-1}\text{m}^{-1}$  are very common (6). The hardness-wear relationship is therefore essentially S-shaped in form, as shown, with the major effects of counterface hardness on wear lying within the range 1000 to 1600 VPN for these types of liners. For composite liners which do not contain glass fibers, a similar curve would be expected but displaced towards lower hardness values. A dry bearing assembly utilising some of the ideas described above is now available as a commercial product and is undergoing trials.

Figure 12 Light wear of a WC-Co counterface after 143 hours sliding (initially  $0.002\mu\text{m Ra}$ )

## 7 CONCLUSIONS

- Accelerated wear tests have shown that very hard, very smooth counterfaces can lead to significant reductions in the wear of composite dry bearing liners compared to the levels presently achieved. Alumina and a WC-Co cermet at a roughness of  $0.002 \mu\text{m Ra}$  give wear rates 10 to

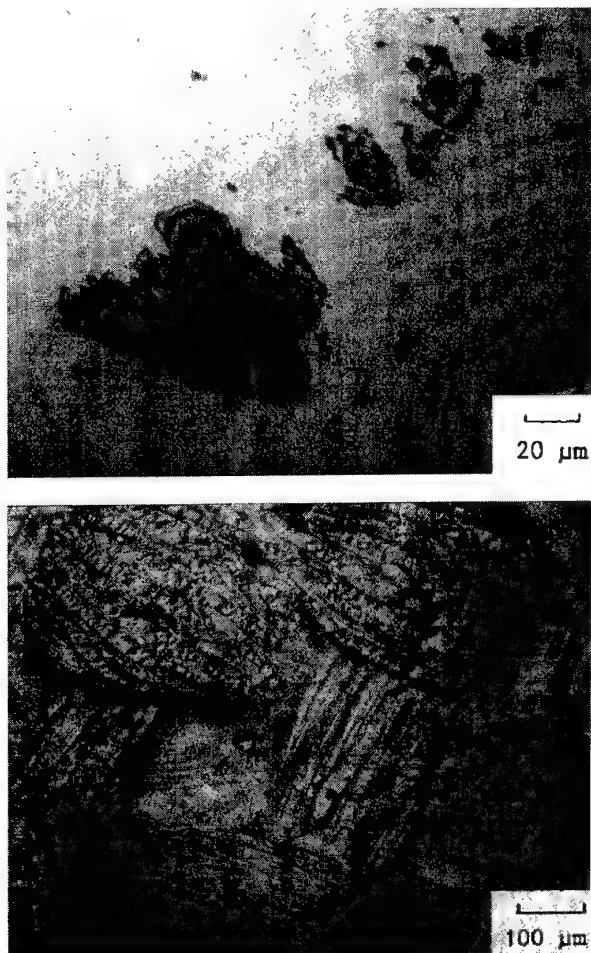


Figure 13 (a) Patches of PTFE transfer film on a single crystal alumina counterface (initial roughness 0.002μm Ra), (b) Liner L after 23 hours sliding against counterface in (a).

100 times lower than those obtained against the conventionally-used 440C stainless steel. If confirmed during full scale bearing trials, this development could lead to the most significant increase in dry bearing performance since composite liners were invented more than 40 years ago (16).

- ii. The reductions in liner wear against smooth, hard counterfaces do not result from any obvious change in the mechanism of wear, but primarily from the fact that transfer and third-body films become extremely thin and smooth. Because hard surfaces cannot be damaged by the constituents of the liner, the initial smoothness of the counterface is maintained.
- iii. The presence of water greatly increases the rate of liner wear even when sliding against a very smooth, hard counterface. This suggests that disruption of the liner via hydrostatic stresses within cracks is the primary factor responsible for the deleterious effects of fluid contamination on wear.

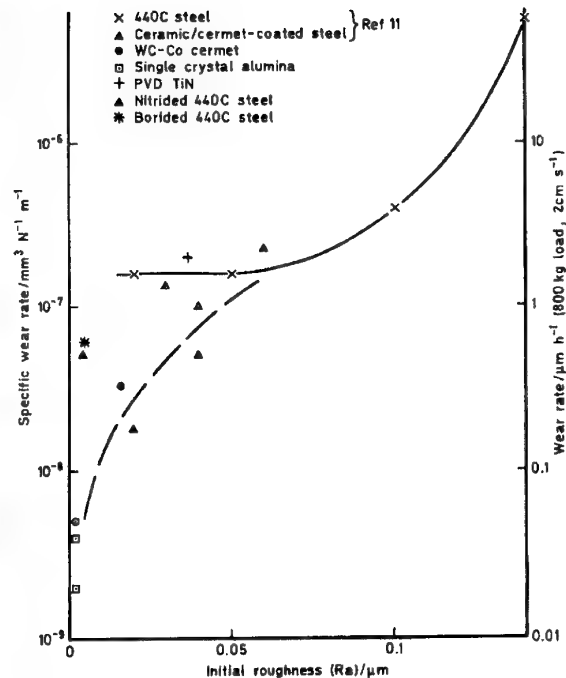


Figure 14 Variation of specific wear of Liner L with initial roughness of the counterface.

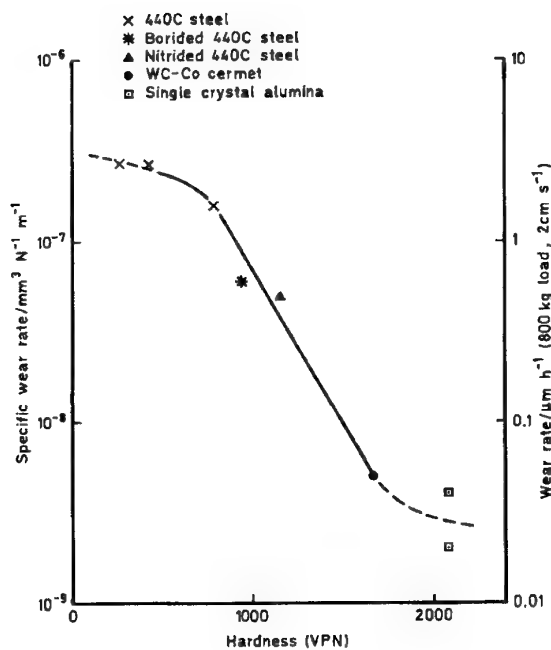


Figure 15 Variation of specific wear with counterface hardness.



# REFERENCES

1. J.K. Lancaster, Trib.Int., 12 (1979) 65
2. J.K. Lancaster, R.W. Bramham, M. Godet, D. Play and R. Waghorne, J. Lub.Tech. (Trans. ASME), 104 (1982) 559.
3. R.W. Bramham, R.B. King and J.K. Lancaster, ASLE Trans., 24 (1981) 479.
4. J.K. Lancaster, In R.G. Bayer (ed) Selection and use of wear tests for coatings, ASTM ST 769(1982)92.
5. A.B. Birkett and J.K. Lancaster, In Proc. JSLE Int Lubrication Conf., Tokyo, 1985, 465
6. MIL-B-81819 Specification. Bearings, plain, self-lubricating, self-aligning, high speed oscillation. MIL-B-81820 Specification. Bearings, plain, self-lubricating, self-aligning, low speed oscillation.
7. J.K. Lancaster, In Proc. 3rd Leeds-Lyon Symposium on Tribology MEP, 1978, 33
8. J.K. Lancaster, D. Play and M. Godet, J.Lub.Tech. (Trans. ASME) 102 (1980) 236.
9. R.B. Lewis, In J.V. Schmitz and W.E. Brown (eds) Testing of Polymers, Vol.3, Interscience, 1967.
10. D. Dowson, J.M. Challen, K. Holmes and Atkinson, In Proc. 3rd Leeds-Lyon Symposium on Tribology MEP, 1978, 99.
11. K. Tanaka and T. Nagai, In K.C. Ludema (ed) Wear of Materials, ASME, Vancouver, 1976 397.
12. K. Tanaka, S. Veda and T. Nagai, In Ann.Meeting JSLE, Tokyo, 1985, 177.
13. C.M. Pooley and D. Tabor, Proc.Roy.Soc., A329 (1972) 251.
14. B.C. Arkles and W.R. Peterson, In L.H. Lee (ed) Adv in Polymer Friction and Wear, Plenum Press, New York, 1974, 453.
15. F.J. Williams, Rockwell Int. Report TFD-75-1362, Los Angeles, 1975.
16. C. White, UK Patent 845, 547 (1956).

© British Crown Copyright 1996 /DERA

Published with permission of the controller of Her Britannic Majesty's Stationery Office

# ANALYSIS OF FRETTING AND FRETTING CORROSION IN AIRFRAME RIVETED CONNECTIONS

K. Iyer, M. Xue, P. C. Bastias, C. A. Rubin and G. T. Hahn

Department of Mechanical Engineering  
Box 1592, Station B  
Vanderbilt University  
Nashville, TN 37235  
United States

## SUMMARY

This paper examines the contributions of fretting and fretting corrosion to the deterioration of one-rivet row lap joints under cyclic loading. Two- and three-dimensional, finite element models of the riveted lap joint are used to define the joint distortion and compliance and to evaluate the mechanical parameters that govern fretting wear and fretting fatigue including the local stresses, cyclic slip amplitudes and corresponding contact pressures at the rivet-panel and panel-panel interfaces. Effects of rivet geometry and plasticity are examined. A piezoelectric fretting wear machine is used to reproduce the relevant contact pressures and slip amplitudes and to measure fretting wear rates for uncoated 2024-T3 and 7075-T6 aluminum sheet in contact with hardened steel and aluminum in relatively dry, laboratory air and 3.5% saline solution. The effects of slip amplitudes in the range  $5\text{ }\mu\text{m}$  to  $35\text{ }\mu\text{m}$  on the specific wear rate and coefficient of friction have been evaluated. Predictions based on the results of the modeling and fretting wear and fretting fatigue criteria are compared with experimental observations of cyclically loaded riveted connections.

## LIST OF SYMBOLS

A	cross sectional area of panel
C	compliance contributed by lap joint $C = C' - C''$
C'	compliance of joined panels. $C = \Delta / P$
C''	compliance of a continuous panel. $C'' = L/(EA)$
E	Young's modulus
F <sub>1</sub>	fretting wear parameter. $F_1 = \mu p \delta$
F <sub>2</sub>	fretting fatigue parameter. $F_2 = \sigma \tau \delta$
f	loading frequency
M	plastic modulus
N	number of fretting cycles
P	applied load
p	contact pressure
V	volume of the wear scar
W <sub>s</sub>	specific wear rate
y	depth of wear scar
$\Delta$	total displacement
$\delta$	slip amplitude; amount of relative movement between the contacting surfaces
$\theta$	standard angular location. 3 o'clock corresponds to $\theta = 0^\circ$ , 12 o'clock to $\theta = 90^\circ$ , 9 o'clock to $\theta = 270^\circ$ , etc. The $\theta = 90^\circ$ direction corresponds with the longitudinal tensile loading direction.
$\mu$	coefficient of friction
$\sigma$	the cyclic stress range parallel to the contacting surfaces
$\Delta\sigma$	cyclic stress range applied to riveted panels
$\sigma_k$	kinematic yield strength
$\tau$	frictional shear stress; $\tau = \mu p$

## 1. INTRODUCTION

Cyclically loaded riveted connections are subject to fretting, i.e., the contacting interfaces experience small, repeated relative rubbing motions. These produce wear and can promote fatigue and corrosion damage that foreshorten the joint life (1-6). The tribological conditions favoring fretting wear are large values of the fretting wear parameter,  $F_1$  (4), and the material specific wear rate,  $W_s$ , which together determine  $y$ , the depth of the wear scar for cyclic loading:

$$y = N (W_s / \mu) F_1 \quad (1)$$

Previous work (6,7) has shown that  $W_s$  depends on the slip amplitude,  $\delta$ , increasing by as much as 500-fold in the range  $\sim 10\text{ }\mu\text{m} < \delta < \sim 100\text{ }\mu\text{m}$ . Fretting wear rates for aluminum against aluminum (8) and steel against steel (9) are heightened by corrosive conditions. Material loss for an age hardened Al-Zn-Mg alloy, fretting with itself, increased by a factor of 4.5x when a wet air environment was substituted for dry air.

According to Vingsbo and coworkers (7,10) and others (11-13), fretting fatigue is favored by "mixed slip and stick" or "partial slip" tribological conditions. Alternatively, Ruiz et al. (14), Kuno et al. (15) and Nowell and Hills (16) have correlated the fatigue crack initiation life with the peak value of the parameter  $F_2$ . Nowell and Hills (16) have shown that the threshold for fretting fatigue crack initiation in an Al-4%Cu alloy is  $F_1 \geq 4.2 \cdot 10^9\text{ Pa}\cdot\text{m}$ . Kuno et al. find rapid crack initiation in hardened 52100 steel when  $F_2 \geq 50 \cdot 10^9\text{ Pa}\cdot\text{m}$  with the site of initiation corresponding with the location of the peak  $F_2$  - value. The slip amplitudes responsible for initiation in these 2 cases are of the order of  $\delta = 1\text{ }\mu\text{m}$ . Synergism between fretting fatigue and corrosion has been reported by Waterhouse (17).

The quantities  $p$ ,  $\delta$ ,  $\sigma$  and  $\tau$ , which govern the values of  $F_1$  and  $F_2$  in riveted connections, are becoming accessible to numerical analysis. Simple, 2-dimensional analyses have been performed by Swenson et al. (18), Hutchinson and coworkers (19,20) and Iyer et al. (21). The calculated variations of  $F_1$  and  $F_2$  inside the rivet hole of the 2 dimensional connection are shown in Fig. 1. More realistic, 3-dimensional finite element analyses have been performed by Sherbourne and Bahaari (22), Weissberg et al. (23), Fung and Smart (24) and by the present authors (25,26). This paper presents results for a simple, one rivet-row lap joint with 3 different rivet shapes and 2 levels of mesh refinement. The results describe the compliance of the connection, the rivet tilt and the local values of the quantities  $p$ ,  $\delta$ ,  $\sigma$  and  $\tau$ , which provide a basis for estimating the fretting parameters  $F_1$  and  $F_2$ .

The contact conditions, comparable to those determined for the lap joint, are reproduced on small laboratory samples with a piezoelectric fretting machine. Values of  $W_s$  for

7075-T6 and 2024-T3 in contact with steel and aluminum in dry air and 3.5% salt solution are derived from profilometer measurements of the wear scar. These findings, taken together with the results of the finite element calculations, are compared with the fretting wear and fatigue damage observed in cyclically loaded, one rivet-row, 7075-T6 lap joints.

## 2. ANALYTICAL AND EXPERIMENTAL PROCEDURES

### 2.1 3D Finite Element Models of a Riveted Lap Joint

The model geometry, shown in Fig. 2a and 2b, consists of two (upper and lower) sheets and a rivet. The overall length of the model is 168.3 mm; the length of the overlap region is 30.6 mm; the width of the panels (repeat distance) is 30.6 mm; the thickness of the panels is 1.53 mm; the rivet shank diameter, head diameter and height are 6.12 mm, 9.792 mm and 3.83 mm, respectively. The mating panel holes have the same diameters and thickness as the rivet shank and countersunk head, i.e., there is no interference or lateral preload. Three rivet geometries: A, B, and C, described in Table 1 are examined. Models A1, B1 and C1 simulate purely elastic material behavior and have a relatively coarse finite element mesh. Model B3 differs from B1 only in that it models elastic linear kinematic hardening plastic (ELKP) behavior [27]. The refined elastic models are denoted as A1R, B1R and C1R.

A cyclic tensile load is applied at the non-overlapping end face of the upper sheet while the corresponding face belonging to the lower sheet is fixed along the x-axis (the stress axes are defined in Fig. 2). Fig. 3 shows the main features of the more refined models used in the present study. In addition, the edges A and B are fixed in the z-direction to prevent unrestrained rotation of the body in space. The geometry shown in Fig. 2a represents one unit of a multi-riveted, single row, long panel extending in the positive and negative y-directions. Lines CD and EF represent the symmetry planes and are constrained against motion in the y-direction. Material properties are defined by the following parameters:  $E = 70$  GPa,  $\sigma_K = 369.9$  MPa, and  $M = 57.5$  GPa, the elastic-plastic parameters used in Model B3. The compliance contributed by the lap joint is defined here as  $C = C' - C''$ . As the load is applied and the rivet tilts, the panels displace, bend and deform around the rivet hole, distortions which are absent in the continuous panel. The joint compliance is related to these factors.

The coarse finite element meshes, features of which are shown in Fig. 3a, typically consist of 1837 nodes, 390 user defined elements and 175 internally generated contact elements. Typical figures for the total number of variables and estimated RMS wavefront are 4554 and 519, respectively. A problem with ABAQUS Version 5.4-1 prevented the modeling of only half of the symmetric plates and rivet. Calculations with elastic material response consumed between 1400s to 6400s of CPU time, depending on the value of the friction coefficient. Elastic-plastic calculations consumed about 12000s (3.3 hours) of CPU time. In all cases, 8 noded, linear brick, incompatible modes elements (C3D8I) defined the bodies. For these elements, in addition to the displacement degrees of freedom, incompatible modes are added internally enabling element shearing without locking. This enhances the models' kinematic response to bending.

A more refined mesh, shown in Fig. 3b, is obtained by doubling the number of elements along the circumferential edges and increasing the number of radial divisions in the overlapping portions of the sheets by 1. The refinement along the depth was not changed. These models consist of 4569 nodes out of which 991 are user defined, 640 user defined elements and 429 internally generated contact elements. Typical figures for the total number of variables

and estimated RMS wavefront are 11332 and 739 respectively. Calculations were performed for rivet types A, B and C, elastic material response and  $\mu = 0.2$ , consuming about 2800s of CPU time. It is suspected that the lower coefficient of friction and the faster convergence due to improved modeling of the contact contributed to lowering the overall CPU time, while the larger size of the model contributed to an increase.

### 2.2 Fretting Wear Measurements

Fretting wear measurements were performed with a unique wear machine which utilizes a stacked, piezoelectric actuator. The actuator moves the specimen thru very small and controllable slip amplitudes relative to a fixed contacting surface. A schematic drawing of the machine is shown in Fig. 4. The machine can accommodate corrosive media at the contacting interface. The contacting surfaces consist of a flat plate which is moved by the piezoelectric actuator against either a hardened 38.1 mm- (1.5 in-) diameter steel hemisphere or a 9.5 mm- (0.375 in-) diameter cylindrical, 2024-T3 aluminum counterface. The normal force between the contacting surfaces is provided by 2 weights (shown schematically in Fig. 4) acting through 2 levers, one in front and one in the rear, with a mechanical advantage of  $\sim 9\times$ . The contact force was calibrated by applying known weights, and measuring the normal force generated, on a Chatillon force gage normal to the mass A. The slip amplitude is regulated by the piezoelectric controller which compensates for hysteresis and drift. The friction force is deduced from the input voltage to the controllers piezoelectric translator. Both the local slip amplitude and the coefficient of friction are deduced from the friction force-nominal slip-hysteresis loop.

Wear and friction measurements were performed on 2.0 mm- (0.080 in-) thick, commercial AA7075-T6 sheet material and 3.08 mm- (0.12 in-) thick AA 2024-T3 sheet in the as received condition. The specimens, 38.1 mm x 17.0 mm rectangular blanks, were hand polished through 600 grit silicon carbide paper. The final polishing direction was parallel to the fretting direction. Specimens were rinsed with acetone before tests. The counterface used was a 38.1 mm-diameter, hardened 52100 ball with a hardness of HRC 62. All tests were conducted at room temperature and a frequency of 5 Hz, either under dry conditions or with the contact region immersed in 3.5% NaCl solution.

The normal force was fixed at  $P = 37.28$  N which yields a peak contact pressure of 407 MPa at the center of a Hertzian, 420  $\mu$ m-diameter contact patch. After each fretting test, a profilometer was used to measure the wear scar along and across the fretting direction. In most cases, the profile of the wear scar on the aluminum sample, immediately after testing, reflects a build-up of material and a volume increase arising from the accumulation of wear debris as shown in Fig. 5. For this reason, the profile was measured a second time after the samples were washed in hot water in an ultrasonic cleaner. While this cleaning usually uncovered a wear scar in the form of a depression in the surface (see Fig. 5), it is not certain that all of the wear debris is removed by the cleaning. Profilometer traces of the wear scar on the steel sphere revealed small amounts of aluminum build up, and essentially no wear. The specific wear rate  $W_s$  is deduced from  $V$ , the volume of the wear scar revealed by the profilometer trace:

$$W_s = V / (2 \cdot \delta \cdot N \cdot P) \dots\dots (2)$$

where  $V$  is the wear volume,  $\delta$  is the slip amplitude.

### 2.3 Tests of Riveted Connections

Cyclic tension tests were performed on one-row/3-rivet lap joints. The connections were fabricated from 1.53 mm- (0.060 in-) thick, and 2.03 mm- (0.080 in-) thick 7075-T6 aluminum sheet with countersunk aluminum rivets installed

7075-T6 and 2024-T3 in contact with steel and aluminum in dry air and 3.5% salt solution are derived from profilometer measurements of the wear scar. These findings, taken together with the results of the finite element calculations, are compared with the fretting wear and fatigue damage observed in cyclically loaded, one rivet-row, 7075-T6 lap joints.

## 2. ANALYTICAL AND EXPERIMENTAL PROCEDURES

### 2.1 3D Finite Element Models of a Riveted Lap Joint

The model geometry, shown in Fig. 2a and 2b, consists of two (upper and lower) sheets and a rivet. The overall length of the model is 306 mm; the length of the overlap region is 30.6 mm; the width of the panels (repeat distance) is 30.6 mm; the thickness of the panels is 1.53 mm; the rivet shank diameter, head diameter and height are 6.12 mm, 9.792 mm and 3.83 mm, respectively. The mating panel holes have the same diameters and thickness as the rivet shank and countersunk head, i.e., there is no interference or lateral preload. Three rivet geometries: A, B, and C, described in Table 1 are examined. Models A1, B1 and C1 simulate purely elastic material behavior and have a relatively coarse finite element mesh. Model B3 differs from B1 only in that it models elastic linear kinematic hardening plastic (ELKP) behavior [27]. The refined elastic models are denoted as A1R, B1R and C1R.

A cyclic tensile load is applied at the non-overlapping end face of the upper sheet while the corresponding face belonging to the lower sheet is fixed along the x-axis (see stress axes in Fig. 2). Fig. 3 shows the main features of the more refined models used in the present study. In addition, the edges A and B are fixed in the z-direction to prevent unrestrained rotation of the body in space. The geometry shown in Fig. 2a represents one unit of a multi-riveted, single row, long panel extending in the positive and negative y-directions. Lines CD and EF represent the symmetry planes and are constrained against motion in the y-direction. Material properties are defined by the following parameters:  $E = 70$  GPa,  $\sigma_k = 369.9$  MPa, and  $M = 57.5$  GPa, the elastic-plastic parameters used in Model B3. The compliance contributed by the lap joint is defined here as  $C = C' - C''$ , where  $C' = 93.4$  m/GN. As the load is applied and the rivet tilts, the panels displace, bend and deform around the rivet hole, distortions which are absent in the continuous panel. The joint compliance is related to these factors.

The coarse finite element meshes, features of which are shown in Fig. 3a, typically consist of 1837 nodes, 390 user defined elements and 175 internally generated contact elements. Typical figures for the total number of variables and estimated RMS wavefront are 4554 and 519, respectively. A problem with ABAQUS Version 5.4-1 prevented the modeling of only half of the symmetric plates and rivet. Calculations with elastic material response consumed between 1400s to 6400s of CPU time, depending on the value of the friction coefficient. Elastic-plastic calculations consumed about 12000s (3.3 hours) of CPU time. In all cases, 8 noded, linear brick, incompatible modes elements (C3D8I) defined the bodies. For these elements, in addition to the displacement degrees of freedom, incompatible modes are added internally enabling element shearing without locking. This enhances the models' kinematic response to bending.

A more refined mesh, shown in Fig. 3b, is obtained by doubling the number of elements along the circumferential edges and increasing the number of radial divisions in the overlapping portions of the sheets by 1. The refinement along the depth was not changed. These models consist of 4569 nodes out of which 991 are user defined, 640 user defined elements and 429 internally generated contact elements. Typical figures for the total number of variables

and estimated RMS wavefront are 11332 and 739 respectively. Calculations were performed for rivet types A, B and C, elastic material response and  $\mu = 0.2$ , consuming about 2800s of CPU time. It is suspected that the lower coefficient of friction and the faster convergence due to improved modeling of the contact contributed to lowering the overall CPU time, while the larger size of the model contributed to an increase.

### 2.2 Fretting Wear Measurements

Fretting wear measurements were performed with a unique wear machine which utilizes a stacked, piezoelectric actuator. The actuator moves the specimen thru very small and controllable slip amplitudes relative to a fixed contacting surface. A schematic drawing of the machine is shown in Fig. 4. The machine can accommodate corrosive media at the contacting interface. The contacting surfaces consist of a flat plate which is moved by the piezoelectric actuator against either a hardened 38.1 mm- (1.5 in.-) diameter steel hemisphere or a 9.5 mm- (0.375 in.-) diameter cylindrical, 2024-T3 aluminum counterface. The normal force between the contacting surfaces is provided by 2 weights (shown schematically in Fig. 4) acting through 2 levers, one in front and one in the rear, with a mechanical advantage of  $\sim 9\times$ . The contact force was calibrated by applying known weights, and measuring the normal force generated, on a Chatillon force gage normal to the mass A. The slip amplitude is regulated by the piezoelectric controller which compensates for hysteresis and drift. The friction force is deduced from the input voltage to the controllers piezoelectric translator. Both the local slip amplitude and the coefficient of friction are deduced from the friction force-nominal slip-hysteresis loop.

Wear and friction measurements were performed on 2.0 mm- (0.080 in.-) thick, commercial AA7075-T6 sheet material and 3.08 mm- (0.12 in.-) thick AA 2024-T3 sheet in the as received condition. The specimens, 38.1 mm x 17.0 mm rectangular blanks, were hand polished through 600 grit silicon carbide paper. The final polishing direction was parallel to the fretting direction. Specimens were rinsed with acetone before tests. The counterface used was a 38.1 mm-diameter, hardened 52100 ball with a hardness of HRC 62. All tests were conducted at room temperature and a frequency of 5 Hz, either under dry conditions or with the contact region immersed in 3.5% NaCl solution.

The normal force was fixed at  $P = 37.28$  N which yields a peak contact pressure of 407 MPa at the center of a Hertzian, 420  $\mu$ m-diameter contact patch. After each fretting test, a profilometer was used to measure the wear scar along and across the fretting direction. In most cases, the profile of the wear scar on the aluminum sample, immediately after testing, reflects a build-up of material and a volume increase arising from the accumulation of wear debris as shown in Fig. 5. For this reason, the profile was measured a second time after the samples were washed in hot water in an ultrasonic cleaner. While this cleaning usually uncovered a wear scar in the form of a depression in the surface (see Fig. 5), it is not certain that all of the wear debris is removed by the cleaning. Profilometer traces of the wear scar on the steel sphere revealed small amounts of aluminum build up, and essentially no wear. The specific wear rate  $W_s$  is deduced from  $V$ , the volume of the wear scar revealed by the profilometer trace:

$$W_s = V / (2 \cdot \delta \cdot N \cdot P) \dots\dots (2)$$

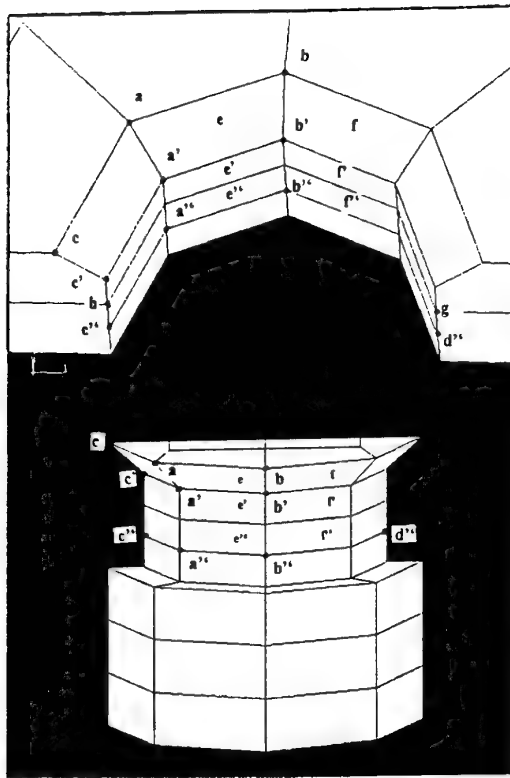
where  $V$  is the wear volume,  $\delta$  is the slip amplitude.

### 2.3 Tests of Riveted Connections

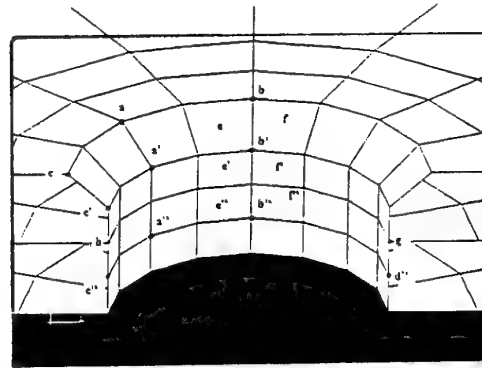
Cyclic tension tests were performed on one-row/3-rivet lap joints. The connections were fabricated from 1.53 mm- (0.060 in.-) thick, and 2.03 mm- (0.080 in.-) thick 7075-T6 aluminum sheet with countersunk aluminum rivets installed

**Table 1.** The finite element models.

Model	Rivet heads	Coefficient of Friction, $\mu$	Mesh	Material Behavior
A1	1 standard, included angle $100^\circ$ 1 countersunk (to $\frac{1}{2}$ panel thickness)	0.2	coarse	elastic
B1	1 standard, included angle $60^\circ$ 1 countersunk (to full panel thickness)	0.2	coarse	elastic
B3	1 standard 1 countersunk (to full panel thickness)	0.2	coarse	ELKP
C1	2 standard	0.2	coarse	elastic
A1R	1 standard, included angle $100^\circ$ 1 countersunk (to $\frac{1}{2}$ panel thickness)	0.2	refined	elastic
B1R	1 standard, included angle $60^\circ$ 1 countersunk (to full panel thickness)	0.2	refined	elastic
C1R	2 standard	0.2	refined	elastic



(a)



(b)

Figure 3. Details of the meshes of Model A1 (see Table 1) showing the rivet and adjacent panel: (a) "coarse" mesh and (b) "fine" mesh. Values of the stresses and slip amplitudes at locations a-h are given in Table 2.

Table 2. Comparison of results from two sets of meshes

MODEL		A1	B1	B3		C1	A1R	B1R	C1R
Feature	Location			Loading	Unloading				
Joint Compliance (m/GN)	—	40.8	32.9	—	—	25.4	34.7	34.2	27.7
Rivet Tilt, degrees	—	3.2	3.3	7.33	3.33	2.6	4.3	4.2	3.0
Total in-plane slip at rivet-panel interface ( $\mu\text{m}$ )	a	62.4	61.2	692.31	638.58	27.7	28.6	29.1	25.0
	a'	89.8	45.2	471.94	442.98	37.0	17.1	31.9	18.2
	a''	-67.5	-61.1	-96.44	-35.54	-67.5	-64.9	-67.9	-67.2
	b	114.4	73.8	725.54	648.92	49.3	64.5	64.7	48.0
	b'	110.3	87.4	877.8	763.7	49.7	75.7	75.7	52.0
	b''	-31.5	-56.5	-111.09	-52.88	-36.4	-67.3	-68.1	-73.0
Total in-plane slip at panel-panel interface ( $\mu\text{m}$ )	g	225.4	184.4	1072.35	852.63	122.1	160.2	176.4	120.7
	h	215.3	201.1	1116.9	874.13	159.3	159.3	166.7	135.8
Total out-of-plane slip ( $\mu\text{m}$ )	c	-50.9	-3.4	-2.58	-12.3	4.37	-1.8	-33.3	-5.4
	c	-30.2	23.5	246.25	235.66	5.85	-8.6	-32.1	0.0
	c''	24.1	21.9	19.3	-0.65	22.83	16.0	10.2	7.0
	d''	0.8	-1.3	-8.48	-2.52	0.3	2.4	0.3	-2.0
Peak tensile stress in elements adjacent to rivet hole (MPa)	e	443.4	407.8	43.8	-166.9	389.0	455.8	392.5	447.7
	e'	370.3	380.3	210.3	-190.6	248.2	700.0	591.1	414.4
	e''	550.9	488.8	352.3	-143.9	545.1	532.6	528.1	505.1
	f	213.9	481.9	107.8	-21.6	191.6	311.8	236.9	341.6
	f'	590.5	589.1	277.9	-206.2	339.5	747.5	697.9	434.6
	f''	330.8	300.0	133.8	-110.8	324.1	419.7	408.4	440.2
Contact Pressure (MPa)	panel-panel	—	—	—	—	—	-79.2	-111.5	-115
	panel-rivet head	—	—	—	—	—	-93.6	-117	-74.9

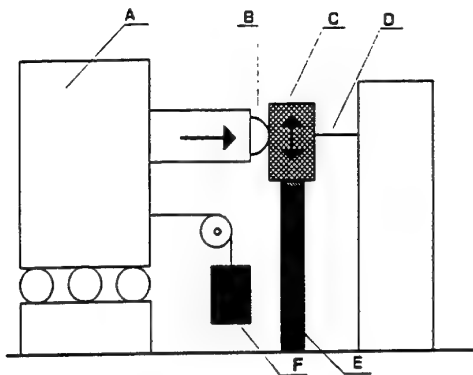


Figure 4. Schematic of piezoelectric fretting wear machine: (A) mass, (B) counterface, (C) sample, (D) leaf spring, (e) piezotranslator and (F) weight.

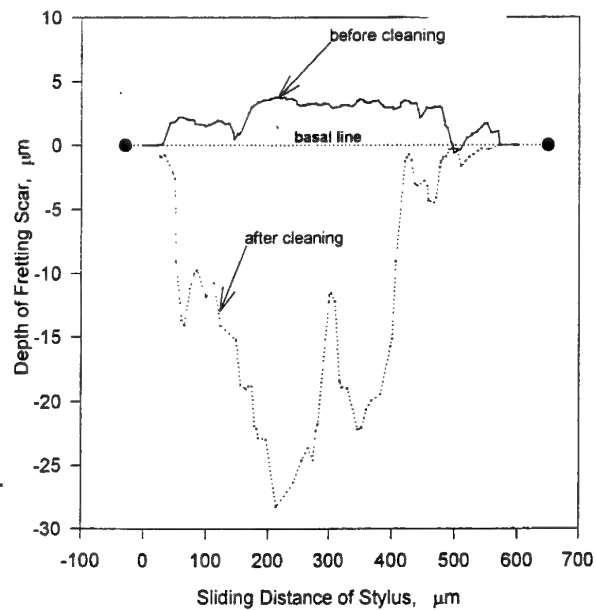


Figure 5. Profilometer measurements of the wear scar produced by  $N = 10^4$  fretting cycles for a hardened 52100 steel sphere against 7075-T6 sheet in air at room temperature for a contact pressure of 407 Mpa. Fretting produces a build-up of debris. Removal of the debris by washing reveals a 25  $\mu\text{m}$ -deep wear scar.

"dry" (without a protective coating). The tests were performed on 204 mm-wide and 91.8 mm-wide panels at nominal cyclic stress ranges,  $\Delta\sigma = 23$  MPa and 106 MPa, respectively, in air with a frequency of 1 Hz. These tests were performed to provide evidence of fretting wear, and determine the role of fretting in the initiation of fatigue cracks. Tests of the 1-row samples were terminated after from  $N = 3000$  to  $N = 10,000$  load cycles to obtain samples showing evidence of fretting wear and with small fatigue cracks that are still intact.

### 3. RESULTS

#### 3.1 3D Finite Element Models of a Lap Joint

Table 2 summarizes the results of the 3-dimensional analyses described above. It refers to locations in the mesh identified in Figs. 3a and 3b. There are significant differences between the results obtained using the coarser and more refined meshes. For example, peak stresses are as much as 50% higher, rivet tilts are 25% higher and slip amplitudes are in most cases 30% smaller for the more refined models. Generally, it is seen that the coarse models under-predict the rivet tilt while they over-predict the slip magnitudes.

Figs. 2c-2e present the displaced meshes for the three cases. Noticeable bending of panels and tilting of rivets produce stress and strain gradients in the thickness direction which are absent in the 2-D representation. Countersinking makes the connection more compliant and increases rivet tilt. Rivet tilt is accompanied by local bending of the panels. The C'-compliance values for the single row, rivet models examined here, between 121 m/GN and 128 m/GN, are about 3x the values reported by Weissberg et al. (23) for a 2-row, bolted joint; these values ranged between 20 m/GN and 65 m/GN.

As shown in Fig. 6a, tensile stresses are higher near the inside panel surfaces, consistent with panel bending. For the countersunk panel this coincides with the thinned section. Peak tensile stresses in the fully countersunk case are highest. The peak stresses vary directly with tilt and bending (see Table 2). The peak stress concentrations in the 3-D models are: 6.0, 5.6 and 4.0 for A1R, B1R and C1R, respectively; the stress concentration obtained from the 2D model is 6.3 (21). The peak tensile stress for the plastically deformed case is 470.0 Mpa. The relative slip at the panel-panel interface produced by plastic deformation during the first loading cycle is 5.7x larger than obtained for elastic deformation at the same load.

Figure 6c shows the locations of peak stresses; the 90°-direction corresponds with the direction of tensile loading. The peak tension in the countersunk panels is observed at  $\theta = 11^\circ$ , and  $\theta = 169^\circ$ ; in the non-countersunk case, the peaks are at  $\theta = 22^\circ$  and  $\theta = 158^\circ$ . The corresponding results for the 2-D model are at  $\theta = 176^\circ$  and  $\theta = 356^\circ$ . Fig. 6b describes the distribution of longitudinal stress acting at the rivet interface. For angular positions close to  $\theta = 270^\circ$ , this approximates the contact pressure at the surface. In contrast with the 2-D representation, where pressures are uniform along the pin and panel thickness direction (direction 3), the contact pressures in the 3-D case is concentrated in the center of the contacting section. These non-uniform distributions lead to peak pressures in the range 1.1 GPa to 1.5 GPa, higher than the  $p = 0.8$  GPa peak value obtained with the 2-D representation (21). For case B3, the high pressures produce a plastic buckling of the rivet head.

#### 3.2 Fretting Wear Measurements

The coefficient of friction between the flat 7075-T6 sheet and the 52100 steel sphere varies directly with slip amplitude, increasing from about  $\mu = 0.25$  to  $\mu = 0.5$  as the slip amplitude increases from  $\delta \sim 5 \mu\text{m}$  to  $\delta \sim 35 \mu\text{m}$ . Micrographs of the wear scars are reproduced in Fig. 7. Energy dispersive spectroscopy (EDS) indicates that the debris consists of both aluminum oxide and iron oxide. The

fretting wear rates increase significantly at the test pressure for slip amplitudes  $\delta > 5 \mu\text{m}$ . Four sets of measured specific wear rate values are summarized in Fig. 8: (i) 7075-T6 in contact with the steel sphere, (ii) 2024-T3 in contact with the steel sphere, (iii) 52100 steel (sphere) in contact with 2024-T3 (flat) and (iv) 2024-T3 in contact with the 2024-T3 cylinder. These show that the specific fretting wear rates are in the range:  $10^{-15} \text{ m}^3/\text{Nm} < W_s < 10^{-13} \text{ m}^3/\text{Nm}$ , for dry contacts and  $10^{-13} \text{ m}^3/\text{Nm} < W_s < 10^{-12} \text{ m}^3/\text{Nm}$ . The specific wear rates tend to be higher for the 2024-T3 alloy and for contact with steel. The result for 2024-T3 against 2024-T3 are similar to the findings of Goto, Ashida and Endo [7] for higher slip amplitudes, e.g.,  $50 \mu\text{m}$  to  $100 \mu\text{m}$  which may represent the remote rather than the local values of the slip amplitudes. The values for contact with steel in the salt environment are 5 x the highest values reported by Endo et al [7]. The corresponding fretting wear rate for the 52100 steel (in contact with 2024-T3) is:  $W_s = 4.0 \times 10^{-15} \text{ m}^3/\text{Nm}$ .

#### 3.3 Tests of Riveted Connections

Figs. 9 and 10 illustrate examples of fretting wear and fretting fatigue observed in 1.53 mm-thick, 1-row/3-rivet samples subjected to cyclic loading in air. Evidence of fretting wear is observed in the middle of the countersunk, rivet-panel interface in the sector  $185^\circ < \theta < -5^\circ$ . Consistent with the location of the peak values of  $F_t$  in Fig. 1a, fretting wear is prominent in 2 sectors:  $185^\circ < \theta < 210^\circ$  and  $5^\circ > \theta > -30^\circ$ , and relatively light in the intermediate sector:  $210^\circ < \theta < 330^\circ$ . Fig. 9b shows examples of fatigue cracks associated with these fretted regions.

Fig. 10 illustrates examples of a second, crescent-shaped region of fretting wear observed at the panel-panel interface on the countersunk panel in the sector:  $190^\circ < \theta < 350^\circ$ . The corresponding sector of the edge of the hole of the contacting panel also shows signs of wear. Radial fatigue cracks emanate from the hole at the edge of the crescent, typically at  $191^\circ < \theta < 195^\circ$  and  $356^\circ < \theta < 351^\circ$ .

### 4. DISCUSSION

In view of the large differences in the results obtained with the coarse and more refined 3-D models examined here, and other evidence, the adequacy of the mesh refinement of models A1R, B1R and C1R is open to question. Interpenetration between the upper sheet and rivet occurred in the coarse mesh due to an excessively coarse representation of each body; this was partly responsible for increasing computation time for the coarse models, and has been eliminated in the more refined meshes. The more refined models have begun to capture gross features such as correlation between rivet tilt and compliance. Stress and slip gradients through the depth have smoothed considerably even though the number of elements along the depth axis remains unchanged. Yet there is further evidence that a convergent solution has not yet been reached; the calculated stress concentration factor continues to increase with mesh refinement.

The stress concentration factor obtained from the 2-D elastic model is about 6.3 [4], in the absence of countersinking and sheet bending. Shivakumar and Newman (28) calculate stress elevation factors of 1.25 each for the two effects. The stress contours in Fig. 6a indicate a total stress elevation of 1.4 from bending and the countersunk hole. However, the clamping effect of the rivet head, which can reduce bending at the location of the peak stresses, is probably not accurately modeled here. Based on these considerations, a peak stress concentration of about 8 to 10 appears likely. The peak value of 10 reported by Fung and Smart (24) may reflect their larger countersink angle and/or more compliant rivet head. The present calculations show that the stress concentration increases with rivet tilt and the severity of countersinking. These observations suggest that even the relatively



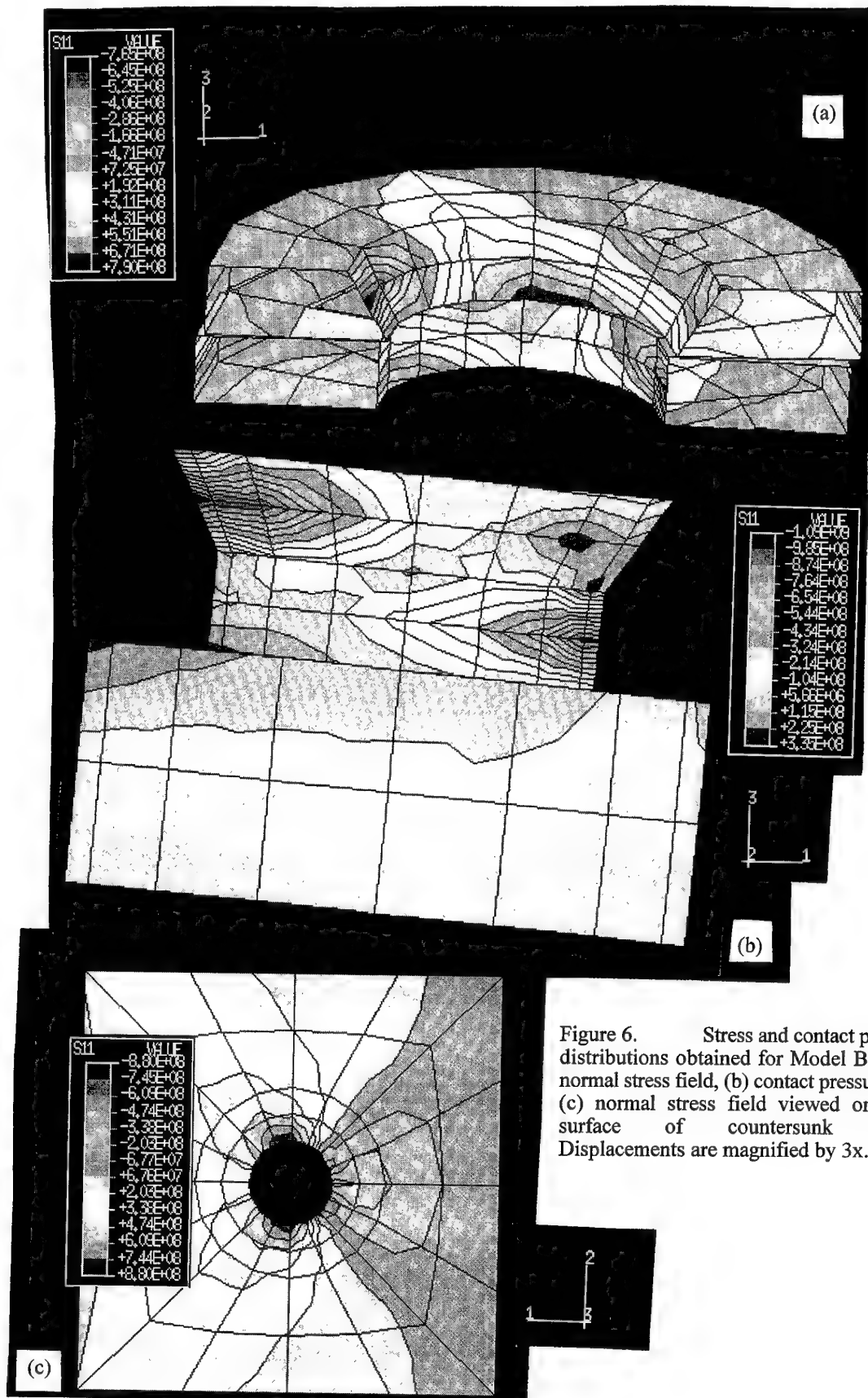


Figure 6. Stress and contact pressure distributions obtained for Model B1R: (a) normal stress field, (b) contact pressure, and (c) normal stress field viewed on inner surface of countersunk panel. Displacements are magnified by 3x.



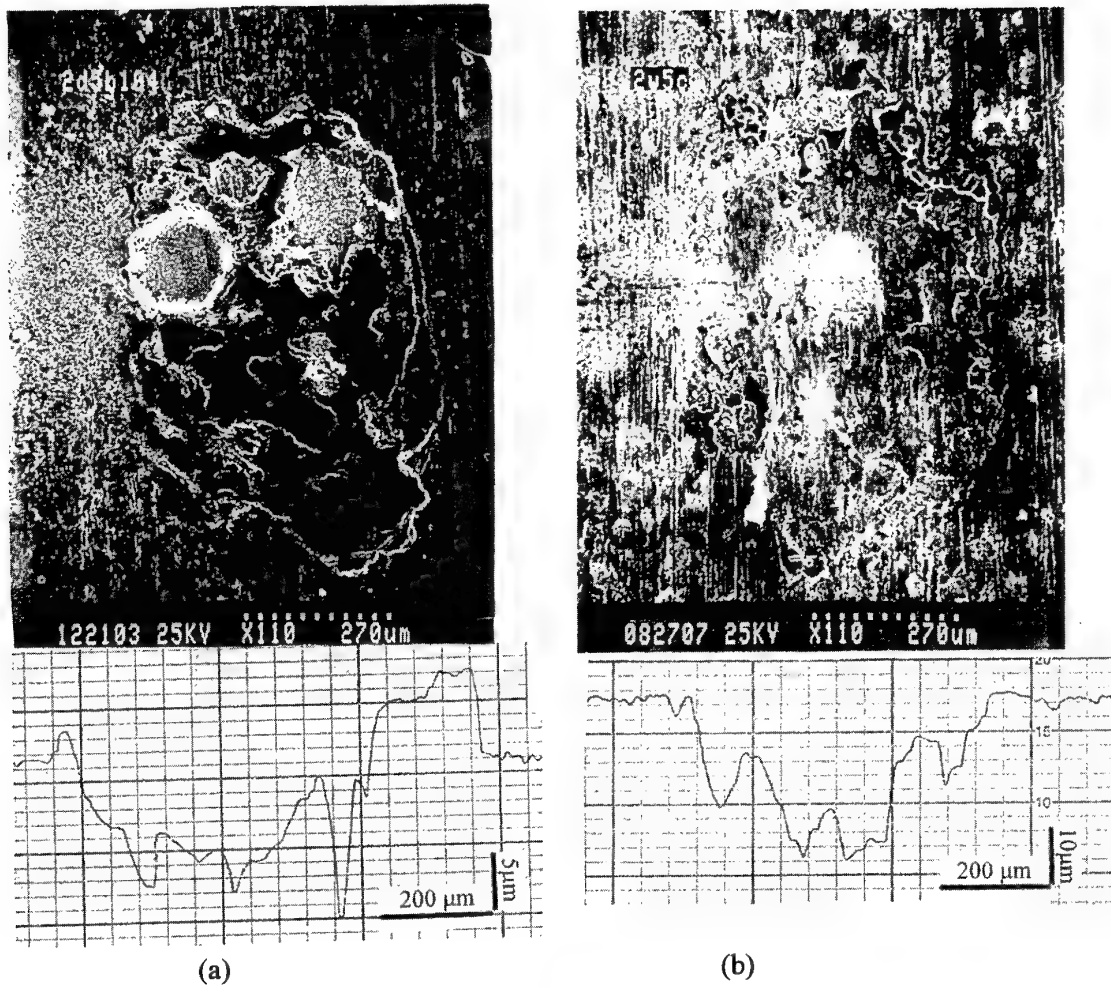


Figure 7. Examples of wear scars and profilometer traces obtained after  $N = 5 \cdot 10^4$  fretting cycles for  $p = 407$  Mpa,  $\delta = 25 \mu\text{m}$  and  $f = 1$  Hz for a hardened, 52100 steel sphere against 2024-T3: (a) dry air,  $W_s = 26.6 \cdot 10^{-15} \text{ m}^3/\text{Nm}$  and (b) saline solution,  $W_s = 275 \cdot 10^{-15} \text{ m}^3/\text{Nm}$ .

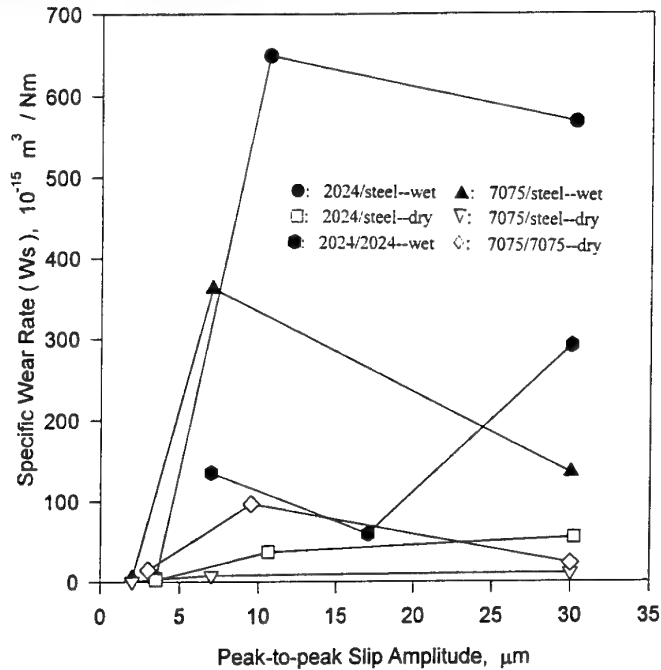
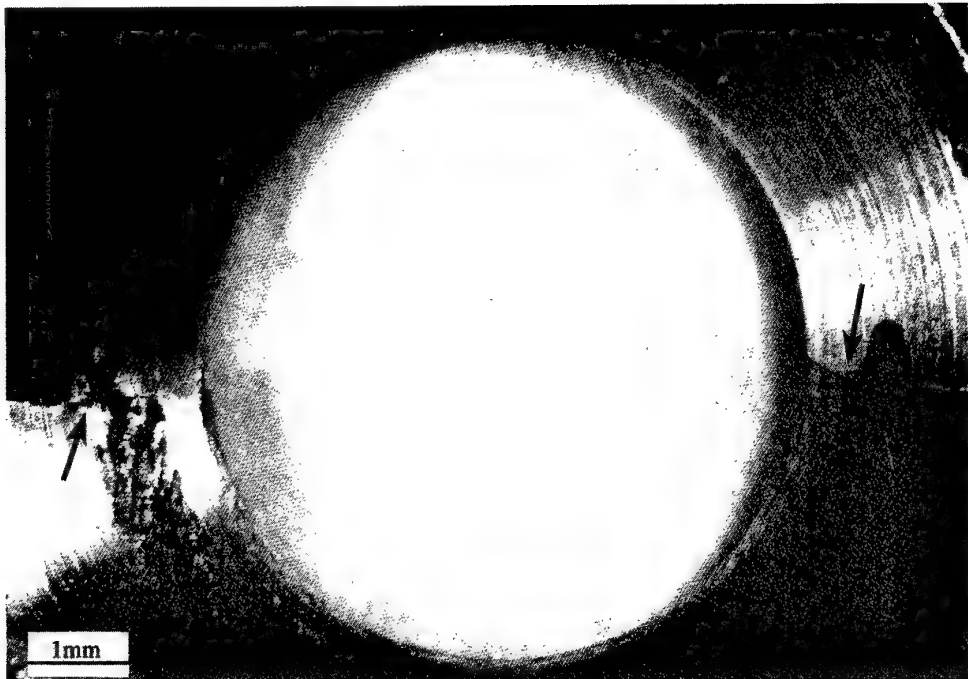
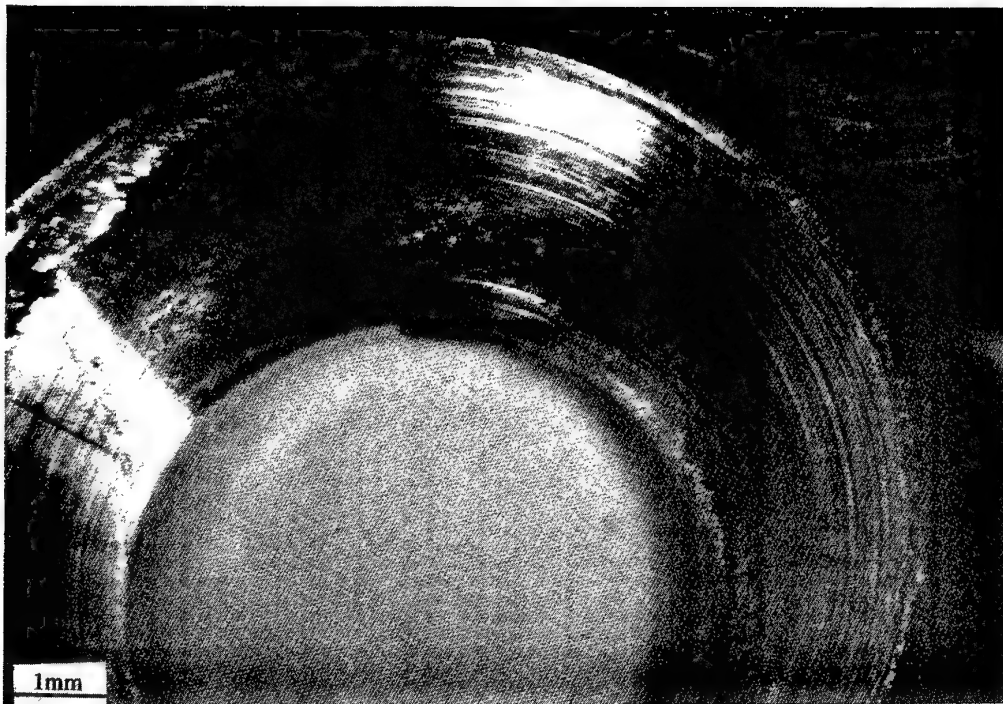


Figure 8. Variation of the specific fretting wear rate,  $W_s$ , with slip amplitude,  $\delta$ , for 2024-T3 and 7075-T6 against itself and 52100 steel in air and in 3.5% salt solution for  $N = 10^4$  fretting cycles,  $f = 1$  Hz and  $p = 407$  Mpa.



(a)



(b)

Figure 9. Fretting damage inside the countersunk hole after  $N = 10^4$  stress cycles at with a stress range of  $\Delta\sigma = 22.8$  MPa and  $R = 0.1$ : (a) 2 fatigue cracks associated with fretting damage, and (b) variation of fretting damage with angular position.

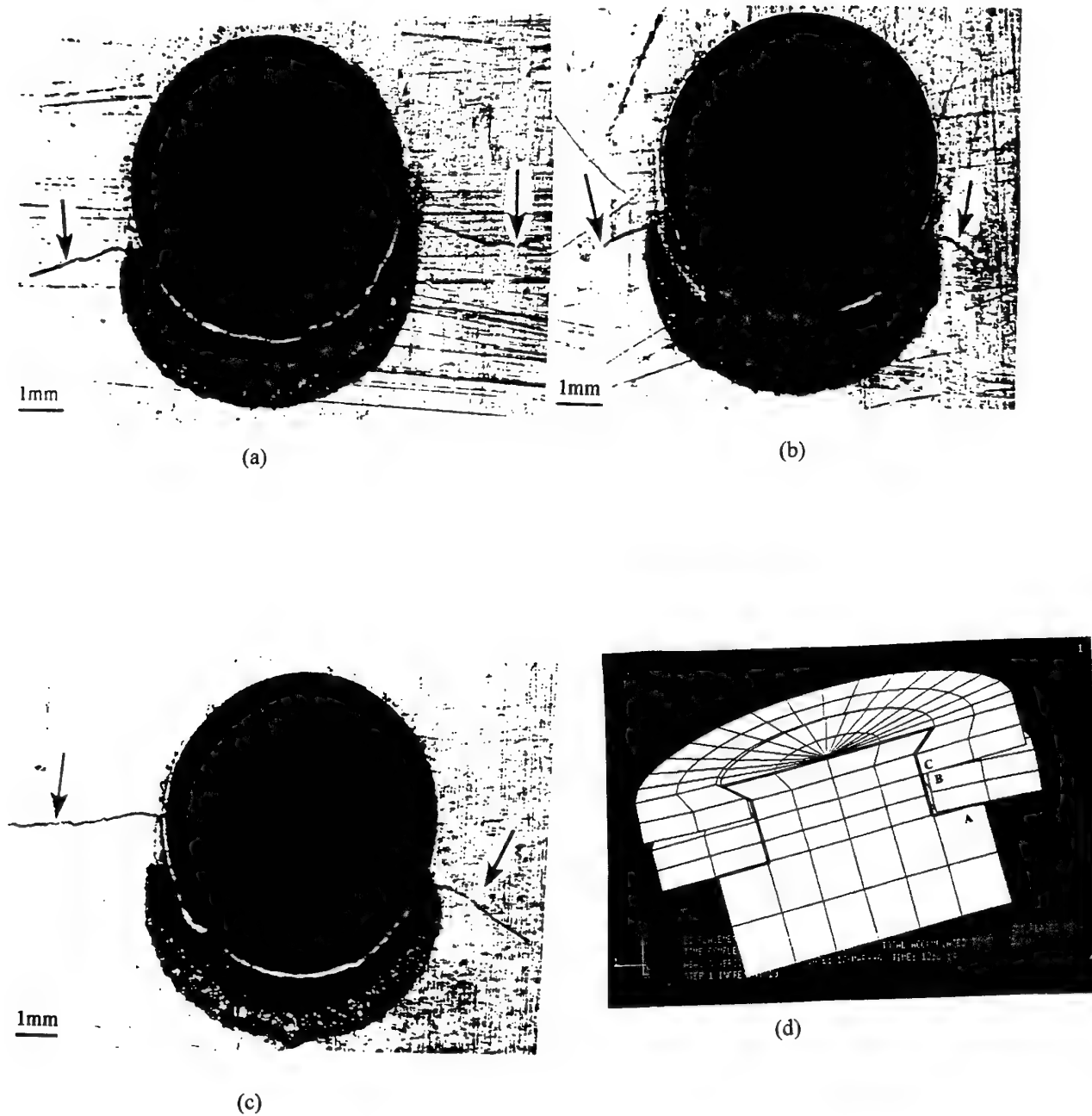


Figure 10. Examples of fretting damage and fatigue cracks produced in a 7075-T6, 3 rivet, single row lap joint nearly identical to finite element Models B1 and B1R and subjected to  $N = 3261$  load cycles with a cyclic stress range,  $\Delta\sigma = 106$  MPa and  $R = 0.1$ : (a-c) are micrographs of the 3 adjacent rivet holes viewed on the inner surface of the countersunk panel which show the location of the fatigue cracks and the "crescent" shaped region of fretting damage, and (d) schematic showing how the tilted rivet head (A) presses the lower panel hole edge against the upper panel to produce the "crescent" fretting damage as the panels slip relative to each other.

refined finite element mesh represents sheets which are excessively stiff in bending. Indications are quite clear that localized mesh refinement around the interfacial region alone is insufficient. Even regions far removed from the interfacial areas are subject to significant bending and should be sufficiently refined in order to transmit the correct response to the interface. The presence of a clamping force on the rivet head will in fact push the region of the sheet, where severe local bending begins, outward from the center of the rivet, accentuating the need for a uniformly refined mesh. Calculations with more refined meshes are currently in progress.

The 3-D calculations also demonstrate that a 2-D model does not offer reliable descriptions of the deformation of a single rivet-row lap joint. The 2-D model cannot provide for countersinking and clamping, and does not account for the effects of rivet tilt and panel bending. It understates slip amplitudes, the peak contact pressures and the peak stress concentration. Panel bending shifts the peak stresses to the interior panel surfaces where fatigue cracks are observed to grow most rapidly. The fact that the peak stresses at that location are higher for the fully countersunk case than for the partially countersunk panel is consistent with experience that fully countersunk installations are inferior.

According to Fig. 1a, the peak value of the fretting wear parameter for the rivet panel interface and  $\mu = 0.2$  is  $F_1 = 2$  kPam. The predicted depths of the wear scar in the rivet hole for  $N = 4 \cdot 10^4$  stress cycles and  $W_s = 10^{-14}$  m<sup>3</sup>/Nm (air) and  $W_s = 2 \cdot 10^{-13}$  m<sup>3</sup>/Nm (corrosive environment) are  $y \sim 2$   $\mu$ m and  $y \sim 40$   $\mu$ m, respectively. It appears from this that fretting wear is not likely to be a serious problem in the rivet hole. However, the corresponding fretting fatigue parameter (for  $\mu = 0.2$ ),  $F_2 \sim 50 \cdot 10^{10}$  kPam, is about 100x larger than the threshold value for fretting fatigue (16). This would account for the crack initiation and significant growth in  $N = 10^4$  stress cycles. It should be noted that results obtained for a 2D model, summarized in Fig. 1, demonstrate that interference is highly effective in reducing the peak values of  $F_1$  and  $F_2$  for in-plane fretting at the rivet panel interface.

Fig. 10d (derived from an even more refined mesh) illustrates that the tilting of the rivet head produces contact pressure on the rivet head-panel interface at A (see Fig. 9d) and on the panel-panel interface at B, close to the edge of the hole in the sector:  $180^\circ < \theta < 360^\circ$ . Fig. 10d shows that this curls the lower panel hole edge forcing a sharp corner against the upper panel hole edge (at C). The pressure applied to the sharp corner can produce contact pressures as high as 3x the material yield strength or  $\sim 200$  Mpa. The contact pressure combined with the relatively large,  $\delta = \sim 200$   $\mu$ m cyclic slip at the panel-panel interface (see Table 2) produces the crescent-shaped fretted region evident just below the rivet hole in Figs. 9a-9c. Under these conditions:  $\mu = 0.35$ ,  $p \sim 100$  Mpa and  $\delta = 100$   $\mu$ m, the value of the fretting wear parameter,  $F_1 \sim 7$  kPam, which exceeds the peak value at the rivet panel interface (Fig. 1a):  $F_1 \sim 2$  kPam. Consistent with this, the fretting wear appears to be more intense in the crescent than at the rivet panel interface. The predicted depths of the wear scar in the crescent for  $N = 4 \cdot 10^4$  stress cycles and  $W_s = 10^{-14}$  m<sup>3</sup>/Nm (air) and  $W_s = 10^{-13}$  m<sup>3</sup>/Nm (corrosive environment) are  $y \sim 16$   $\mu$ m and  $y \sim 160$   $\mu$ m, respectively. It appears from this that fretting wear is not likely to be a serious problem in this location. However, the repeated flexing of the edge of the sheet that accompanies the cyclic tilting of the rivet along with corrosive conditions may promote exfoliation corrosion in the 7075-T6 alloy.

There are 2 indications that fretting is responsible for the fatigue cracks associated with the crescent. First, the cracks originate at angular positions, e.g.,  $\theta = 193^\circ$  and  $\theta = -13^\circ$ , where the cyclic stresses are  $\sim 30\%$  below their peak value,

positions about  $24^\circ$  from the sites of the peak cyclic stress ( $\theta = 169^\circ$  and  $\theta = 11^\circ$ ) and. Secondly, the potential for fretting fatigue (for  $\sigma = 500$ MPa,  $\mu = 0.35$ ,  $p \sim 100$  Mpa and  $\delta = 100$   $\mu$ m) is  $F_2 \sim 175 \cdot 10^{10}$  kPam, which is about 3x the peak value of  $F_2$  at the rivet panel interface (see Fig. 1b) and  $\sim 100$ x the threshold value fretting fatigue (16). The implication is that the fatigue crack originates at the crescent corner because the superposition of the fretting stresses and bulk cyclic stresses produces the peak cyclic stresses at this location.

The results for the 2D-model (see Fig. 1) indicate that 1% interference between the fastener and the hole can reduce the values of  $F_1$  and  $F_2$  generated at the fastener hole by an order of magnitude. The fretting parameters also vary directly with the coefficient of friction. The 3D-model calculations indicate that reductions in rivet tilt and joint compliance will reduce the stress concentration and fretting at the panel-panel interface. The effect of interference and lateral clamping on the fretting conditions in the "crescent" region will be examined with the 3D-models.

## 5. CONCLUSIONS

5.1 Relatively coarse, 3-dimensional, finite element models of a single-row, riveted lap joint reproduces many features and details of the mechanical behavior, including the tilting of the rivets and the local bending of the panels, which are not accessible with 2-dimensional models. However, more refined meshes than the ones employed here are needed to obtain reliable values of the local bending and local stresses and contact pressures.

5.2 The rivet tilt of the single, rivet-row lap joint, the joint compliance, slip amplitudes, panel bending and peak stresses are directly related.

5.3 The peak tensile stress concentration of a single, rivet-row lap joint can be as high as 8 to 10 in the absence of interference, clamping and adhesives.

5.4 Specific fretting wear rates for 7075-T6 and 2024-T3 in contact with 52100 steel, and 2024-T3 in contact with itself, have been measured for contact pressures and slip amplitudes comparable to those generated in the riveted lap joints. The largest specific fretting wear rates observed for dry and wet fretting of 7075-T6 aluminum alloy sheet alloys are  $W_s = 10^{-14}$  m<sup>3</sup>/Nm and  $W_s = 3 \cdot 10^{-13}$  m<sup>3</sup>/Nm. These values, taken together with estimates of the fretting wear parameter,  $F_1$ , indicate that the fretting wear at the rivet-panel interface and panel-panel interface is not likely to be a serious problem for connections subject to  $N \approx 40,000$  stress cycles.

5.5 Fretting wear at the interface between the 2 panels can be a more serious problem when the tilting of the rivet presses the rivet head against the panel at the edge of the hole. The resulting curling of the edge of the hole brings the sharp edge in contact with the surface of the adjacent panel. The contact pressure combined with the relatively large,  $\delta = \sim 200$   $\mu$ m cyclic slip at the panel-panel interface produces the crescent-shaped fretted region evident just below the rivet hole in the countersunk panel. Estimates of the values of  $F_1$  suggest that fretting wear in the crescent may be more severe than that obtained in the countersunk rivet hole.

5.6 Fatigue cracks are associated with both the fretted region in the countersunk rivet hole and the crescent-shaped fretted zone at the panel-panel interface. In the absence of interference, the peak values of the fretting fatigue parameter at the rivet-panel interface are  $F_2 \approx 50 \cdot 10^{10}$  Pa<sup>2</sup>m and  $F_2 \sim 175 \cdot 10^{10}$  Pa<sup>2</sup>m for the rivet hole and crescent-shaped region, respectively. Both of these values are  $\sim 100$ x higher than the threshold value for fretting fatigue. This is consistent with the initiation and growth of fatigue cracks at

these loactions in from  $N = 10^3$  to  $N = 10^4$  stress cycles.

5.7 The results for the 2D-model show that 1% interference between the fastener and the hole can reduce the values of  $F_1$  and  $F_2$  generated at the fastener hole by an order of magnitude. The fretting parameters also vary directly with the coefficient of friction. The 3D-model calculations indicate that reductions in rivet tilt and joint compliance will reduce the stress concentration and fretting at the panel-panel interface.

#### ACKNOWLEDGMENTS

The authors wish to thank J. Veciana and T. Warrion of Textron Aerostructures for supervising the fastener installations. They also wish to acknowledge the contribution of R. Turvaille, who performed some of the cyclic tests. They are grateful for the permission granted by Hibbitt, Karlsson and Sorensen, Inc. for the use of the finite element code ABAQUS. They also wish to thank W. Gentry, J. Hightower and T. Taylor for their assistance with different aspects of the work. This research was supported with a grant from the Air Force Office of Scientific Research (F49620-93-1-0488).

#### REFERENCES

1. Forsyth, P.J.E., "Occurrence of Fretting Fatigue in Practice", Fretting Fatigue, R.B. Waterhouse (ed), Applied Science, London, ISBN 0-85334-932-0, 1981, pp. 99-125.
2. Schijve, J., "Multiple-Site-Damage Fatigue of Riveted Joints", Durability of Metal Aircraft Structures, S.N. Atluri, C.E. Harris, A. Hoggard, N. Miller and S.G. Sampath (eds), Atlanta Technology Publications, ISBN 0-9613474-6-5, 1992, pp. 2-27.
3. Mitchell, T. G., "An Airline View of the Corrosion Problem," Ind. Corr. July 1983, pp. 11-17.
4. Waterhouse, R. B., "Fretting Wear," ASM Metals Handbook, No. 18, 1992, pp. 242-256.
5. Waterhouse, R. B., "Fretting Corrosion," Pergamon Press, New York, 1972.
6. Waterhouse, R. B. "Avoidance of Fretting Fatigue Failures," Fretting Fatigue, pp. 221-240. Ed.R. B. Waterhouse, Applied Science Publishers LTD, (ISBN 0-85334-932-0) London, 1981.
7. Vingsbo, O., and S. Soderberg, "On Fretting Maps," Wear, Vol. 126, 1988, pp. 131-147.
8. Goto, H., Ashida, M. and K. Endo, "The Influence of Oxygen and Water Vapor on the Friction and Wear of an Aluminum Alloy Under fretting Conditions," Wear, Vol. 116, 1987, pp 141-155.
9. Pearson, B. R. and R. B. Waterhouse, "The Fretting Wear of Steel Ropes in Sea Water -- Effect of Cathodic Protection," Wear of Materials, 1985, K. C. Ludema, Ed. ASME.
10. Vingsbo, O., Odvalk, M., and Shen, N.E., "Fretting Maps and Fretting Behavior of Some FCC Metals and Alloys", Wear Materials, K. C. Ludema, Ed., ASME, New York, 1989, pp. 275-282.
11. O'Connor, J.J., "The role of Elastic Stress Analysis in the Interpretation of Fretting Fatigue Failures", Fretting Fatigue, R.B. Waterhouse (ed), Applied Science, London, ISBN 0-85334-932-0, 1981, pp. 23-66.
12. Vincent, L., Berthier, Y., and Godet, M., "Mechanics and Materials in Fretting", Wear, Vol. 153, 1992, 135-148.
13. Zhou, Z.R., Fayeulle, S., and Vincent, L., "Cracking Behavior of Various Aluminum Alloys During Fretting Wear", Wear, Vol. 155, 1992, pp. 317-330.
14. Ruiz, C., Boddington, P.H.B., and Chen, K.C., "An Investigation of Fatigue and Fretting in Dovetail Joints", Exp. Mech., Vol. 24, 1984, pp. 208-217.
15. Kuno, M., Waterhouse, R.B., Norell, D. and Hills, D.A., "Initiation and Growth of Fretting Fatigue Cracks in the Partial Slip Regime", Fatigue Fracture Engineering Materials and Structures, Vol. 12, 1989, pp. 387-398.
16. Novell, D. And Hills, D.A., "Crack Initiation Criteria in Fretting Fatigue", Wear, Vol. 136, 1990, pp. 329-343.
17. Waterhouse, R. B., "Fretting Fatigue," Inter. Materials Reviews, Vol. 37, No. 2, 1992, pp. 77-97.
18. Swenson, D.V., Gondhalekar, S. R., Dawicke, D. S., "Analytical Developments in Support of the NASA Aging Aircraft Program with an Application to Crack Growth from Rivets", (ISSN 0148-7191), SAE General, Corporate and Regional Aviation Meet'g and Expo. Wichita, Kansas, 1993.
19. Beuth, J. L., and Hutchinson, J. W., "Fracture Analysis of Multi-site Cracking in Fuselage Lap joints," Computational Mechanics, Vol. 13, 1994, pp. 315-331.
20. Nilsson, K. F. and Hutchinson, J. W., "Interaction Between a Major Crack and Small Crack Damage in Aircraft Sheet Material," Int. J. of Solids and Structures, Vol 31, 1994, pp. 2331-2346.
21. K. Iyer, G. T. Hahn, P. C. Bastias and C. A. Rubin, "Analysis of Fretting Conditions in Pinned Connections," Wear, Vol 181-183, 1995, pp. 524-530.
22. A. N. Sherbourne and M. R. Bahaari, "3D Simulation of End-Plate Bolted Connections," J. Structural Eng. Vol 120, 1994, pp. 3122-3136.
23. V. Weissberg, K. Wander and R. Itzhakov, "A New Approach to Load Transfer in Bolted Joints," Proc. Int. Council of Aeronautical Sciences, Vol.1, 1988, pp. 96-101.
24. C. P. Fung and J. Smart, "An Experimental and Numerical Analysis of Riveted Single Lap Joints," Proc. Inst. Mech. Eng., Part g, J. Aerospace Eng., Vol 208, 1994, pp. 79-90.
25. K. Iyer, M. Xue, R. Kasinaduhni, P. C. Bastias, C. Rubin, J. J. Wert and G. T. Hahn, "Contribution of Fretting to the Fatigue and Corrosive Deterioration of a Riveted Lap Joint," Proc. Symp. Structural Integrity in Aging Aircraft, San Francisco, Nov. 15, 1995.
26. Iyer, K., Bastias, P. C., Rubin, C. A., and Hahn, G. T., "Local Stresses and Distortions of a Three-Dimensional, Riveted Lap Joint", Proc. 1995 USAF Structural Integrity Program Conference, San Antonio, Tx., Nov. 2 -30, 1995.
27. Hahn, G.T., Bhargava, V., Rubin, C.A., Chen, Q. and Kim, K., "Analysis of the Rolling Contact Residual Stresses and Cyclic Plastic Deformation of an SAE 52100 Steel Ball Bearing," Journal of Tribology, Vol. 109, pp. 618-626, 1987.
28. Shivakumar, K., N., Newman, J., C., Jr., "Stress Concentration Equations for Straight-Shank and Countersunk Holes in Plates," Journal of Applied Mechanics, Vol 62, 1995, pp. 248-249.

## EHD Analysis of a Roller/Inner Ring Contact in a Jet Engine Roller Bearing

J. SEABRA  
DEMEGI

Faculdade de Engenharia da Universidade do Porto  
Rua dos Bragas - 4099 PORTO CODEX - PORTUGAL

A. CAMPOS  
INEGI - CETRIB

Faculdade de Engenharia da Universidade do Porto  
Rua dos Bragas - 4099 PORTO CODEX - PORTUGAL

### ABSTRACT

This paper deals with the analysis of an EHD roller/inner ring contact, in a roller bearing for a jet engine application.

The equations for the EHD lubrication problem, with longitudinal roughness, and their numerical solution for a Newtonian fluid are presented.

A typical geometry of a jet engine roller bearing is studied in detail, both in terms of lubricant film thickness and of elastic deformation of the roller. The results obtained show that the geometry of the roller in the transverse direction, produces a contact area of particular shape, avoiding the appearance of significant edge over-pressures, independently of the operating conditions.

The influence of the load and rolling speed on the film thickness, both for smooth and waved surfaces, was also investigated.

The results obtained permit to conclude that the surface waviness considered produce a small decrease of the film thickness, when compared with the smooth case, and that the elastic deformation of the waviness is strongly dependent on the rolling speed.

Finally a correlation of the EHD film thickness results for the roller/inner ring contact is obtained and compared with known solutions.

### 1-INTRODUCTION

The analysis of an elastohydrodynamic lubrication problem might be very complex. In fact, in order to take into account all the physical phenomena involved in the formulation of this problem, it is necessary to consider several aspects, like [3,5,6]:

- i) the geometry and the micro-geometry of the contacting surfaces;
- ii) the lubricant flow between the surfaces;
- iii) the elasticity of the solids;
- iv) the physical and rheological behaviour of the lubricant;
- v) the equilibrium of the applied loads;
- vi) the temperature variation of the lubricant and of the solids.

A simultaneous solution of these equations, leads to a very sophisticated and time consuming numerical solution, of difficult convergence.

A simple EHL model, capable of taking into account some of the phenomena mentioned above, is used to evaluate the lubricant film thickness and the pressure distribution inside the EHD contact.

In order to avoid some of the complexity mentioned above, the model is isothermal (no temperature variation is considered inside the contact), the lubricant is taken as a Newtonian fluid, and supposes the contact is fully flooded with lubricant. On the other hand it is able to consider the longitudinal waviness or roughness of the contacting surfaces. This is a classic procedure already proposed by several authors [3, 4, 6, 11, 13].

However, this EHL model presents an important limitation: The lubricant film geometry and the normal pressure distribution are both influenced by the non-Newtonian behaviour of the lubricant and by the temperature variation inside the contact [5, 7, 15], and this is not considered. The main advantage is that it is very simple and easy to implement.



## 2- ELASTOHYDRODYNAMIC EQUATIONS AND NUMERICAL SOLUTION

Several equations are necessary for the formulation of an EHD problem. In this analysis the inertial effects are neglected, the film thickness is considered very small, when compared with the other dimensions of the contact, the pressure across the lubricant film thickness is taken constant, the surface speeds are constant inside the contact zone, no sliding occurs between the lubricant fluid and the contacting surfaces, the temperature is constant, and steady state flow conditions exist.

Considering the above assumptions, it is possible to write the Reynolds equation in the following configuration:

$$\frac{\partial}{\partial x} \left[ \frac{\rho}{\eta} (H_1 + H_2)^3 \frac{\partial p}{\partial x} \right] + \frac{\partial}{\partial y} \left[ \frac{\rho}{\eta} (H_1 + H_2)^3 \frac{\partial p}{\partial y} \right] = 6(U_1 + U_2) \frac{\partial}{\partial x} [\rho(H_1 + H_2)] \quad (1)$$

The viscosity of any lubricant depends on its pressure and temperature. In this work, the influence of pressure is represented by the Barus law, which states that [9],

$$\eta = \eta_0 \exp[\alpha p] \quad (2)$$

The temperature (T) and the density ( $\rho$ ) of the lubricant fluid are considered to be constant [3].

In the Hertzian contact zone, the high level of the pressure distribution promotes the elastic deformation of the contacting surfaces. The same phenomena is observed in an elastohydrodynamic contact, where the elastic deformation affects the lubricant film geometry, which can be defined by the following equation:

$$H(x, y) = H^0(x, y) + H_c + u_n(x, y) - W_c \quad (3)$$

where  $H^0(x, y)$  is the non-deformed geometry of the contact ( $H^0(x, y) = H_1^0 + H_2^0$ ),  $H_c$  ( $H_c = H_{c1} + H_{c2}$ ) is the lubricant film thickness at the contact centre,  $u_n(x, y)$  is the difference between the normal elastic displacements of both surfaces, and  $W_c$  is the value of the  $u_n$  at the contact centre ( $W_c = W_{c1} + W_{c2}$ )

The elastohydrodynamic pressure in the contact zone must balance the load that is being transmitted between the two bodies, that is:

$$F_n = \int_S p(x, y) dx dy \quad (4)$$

The solution of this system of equations has already been presented by the authors in previous works [2, 12, 13].

The algorithm, used to evaluate the lubricant film thickness and the normal pressure distribution in the roller/inner ring contact, is able to consider both the macro and micro geometry of the contacting solids, their elastic properties, the lubricant characteristics, and the load applied to the contact.

Several algorithms had been presented and described in the literature [4, 6, 11, 13] to solve the set of equations (1) to (4). This one was developed by Seabra [12] and has received several updates [1, 2]. Its main characteristic is to split the contact area in two zones, the low pressure and the high pressure zones, where the Reynolds equation is solved, respectively by the direct and inverse methods [4, 12]. The low and the high pressure zones, overlap each other, allowing the compatibility between the direct and the inverse solutions of the Reynolds equation. A complete description of the algorithm is given in reference [2], including the discretization of the contact surface and of the several equations involved, as well as, a detailed description of the numerical procedure implemented.

## 3 - ROLLER/INNER RING GEOMETRY AND OPERATING CONDITIONS

The roller/inner ring contact, under analysis, was taken from a real roller bearing application, in a jet engine. The operating conditions, like the load, the rolling speeds and the temperature are severe and characteristic of the application considered.

### 3.1 - Macro and micro geometry of the contact

Only one roller bearing geometry was considered. The global geometry of the contacting bodies is presented in figure 1. The roller has got a complex geometry with three different zones: the central part is cylindrical, followed by two ellipsoidal zones on each side; the first one with a radius of 250mm and the second with a radius of 0.6mm. This type of geometry permits to reduce considerably the well known "edge effect", observed, for instance, in the pure cylindrical rollers, where severe geometric variations are present [8, 10].

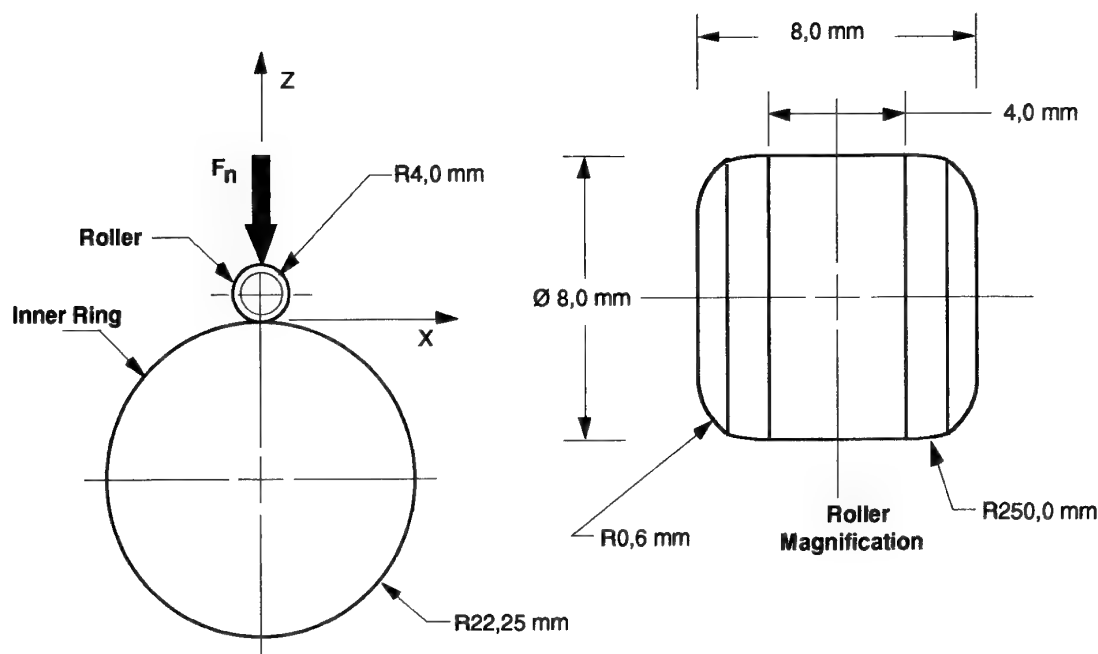


Figure 1 - Geometry of the contacting bodies.

In what concerns the micro geometry of the contacting surfaces, two cases were analysed. In first one both the roller and the inner ring have smooth surfaces and in the other case the roller is considered smooth and the inner ring has a longitudinal waviness, of the sinusoidal type. The amplitude of the waviness is equal to  $0.25 \mu\text{m}$  and the wavelength is equal to  $0.4 \text{ mm}$ , which permits to simulate an equivalent roughness typical of this type of roller bearings, corresponding, approximately, to a value of  $\sigma$  (RMS) equal to  $0.35 \mu\text{m}$ . Only this amplitude and wavelength are considered.

### 3.2 - Materials and lubricant characteristics

The roller and the ring are made of steel. The material has got the following elastic characteristics: Young modulus,  $E$ , equal to  $210 \text{ GPa}$ , and Poisson's coefficient,  $\nu$ , equal to  $0.3$ .

The lubricant dynamic viscosity at  $373\text{K}$  (constant temperature of  $100^\circ\text{C}$ ) is  $5.021 \times 10^{-3} \text{ Pa.s}$ .

### 3.3- Operating conditions

Table 1 shows the loads considered for the roller/inner ring contact under analysis. The correspondent maximum Hertzian pressures are in the range  $0.5$  to  $2.0 \text{ GPa}$ .

The angular speed of the inner ring is in the range  $1000 \text{ rpm}$  to  $40000 \text{ rpm}$ , corresponding to a rolling speed ( $U_1+U_2$ ) between  $4.7$  and  $186.4 \text{ m/s}$ , if the outer ring is stationary.

## 4- LUBRICANT FILM GEOMETRY AND NORMAL PRESSURE DISTRIBUTION FOR SMOOTH SURFACES

The roller/inner ring contact was analysed considering several loads and rolling speeds, in pure rolling conditions. For each case, the lubricant film geometry and the normal pressure distribution were determined. A total number of  $18$  cases were analysed.

Load Case	Normal Load $F_n$	Non-dimensional load, $W$	Hertz equivalent* pressure, $p_H$
I	92.3 N	$2.949 \times 10^{-5}$	$0.5 \text{ GPa}$
II	370 N	$1.182 \times 10^{-4}$	$1.0 \text{ GPa}$
III	831 N	$2.655 \times 10^{-4}$	$1.5 \text{ GPa}$
IV	1477 N	$4.719 \times 10^{-4}$	$2.0 \text{ GPa}$

Table 1- Load cases considered for the roller/inner ring contact.

(\* line contact between two cylinders with a length,  $\ell$ , equal to  $4 \text{ mm}$ ).



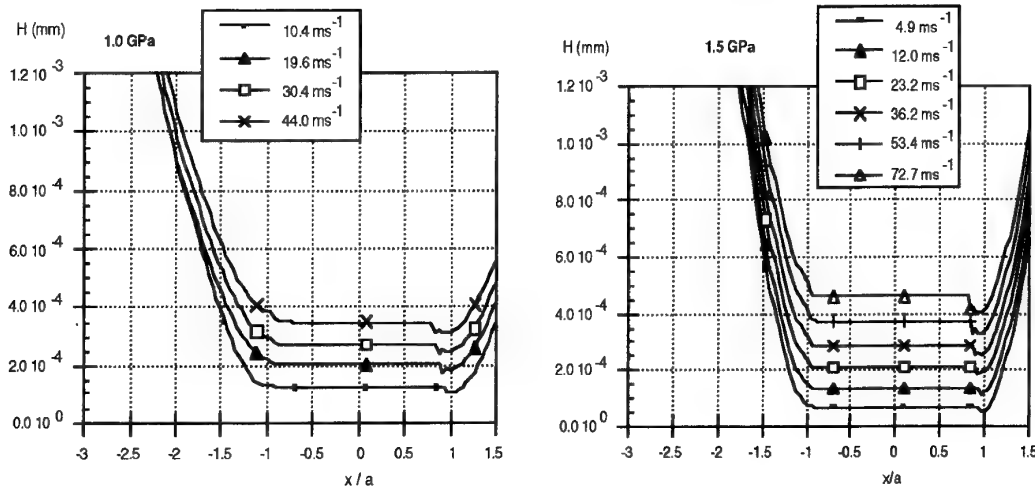


Figure 2 - Lubricant film geometry for several loads and rolling speeds ( $G=2.64 \times 10^3$ ).

#### 4.1- Influence of the operating conditions on the lubricant film geometry

Figure 2 puts into evidence the influence of the rolling speed on the film thickness of the roller/inner ring contact. For all the cases analysed, a global increase of the lubricant film thickness is observed when the rolling speed increases, together with a more significant film thickness restriction, that moves towards the inlet zone.

Figure 3 shows the contact geometry for a given rolling speed at two different loads. It can be observed that when the load increases (between  $W = 2.949 \times 10^{-5}$ ,  $p_H = 0.5$  GPa and  $W = 2.655 \times 10^{-4}$ ,  $p_H = 1.5$  GPa), no significant changes in the centre film thickness are produced. These are known results, that have already been presented and discussed by other authors [3, 14].

#### 4.2- Influence of the roller geometry

Looking at figure 3 it can be observed that when the load increases (from  $p_H = 0.5$  GPa to  $p_H = 1.5$  GPa) it produces an augmentation of the high pressure contact zone dimensions,  $a$  and  $b$ , both along OX and OY directions.

In figure 4 the corresponding high pressure contact zones are shown, respectively for 0.5 and 1.5 GPa. For the small load the high pressure zone is almost rectangle, like in a line contact, meaning the only the cylindrical part of the roller is deformed. Increasing the load, and thus the pressure, the contact zone dimensions increase, but not in the same proportion, as in a point contact.

Now both the cylindrical and the "lateral" parts of the roller are elastically deformed, and the contact

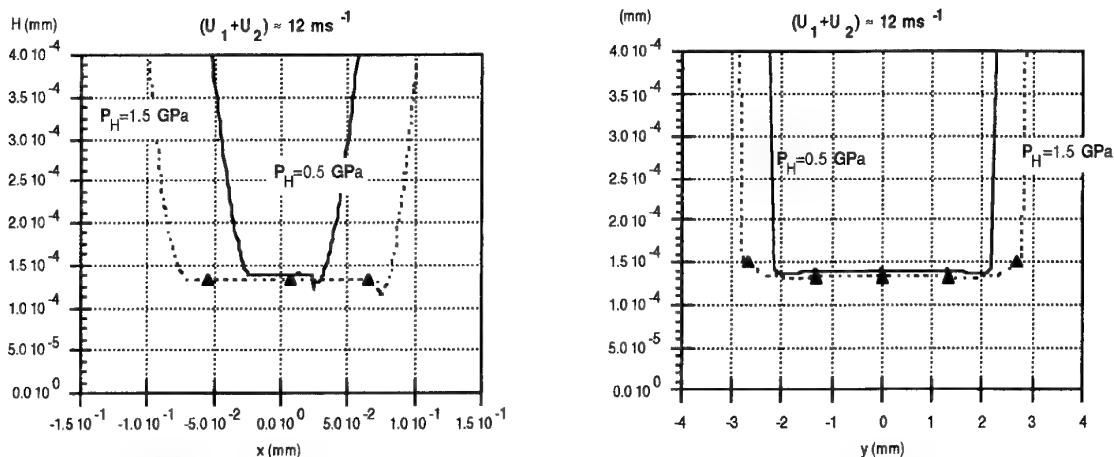


Figure 3 - Lubricant film geometry for  $W = 2.949 \times 10^{-5}$  ( $p_H = 0.5$  GPa) and  $W = 2.655 \times 10^{-4}$  ( $p_H = 1.5$  GPa) ( $U=3.7 \times 10^{-11}$  and  $G=2.64 \times 10^3$ ).

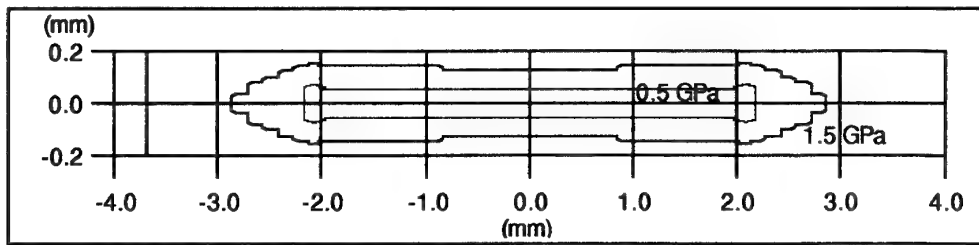


Figure 4 - High pressures contact zones for 0.5 GPa and 1.5 GPa.

high pressure zone has a particular shape, different from a rectangle or an ellipsis, meaning it's neither a line or a point contact.

At the edge of the roller a significant elastic deformation is observed (see figure 4) which keeps the EHD contact pressure almost at the level of the contact centre, avoiding edge over-pressures, as shown in figure 5.

The evolution of the high pressure zone dimensions, along OX and OY, with increasing loads is shown in figure 6.

This type of roller geometry presents a significant advantage in relation to the pure cylindrical geometry, because the edge over-pressures are only slightly higher than the contact centre pressure, and thus the pressure distribution is almost constant inside the contact zone. For the highest load the edge pressure is only 20% higher than the centre pressure.

These results show the significant importance of the roller geometry in avoiding the edge over-pressures, and producing an almost constant pressure along the transversal direction (OY).

## 5 - LUBRICANT FILM GEOMETRY - AND NORMAL PRESSURE DISTRIBUTION FOR WAVED SURFACES

Significant changes are observed in the film geometry and in the pressure distribution when the surface waviness of the inner ring is taken into consideration. Since a longitudinal waviness is considered, those changes occur in the OY direction. A total number of 22 load-rolling speed combinations were analysed.

### 5.1 - Influence of the operating conditions

Figure 7 shows the lubricant film geometry and the normal pressure distribution, along OX and OY directions. In this case, the equivalent smooth maximum Hertzian pressure and the rolling speed

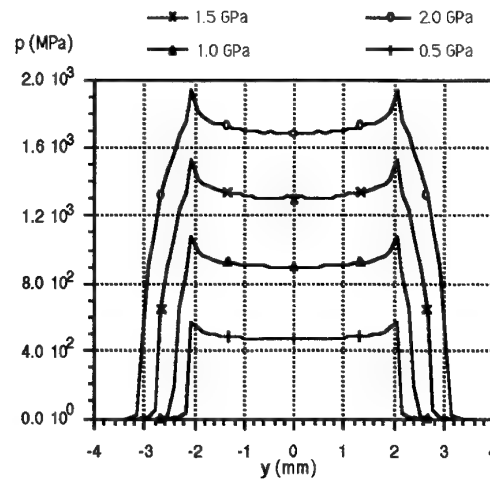


Figure 5 - EHD pressure distribution along OY for several loads.

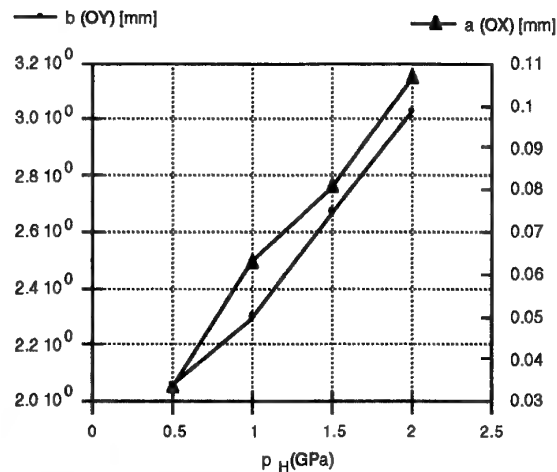


Figure 6 - Semihertzian lengths modifications with Hertzian pressure ( $p_H$ ).

are equal, respectively, to 0.5 GPa and 21.3 m/s, corresponding to the following non-dimensional parameters:  $U = 6.834 \times 10^{-11}$ ,  $G = 2.64 \times 10^3$  and  $W = 2.949 \times 10^{-5}$ .

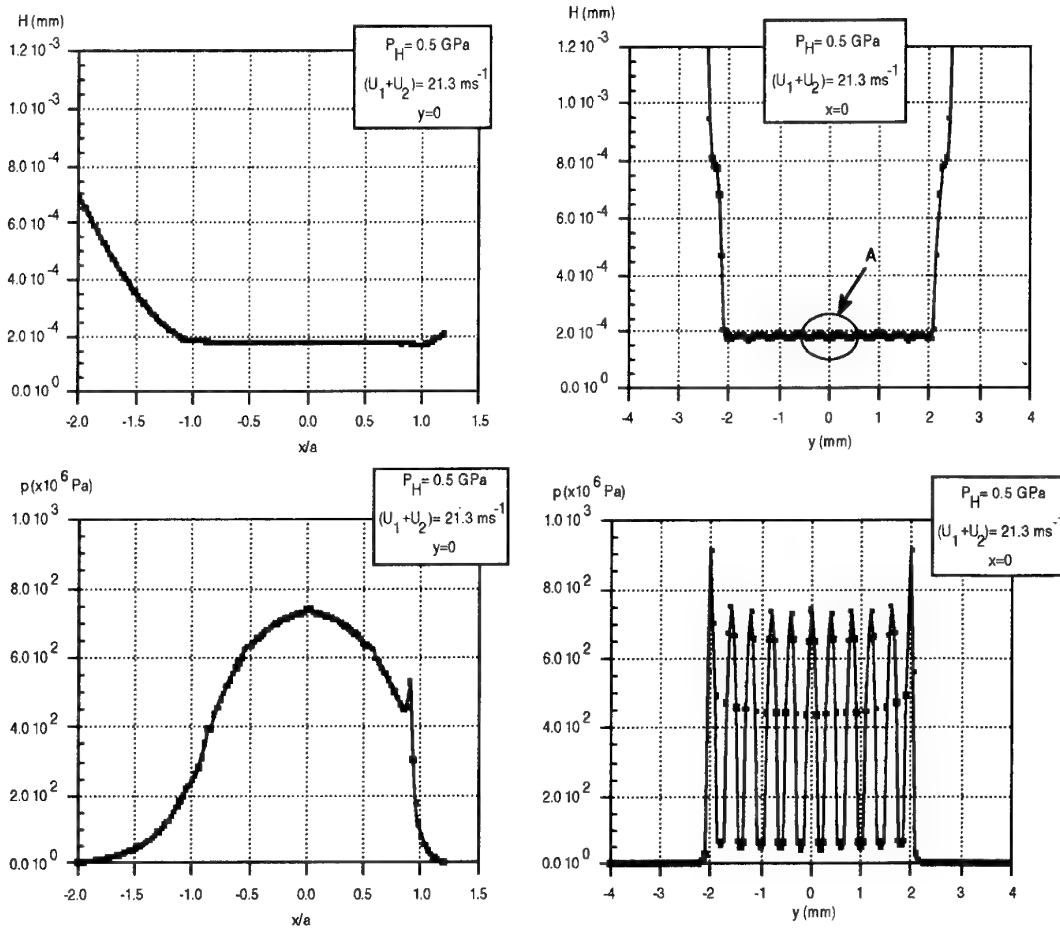


Figure 7 - Lubricant film geometry and the normal pressure distribution, along OX and OY directions, for  $U=6.834 \times 10^{-11}$ ,  $G=2.64 \times 10^3$  and  $W=2.949 \times 10^{-5}$ .

It can be noticed that along OY direction the surface waviness shows a very significant elastic deformation (see detail A), to which corresponds a very wavy normal pressure distribution, ranging almost from 0.0 to 0.75 GPa, in the high pressure zone. This means that, when the non-dimensional speed parameter is small, a strong elastic deformation of the surface waviness takes place, even for a small load, like in the present case, in order to create a lubricant film separating the surfaces.

Figure 8 shows the opposite case, where important rolling speed and load are considered, that is,  $(U_1 + U_2) = 130.6 \text{ m/s}$  and  $p_H = 1.5 \text{ GPa}$ , corresponding to the following non-dimensional parameters:  $U = 4.190 \times 10^{-10}$ ,  $G = 2.64 \times 10^3$  and  $W = 2.655 \times 10^{-4}$ .

Despite of the much higher load, the elastic deformation of the surface waviness is much smaller than in the previous case (see detail B).

The pressure distribution is still wavy, ranging, approximately, between 1.0 and 1.5 GPa, in the high pressure zone, meaning that pressure waviness is smaller in this case.

These two examples show the importance of the rolling speed (or non-dimensional speed parameter), on the elastic deformation of the surface waviness, putting into evidence the influence of the contact hydrodynamics, on the lubricant film geometry and on the normal pressure distribution.

Figure 9 shows the lubricant film geometry along the transversal direction OY, for two loads and for several rolling speeds.

As observed for the smooth cases, an increase in the non-dimensional speed parameter (or rolling speed) produces a global augmentation of the contact film thickness.

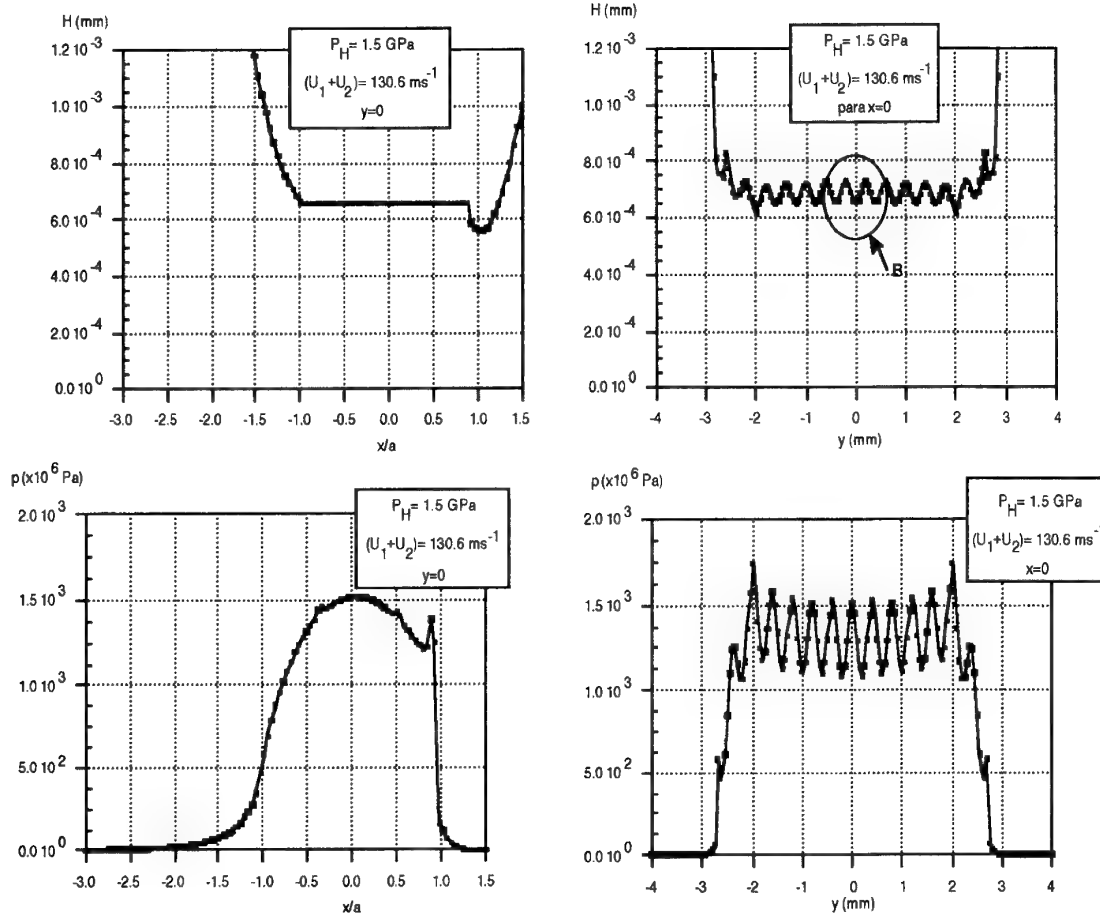


Figure 8 - Lubricant film geometry and the normal pressure distribution, along OX and OY directions, for  $U = 4.190 \times 10^{-10}$ ,  $G = 2.64 \times 10^3$  and  $W = 2.655 \times 10^{-4}$ .

It can also be observed that, for all the load cases considered, an increase in the non-dimensional speed parameter, promotes a decrease in the elastic deformation of the surface waviness and a decrease in the waviness of the pressure

distribution. This means that for the higher rolling speeds the hydrodynamic effect is more important than the elastic effect, in the elastohydrodynamic problem.

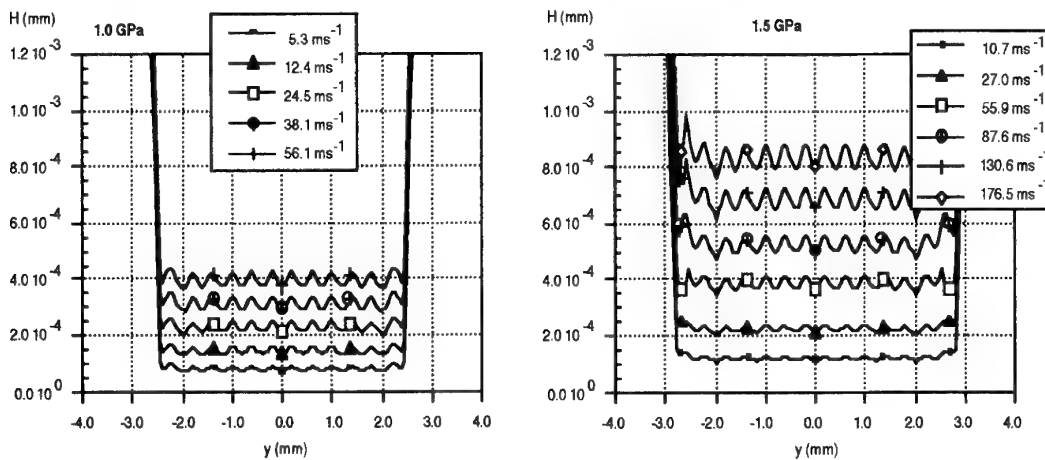


Figure 9 - Lubricant film geometry, along OY direction for two loads and several rolling speeds.

## 5.2- Surface waviness and "edge" pressures

Figure 10 shows the waved pressure distributions along OY direction, for two load cases. The load increase produces an augmentation of the high pressure zone dimensions of the same magnitude of the one obtained for the smooth case.

Those pressure distributions also show "edge" over-pressures, due to the geometry of the roller in the transverse direction, similar to those found in the smooth case, only slightly greater.

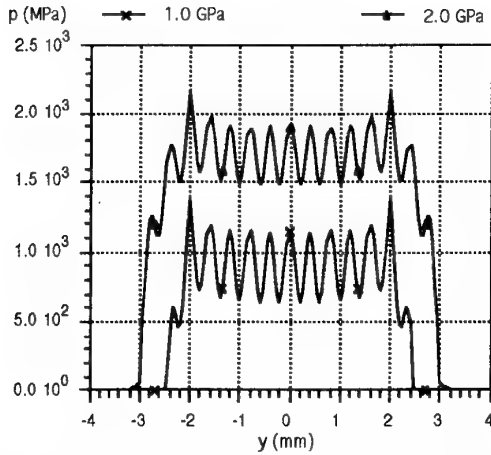


Figure 10 - Influence of the load on the pressure distribution along OY.

## 6 - CORRELATION OF THE FILM THICKNESS RESULTS

The lubricant film geometry, is usually represented by the centre film thickness,  $H_c$ , and by the minimal film thickness in the contact,  $H_m$  [3, 14]. The correlations of the numerical values, obtained for the non-dimensional centre and minimum film thickness, function of the non-dimensional load ( $W$ ) and speed ( $U$ ), were obtained. These correlations allowed the definition of two equations for predicting the centre and the minimum film thickness, but they are only valid for the geometry of the roller/inner ring considered, and for the lubricant used.

The non-dimensional centre and minimum film thickness are defined as:

$$\bar{H}_c = \frac{H_c}{R_x} \quad \text{and} \quad (5)$$

$$\bar{H}_m = \frac{H_m}{R_x} \quad (6)$$

with

$$\frac{1}{R_x} = \frac{1}{2} \left( \frac{1}{R_{x1}} + \frac{1}{R_{x2}} \right) \quad (7)$$

### 6.1 - Equations for smooth and waved film thickness

The equation obtained for the non-dimensional centre film thickness are:

$$\bar{H}_c^\ell = 242.65 U^{0.705} W^{-0.068} \quad (8)$$

and

$$\bar{H}_c^r = 303.78 U^{0.690} W^{0.007} \quad (9)$$

respectively for smooth ( $\ell$ ) and waved ( $r$ ) surfaces, with correlation coefficients of 0.9990 and 0.9987.

The analysis of the non-dimensional minimum film thickness results produced equations similar to expressions (8) and (9):

$$\bar{H}_m^\ell = 145.52 U^{0.702} W^{-0.100} \quad (10)$$

and

$$\bar{H}_m^r = 224.29 U^{0.690} W^{-0.002} \quad (11)$$

respectively for smooth and waved surfaces. The correlation coefficients, in this case, are 0.9967 and 0.9905.

### 6.2 - Comparison between smooth and waved film thickness

Figure 11 compares the lubricant film geometry, along OY direction, for smooth and waved surfaces, considering two different sets of operating conditions. It can be observed that in both cases, and globally, the film thickness is not significantly modified by the surface waviness.

This explains the reason why no significant differences are observed in the exponents obtained for the non-dimensional speed parameter, between the expressions predicting the film thickness for smooth and waved surfaces.

The equations developed to predict the centre and the minimum film thickness, for smooth and waved surfaces, can be compared in order to analyse the influence of the waviness.

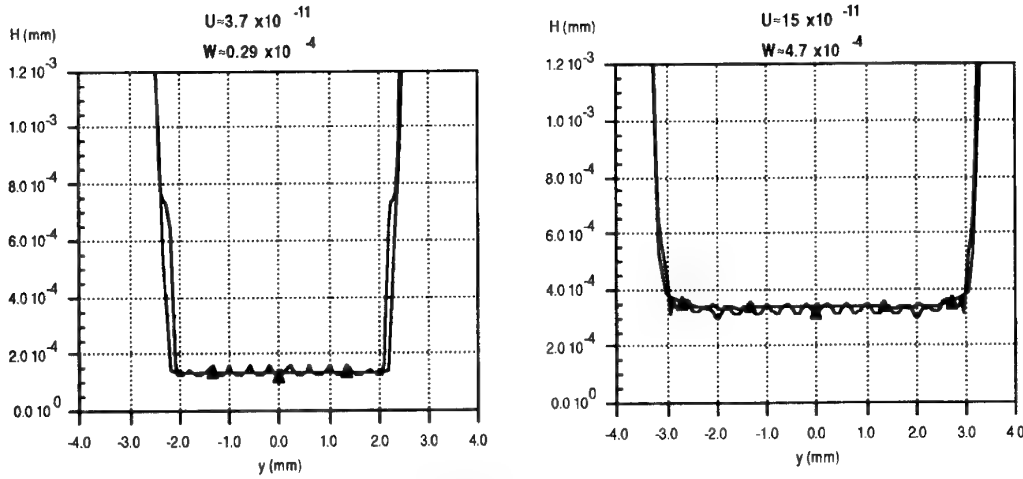


Figure 11 - Lubricant film geometry, along OY direction, comparing smooth and waved surfaces, for the same operating conditions.

For the centre film thickness the decrease in film thickness can be defined by the parameter  $\epsilon_c$  :

$$\epsilon_c = \frac{\bar{H}_c^\ell - \bar{H}_c^r}{\bar{H}_c^\ell} \times 100 = \left( 1 - \frac{\bar{H}_c^r}{\bar{H}_c^\ell} \right) \times 100 \quad (12)$$

which represents the percentual decrease of the centre film thickness in presence of the inner ring waviness. Considering the equations obtained for  $\bar{H}_c^\ell$  and  $\bar{H}_c^r$ , it can be written that:

$$\epsilon_c = \left( 1 - 1.252 U^{-0.015} W^{0.075} \right) \times 100 \quad (13)$$

Within the range of the non-dimensional parameters considered in this work, equation (13) permits to evaluate, in a simple way, the influence of the surface waviness on the centre film thickness (see figure 12). The waved centre film thickness is always smaller than the smooth one, but that decrease ( $\epsilon_c$ ) is, always, smaller than 13%.

For small values of the non-dimensional speed parameter, the differences between smooth ( $\ell$ ) and waved ( $r$ ) centre film thickness are not significant. In fact, for the low speeds the surface waviness shows a very significant elastic deformation, and the contact centre high pressure zone is almost flat, as shown in figure 11. For higher values of the speed parameter, the differences between smooth and waved film thickness become more important. Thus, the minimum differences between smooth and waved centre film thickness, are found for the smallest speed and the highest load parameters.

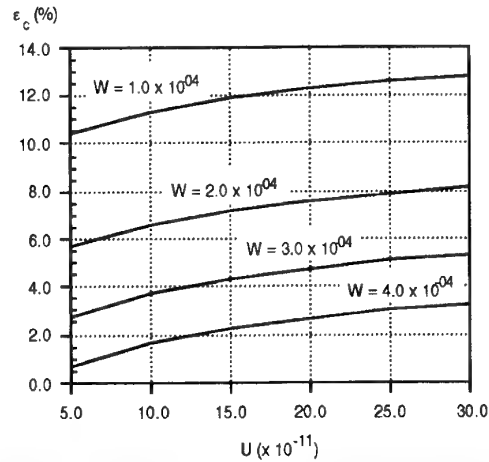


Figure 12 - Influence of the inner ring longitudinal surface waviness on the centre film thickness.

A similar expression to equation (13) can be produced for the minimum film thickness, giving,

$$\epsilon_m = \left( 1 - 1.541 U^{-0.012} W^{0.098} \right) \times 100 \quad (14)$$

Within the range of the non-dimensional parameters considered in this work, equation (14) permits to evaluate, the influence of the surface waviness on the minimum film thickness. The waved minimum film thickness is always smaller than the smooth one, but that decrease ( $\epsilon_m$ ) is, in general, smaller than 10%.

The results and the correlations presented in this work have some limitations. They correspond only to one roller/inner ring geometry, and the geometry of the roller is of great importance.

Another limitation is that only one amplitude and one wavelength were considered for the surface waviness. Although the amplitude considered is reasonable for a roller bearing, no investigation was produced about the influence of the wavelength.

Finally, only one lubricant was considered, although typical of jet engine roller bearing application.

## 7 - CONCLUSION

The roller geometry, along the transverse direction, plays a very important role in the elastohydrodynamic behaviour of the roller/inner ring contact. In fact, for high loads the roller deforms significantly in the transverse direction, supporting the load, and avoiding the appearance of important "edge" over-pressures or significant reductions of EHD film thickness. This shows the importance of the "transition" geometry between the cylindrical part of the roller and the roller end. Some "edge" pressures and film thickness reductions are observed, but they are very small when compared with the centre values.

The surface waviness considered produces a considerable perturbation of the normal pressure distribution, with high local pressures. As a consequence, high local sub-surface stresses are produced inside the inner ring which are very important for the fatigue life behaviour of the roller bearing.

The centre and the minimum film thickness, of the roller/inner ring contact, show a small reduction due to the presence of the surface waviness. But the elastic deformation of the surface waviness is extremely dependent on the non-dimensional speed parameter. For small values of the parameter  $U$  the surface waviness shows an important deformation, no matter the applied load.

## ACKNOWLEDGEMENTS

This work was developed within the BRITE-EURAM project "Bearing with minimum Lubrication" (Roller Bearings), Contract Aero - 0007 - A(c), Proposal Number PL 1103. The authors are grateful for the financial support conceded to this project by the European Community.

The authors appreciated the kind collaboration of all the other partners involved in the project, TURBOMECA (F), BMW/Rolls-Royce GmbH (G), MTU GmbH (G), Rolls Royce plc (UK), Hispano Suiza (F), Leeds University - The Industrial Unit of Tribology (UK), GLCS (F) and INSA de Lyon - Laboratoire de Mécanique des Contacts (F).

Finally, the authors express their gratitude to Professor Louis Flamand and Dr. Daniel Nelias, from the Laboratoire de Mécanique des Contacts, INSA de Lyon, France, for their confidence in the research team of CETRIB (FEUP) and for their scientific support in the development of this work.

## NOMENCLATURE

a- Hertzian semi-length

$F_n$  - normal force applied to the contact

G- non-dimensional material parameter

H- lubricant film geometry

$H_i$ - geometry of the surface  $i$

$H_c$ - centre film thickness

$H_m$ - minimum film thickness

$\bar{H}_c$  - non-dimensional centre film thickness

$\bar{H}_m$  - non-dimensional minimum film thickness

p- normal pressure on a point (x,y)

$R_x$ - equivalent radii in x

$R_{xi}$ - radii in x of surface  $i$

U- non-dimensional speed parameter

$U_i$ - speed of the surface  $i$

W- non-dimensional load parameter

$\alpha$  - piezosviscosity coefficient

$\eta$  - dynamic viscosity

## REFERENCES

- [1] - CAMPOS, A., "A lubrificação elastohidrodinâmica isotérmica em rolamentos de rolos", Proceedings do 3º Encontro de Mecânica Computacional, Coimbra, Portugal, 28 a 30 de Setembro de 1992, Vol.2, F18.1-12.
- [2] - CAMPOS, A., "Determinação da geometria do filme lubrificante, da distribuição de pressão e das tensões de corte num contacto elastohidrodinâmico. Aplicação a rolamentos de rolos", Dissertação para obtenção do Grau de "Mestre em Engenharia Estrutural", Departamento de Engenharia Mecânica da Faculdade de Engenharia da Universidade do Porto, Porto, 1994, 170 páginas.
- [3] - DOWSON, D., HIGGINSON, G. R. J., "Elastohydrodynamic Lubrication", SI Edition, Materials Science and Technology Volume 23, Pergamon Press Ltd. 1977.
- [4] - EVANS, H. P., SNIDLE, R. W., "The isothermal elastohydrodynamic lubrication of spheres", Journal of Lubrication Technology, vol. 103, 1981, pp. 547 - 557.
- [5] - GOAR, R., "Elastohydrodynamics", Ellis Horwood Series in Mechanical Engineering, John Wiley & Sons, 1988.
- [6] - HAMROCK, B. J., DOWSON, D., "Isothermal Elastohydrodynamic Lubrication of Point Contacts: Part I - Theoretical Formulation", Journal of Lubrication Technology, Vol. 98, 1976, pp. 223 - 229.
- [7] - HOUPERT, L., "Contribution a l'étude du frottement dans un contact elastohydrodynamic". Thèse de Docteur nº IDI 3-8019, I.N.S.A. Lyon 1980.
- [8] - CHIU, Y. P., HARTNETT, M. J., "A numerical solution for the contact problem involving bodies with cylindrical surface considering cylinder effect", Journal of Tribology, vol. 109, 1987, pp. 479 - 486.
- [9] - HOUPERT, L. "New results of tractions force calculations in elastohydrodynamic contacts". ASME Journal of Tribology, vol.107, 1985, pp. 241-248.
- [10] - REUSNER, H., "El perfil logarítmico en los modernos rodamientos de rodillos cilíndricos y cónicos", Revista de rodamientos 230, pp. 2 - 10.
- [11] - LUBRECHT, A. A., NAPEL, W. E., BOSMA, R., "Multigrid, an alternative method for calculating film thickness and pressure profiles in elastohydrodynamically lubricated line contacts", Journal of Tribology, vol. 108, 1986, pp. 551 - 556.
- [12] - SEABRA, J., "Influence de l'ondulation des surfaces sur le comportement des contacts Hertiens secs ou lubrifiés", Tese de doutoramento, nº 81SAL 0018, INSA, Lyon, 1988.
- [13] - SEABRA, J. e BERTHE, D., "Elastohydrodynamic point contacts part I: formulation and numerical solution", Wear, vol. 130, 1989, 301 - 318.
- [14] - HAMROCK, B., DOWSON, D., "Ball bearing lubrication - The elastohydrodynamic of elliptical contacts", John Willey and Sons, 1981.
- [15] - VERGNE, F., "Le contact elastohydrodynamic pontuel lubrifié par un fluid visqueux lineaire ou non". Thèse de Docteur nº 13-89, I.N.S.A. Lyon 1989.



# ROLLING CONTACT TESTING OF VAPOR PHASE LUBRICANTS

Nelson H. Forster

Aero Propulsion and Power Directorate  
Wright Laboratory, Fuels & Lubricant Div, WL/POSL  
Bldg 490, 1790 Loop Road North  
Wright-Patterson AFB, OH 45433-7103, USA

## EXPERIMENTAL

### ABSTRACT

Material screening tests have been performed with four candidate vapor phase lubricants under rolling contact conditions. The lubricants evaluated were; t-butyl phenyl phosphate (TBPP), polyalphaolefin (PAO), cyclophosphazine (X-1P), and PAO blended with 15 percent TBPP (PAO+). A factorial analysis was used to separate the effects of lubricant; bearing steel, T15 vs. thin dense chrome coated T15; cage material, AISI 4340 vs. Monel 400; and ball material, T15 vs. NBD 200 Si<sub>3</sub>N<sub>4</sub>. Response variables included in the analyses were the bearing friction coefficient, wear rate, and life under accelerated conditions. The type of lubricant was significant at the 90 percent confidence level for all three response variables, with the PAO+ and TBPP showing the best results. In general, bearing materials containing Fe showed improved performance over materials which do not contain Fe at the bearing surface.

### INTRODUCTION

The concept of lubricating high temperature bearing surfaces with organic vapors has existed for at least forty years (1). However, it was not until the 1980's that vapor phase lubrication achieved a sustained level of effort, which today exists in three distinct forms: vapor phase deposition (VPD), where organic vapors are intentionally reacted with a hot bearing surface to form the lubricating film (2-12); vapor phase condensation (VPC), where vapors are condensed on a bearing surface to essentially maintain liquid lubrication (12); and gaseous lubrication, where light-weight hydrocarbon gases are deposited on a hot catalytic nickel surface (13,14). The research described in this paper focuses on VPD lubrication.

The objective of this research was to screen candidate VPD lubricants for future application in high speed/high temperature rolling element bearings. To simulate the bearing environment, a ball-on-rod tester modified for high temperature was used (15). Criteria considered in the lubricant selection were; toxicity, fire resistance, boundary film lubrication characteristics, thermal and oxidative stability, and temperature-viscosity index. The following lubricants were selected based on these criteria; a blend of tertiary-butyl phenyl phosphate isomers (TBPP) (16), a blend of cyclophosphazine isomers (X-1P) (17), a 2 cSt unformulated polyalphaolefin (PAO), and the PAO fluid blended with 15 percent TBPP (PAO+). Tricresyl phosphate (TCP), by far the most widely used VPD lubricant, was not considered due to toxicity considerations with the ortho-isomer (18,19). Polyol esters were also not considered due to a highly toxic reaction which occurs between trimethylolpropane esters and triaryl phosphate esters at elevated temperatures (20).

### Material Properties and Selection

The molecular structures for TBPP and X-1P isomers are shown in Fig.'s 1 and 2. Structurally TBPP is similar to TCP, with the exception of the substituent on the phenyl ring. The size of the t-butyl substituent sterically hinders the formation of the ortho-isomer, substantially reducing the risk of neurotoxicity. Oral dose testing with TBPP isomers applied to the adult hen in the neat condition have shown little or no neurotoxic effect (21,19). However, TBPP has been associated with reproductive toxicity in rodents when administered in an oral dose of 1.7 g/kg (22,23). In comparison, TCP is a more severe reproductive toxicant at an oral dose of 0.4 g/kg (22,23). Preliminary toxicity testing with X-1P has shown the oral LD<sub>50</sub> in rats to be >2.0 g/kg (17). Toxicity testing with TBPP and X-1P vapors is underway to evaluate toxicity effects from the vapor phase. In reference to the other selection criteria, both TBPP and X-1P have excellent fire resistance (16,24), boundary film lubrication (16,25), and thermal/oxidative stability (26,17). However, both lubricants have relatively poor temperature-viscosity properties.

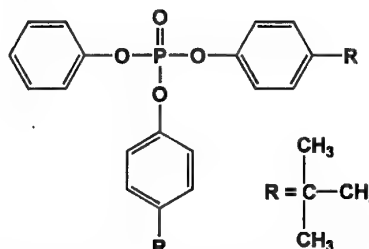


Figure 1. The molecular structure of the TBPP isomer Di(p-t-butylphenyl), Phenyl Phosphate.

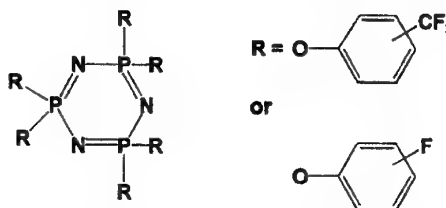


Figure 2. The molecular structure of isomers found in X1-P.

In application, tribological systems using VPD lubrication will likely go through a start-up period requiring liquid lubrication. During this period temperature-viscosity and other liquid lubrication properties may be critical. The PAO fluid was selected to potentially bridge this gap. However, preliminary VPD tests with the PAO fluid in the neat condition showed essentially no lubricating effect. To improve performance, the bearing specimens were pretreated

for a period of 2 hours of operation with the TBPP vapor followed by testing with the unformulated PAO vapor. As a second approach, the PAO fluid was blended with 15 percent TBPP and used without pretreatment. Klaus and Duda used a similar approach, blending super refined mineral oil with TCP (12). The authors found the blended lubricant produced lower wear scars in the sliding four-ball test than either mineral oil or TCP alone. In the present effort, both pretreatment and blending were sufficient to make the PAO a viable vapor phase lubricant. Important physical properties for the TBPP, X-IP, PAO, and PAO+ lubricants are summarized in Table 1.

Table 1 - Physical Properties of Candidate Lubricants

	TBPP	X-IP	PAO	PAO+
Viscosity @ 40°C, (cSt)	119.2	210.0	5.12	6.21
Viscosity @ 100°C, (cSt)	8.59	10.80	1.75	1.90
Flash Point, (°C)	254	>270	125	
Specific Gravity, (g/cm <sup>3</sup> )	1.12	1.45	0.81	0.83

Candidate bearing materials were selected based on high temperature properties and chemical composition. One of the goals in the bearing material evaluation, was to assess the relative importance of Fe in the VPD process. TCP is known to react with ferrous alloys in the liquid state (27,28) and from the vapor phase (3,4). To generate a ferrous based system, T15 tool steel was selected as the material for the bearing races and rolling elements, with AISI 4340 steel for the bearing cages. The T15 steel was heat treated to achieve a retempered martensitic structure with a Rockwell C hardness of 64. T15 resists retempering at temperatures up to 450°C, which gives the steel excellent hardness retention at elevated temperatures. For the nonferrous system, the T15 races were coated with thin dense chrome (TDC), NBD 200 Si<sub>3</sub>N<sub>4</sub> was used for the rolling elements, and Monel 400, a nickel/copper alloy was used for the bearing cage. A secondary consideration in the selection of the nonferrous materials was their inherent oxidation resistance at elevated temperatures. The nominal thickness of the TDC coating was 2 microns.

#### Test Apparatus and Procedure

A cross section of the high temperature rolling contact tester is shown in Fig. 3. The tester is based on the ball-on-rod tester originally developed by Glover for rolling contact fatigue testing of bearing steels at ambient temperature (30).

In the present configuration the tester is used to screen high temperature materials prior to full-scale bearing tests. The bearing test specimens consist of the rotating rod, three balls, a bearing cage, and two tapered races. The diameters of the ball and rod are 12.70 mm and 9.52 mm, respectively. The material used for the rod and tapered races is collectively referred to as the race material in the RESULTS.

As shown in Fig. 3, the outer structure containing the tapered races is supported by a hydrostatic air bearing. Rotation of the structure is restrained by a thin wire connected to a load transducer. The friction coefficients

tabulated in the RESULTS were calculated from the friction force at the tapered races divided by the applied normal load.

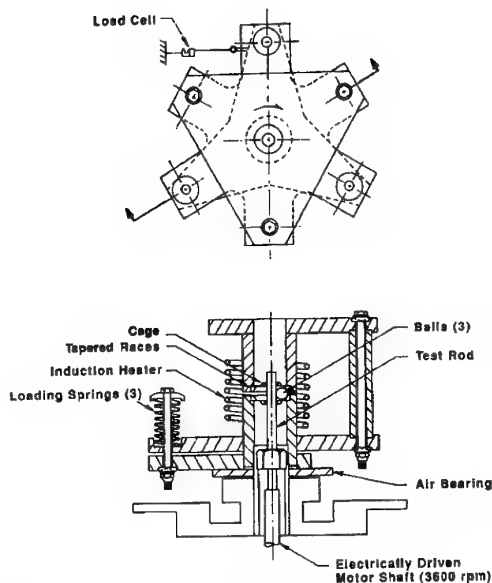


Figure 3. Cross section of the high temperature ball-on-rod tester.

To accelerate bearing failure, unusually high Hertzian contact stresses were used. The maximum Hertzian contact stress was 3.34 GPa for the metallic specimens and 3.65 GPa for combinations with Si<sub>3</sub>N<sub>4</sub> rolling elements. An accelerometer measures the bearing vibration and the resulting signal is used to terminate the test if the vibration reaches a level consistent with rolling contact fatigue initiation. The tests were suspended at 96 hours if they did not fail from vibration.

After test, the wear track on each rod was examined using a metallurgical microscope and by profilometry measurements. The volumetric wear rate was calculated for each track using the averaged wear volume from three profilometry traces and the number of stress cycles completed.

The vapor phase lubrication system is shown in Fig. 4. Vapor was generated by introducing the liquid at ambient conditions into a heated stainless steel tube, 25 mm in diameter by 200 mm long. Shop air was used as the carrier gas at a flow rate of 283 l/hr. A thermocouple on the downstream side of the vapor chamber was used to monitor and control the vapor temperature.

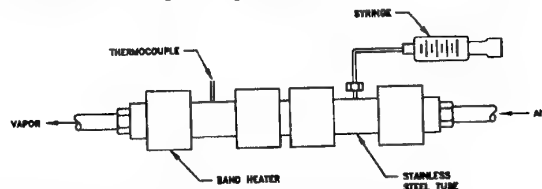


Figure 4. Vapor phase lubrication system.

Environmental operating conditions are summarized in Table 2. The lubricant flow rate for the TBPP and X-1P was set at 1.17 ml/hr based on previous work conducted by Rao (9). A higher flow rate of 3.4 ml/hr was used with the PAO and PAO+ tests to improve bearing performance. The vapor temperatures were selected based on the level required to generate a clearly visible stream of vapor exiting the test head. The bearing operating temperature is monitored and controlled by a thermocouple mounted to the upper race. The ambient air temperature near the ball rod contact is typically 25°C less than the tapered race temperature.

Table 2 - Test Conditions

Speed: 3600 rpm

Load:	Metallic 3.34 GPa		Hybrid 3.65 GPa
	Temperature (°C) Vapor	Bearing	Lubricant Flow Rate (mL/hr)
TBPP	330	370	1.17
PAO+	243	370	3.40
PAO*	243	370	3.40
X-1P	370	370	1.17

\* Initially pretreated for a period of 2 hours with TBPP at 330°C

### Factorial Design

A half fraction factorial design (31) was used to generate the test matrix for the cage, race, and ball material. This matrix was then repeated for each lubricant. The type of lubricant, cage material, race material, and ball material are referred to as the design factors. Within each factor are levels, i.e. TDC vs. T15 represents two levels for the factor, race material. Bearing friction, wear, and life were used as the response variables to measure the bearing performance. Analysis of variance (ANOVA) (32) with Type I Sum of Squares was used to determine if a factor made a statistically significant contribution to the bearing performance. The significance of a factor was determined from the F-ratio, which represents the ratio of the estimated variance within factors to the estimated variance between factors. If this ratio is high, then the probability that the factor is significant in determining the measured response, is also high. The significance level in the ANOVA table represents the probability of obtaining the F-ratio by chance. A low significance level indicates the factor was influential in determining the measured response. If the significance level is less than or equal to 0.10, then the factor can be interpreted as being statistically significant at the 90 percent confidence level. The Tukey method of multiple comparisons (33) was used to determine if a particular level had an adverse or beneficial effect on bearing performance.

## RESULTS

### Factorial Analysis

Results for the factorial design are summarized in Tables 3-6. Analysis of the residuals was performed as a preliminary step to determine the suitability of the ANOVA model for the response data. For the friction coefficient response, the logarithm of the friction coefficient was used to stabilize the variance (34). This provided a small but beneficial improvement in the model response. The residual analysis for wear and life indicated that the model was suitable without transformation of the response variable.

Table 3 - Test Matrix and Results

LUBE	CAGE	ROD/ RACES	BALL	FRICTION COEFFx10 <sup>4</sup>	WEAR RATE (µm <sup>3</sup> /cycle)	TIME (hrs)
TBPP	Monel	T15	Si <sub>3</sub> N <sub>4</sub>	7.91	41.08	96.0
TBPP	4340	TDC	Si <sub>3</sub> N <sub>4</sub>	6.13	28.75	96.0
TBPP	4340	T15	T15	3.13	8.88	96.0
TBPP	Monel	TDC	T15	5.06	28.55	96.0
PAO	Monel	T15	Si <sub>3</sub> N <sub>4</sub>	3.91	9.25	77.8
PAO	4340	TDC	Si <sub>3</sub> N <sub>4</sub>	6.91	7.39	23.5
PAO	4340	T15	T15	3.70	10.03	61.8
PAO	Monel	TDC	T15	4.76	1.08	12.2
X-1P	Monel	T15	Si <sub>3</sub> N <sub>4</sub>	8.48	28.01	96.0
X-1P	4340	TDC	Si <sub>3</sub> N <sub>4</sub>	7.17	33.57	50.5
X-1P	4340	T15	T15	5.80	21.39	96.0
X-1P	Monel	TDC	T15	16.10	17.84	96.0
PAO+	Monel	T15	Si <sub>3</sub> N <sub>4</sub>	7.58	20.10	96.0
PAO+	4340	TDC	Si <sub>3</sub> N <sub>4</sub>	2.87	5.56	51.6
PAO+	4340	T15	T15	3.59	0.70	96.0
PAO+	Monel	TDC	T15	3.78	3.46	96.0
TBPP	4340	T15	T15	5.68	17.24	96.0

Table 4 - Analysis of Variance Results for the LOG (Friction Coefficient)

Source of Variation	Sum of Squares	d.f.	Mean Square	F-ratio	Sig. level
MAIN EFFECTS					
Lube	1.2640258	3	0.4213419	3.316	0.0653
Cage	0.3950979	1	0.3950979	3.110	0.1083
Steel	0.0385501	1	0.0385501	0.303	0.5996
Ball	0.1115433	1	0.1115433	0.878	0.3806
RESIDUAL	1.2705758	10	0.1270576		
TOTAL	3.0797929	16			
(CORRECTED)					

Table 5 - Analysis of Variance Results for the Wear Rate - Type I Sums of Squares

Source of Variation	Sum of Squares	d.f.	Mean Square	F-ratio	Sig. level
<b>MAIN EFFECTS</b>					
Lube	1348.3293	3	449.44311	9.711	0.0026
Cage	98.9022	1	98.90220	2.137	0.1745
Race	3.3620	1	3.36196	0.073	0.7958
Ball	461.2742	1	461.27419	9.966	0.0102
<b>RESIDUAL</b>	<b>462.83788</b>	<b>10</b>	<b>46.283788</b>		
<b>TOTAL (CORRECTED)</b>	<b>2374.7055</b>	<b>16</b>			

Table 6 - Analysis of Variance Results for the Bearing Life

Source of Variation	Sum of Squares	d.f.	Mean Square	F-ratio	Sig. level
<b>MAIN EFFECTS</b>					
Lube	6653.0467	3	2217.6822	7.803	0.0056
Cage	532.6881	1	532.6881	1.874	0.2009
Race	2344.6611	1	2344.6611	8.250	0.0166
Ball	200.5102	1	200.5102	0.706	0.4293
<b>RESIDUAL</b>	<b>2841.9624</b>	<b>10</b>	<b>284.19624</b>		
<b>TOTAL (CORRECTED)</b>	<b>12572.868</b>	<b>16</b>			

The ANOVA results for the friction coefficient indicate that the lubricant is the most significant factor. The graph for the lubricant level response in Fig. 5(a), indicates that X-1P produces the highest friction and the measured response is statistically different than the PAO+ fluid at the 90 percent confidence level. In general, Fig. 5(a) suggests that ferrous systems generate lower friction than nonferrous systems.

The ANOVA results for the bearing wear rate indicate the type of lubricant and ball material have the most effect on the bearing response. The response of the factor levels are graphed in Fig. 5(b). Results indicate that the PAO and PAO+ lubricants produce a similar response and the wear generated is less than that obtained with the TBPP or X-1P lubricants. The results also indicate that  $\text{Si}_3\text{N}_4$  rolling elements produce more wear than T15 rolling elements. The ANOVA results for the bearing life indicate that the type of lubricant and race material have the most effect on bearing life. The response of the factor levels are graphed in Fig. 5(c). Results indicate that the PAO fluid and TDC races have an adverse effect on bearing life. Due to the number of suspensions, the lubricant which promotes the longest life cannot be determined. Fig. 5(c) also indicates that Monel 400 may have a beneficial effect on life; however, the results are not conclusive at the 90 percent confidence level.

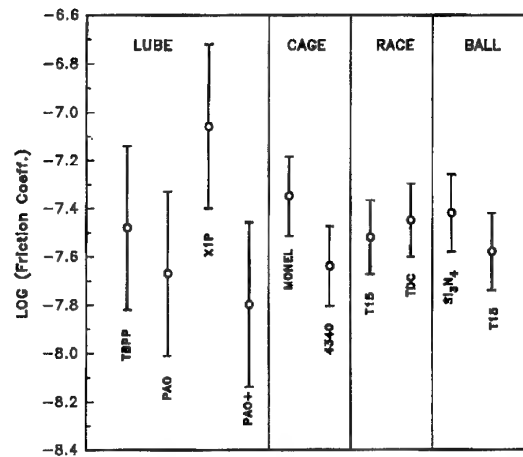


Figure 5(a). Ninety percent confidence bands for the mean response of the factor levels on the measured response for the logarithm of friction coefficient.

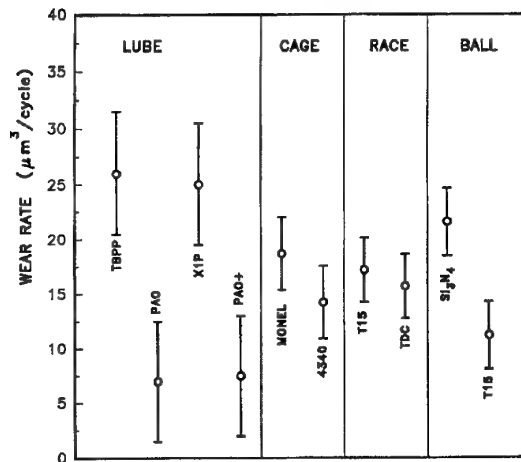


Figure 5(b). Ninety percent confidence bands for the mean response of the factor levels on the measured response for the bearing wear rate.

#### Post Test Examination

A photograph of the bearing track generated on the rod with TBPP vapor and the ferrous alloy system is shown in Fig. 6(a). The track has a highly polished surface, with surface damage consistent with micropitting from corrosion. From the profilometer trace of the wear track shown in Fig. 6(b), the depth of wear transverse to the rolling direction is closely approximated by an arc of 8.62 mm radius. The resulting maximum Hertzian contact pressure is 2.26 GPa, a 32 percent reduction from the initial contact stress. Superimposed on Fig. 6(a), are the initial and post-test major axes of the contact ellipse calculated from the Hertzian solution. Also from the Hertzian solution, the maximum tensile stress and surface shear stress due to elastic deformation occur at the contact boundary. Using the

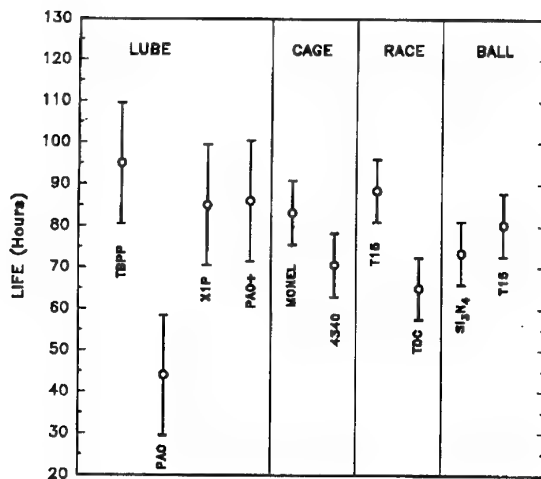


Figure 5(c). Ninety percent confidence bands for the mean response of the factor levels on the measures response for bearing life.

equations of Timoshenko (35), the magnitude of these stresses at the point where the elliptical boundary intercepts the major axes is 0.49 GPa. Microslip in the ball-on-rod contact will also occur in this vicinity to minimize the overall tractive forces. The surface distress seen in the vertical bands of Fig. 6(a), is attributed to an excess of the phosphate ion, tensile stress, and surface shear stress due to elastic deformation and sliding. Running horizontally in Fig. 6(a) is a denser region of micropitting distress. There

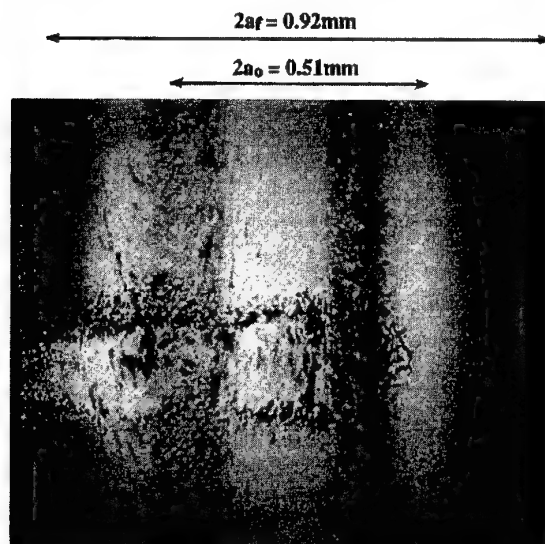


Figure 6(a) Wear track developed after 96 hours of testing with a T15 rod and TBPP vapor delivered at 1.17 ml/hr. The surface distress is attributed to corrosion accelerated by the phosphate ion and a high Hertzian contact stress field.

are three such regions in the bearing track corresponding to the ball spacing under static conditions. This damage occurred post-test before removing the specimens from the tester. The density of voids is attributed to corrosion along the crevice created by the ball and rod contact, accelerated by the phosphate ion, tensile stress, and elastic shear stress.

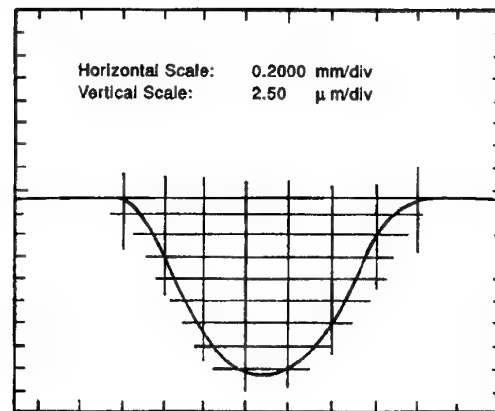


Figure 6(b). Profilometer trace of the wear track shown in Fig. 6(a).

The wear track generated with the PAO lubricant following pretreatment with TBPP is shown in Fig. 7. Deposits attributed to oil varnish are present on the bearing surface. All of the specimens lubricated with the PAO in the vapor phase, show the same type of deposits in the bearing track. While these deposits likely reduced the wear rate, they also contributed to bearing vibration. The shorter lifespan with PAO lubricant is largely attributed to vibration from varnish deposits.

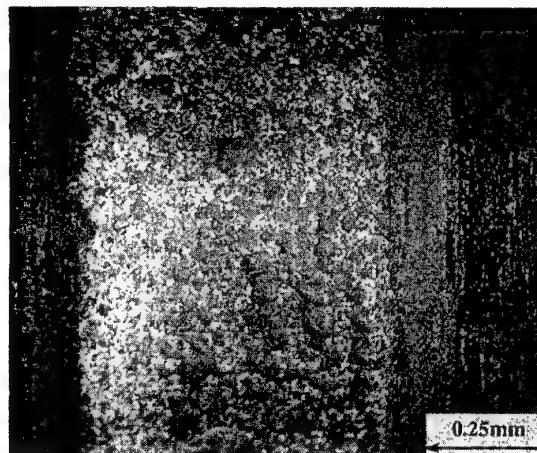


Figure 7. Wear track developed with a T15 rod and PAO vapor delivered at 3.40 ml/hr. The rod was initially lubricated for 2 hours with TBPP vapor delivered at 1.17 ml/hr. The deposits are attributed to oil varnish from the PAO vapor. The test failed due to bearing vibration at 61.8 hours.

The wear track generated with the X-1P lubricant and the ferrous alloy system is shown in Fig. 8. At a concentration of 1.17 ml/hr, the cyclophosphazene fluid generates a matte texture with a surface finish of 100 nm  $R_a$ . Although the as-ground surface finish is also 100 nm  $R_a$ , the topography produced by the X-1P fluid is very different.

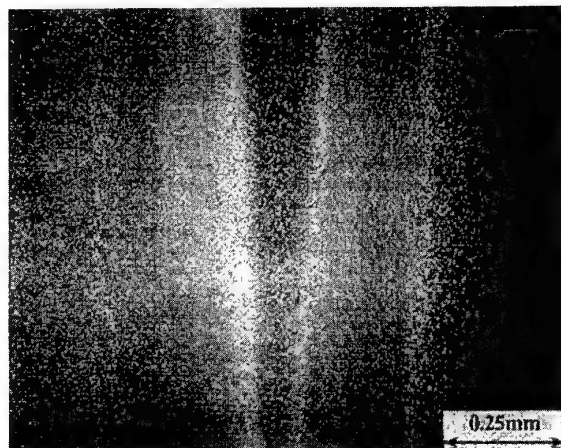


Figure 8. Wear track developed after 96 hours of testing with X-1P delivered at 1.17 ml/hr. The width of the track spans the entire picture. The matte finish is attributed to the presence of fluorine in X-1P.

The bearing track for the PAO+ lubricant and the ferrous system is shown in Fig. 9. A highly polished surface, similar to the track generated with the TBPP vapor is evident. However, there are no signs of the surface pitting which was produced with the TBPP at a concentration of 1.17 ml/hr. The surface finish in the track is 10 nm  $R_a$ . The material combination with the PAO+ lubricant, TDC races,  $Si_3N_4$  rolling elements, and 4340 cage, also produces a mirror surface finish. This type of finish was not seen with the other two PAO+ tests which used a Monel 400 cage, suggesting that debris from the sliding surface of the 4340 cage plays an active role in the polishing effect. This was also consistent for the combinations with the TBPP vapor and the Monel 400 cage.

Examination of the rods coated with TDC using energy dispersive spectroscopy, indicates the TDC coating was not present in the wear track after test. This was not surprising since the depth of wear for the rod specimens was typically an order of magnitude larger than the thickness of the TDC coating, which had a nominal value of 2 microns.

## CONCLUSIONS

Initial tests with a 2 cSt PAO fluid in the neat condition essentially showed no lubricating effect. However, when the surfaces were pretreated with TBPP vapor for a period of 2 hours under dynamic conditions, and then followed by the PAO lubricant in the neat condition, the ferrous alloy system

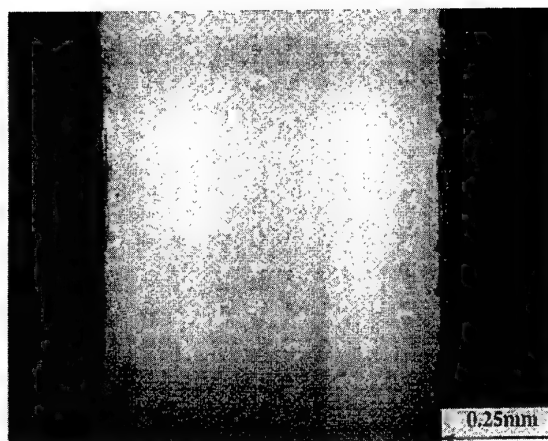


Figure 9. Wear track developed after 96 hours of testing with a T15 rod and a blend of 85 percent PAO with 15 percent TBPP delivered at 3.40 ml/hr. The surface finish in the track is 10 nm compared to 100 nm outside the track.

produced a bearing life of 61.8 hours. The ability to successfully operate a bearing after the TBPP pretreatment is attributed to the initial polishing produced by the TBPP vapor and the generation of a phosphate film. The presence of phosphate in the lubricating film has been detected on all of material combinations listed in Table 2 and will be discussed in a subsequent paper.

The performance of the PAO base stock was further enhanced when blended with fifteen percent TBPP. Overall, the PAO+ showed the best performance of the candidate VPD lubricants for the test conditions listed in Table 2. The performance of the PAO+ lubricant is largely attributed to the highly polished surface generated in the bearing track. The 10 nm finish translates into an order of magnitude improvement in film thickness ratio when compared to the as ground surface finish of 100 nm. Solid or liquid film lubricants have not demonstrated this type of polishing effect in the ball-on-rod test. Thus, an important aspect of the VPD lubrication mechanism appears to be the ability to compensate for thin film lubrication through chemical polishing. The concept of chemical polishing has been applied by Beeck (36,37) and by Klaus and Fenske (38,37) to explain the anti-wear properties of phosphorus containing lubricity additives in the liquid phase. In these early papers, the polishing effect was attributed to the formation of a phosphide eutectic. Subsequent papers by Godfrey (27) and Beiber et.al. (28), showed that TCP deposits a phosphate film rather than a phosphide film, and the role of TCP as a polishing agent was substantially diminished. In the vapor phase it appears that phosphate esters act as both polishing agents and phosphate film formers.

A critical parameter in chemical polishing from the vapor phase appears to be the concentration of TBPP. At a concentration of 1.17 ml/hr TBPP vapor generates a highly polished surface accompanied with micropitting in regions

associated with high tensile and surface shear stress. For the PAO+ test, the concentration of TBPP delivered was 0.51 ml/hr, and did not produce the micropitting seen with the TBPP in the neat condition. Also, the blending of TBPP with the PAO eliminated the oil varnish deposits which occurred with the PAO fluid in the neat condition. The effect of lubricant concentration on bearing performance is discussed in more detail in Part II of the companion paper.

The effect of ferrous alloys cannot be clearly determined from the test results, since the TDC coating was compromised due to wear in the bearing track. However, systems with higher Fe content generally produced lower friction, promoted longer life (except for the specimens with the Monel cage), and reduced the wear rate, particularly for T15 rolling elements compared to  $\text{Si}_3\text{N}_4$  rolling elements. The higher wear rate with  $\text{Si}_3\text{N}_4$  is attributed to the higher modulus of elasticity of ceramics compared to steel, which in turn generates a higher Hertzian contact stress for a given load. Additionally, surface analysis of the  $\text{Si}_3\text{N}_4$  rolling elements did not show the phosphate peaks found on T15 rolling elements and T15 rod specimens. Bearing specimens containing AISI 4340 cages produced a more pronounced polishing effect on the rod than specimens containing Monel 400 cages. Finally, the limited number of tests conducted can only determine the main effects of the design variables using statistical analyses. However, the data strongly suggests that interaction effects exist between the lubricants and bearing materials.

## References

1. Coit, R.A., Sorem, S.A., Armstrong, R.L., Converse, C.A., "Research in High Temperature Bearing Lubrication in the Absence of Liquid Lubricants," Air Force, WADC, TR-56-370, Part III (1957).
2. Graham, E.E., and Klaus, E.E., "Lubrication from the Vapor Phase at High Temperatures," ASLE Trans., **29**, pp 229-234 (1985).
3. Gunsel, S., "Development and Evaluation of a High-Temperature Lubrication System," PhD Dissertation, Pennsylvania State University (1986).
4. Klaus, E.E., Jeng, G.S., Duda, J.L., "A Study of Tricresyl Phosphate as a Vapor Delivered Lubricant," Lubr. Eng., **45**, pp 717-723 (1989).
5. Maki, J.F., and Graham, E.E., "Vapor Phase Deposition on High Temperature Surfaces," Trib. Trans., **33**, 4, pp 595-603 (1990).
6. Maki, J.F. and Graham, E.E., "Formation of Solid Films from the Vapor Phase on High Temperature Surfaces," Lubr. Eng., **47**, pp 199-206 (1991).
7. Groenewig, M., Hakim, N., Barber, G.C., Klaus, E.E., "Vapor Delivered Lubrication for Diesel Engines - Cylinder Kit Rig Simulation," Lubr. Eng., **47**, pp 1035-1039 (1991).
8. Graham, E.E., Nesarikar, A., Forster, N.H., Givan, G.D., "Vapor Phase Lubrication of High Temperature Bearings," Lubr. Eng., **49**, 9, pp 713-718 (1993).
9. Rao, A.M.N., "Identification of an Alternative Lubricant for Vapour Phase Lubrication," M.S. Thesis, Cleveland State University, (1993).
10. Hanayaloglu, B., Fedor, D.C., Graham, E.E., "Vapor Phase Lubrication of a Ni Base Superalloy," Lubr. Eng., **51**, 3 (1994).
11. Hanyaloglu, B., Graham, E.E., "Vapor Phase Lubrication of Ceramics," Lubr. Eng., **50**, 10, pp 814-820 (1994).
12. Klaus, E.E. and Duda, J.L., "Vapor Phase Lubrication Development for Engines," SAE Publ. SP-256, pp 541-550 (1991).
13. Lauer, J.L. and Bunting, B.G., "Catalytic Generation of Lubricants from Carbonaceous Gases on Surfaces Undergoing Friction at High temperatures," SAE Publ. SP-738, pp 51-60 (1988).
14. Lauer, J.L. and Dwyer, S.R., "Tribocchemical Lubrication of Ceramics by Carbonaceous Vapors," Trib. Trans., **34**, 4, pp 521-528 (1991).
15. Trivedi, H.K., Gerardi, D.T., Forster, N.H., Rosado, L., Givan, G.D., "A Modified Ball-on-Rod Contact Fatigue (RCF) Tester for Accelerated Testing of Candidate Lubricants and Bearing Materials," SAE Publ. SP-1069, pp 83-90 (1995).
16. Marino, M.P., and Placek, D.G., "Phosphate Esters," CRC Handbook of Lubrication and Tribology Vol -III, CRC Press, Inc., (1994), Ed. Booser, R.R., pp 269-286.
17. Nader, B.S., Kar, K.K., Morgan, T.A., Pawloski, C.E., Dilling, W.L., "Development and Tribological Properties of New Cyclotriposphazene High temperature Gas Turbine Engines," Trib. Trans., **35**, 1, pp 37-44 (1992).
18. Johnson, M.K., "Organophosphates and Delayed Neuropathy - Is NTE Alive and Well?" Toxic. and Appl. Pharm., **102**, pp 385-399 (1990).
19. Johannsen, F.R., Wright, P.L., Gordon, D.E., Levinkas, G.J., Radue, R.W., Graham, P.R., "Evaluation of Delayed Neurotoxicity and Dose-Response Relationships of Phosphate Esters in the Adult Hen," Toxic. and Appl. Pharm., **41**, pp 291-304 (1977).
20. Centers, P.W., "Potential Neurotoxin Formation in Thermally Degraded Synthetic Ester Turbine Lubricants," Arch. Toxicol., pp 679-680 (1992).
21. Kotkoskie, L.A., Freeman, C. Loeb, W., McConnell, R.F., Weiner, M.L., "Evaluation of the Acute Delayed Neurotoxicity of Durad 200B<sup>®</sup> Triaryl Phosphate in the Domestic Hen," The Toxicologists, **12**, p 280 (1992).



22. Latenderse, J.R., Brooks, C.L., Capen, C.C., "Pathological Effects of Butylated Triphenyl Phosphate - Based Hydraulic Fluid and Tricresyl Phosphate on the Adrenal Gland, Ovary, and Testis in the Fischer - 344 Rat," Toxic. Pathology, **22**, 4, pp 341-352 (1994).
23. Latendresse, J.R., Azhar, S., Brooks, C.L., Capen, C.C., "Pathogenesis of Cholesteryl Lipidosis of Adrenocortical and Ovarian Interstitial Cells in F344 Rats Caused by Tricresyl Phosphate and Butylated Triphenyl Phosphate," Toxic. and Appl. Pharm., **122**, pp 281-289 (1993).
24. Singler, R.E., Bieberich, M.J., "Synthetic Lubricants and High Performance Functional Fluids - Phosphazenes," Army Research Lab. Tech. Rept. ARL-TR-45 (1993).
25. Choa, S.H., Ludema, K.C., Potter, G.E., DeKoven, B.M., Morgan, T.A., Kar, K.K., "A Model for the Boundary Film Formation and Tribological Behavior of Phosphazene Lubricant on Steel," Trib. Trans., **38**, 4, pp 757-768 (1995).
26. Shankwalker, S.G. and Placek, D.G., "Oxidation and Weight Loss Characteristics of Commercial Phosphate Esters," Ind. Eng. Chem. Res., **31**, 7, pp 1810-1813 (1992).
27. Godfrey, D.G., "The Lubrication Mechanism of Tricresyl Phosphate on Steel," ASLE Trans., **8**, pp 1-11 (1965).
28. Beiber, H.E., Klaus, E.E., Tewksbury, E.J., "A Study of Tricresyl Phosphate as an Additive for Boundary Lubrication," ASLE Trans., **11**, pp 155-161 (1968).
29. Morales, W., Hanyaloglu, B., Graham, E.E., "Infrared Analysis of Vapor Phase Deposited Tricresyl Phosphate (TCP)," NASA Tach. Rept. TM-106423 (1994).
30. Glover, D., "A Ball-Rod Rolling Contact Fatigue Tester," ASTM SP-771, pp 107-124 (1982).
31. Box, G.E.P., Hunter, W.G., Hunter, S.J., Statistics for Experimenters, John Wiley & Sons, New York (1978), pp 374-412.
32. Neter, J., Wasserman, W., Kutner, M.H., Applied Linear Statistical Models, Irwin, Inc, Boston (1990), pp 818-836.
33. Neter, J., Wasserman, W., Kutner, M.H., Applied Linear Statistical Models, Irwin, Inc, Boston (1990), pp 580-585.
34. Box, G.E.P., Hunter, W.G., Hunter, S.J., Statistics for Experimenters, John Wiley & Sons, New York (1978), pp 232-234.
35. Timoshenko, S. and Goodier, J.N., Theory of Elasticity, McGraw-Hill Book Co., Inc., New York (1951), pp 376-381.
36. Beeck, O., J. Applied Phys., **12**, 512 (1941).
37. Hatton, R.E., "Phosphate Esters," Chapter 4, Synthetic Lubricants, Reinhold Publ. Co., London (1962), Eds. Gunderson, R.C., Hart, A.W., pp 119-121.
38. Klaus, E.E. and Fenske, M.R., Preprints Petroleum Division of ACS, **1**, 3, p 58 (1956).



## La fiabilité des roulements des petites et moyennes turbines de plus en plus dépendante de la tribologie

Gérard PATY/Brigitte CHEFTEL  
TURBOMECA - 64511 BORDES CEDEX FRANCE

### SUMMARY

Bearings reliability in the mechanical industry was in the past very dependant on material fatigue. Because of their high speed, aeronautical applications added high friction conditions and then generated more surface damages.

The important progress made with steel quality, particularly with vacuum elaborated types used in aeronautic prevent now most of the classical deep initiated fatigue failures.

Defect initiation moved toward contact surface which therefore becomes the research and development center of interest of the future years.

The high speed bearings are lubricated in the most effective manner. The creation of an oil film which separates the surfaces is essential to avoid metal to metal contact.

New computer codes as BEDALES and QUASAR have been developed with the European Community support during the last years which let to better understand and predict this behaviour.

Nevertheless turbine engines continue to suffer defects whose initiations are often linked with tribological weaknesses.

- Skidding is one of the most important. It depends widely on material surface temperature capacity.
- Deviations from good lubrication factor to poor one from external causes.
- Pollution of oil systems with hard particules is one other source currently investigated in terms of damage tolerance.
- Bearing cages have also sometime to withstand severe contact conditions which overlap the capacity of the current technology.
- Surface and subsurface stresses have an essential role in the control of the fatigue failure initiation and development. The investigations on a set of used bearings with new NDT techniques as Barkhausen noise show promising information to develop new tools in this area.

### Liste des symboles

BI : Bague Intérieure.

BE : Bague Exérieure.

Z : Nombre d'éléments roulants

CEC : Commission of the European Community

GAP : Groupe Auxiliaire de Puissance

PV : Facteur produit de la Pression par la Vitesse

N.Dm : Facteur produit de la vitesse de rotation par le diamètre primitif d'un roulement.

BB : Bruit Barkhausen

NDT : Non destructive Testing

Dp : Diamètre primitif (mm).

### 1. INTRODUCTION

Les roulements sont utilisés depuis très longtemps dans l'industrie mécanique pour assurer la liaison et le positionnement des parties tournantes relativement aux parties fixes.

La fiabilité des ensembles mécaniques dépend donc beaucoup de leur capacité d'endurance.

Les turbines aéronautiques qui équipent les avions comprennent des roulements qui sont soumis à des conditions d'utilisation très sévères.

Pour des raisons de sécurité, on exige des taux de panne des moteurs particulièrement bas. Le taux de défaillance accordé aux roulements aéronautiques est donc quasiment nul.

Pour satisfaire cette contrainte, des progrès très importants ont été faits dans le domaine des matériaux, surtout leur qualité de propriété.

La capacité de tenue en fatigue des roulements a fait un bon considérable ces 20 dernières années de telle sorte qu'on a identifié aujourd'hui un seuil de pression de contact en dessous duquel leur endurance est infinie.

Dans le même temps, les conditions de charge, vitesse et température se sont dégradées dans la mesure où tous les nouveaux moteurs sont conçus pour atteindre des puissances massives et des consommations spécifiques améliorées.

Des cas de fonctionnement plus pénalisant tels que l'interruption transitoire de lubrification, les facteurs de charges ou effets gyroscopiques aggravent leur fonctionnement en régime permanent.

Ces évolutions ont fait que le mode de défaillance des roulements (réduit en fréquence) s'est modifié en nature d'initiation. On observe désormais une majorité de dégradations initiées aux surfaces de contact de la plupart des éléments constituant un roulement (ref. 1).

Des efforts de recherche et développement se poursuivent et s'intensifient dans le secteur de la tribologie pour faire face à ces nouveaux modes de défaillance. L'industrie des turbines aéronautiques apporte un soutien actif à cette activité.

## 2. LES POINTS DE CONTACT ET LIAISONS D'UN ROULEMENT

Les différents éléments qui composent un roulement sont les suivants :

- La bague intérieure (BI). Elle est la plupart du temps liée à l'arbre et est l'organe moteur.
- La bague extérieure (BE). Elle est la plupart du temps liée aux parties fixes.
- Les éléments roulants (billes ou rouleaux).
- La cage (ou séparateur) qui a pour rôle d'éviter le contact entre eux des éléments roulants.

Le tableau 1 décrit en détail les interactions entre éléments, leurs modèles et les paramètres de sortie d'un code de calcul.

Contacts	Assumptions	Models	Results
1 Windage	Air-oil mixture generates oleodynamic drag	Bearing test • experimental results	• windage torque
2 Cage/ring	• light load • rigid surfaces • laminar or turbulent flow	Hydrodynamic • 'short journal bearing'	• load • torque • attitude angle as function of the eccentricity
3 Roller/ring raceway	• from none up to heavy load (inner ring)  • elastic deformations • rolling and sliding speeds	Elastohydrodynamic • Cheng theory • Gupta, Cheng et al. factor  Elastohydrodynamic • Johnson and Tevaarwerk theory	• lubricant film thickness • thermal reduction factor  • friction force
4 Roller/cage pocket	• light load • rigid surfaces	Hydrodynamic • Martin theory	• normal load • friction force as function of the roller position
5 Roller edges/pocket edges	• no load • no skewing	Hydrodynamic • couette flow	• friction force
6 Roller edges/ring riding	• no load • no skewing • with race flange angle	Hydrodynamic • couette flow	• friction force • friction torque

Tableau 1 : Interaction des éléments d'un roulement à rouleaux

## Les surfaces de contact d'un roulement à billes :

Chaque bille est en contact avec le BI, la BE et l'alvéole de cage :

soit :  $Z \times 3$  points de contact.

La cage est en contact avec une des deux bagues (centrage) par deux zones de contact.

Chaque bague est en interface de contact avec une autre pièce.

Le nombre de contacts d'un roulement à billes est donc :

$$4 + (Z \times 3).$$

ex : roulement à 15 billes --> 49 surfaces de contact.

## Les surfaces de contact d'un roulement à rouleaux

Les roulements à rouleaux sont en plus du roulement à billes dotés d'épaulements sur une des deux bagues pour guider les éléments roulants.

Cette différence fait qu'on dénombre  $2 \times Z$  contacts en plus par rapport au roulement à billes :

$$4 + (Z \times 5) \text{ points de contact.}$$

Ex : roulement à 15 rouleaux --> 79 surfaces de contact.

## La nature des contacts

On peut à priori isoler les deux contacts de liaisons des bagues avec leur environnement direct. En effet, tous les autres contacts sont lubrifiés par l'huile adressée au roulement et leur analyse découle de l'exploitation des résultats de codes de calculs dynamiques utilisant des modèles appropriés et validés.

Le comportement des premiers est de type contact métal/métal.

Le comportement des second qui concerne la majorité des problèmes est de type contacts lubrifiés.

## 3. DEFINITION DES ROULEMENTS ET TRIBOLOGIE

Il en va pour les roulements comme pour tous les mécanismes : leur comportement est d'autant meilleur que les frottements internes et dissipation d'énergie sont faibles (minimisation des usures et des échauffements).

Leur dimensionnement a donc comme

objectif important d'identifier les contacts qualitativement et quantitativement.

Ces contacts et leurs comportements dépendent d'un grand nombre de facteurs qui sont les suivants :

- Géométrie des surfaces en contact
- Qualité de l'état de la surface des deux corps.
- Propriété des matériaux en présence.
- Caractéristique du lubrifiant et nature du film d'huile.
- Température de masse, températures locales et leurs évolutions.
- Pressions de contact ou plus généralement état de contrainte des corps (en surface et sous couche).
- Vitesses de glissements locales.
- Niveau de pollution du lubrifiant et de l'environnement immédiat du roulement.

Les codes de calculs à la disposition des concepteurs permettent de prévoir les paramètres en fonction des conditions de travail imposées.

Les régimes de fonctionnement d'un moteur sont variables et donc les états d'équilibre des roulements le sont aussi. Il est essentiel de bien connaître l'ensemble de ces éléments pour optimiser la définition.

La géométrie des roulements est dans un premier temps faite pour satisfaire les niveaux de contraintes inférieurs au seuil de fatigue des aciers utilisés.

A partir d'une géométrie définie, des moyens de calculs de plus en plus performants sont utilisés pour prédire leur comportement exact dans tous les domaines d'utilisation.

Les motoristes, Européens ont par exemple réuni leurs moyens avec ceux d'universités Anglaise et Française pour développer deux codes de calculs (l'un pour les roulements à billes, l'autre pour les roulements à rouleaux) dans le cadre du projet "Bearing Lub - projet PL 1103" soutenu par la CEC (réf. 2).

Ces codes de calculs, respectivement BEDALES (billes) et QUASAR (rouleaux) permettent de prédire les puissances dissipées exactes par les roulements en fonction des modes et débits de lubrification. (Figures 2 et 3 : comparaison des puissances dissipées et vitesses de cage mesurées et calculées par BEDALES pour deux roulement différents).

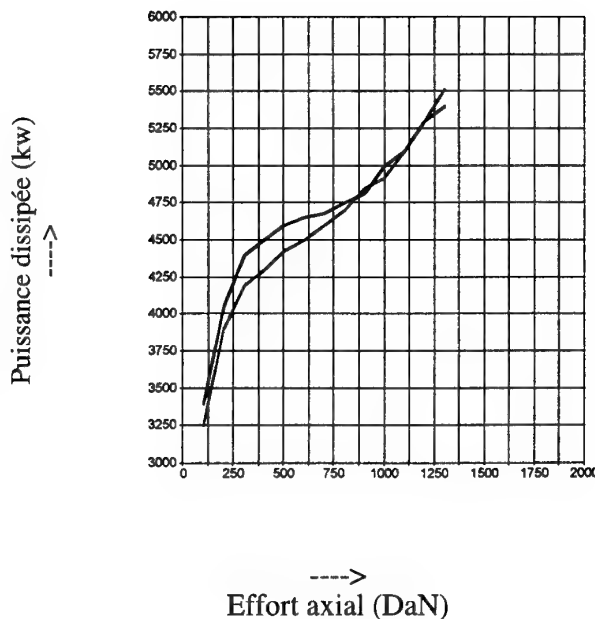


Fig. 2 : Puissance dissipée totale d'un roulement. Résultats de calcul et de mesure

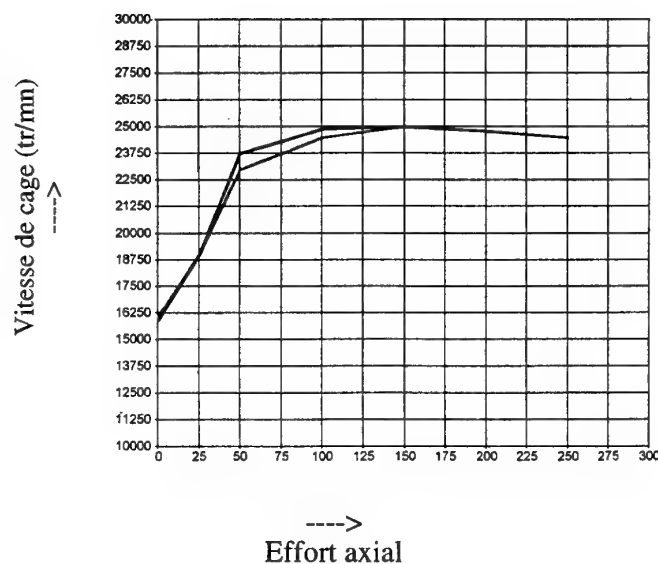


Fig. 3 : Vitesse de cage - Résultats de calculs et d'essais (Narbre = 54300 tr/mn).

Ils livrent également les vitesses exactes des éléments et donc permettent le calcul précis de l'état des contacts éléments roulants/pistes.

Entre autre, les épaisseurs de film d'huile sont estimées avec une précision améliorée.

En théorie donc les conditions sont réunies pour que les roulements ne subissent pas d'avarie par rapport aux paramètres de fonctionnement pour lesquels ils ont été conçus.

Dans la pratique on observe des défaillances aux origines variées dont une bonne partie suite à des dégradations des contacts. Les lignes qui suivent tentent de décrire les cas qui se rapportent à des problèmes tribologiques en illustrant d'exemples concrets rencontrés sur moteur en service par TURBOMECA.

#### 4. LES DEFAILLANCES INITIEES EN SURFACE :

##### 4.1 La privation de lubrification et ses conséquences sur les surfaces

Toutes les surfaces de contact où ont lieu des déplacements relatifs sans charge nécessitent une lubrification ininterrompue pour éviter le contact métal/métal, les concentrations de contrainte et frottements excessifs.

Bien qu'on apporte un soin particulier aux systèmes d'alimentation en huile les roulements ont à subir des défauts de lubrification volontaires ou involontaires.

##### Interruptions de lubrification - cas connus d'utilisation :

- Les Groupes Auxiliaires de Puissance (GAP).

La nécessité pour ces moteurs auxiliaires d'avions civils de démarrer par temps froid en un temps limité oblige à mettre hors service le circuit d'huile pendant cette phase ainsi qu'à l'arrêt.

Les roulements ne sont donc pas lubrifiés pendant des durées non négligeables (30 s au démarrage - 45 s à l'arrêt).

- Les turbomoteurs d'hélicoptères effectuent des manoeuvres qui induisent des effets gyroscopiques ou des facteurs de charge importants. Ces situations peuvent conduire au désamorçage de la pompe de lubrification pendant plusieurs secondes.

- La tendance dans le domaine des applications militaires est d'accroître les exigences de durée de fonctionnement sans huile.

#### Rupture de film d'huile - occurrence aléatoire

Cette situation ne correspond pas à une défaillance d'alimentation en lubrifiant du moteur mais à une rupture du film d'huile d'un ou plusieurs contacts.

#### LE SKIDDING

Le cas le plus typique est l'endommagement par skidding. Cette défaillance intervient dans un contexte bien particulier de charge et de vitesse du roulement.

L'état d'équilibre normal du roulement est tel que les éléments roulants sont entraînés à une vitesse de rotation épicycloïdale de valeur théorique connue. Ceci est vrai à condition que l'effort de traction motrice des contacts BI/éléments roulants soit suffisant pour équilibrer les efforts de frottement interne des autres contacts. Or cette condition n'est pas remplie pour certaines combinaisons de charge faible et vitesse de rotation élevée ce qui se traduit par un taux de glissement au contact BI/éléments roulants (le moyen pratique de le constater étant la mesure vitesse de la cage qui n'est pas conforme à sa valeur théorique). Voir figure 4.

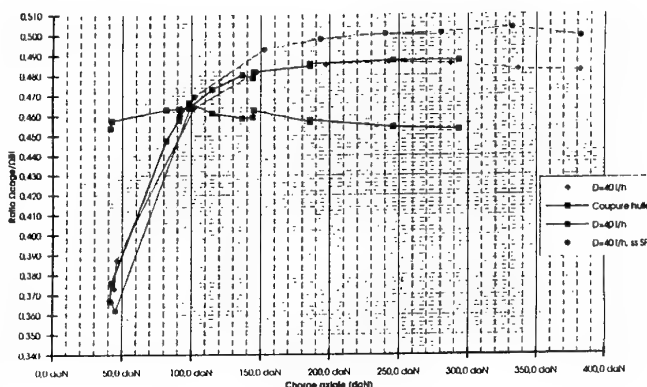


Fig. 4 : Ratio vitesse/cage en fonction de la charge axiale (NBI = 49300 tr/mn)

En situation de glissement stabilisé un film d'huile reste la plupart du temps établi aux contacts.

Pourtant, l'observation des contacts tels que ceux endommagés sur la fig. 5 font apparaître une transformation métallurgique de surface qui reflète une forte élévation de température locale témoignant un contact métal/métal (perte de caractéristique des matériaux).

Une explication possible est la rupture temporelle du film d'huile par échauffement ponctuel. Ceci peut être la conséquence d'un changement d'état d'équilibre du roulement vers moins de glissement par accroissement de charge (régime moteur différent).

Les contacts du roulement sous état de glissement reçoivent alors très transitoirement une élévation de contrainte combinée à une vitesse locale élevée (avant rétablissement du régime proche du théorique épicycloïdale).

Le facteur PV local élevé est source de calories (effet de flash température) dégradant très superficiellement le métal.

L'aspect des pistes qu'illustre la fig. 5 est caractéristique des premiers symptômes d'un roulement subissant du skidding (aspect satiné).

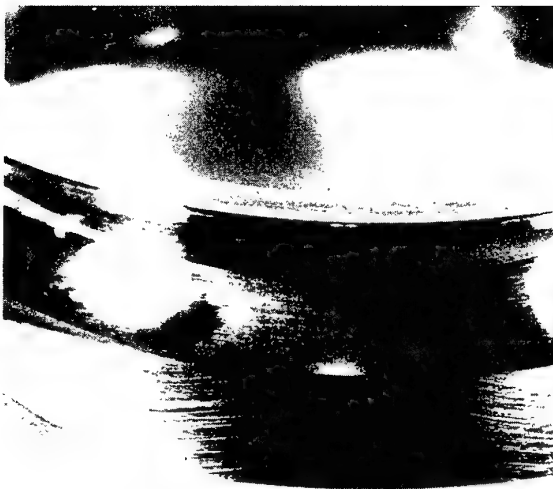


Fig. 5 : Traces superficielles de skidding sur un roulement à billes

Un fonctionnement prolongé conduira à une usure progressive plus ou moins importante des pistes intérieures et éléments roulants (figure 6).

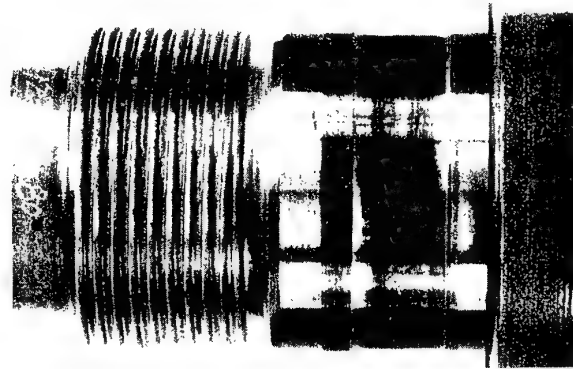


Fig. 6 : Usure par skidding d'une piste intérieure de roulement à rouleaux (0,1 à 0,2 mm de profondeur)

La géométrie interne du roulement se dégrade progressivement altérant ses fonctions de positionnement des pièces mobiles.

En final, le roulement se détruira complètement, pouvant entraîner des dommages très importants au moteur.

Le **skidding** est un des problèmes majeurs auquel doivent faire face les motoristes. L'accroissement des vitesses de rotation des turbines futures les exposera toujours plus à ce phénomène.

Pour y faire face, les moyens suivants sont employés :

- Usage d'acier à capacité élevée en température : TURBOMECA a pu dans le passé éviter des dégradations par skidding en utilisant du M50 (température de revenu environ 550° C) en lieu et place de l'acier 52100 (température de revenu 235°C).

On peut supposer que l'usage d'acier à capacité en température plus élevée apporterait un gain significatif. Malheureusement les volumes d'acier consommés par l'industrie aéronautique du roulement ne sont pas toujours suffisant pour susciter les développements de nuances nouvelles.

On observe avec intérêt l'arrivée annoncée depuis longtemps de la céramique sur les éléments roulants. Ils ne représentent cepen-

dant qu'une moitié du contact.

Faute de disposer des pistes en matière à capacité en température adéquate, on peut imaginer que des revêtements performants seraient apte à remplir ce rôle de bouclier thermique de protection d'un phénomène de surface.

Les revêtements testés jusqu'alors n'ont pas démontré leur attitude à jouer ce rôle combiné de capacité thermique à faible charge/glissement élevé et d'accrochage à la sous-couche sous forte pression de contact.

Le problème posé est typiquement un problème tribologique dont la solution aurait des retombées industrielles très positives.

- Les autres moyens pour éviter le skidding consistent à faire des choix de construction des roulements qui minimisent les contacts de frottement récepteurs et maximisent les frottements moteurs.

On obtient aussi de bons résultats en dimensionnant au plus juste le roulement en capacité de charge afin de bénéficier d'une pression de contact ponctuelle élevée aux interfaces éléments roulants/Bi.

Il faut cependant veiller à rester dans les limites d'endurance en fatigue des matériaux.

On peut noter cependant que tout progrès dans la tenue en fatigue des matériaux et leur bonne maîtrise a des retombées positive sur les moyens pour faire face au skidding.

## LE FACTEUR DE LUBRIFICATION

On a vu que la présence d'un film d'huile aux contacts est indispensable pour assurer la survivance mécanique. Le paramètre qui permet de juger que la lubrification est efficace est :

$$\lambda = h_o / (\sigma_1^2 + \sigma_2^2)^{1/2}$$

où  $h_o$  est la hauteur minimum calculée au film d'huile.

Les modèles de film d'huile utilisés dans les codes de calculs de roulements sont généralement :

Roulement à billes : Hamrock and Dowson  
 $H_o = 2,69 U^{0.67} G^{0.53} Q^{-0.13} (1-e^{-.73 K})$

Roulement à rouleaux : Dowson and Higginson :

$$H_o = 2,65 U^{0.7} G^{0.54} Q^{-0.13}$$

$\sigma_1$  et  $\sigma_2$  sont les rugosités des deux surfaces en contact.

On vérifie que le paramètre  $\lambda$  n'est pas inférieur à 1,5 en fonctionnement ce qui assure une séparation totale des deux surfaces.

Paramètre de lubrification		
Position du roulement	Huile type MILL 23699	Huile type MILL 7808G
1	2.8	1.9
2	2.8	1.9
3	3	1.95
4	2.5	1.5
5	2.2	1.4
6	2.4	1.5
7	2.4	1.5
8	1.65	1
9	2.6	1.5
10	2.65	1.5
11	2.2	1.6
12	2.6	1.5

Tableau 2 : paramètre des roulements d'un turbomoteur en fonction du type d'huile (aux température et puissance maxi de fonctionnement).

Le tableau 2 illustre le cas d'un moteur en service et laisse apparaître le peu de marge de sécurité disponible dans le cas d'usage de l'huile la plus défavorable en viscosité.

Toute divergence d'un des facteurs influant sur le paramètre  $\lambda$  crée une situation de lubrification marginale et un risque de dommage aux surfaces (ref. 3).

Les facteurs qui influent sont :

- La température (élévation anormale transitoire).
- La charge (dégradation en balourd des mobiles par exemple).
- La rugosité (pollution générant des empreintes).
- Le frottement de glissement.

L'exemple du tableau 3 contient la liste des valeurs de rugosité mesurées sur les bagues intérieures d'un lot de roulement.

Ils occupaient tous la même position à l'intérieur du moteur et ont effectué entre 500 H et 2500 H en service sur hélicoptère. (La valeur maxi spécifiée à la définition est de 0.15).

Ce roulement est celui qui a le taux de fiabilité le plus faible parmi 15 exemplaires sur ce moteur. On constate que 3 individus ont vu leur rugosité se dégrader en service, dont un a plus que doublé la valeur maxi tolérée en neuf.

Cette observation est sans doute à mettre en rapport avec les défaillances constatées.

Rugosité mesurée Ra		
0,08	0,09	0,17
0,31	0,07	0,13
0,08	0,10	0,10
0,27	0,06	0,10
0,14	0,15	0,13
0,08	0,08	

Tableau 3

Dans ce contexte de défaillance de surface initiée par un défaut de film de lubrifiant les motoristes aéronautiques Européens supportent avec le soutien de la CEC le programme de recherche "ELABOMM" se rapportant à l'analyse des paramètres influents sur la limite d'endurance en fatigue des roulements. Les travaux entrepris s'appliquent en partie à une meilleure description des conditions de création complète ou partielle des films d'huile et leur conséquence sur l'état de contrainte de surface. Les résultats de ces travaux seront publiés en 1997.

## 4.2 La pollution des systèmes de lubrification

Le lubrifiant adressé aux organes mécaniques d'un moteur est normalement débarrassé des particules polluantes de taille supérieure au niveau de filtration prévu à la conception du circuit d'huile.

Le schéma illustré par la fig. 7 montre que le circuit de récupération de l'huile de la machine peut être aussi équipé de moyens de filtration (double effet).

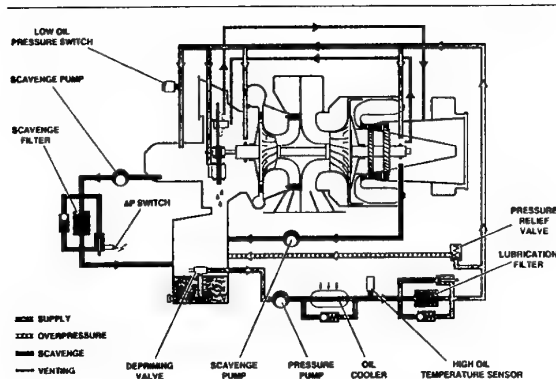


Fig. 7 circuit d'huile d'une turbine

Cependant, leur efficacité est limitée dans la plupart des moteurs à une taille de 20  $\mu$ .

Par ailleurs, les filtres sont court circuités en cas de démarrage temps froid ou systématiquement (dans le contexte des GAP) au démarrage et à l'arrêt.

De même, les particules générées par le moteur au cours de son fonctionnement peuvent migrer directement dans l'enceinte d'un roulement.

Enfin, et bien qu'on y apporte un soin particulier, le nettoyage et la dépollution des pièces neuves laissent parfois subsister des corps étrangers.

Par conséquent, la pollution par particules est une source d'endommagement de surface non négligeable pouvant affecter le bon fonctionnement des roulements.

Le schéma de la figure 8 représente un pignon en appui sur 2 roulements à rouleaux et dont l'effort axial est communiqué à un piston à huile (installation de moteur d'hélicoptère).

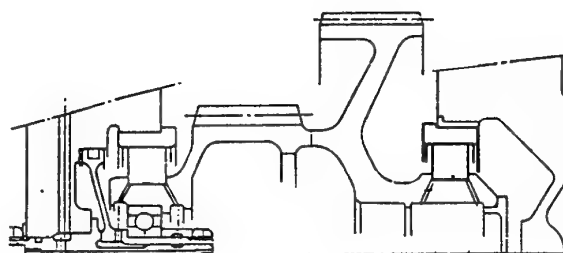


Figure 8 : Montage d'un pignon sur 2 roulements à rouleaux

Par un mouvement d'ouverture d'un diaphragme qui entraîne un déplacement du pignon de 0,1 mm (maximum) la pression d'enceinte du piston se règle à une valeur image du couple moteur qui est un paramètre exploité par le pilote de l'hélicoptère.

La précision exigée est importante et peut se trouver altérée par une dégradation des frottements parasites, en particulier ceux du contact rouleaux/piste de BE des roulements.

Des cas ont été effectivement rencontrés de rayures provoquées par des corps étrangers très dur qui ont entraîné un dysfonctionnement de la mesure de couple.

La réponse tribologique apportée pour améliorer la situation a été de durcir les pistes par un revêtement approprié pour que la présence d'une particule dure ne provoque plus la dégradation de surface constatée.

#### 4.3 Les contacts particuliers intervenant sur les cages

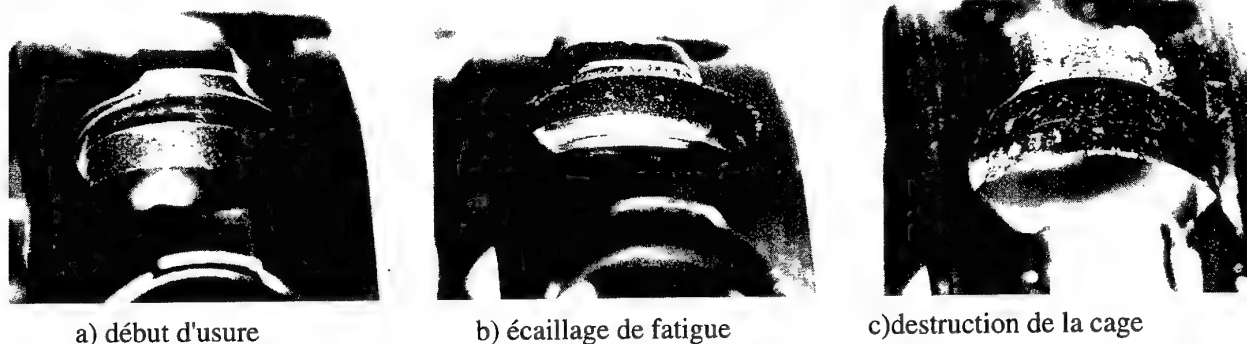


Figure 9

Tous les roulements sont équipés d'une cage qui sépare les éléments roulants. L'importance de ce composant est grande dans les applications aéronautiques du fait des vitesses très élevées.

La majorité des roulements fonctionne aujourd'hui à des N.Dm (\*) compris entre  $2,5 \times 10^6$  et  $3 \times 10^6$ . Ils dépasseront de beaucoup  $3 \times 10^6$  à l'avenir. Les cages sont donc définies avec soin pour être positionnées correctement du fait de leur vitesse élevée. Cette localisation relativement aux autres pièces se fait par des zones de contact aux vitesses élevées.

Son centrage sur l'axe de rotation est obtenu sur un diamètre dit de centrage par rapport à la BI ou la BE. C'est le lieu d'un contact à vitesse élevée sous charge faible ou modérée. Ce contact acier (bague) contre argent (revêtement antigrippant de la cage) ne pose pas de problème particulier s'il est alimenté correctement en lubrifiant.

Cependant, des cas d'usures très importantes ont été rencontrés avec l'arrivée d'un nouveau matériau de bague (M50-NIL) acier de cémentation de nouvelle génération. Des revêtements appropriés

ont permis de faire face aux dégradations.

L'autre contact caractéristique est celui des éléments roulants avec les faces des alvéoles de la cage dans laquelle ils sont contenus.

Les efforts de contacts sont théoriquement modestes en conditions normales. (Charge axiale pure des roulements à billes par exemple).

L'exemple des fig. 9 est caractéristique d'un couple pression de contact/vitesse dépassant les capacités tribologiques du contact billes acier/cage argentée (vitesse de frottement 72 m/s).

La progression de l'endommagement est la suivante :

Fig. 9a) : refoulement de l'argent pour arriver au contact métal/métal.

Fig. 9b) : progression de l'écaillage en fatigue.

Fig. 9c) : rupture de la cage (perte d'intégrité) qui va engendrer la destruction du roulement.

Faute de disposer de matériaux et revêtements de cages mieux adaptés aux contraintes imposées, les voies d'amélioration possibles sont :

- réduction de la valeur de l'effort de contact
- adaptation de la géométrie des alvéoles pour diminuer la pression de contact à charge égale.

#### 5. MAITRISE DES CONTRAINTES RESIDUELLES AU PROFIT DES SURFACES ET DES SOUS-COUCHES

Les événements initiés en surface prenant une place prépondérante, on s'intéresse dés-

(\*) N.Dm facteur représentatif de la sévérité de fonctionnement (N, vitesse de rotation en tr/mn et Dm, diamètre primitif en mm).



ormais plus à l'état de contrainte de la surface et les massifs immédiatement proches.

Il a été démontré qu'à l'état neuf un roulement devait avoir sa surface sous un état de contrainte de compression. Des essais ont en effet mis en évidence que ces contraintes de compression étaient propres à ralentir ou contenir les micro-fissures qui dégénèrent en écaillage.

On s'intéresse donc de près au profil de contrainte des pistes en fonction de la profondeur.

De même, un roulement après fonctionnement montre un profil de contraintes résiduelles différent de l'initial du fait des conditions de contact imposées durant sa vie (pression de hertz, frottement, contraintes tangentielles centrifuges et thermiques, voir transformation métallurgique).

C'est là aussi le soucis du programme de recherche Européen "ELABOMM" que de corréler l'endurance limite des roulements avec l'état de contrainte observé en fonctionnement pour tenter de déterminer par le profil de contraintes résiduelles le potentiel de vie consommé en service.

Dans le cadre de ce projet, TURBOMECA, avec l'aide de deux partenaires industriels (SNFA (1) et SYSMAT (2)), a entrepris l'évaluation de roulements issus de moteurs ayant fonctionné entre 500 H et 2500 H.

L'étude en cours s'est donnée comme objectif d'essayer de corréler les mesures des contraintes résiduelles (méthode destructive, longue et coûteuse et les mesures de bruit BARKHAUSEN (méthode non destructive).

La méthode du bruit BARKHAUSEN (B.B) consiste à soumettre la pièce à un champ d'induction temporel et de mesurer la réponse de la pièce due aux propriétés magnétiques du matériau et ses liens avec l'état de contrainte.

Dans un premier temps, la relation contrainte résiduelle et bruit BARKHAUSEN a été recherchée.

C'est ce qui apparaît sur le diagramme de la fig. 10.

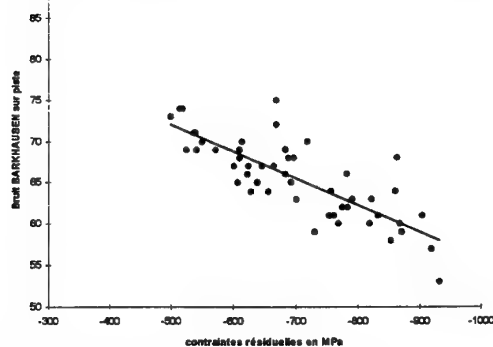


Figure 10 : Relation bruit Barkhausen et contraintes résiduelles

- (1) SNFA : fabricant de roulements aéronautiques  
(2) SYSMAT : fabricant de matériel de contrôle non destructif.

La relation contrainte résiduelle avec le nombre d'heures de fonctionnement ressort du diagramme de la figure 11.

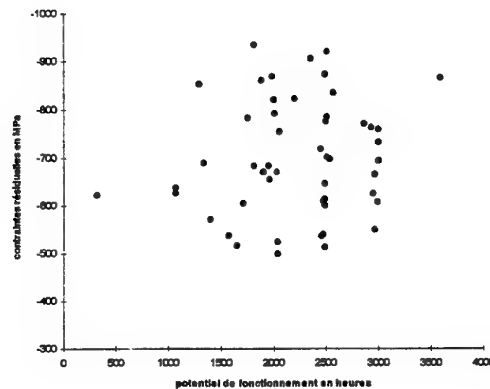


Figure 11 : Relation Bruit Barkhausen en fonction du nombre d'heures

En fait, cette relation n'existe pas. Par contre, la figure 10 démontre que la technique du B.B corréle la mesure de contrainte résiduelle de surface (avec une marge d'erreur).

Des outils plus sophistiqués ont été utilisés pour analyser avec plus de finesse la globalité des pistes (288 points de mesure par pièce);

En particulier, des cartographies de B.B ont pu être construites.

Les figures 12 et 13 représentent un échantillon des résultats :

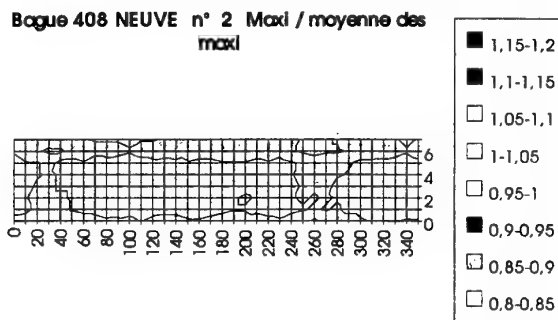


Figure 12 : Cartographie BB d'une bague neuve

Bague 408 n° 797 Maxi / moyenne des maxi

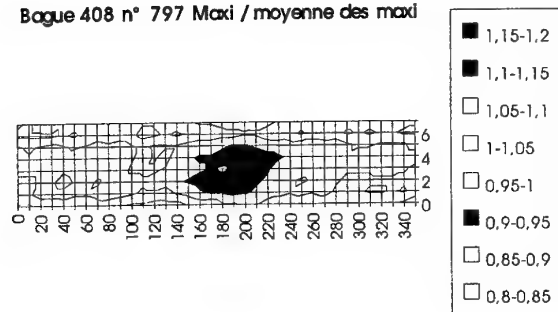


Figure 13 : Cartographie BB d'une bague usagée (770 H)

- La carte de la figure 12 représente la réponse B.B d'une bague "neuve". On y observe une bonne homogénéité des valeurs (peu de dispersion).
- La carte de la figure 13 représente la réponse B.B d'une bague ayant fonctionné sur moteur. On y repère une singularité.

Les travaux se poursuivent actuellement par des coupes micrographiques pour mettre en évidence une éventuelle amorce de fatigue en sous-couche.

Il reste encore du chemin à parcourir pour confirmer la méthode B.B comme un moyen de contrôle NDT efficace et industriellement économique. Les travaux en cours montrent entre autre que chaque matériau a une réponse bien spécifique. Cependant, les premiers résultats sont encourageants.

Leur confirmation aurait probablement des retombées industrielles dans l'évaluation de l'état de fatigue des roulements après service ainsi qu'en contrôle sur chaîne de fabrication.

## 6. CONCLUSION

L'industrie du roulement a dans un passé encore récent conduit des travaux importants pour améliorer le comportement en fatigue des aciers. Les résultats ont été très spectaculaires

et des progrès continuent d'être enregistrés dans ce domaine.

L'industrie des turbines aéronautiques qui utilise les roulements dans des conditions très sévères a été la première à bénéficier de ces retombées.

Cependant, les développements des turbines exigent toujours plus de performances à des organes mécaniques toujours plus sollicités.

Les types d'endommagements qui subsistent pour l'avenir orientent les recherches dans le domaine des surfaces et de la tribologie.

Les voies de recherche sont aujourd'hui tracées mais des travaux importants restent à conduire pour fournir des solutions industrielles.

## REMERCIEMENTS :

Les auteurs adressent leurs remerciements aux institutions ou sociétés suivantes :

**Communauté Economique Européenne** pour son soutien apporté aux programmes de recherche "BEARING LUB" et "ELABOMM".

**SNFA et SYSMAT** pour leur contribution aux travaux du programme "ELABOMM".

**Les Partenaires Industriels et Universitaires** des programmes "BEARING LUB" et "ELABOMM".

## REFERENCES :

1. Averbach B. (MIT ; Cambridge, MA), Van Pelt S. and Pearson P. (The Torrington Co. Torrington, CT), "Initiation of Spalling In Aircraft Gas Turbine Bearings, AIAA/SAE/ASME/ASME, 26th Joint Propulsion Conference, July 16-18, 1990/ORLANDO, FL.
2. Dunker R (EC Aeronautics Research Series, European Commission, DGXII, Brussels), "Advances in Techniques for Engines Applications - Chapter 1 : Bearing with minimum Lubrication".
3. Bailey D.M. (Westland Helicopters) and Sayles R.S (Imperial College of Science/UK), "Effect of Roughness and Sliding Friction on Contact Stresses". Journal of Tribology, Oct 91, Vol 113.
4. Ioannides E. (SKF ERC.BV), Harris T.A., Ragen M. (SKF/MRC Bearings) and Tam H. (SKF/MRC Bearings), "Endurance of Aircraft Gas Turbine Mainshaft Ball Bearings. Analysis Using Improved Fatigue Life. Part 1 and Part 2". Journal of Tribology - 1990.
5. AGARD-CP 323 "Problems in Bearings and Lubrication" 59th symposium of the AGARD Propulsion and Energetics Panel, Ottawa, Canada, on 31 May - 3 June 1982.

# Airseals for Advanced Military Jet Engines

T.J. Uihlein

Daimler-Benz Aerospace  
MTU Motoren- und Turbinen-Union  
München GmbH  
80995 München  
Germany

## 1. SUMMARY

In advanced military jet engines airseals represent one of the most challenging key technologies. Without properly functioning seal systems it is not possible to attain the high pressure ratios needed for high efficiencies and low specific fuel consumption.

Moreover a poorly functioning seal system can result in blade losses and titanium fire, or in heavy damage to the rotor in the case of labyrinth seals, which is even more dangerous.

To overcome these problems a basic understanding of the wear mechanisms of the different seal systems is necessary. This requires rub testing under simulated engine conditions to determine the limitations of each system. Only with this knowledge the design and improvement of abrasives, fin coatings or tip coatings can be successful. Apart from abrasability this optimization also includes, for example, erosion resistance, high cycle fatigue strength of tip coated blades or damage tolerance of abrasives against blade passing frequencies.

## 2. INTRODUCTION

In modern high-pressure and high-temperature turbines gas leakage has become an ever increasingly important parameter to be minimized.

The performance and efficiency of these gas turbines depend on clearances between stationary gas path seal components and rotating blade tips or knife edges of labyrinth seals (Fig. 1). Thus, for instance, an increase of 0.1 mm in the gap of all rotors of a compressor means an additional fuel consumption of 0.3 %, loss of 2.5 % compressor stall and surge margin and loss of 0.4 % efficiency.

To maintain this margin and to reduce the loss of energy, excellent gas-path seals are necessary to diminish gap losses. These seals must be rub tolerant or, precisely speaking, abrasable. Abrasable seal systems represent one of the most significant applications of coatings in gas turbine engines today. They have to withstand rubs at extremely high speeds of up to 500 m/s without developing

destructively high temperatures and stresses with rotating components.

## 3. CAUSES OF RUBBING AND FAILURES

Rubs are mainly caused by:

- Thrust, gust, manoeuvre, landing, centrifugal and gyroscopic loads
- Vibration of rotor and casing
- Rotor orbit and subharmonic orbiting
- Thermally driven dimensional changes and thermal mismatch between rotor and stator
- Engine shaft thermal bow
- Rotor eccentricity and unbalanced parts
- Machining tolerance variations
- Surge-and-stall-caused displacements
- Maldistribution of temperature and cooling air
- Non-axisymmetric structures.

The chance of a rub is highest during the first five to ten flights. And the deterioration is greatest in the first few hours followed by a lower rate of wear-in depending on erosion rate and number of adverse events.

These high frictional rub energy conditions produce heat and the local thermal expansion leads to ever more concentrated contact. This means increased rub, densification of the abrasable, smearing and more violent future interactions. The destructively high temperatures are associated with a change in microstructure of the material, thermal stress cracking, lowering of blade hot hardness, increasing blade and fin wear, oxidation and material transfer to the seal (Fig. 2).

## 4. DESIRABLE GEOMETRY AND PROPERTIES

From the point of view of structural integrity and of maintaining engine efficiency, wear is to affect static components rather than rotor components. This is easily understandable because wear to the stator results in a smaller increase in leakage area than the 360° area increase which occurs with rotor wear. In addition there is a decrease in active blade or fin area (Fig. 3). Another reason is that blading is very

expensive in comparison with cases and difficult to repair.

Besides minimal blade and fin wear and low cost other desirable properties of gas-path seals and especially abrasives are:

- Long-term temperature stability
- Resistance to thermal cycles
- Resistance to blade passing frequencies
- Gas and particulate erosion resistance (not compatible with abrasibility)
- Corrosion resistance to salt water, engine fuels and hydraulic fluids
- No leakage through open porosity
- Little, innocuous and inert debris
- Good, clean chip formation
- Quick removal of the chips
- No adhesive transfer to blade tip and vice versa
- Low energy rub or contact friction
- Avoidance of self ignition and ignition of wear debris
- Smooth surface after wear for minimal aerodynamic losses
- Reproducibility of production of abrasives
- Easy repair.

This long, still incomplete list of requirements illustrates the need for optimization of the respective seal system.

## 5. TYPES OF GAS-PATH SEAL MATERIAL SYSTEMS EMPLOYED IN GAS TURBINE ENGINES

To limit the number of seal systems and clearance control coatings discussed here, the focus shall be on knife edge and blade tip geometries of the compressor, which can be considered to be representative.

### 5.1 Low-density metallic types

These rub materials consisting of metal powders or fibers with 60 to 80% porosity are mostly sintered. Their friable nature allows discrete particles to break off from the seal surface (Fig. 4). Easy fracturing at interparticle boundaries and the brittle release of material are responsible for a low energy rub.

### 5.2 More dense structures

With these materials with less than 30% porosity the local operating temperature and the application temperature range are the primary consideration in the material selection. Production methods are thermal spraying, sintering, which requires brazing, hot pressing or casting for example. This class of materials also contains 100% dense low shear strength abrasives like aluminium alloys filled with plastics or graphite which are subject to plastic deformation by machining mechanisms (Fig. 5).

The most common materials, ranked according to their temperature stability, are:

- Elastomeric and plastic materials filled with fibers, hollow glass spheres, graphite, talcum and other organic and inorganic additives.
- Plastic and aluminium honeycombs with very little material-to-material contact area.
- Low- and high-temperature metals like the above-mentioned aluminium alloys, nickel graphite, nickel alloyed with chromium and/or aluminium and mixed with hexagonal boron nitride, bentonite or calcined clay.
- And for very high temperatures and exacting demands regarding erosion resistance dense metals alloyed with chromium, aluminium and yttrium and filled and unfilled metallic honeycombs.

For labyrinth seals alloys containing copper and silver and bronzes are additionally used.

### 5.3 Inert fillers enhance abrasibility

Fillers (Fig. 6) fulfil various functions by

- reducing stresses in thick coatings
- restricting plasticity and in this way hindering transfer to the rotor and
- lessening the binding surface area around a spray particle and thus acting as a release agent which improves abrasibility.

### 5.4 Blade tip and fin coatings

Especially fin coatings like alumina and wear-resistant coatings like carbides in metal matrix are quite commonly used. Blade tip treatments have so far been restricted to the turbine to protect the tips against fatigue failure from tip grooving and overheating.

Besides wear resistance and chemical compatibility with the blade material, another requirement is that there must be only a minor influence on the vibratory fatigue strength, which represents a big challenge.

## 6. TECHNOLOGY DEVELOPMENT STRATEGY

The aim is to describe and forecast the behaviour and the limits of gas path seals and to develop an understanding or model for further optimization.

Prerequisites for doing so are the availability of abrasibility rigs and wear mechanism studies carried out on service-exposed components (Fig. 7). This is necessary to show the similarity between results obtained in experiments and those in actual engines by comparing the appearance of rubbing surfaces.

Similarity relates to blade tip geometry, rub speed, rate of interaction and seal rub arc length.

Poor repeatability and lack of consistent correlation between test rig and actual turbomachine results can be caused by

- contamination of the rub zone,
- vibratory movements of the blades or shrouds upon initiation of the rub changing the desired incursion rates to deviating effective rates,
- further thermal and vibrational effects after stopping blade/shroud contact at the end of the interaction and
- using a stationary blade against a rotating wheel.

Conversely, the history of in-service interaction conditions in most cases cannot accurately be traced back because of superimposed influences which allow conclusions to be speculations only. At this point rub tests are an efficient means to obtain systematic correlations between wear mechanisms and test parameters. Moreover development time can be shortened, and the risk of failures reduced.

## 7. TEST RIG FOR GAS PATH SEALS

Fig. 8 shows one of MTU's high-pressure compressor test rigs. The rig is equipped for single- and multi-blade contact, for telemetric measurement of blade temperature and stress and for measurement of casing temperature and vibration. Recording of the rub-in procedure by a video or high-speed camera is optional.

## 8. MODELS, MECHANISMS AND LESSONS LEARNED

Fig. 9 gives an idea of the numerous mechanisms involved in a rub-in process depending on the prevailing rotor and stator conditions. To pick up the threads, it is advisable to make a distinction between blade tip and fin geometries. The latter represents a smaller nominal and also constant contact area compared with the blade tip case.

### 8.1 Blade tip geometry

The behaviour can best be described by a true abrasability (Ref. 1) or energy-loss-per-unit-volume theory (Ref. 2) as one extreme and by a smearing (Ref. 1) or low-Reynolds-number theory (Ref. 2) as the other extreme. The former model is based on particulate escape effects (Fig. 10), the removal of discrete particles with minimum plastic deformation with no smearing and no blade wear. This is obtained by low forces of interaction, low interfacial temperatures and low densification leaving a seal surface similar to the unrubbed one. A further characteristic is that the

fracture rate of the particles of the abradable is higher than or equal to the incursion rate.

The opposite relationship is valid for the smearing model, which is based on plastic displacement of seal material in radial direction (Fig. 11). When the incursion proceeds, the density of the material underneath the smeared surface increases, resulting in an ever increasing rate of frictional heating. As a consequence iron- and nickel-base blades show rapid local oxidation. In the case of titanium alloys  $\alpha$ -phase stabilization and melting occurs, which reduces the blade life drastically. The tendency towards smearing increases with high incursion rates and when a stationary blade tip rubs against a rotating seal material.

A bare square ended blade tip is often prone to smearing and densification. Because of this, blade tips spinning at high speeds should act as an efficient cutting tool (Ref. 3). This can be achieved by reducing the contact area, which leads to higher stress concentrations in the abradable. Thus, the release of particles is facilitated and the chance is reduced that fractured particles are trapped and pressed into the seal again (Fig. 12).

Another possibility which has not yet become common practice is the use of very rough or so-called abrasive blade tip structures (Fig. 13). With their help it is possible to cut a path even in erosion resistant seals without smearing. Limitations lie particularly in its capability to withstand stresses and in the small tip area of a compressor blade to be coated.

### 8.2 Knife edge seal geometry

Wear mechanisms involved at knife edge seal geometries are best described by tribo-oxidation (Ref. 4). This severe oxidation or burn-off is produced by the constant contact and can be a life-limiting mechanism leading to rapid performance loss. The wear process is governed by so-called hot spots as a result of thermal-elastic surface instabilities produced by contact. The rubbing can take place over a very small segment with highly localized heat input (Fig. 14). This thermal distortion is most troublesome with rubs at low to intermediate speeds. The local thermal bump expands, rubs harder, aggravates the rubbing and can lead to a catastrophic failure. Another reason for insufficient abrasability is that the debris cannot escape as easily as with blades. Incompatibility of rubbing materials resulting in material transfer between rotor and shaft component can be a further cause for labyrinth air seal failure.

Tribo-oxidation coating can best be prevented by coating a fin with hard oxide-like alumina. But increasing material hardness does not have the desired

effect if the chemical composition determines the wear rate.

Failures can also be prevented by giving rotor and stator components sufficient rigidity and by restricting the amount of axial movements to prevent the thinning of an already frail knife.

### 9. Future outlook

Higher demands for thermal and propulsive efficiency and performance call for increasing pressure ratios, temperatures and speeds. As a consequence the efficiency of sealing systems must be improved. And this results in smaller clearances requiring enhanced abrasability. At the same time higher erosion and oxidation resistance of the abrasable is needed, which is usually not compatible with abrasability.

This problem cannot be solved solely by improving abrasables. More attention must also be paid to engine stiffness, case roundness, case bending or case/rotor dynamics.

To improve abrasability there are different approaches:

- Spraying a blend of a primary coating material and of a second phase consisting of a polymer. Subsequent heat treatment leaves internal voids and at the same time high interparticle strengths. But the improved behaviour is associated with a rather expensive process which is not easy to control.
- The incorporation of high-temperature solid lubricants and release agents like calcium fluoride and hexagonal boron nitride in the abrasable.
- The application of hard abrasive surface treatments to blade tips and knife edges.

Until now it has been difficult to convince design engineers to use relatively expensive coating systems to protect, for example, a cheap compressor blade. But the increasing application of wide-chord blades made of titanium alloys and the performance and life cycle cost benefits will change this. Current practice in compressor design will also be abandoned by the introduction of blisks (blades and disc as an integral component) requiring better abrasability because of the reduced damping capability of the rub-induced vibrations.

The partial replacement of labyrinth seals by metallic and ceramic brush seals will constitute another challenge.

In view of these developments, gas-path seals will remain a fundamental and continuing problem and a key technology.

### 10. Acknowledgements

The author wishes to thank MTU for the permission to publish this paper and all his colleagues for their help.

### 11. References

1. Bill, R.C. and Wisander, D.W., "Friction and Wear of Several Compressor Gas-Path Seal Materials", NASA Technical Paper 1128, 1978
2. Kascak, A.F. and Tomko, J.J., "Effects of Different Rub Models on Simulated Rotor Dynamics", NASA Technical Paper 2220, 1984
3. Etemad, S., "An Experimental Investigation And Numerical Simulation Of The Thermomechanical Phenomena In Compressor Rotor Tip Rubbing", Ph. D. Thesis 1984, University of Washington
4. Schmid, R.K. and Stahl, D., "Tribo-oxidation at High Velocities in Jet Engines", in "Tagungsband zum Statusseminar Reibkorrosion 1994", EMPA Dübendorf, 6. Dezember 1994

- Fig. 1: Position of gas-path seals
- Fig. 2: Blade failures
- Fig. 3: Leakage areas as a function of blade and shroud wear
- Fig. 4: Low density coating
- Fig. 5: Dense coating
- Fig. 6: Abradable with filler and pores
- Fig. 7: Technology development strategy
- Fig. 8: Rub-in rig, schematic
- Fig. 9: Wear mechanisms
- Fig. 10: Low density coating
- Fig. 11: Wear mechanisms of dense coatings
- Fig. 12: Wear mechanisms as a function of blade tip geometry
- Fig. 13: Abrasive coated tip of a compressor blade
- Fig. 14: Tribo-oxidation of labyrinth seals

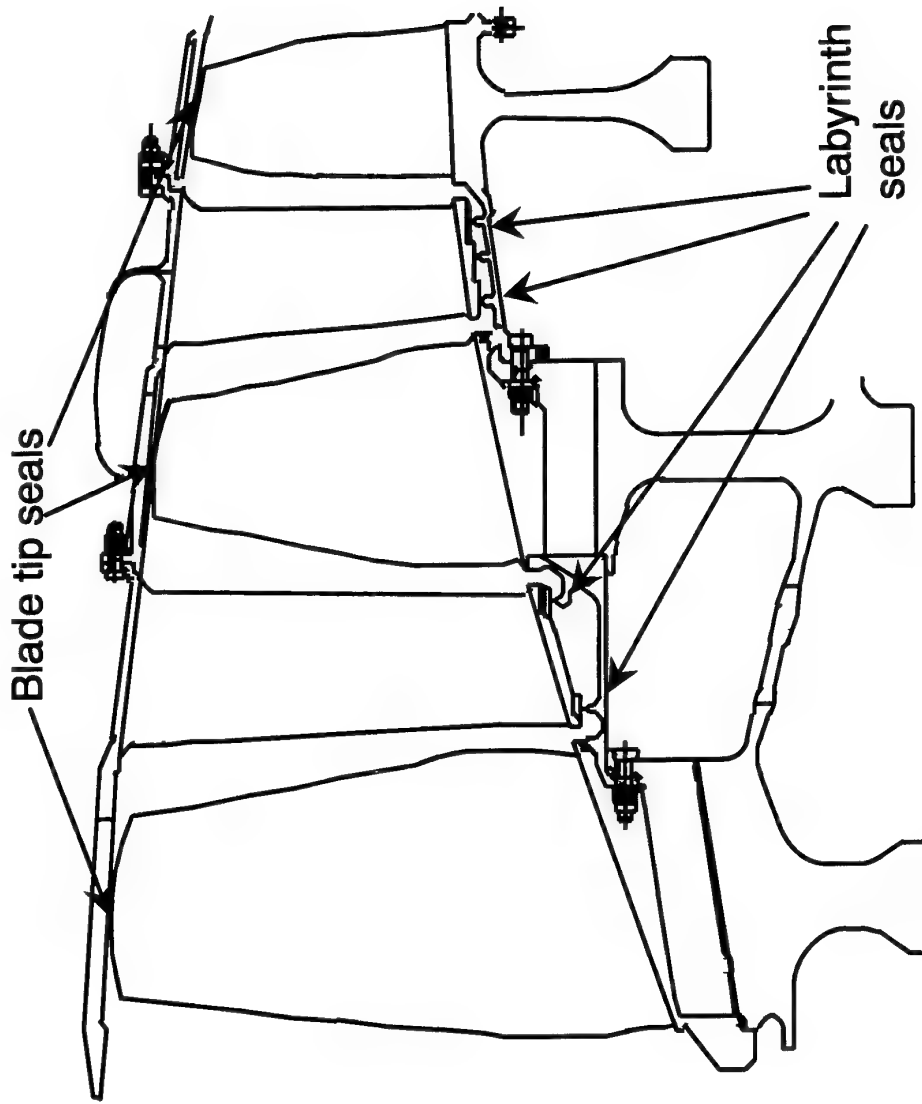
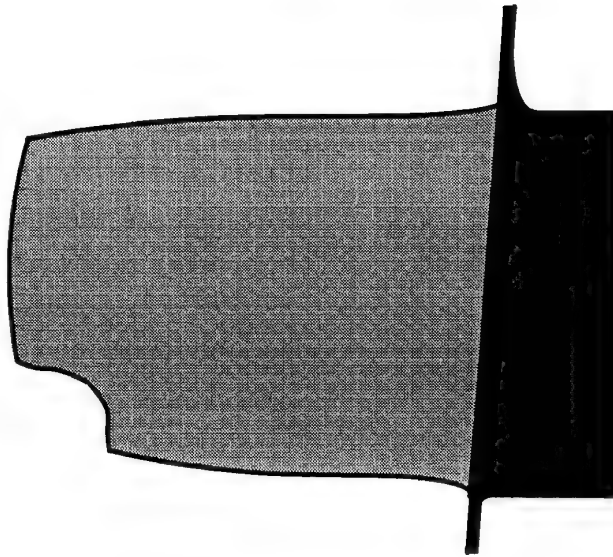


Fig. 1 : Position of gas-path seals



Crack formation



Material transfer to blade tip

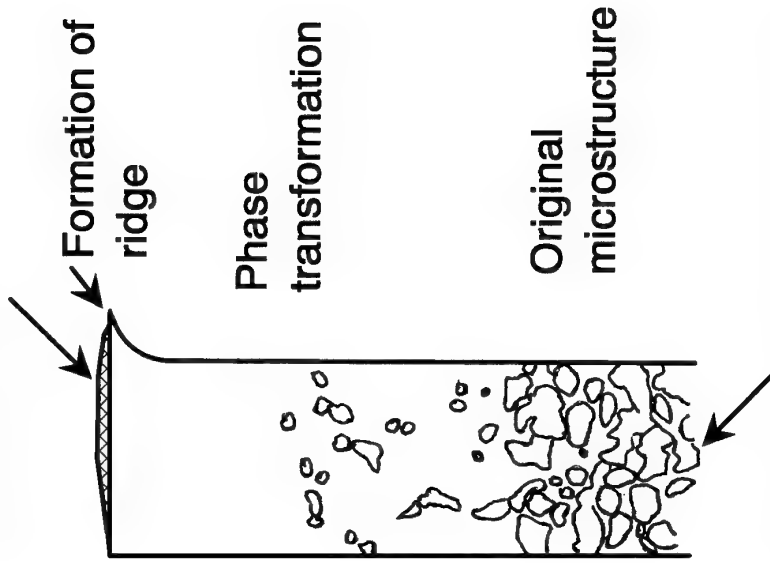


Fig. 2 : Blade failures

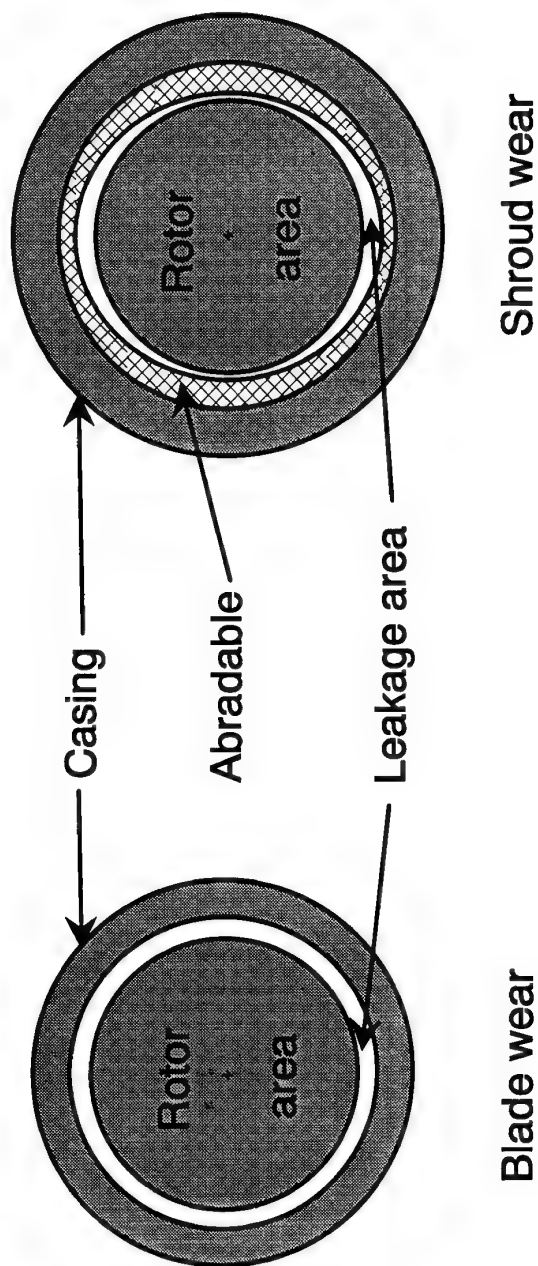


Fig.3 : Leakage areas as a function of blade and shroud wear

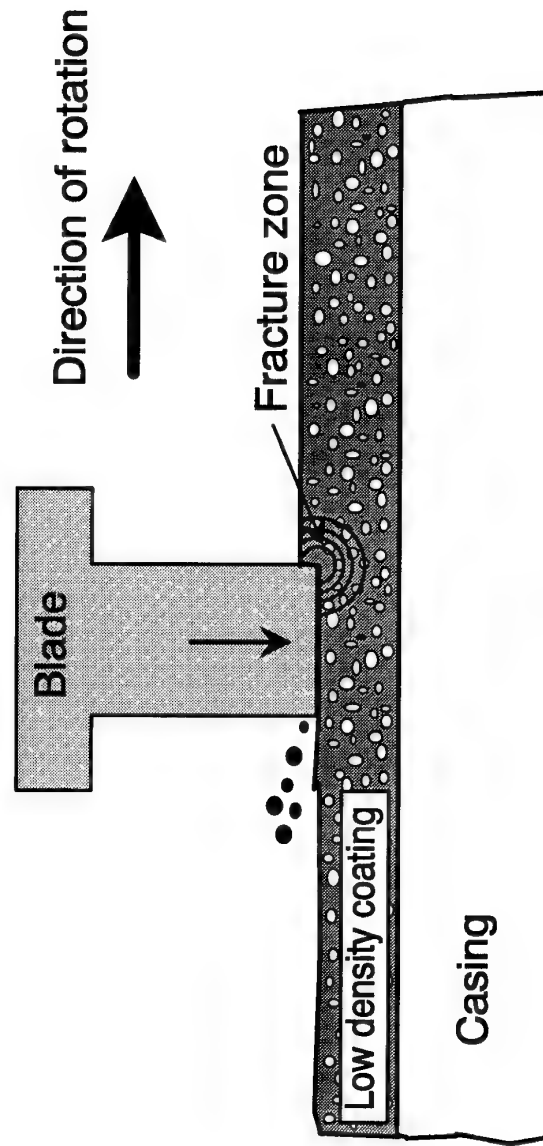


Fig. 4 : Low density coating

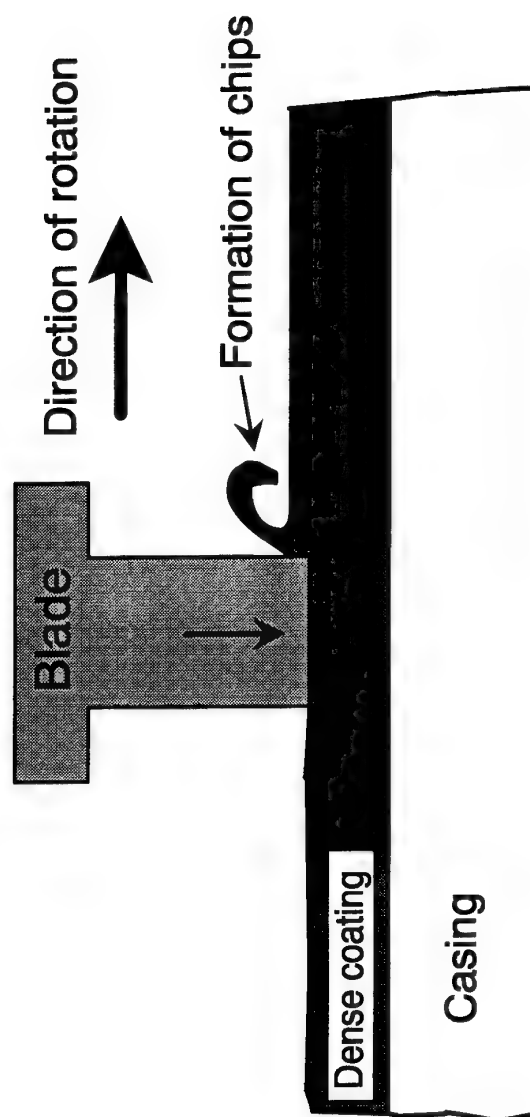


Fig. 5 : Dense coating

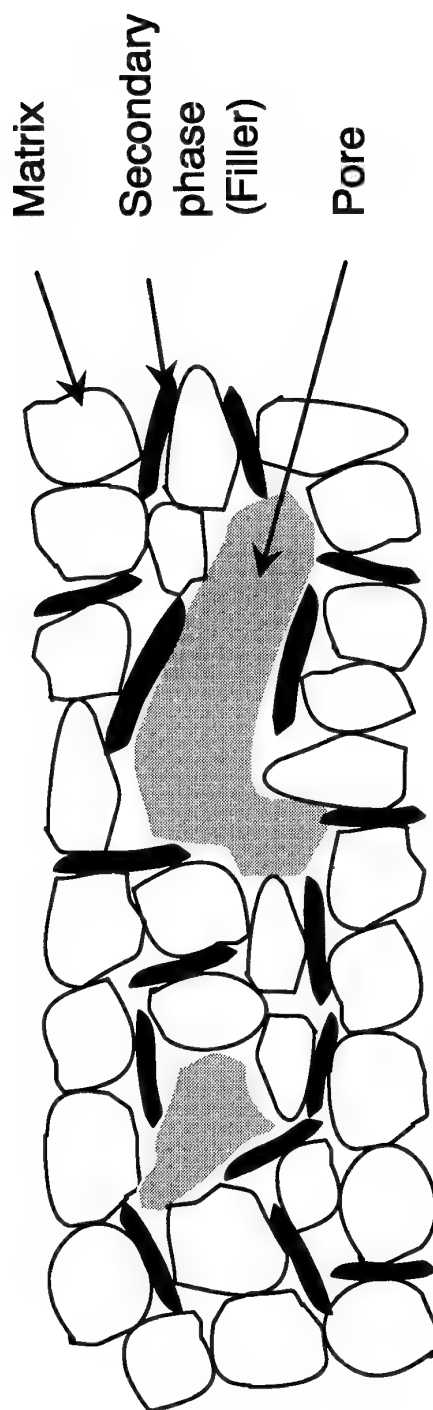
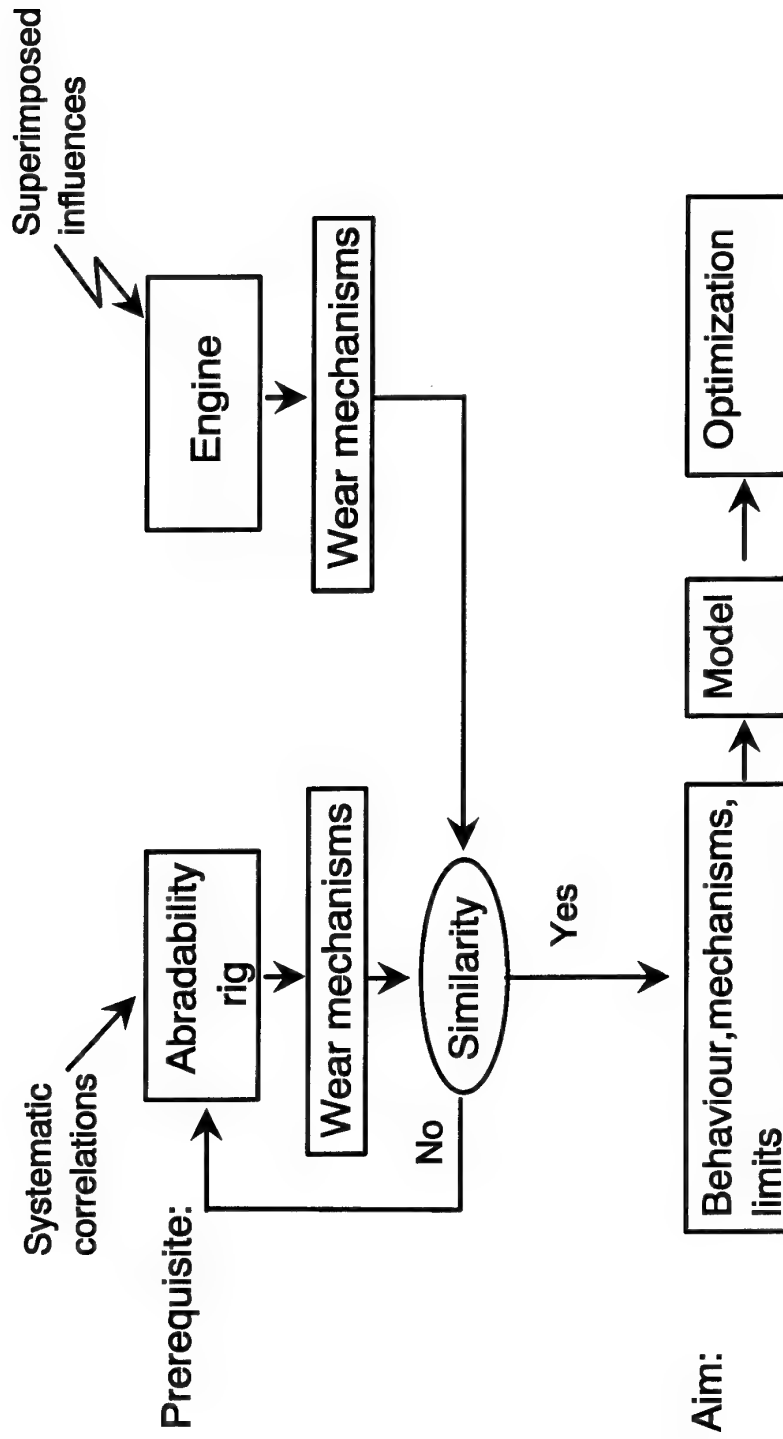
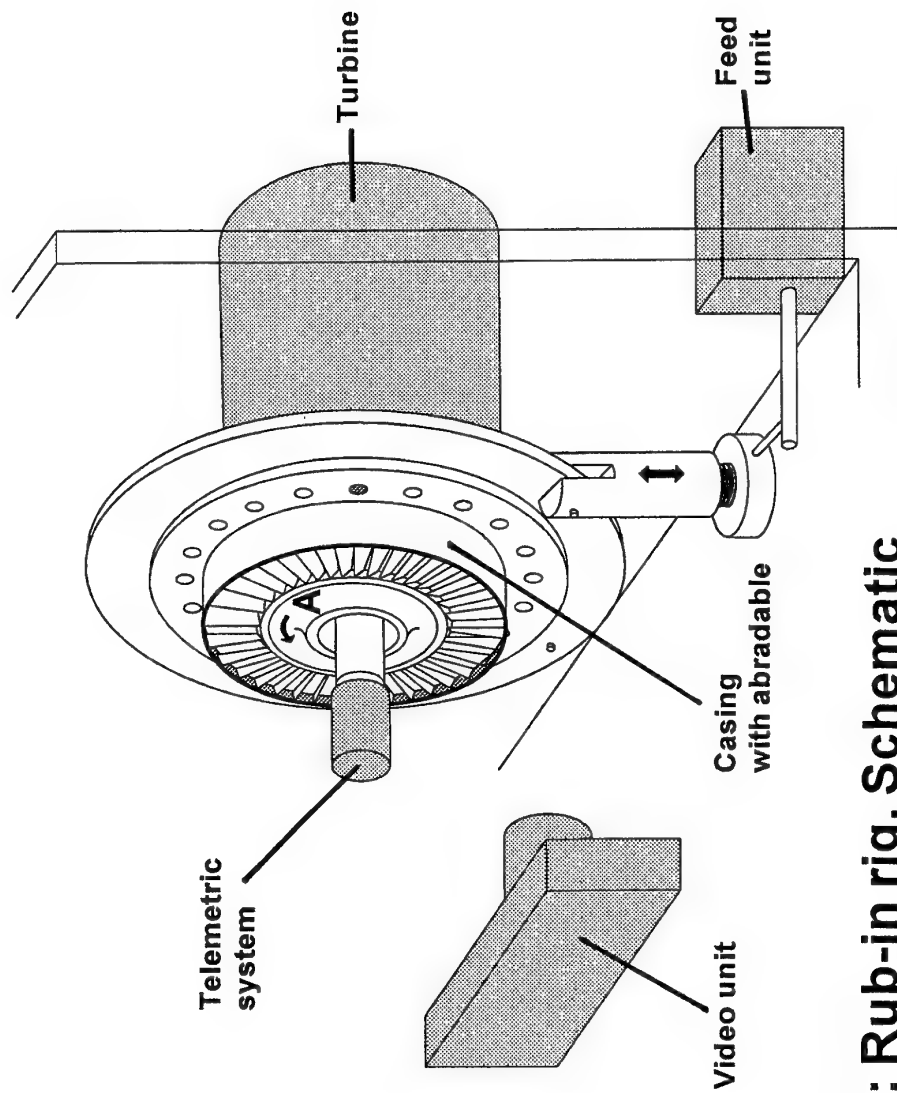


Fig. 6 : Abradable with filler and pores

Fig. 7 : Technology development strategy





**Fig. 8: Rub-in rig, Schematic**

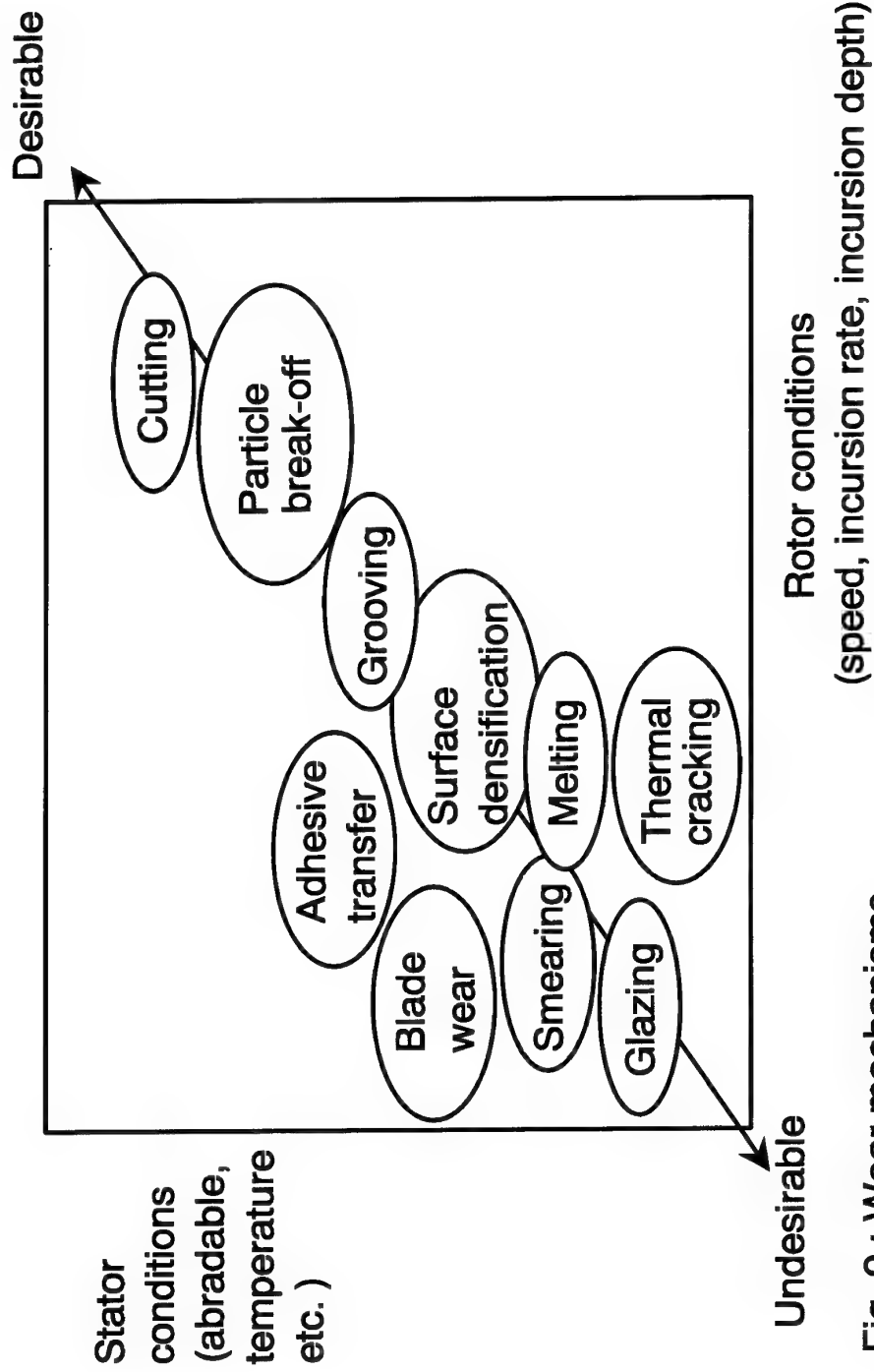
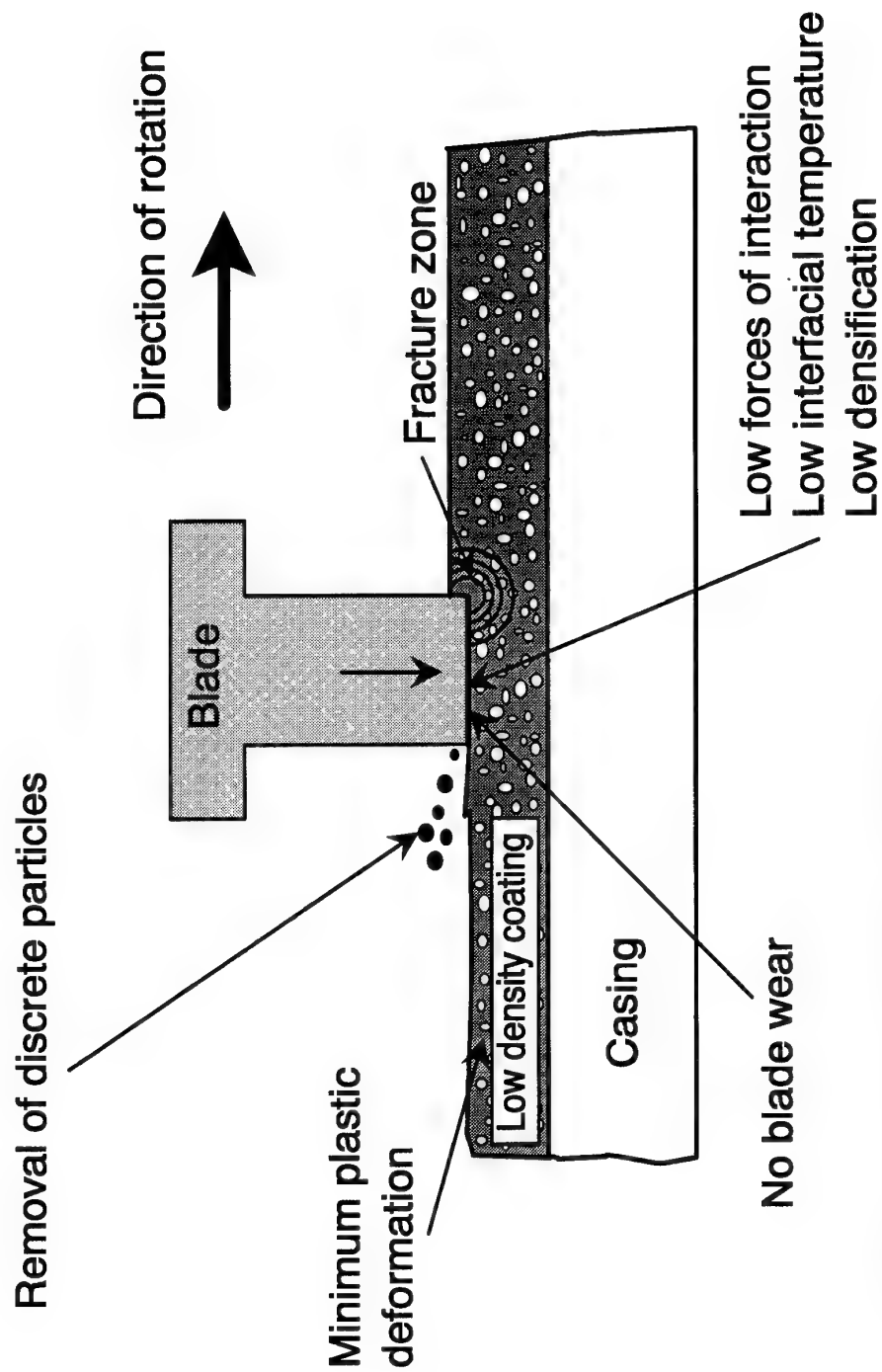


Fig. 9 : Wear mechanisms





**Fig. 10 : Low density coating**

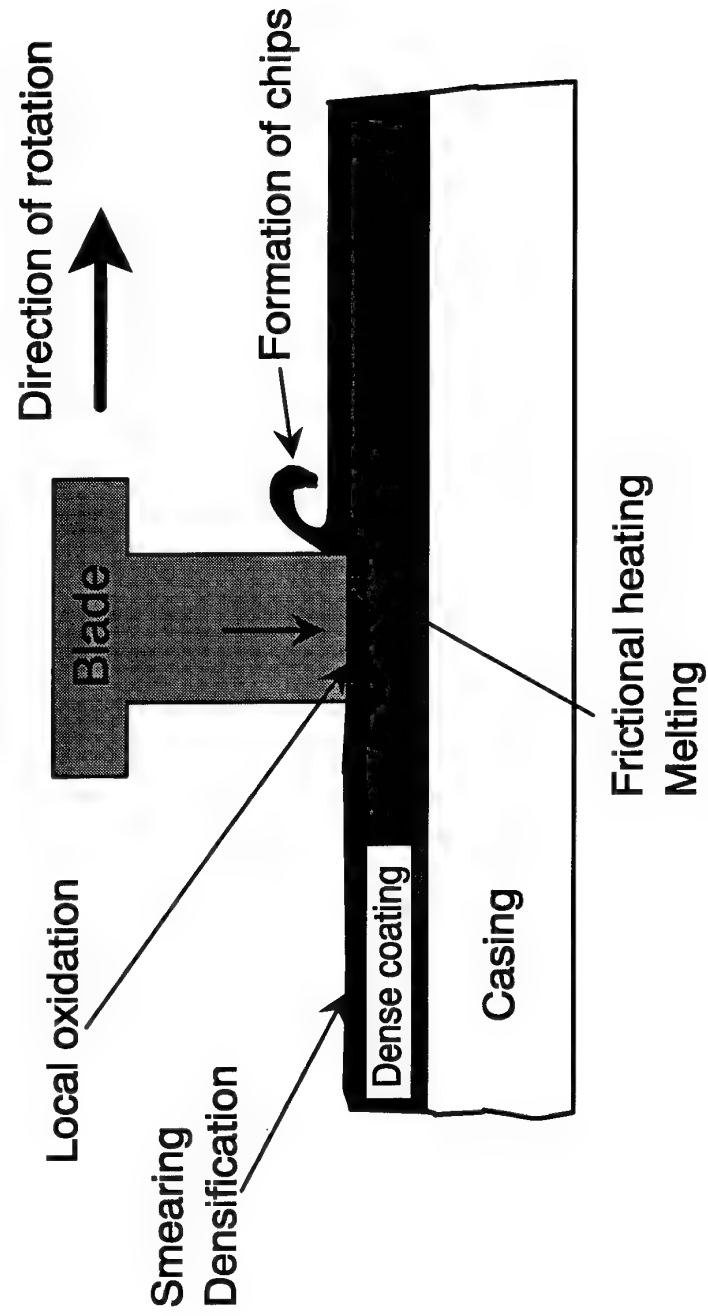
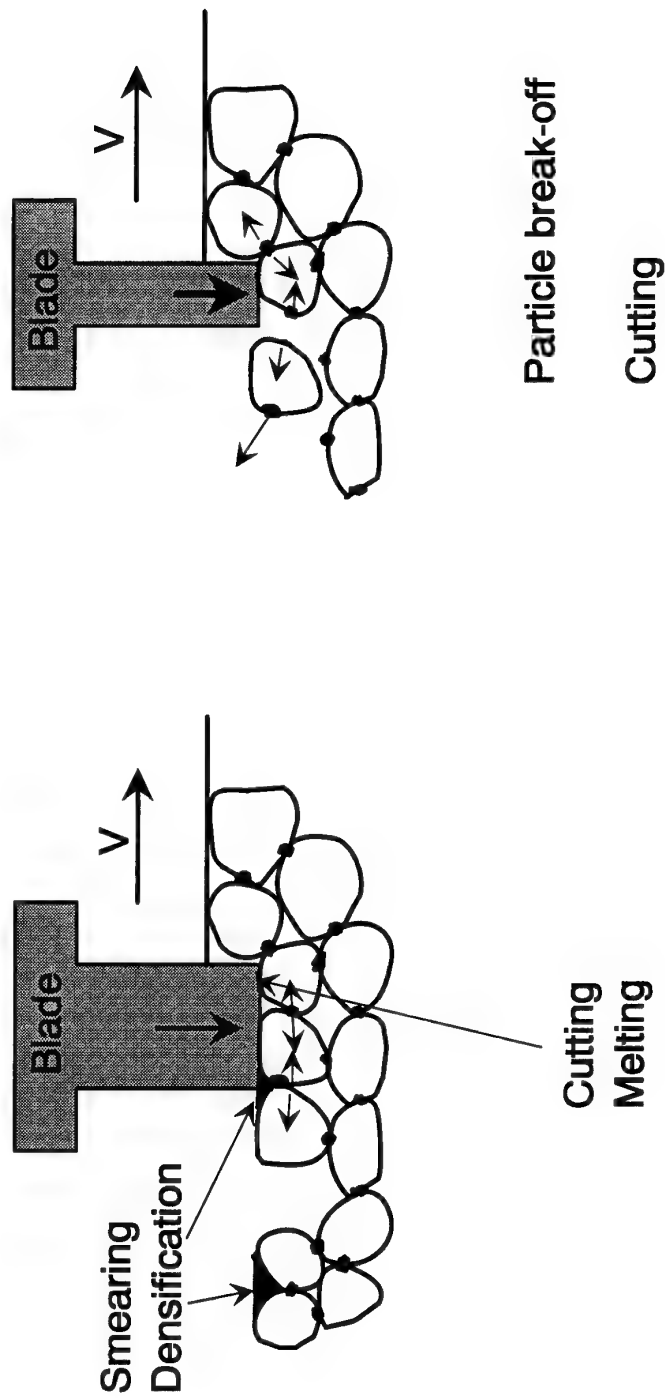


Fig. 11 : Wear mechanisms of dense coatings



**Fig. 12 : Wear mechanisms as a function of blade tip geometry**

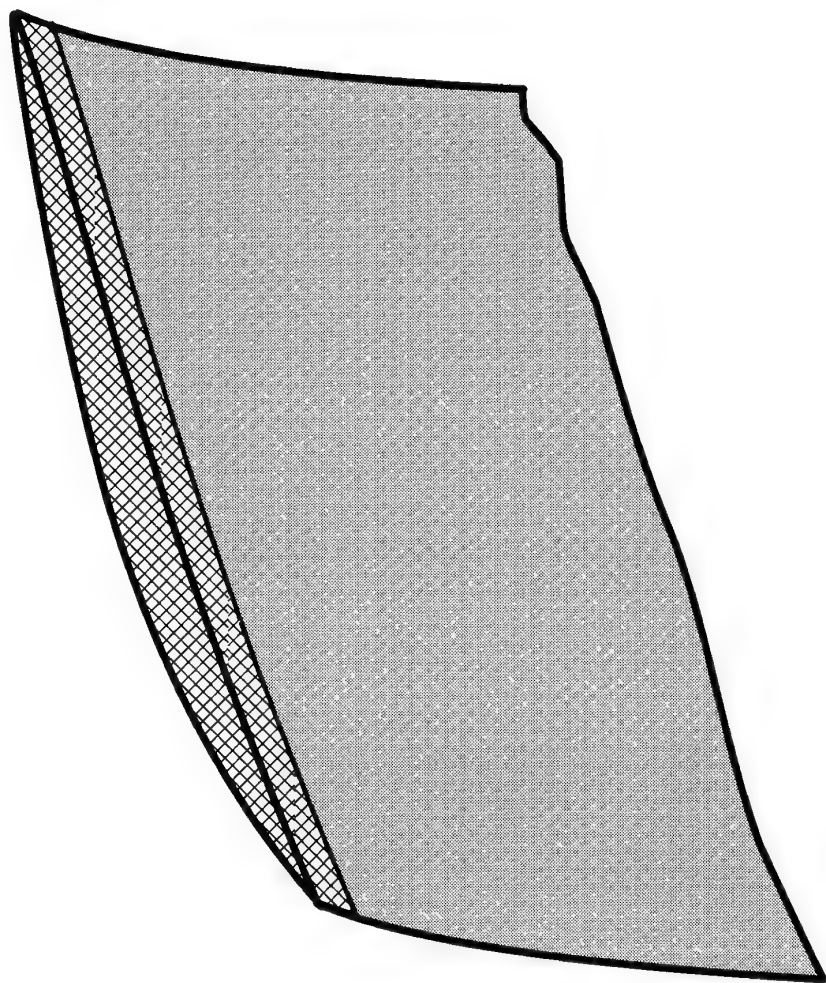


Fig. 13 : Abrasive coated tip of a compressor blade

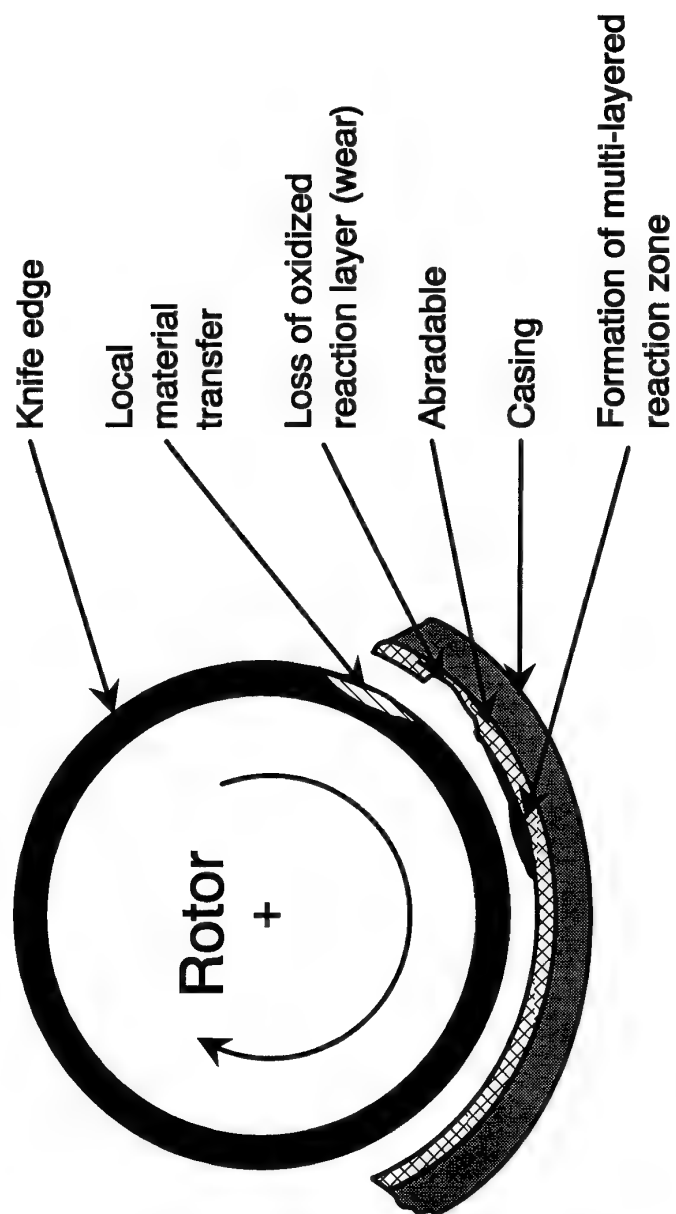


Fig. 14 : Tribo-oxidation of labyrinth seals

## HIGH TEMPERATURE TRIBOLOGY FOR FUTURE DIESEL ENGINES

Walter Bryzik

U.S. Army Tank-Automotive RDE Center (TARDEC)  
AMSTA-TR, Bldg 212, Mail Stop 121  
Warren, Michigan 48397-5000 USA

Roy Kamo

Adiabatics, Inc., 3385 Commerce Drive  
Columbus, Indiana 47201 USA

### SUMMARY

Diesel Engines will be operated at higher cycle temperatures in the future. The higher cycle problems of the top ring, piston, valve seats, valve guides, and cylinder liner. Current lubricating oil with thermal oxidative stability of 204°C is inadequate. Polyol ester base formulated synthetic oil such as Stauffer Chemical SDL-1 or U.S. TACOM MRI-1 with 310°C is inadequate. Polyol ester based synthetic oil such as Stauffer Chemical SDL-1 or U.S. TACOM MRI-1 with 310°C thermal oxidative stability could possibly be the next generation lubricating oil. However, as diesel engines designed by advanced structural ceramics or composites for "adiabatic" operation become feasible, the thermal stability of the lubricating oil will approach 445°C.

To withstand the top ring reversal temperature beyond 310°C, polyphenol ester base oil and other high temperature liquid lubricants will be sought. The highly aromatic polyphenol ether type oil has thus far shown very little promise.

The hybrid piston with solid lubricated top compression rings and a hydrodynamically lubricated oil ring has shown encouraging results. It can be designed to offer as much as 150°C higher top ring reversal temperature capability. If higher hydrodynamically lubricated oil becomes available, the top ring reversal temperature can also be elevated by a temperature difference of approximately 150°C. The hybrid piston conceptually drags thin oil film into the upper dry solid lubricated cylinder liner regions by traversing through the hydrodynamic lubricated region during bottom dead center travel. This small amount of oil film is sufficient to form a hard thin film lubricant of very low coefficient of friction. Densified Cr<sub>2</sub>O<sub>3</sub> coating on Cr<sub>2</sub>O<sub>3</sub> coating has demonstrated the possibility to operate at 380°C top ring reversal temperature with acceptable wear and life. NASA PS212 with Stellite 6B was also tested without liquid lubricant.

### INTRODUCTION

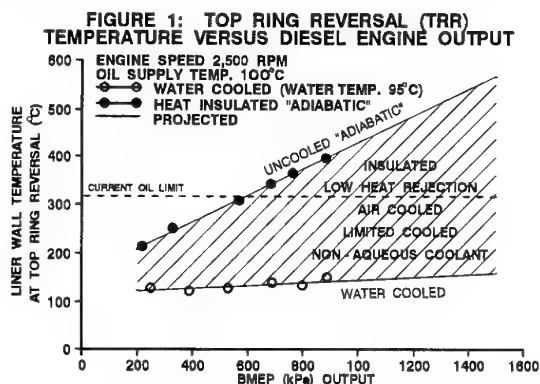
The results presented in this paper represents a ten year effort toward finding a tribological system for future advanced diesel engines. The program was funded by the U.S. Army TARDEC in Warren, Michigan. Considerable in-roads have been made toward improving the high temperature lubrication capability of the future diesel engine. A new synthetic cost competitive polyol ester base lubricant MRI-1 has been

developed. It is available for use in an engine with top ring reversal (TRR) temperature capability of 315°C. With MRI-1 lubricant, a low heat rejection engine (LHRE) with 12 btu/hr-min. heat rejection has been developed. It has successfully passed 100 hours of endurance testing.

In another development a U.S. Army 5-ton truck has been operated without a cooling system and has passed the 400 hour NATO test. Rapid progress is being made in the tribological area. The next milestone could be a lubricant with 425°C TRR capability. Such oil used with a successful solid lubricant ring / liner or a successful hybrid piston design should be able to provide 540°C TRR capability. Success of these developments will require the support and cooperative efforts from the tribology community.

### HIGH TEMPERATURE ENVIRONMENT OF DIESEL ENGINES

The quest for high output, high temperature diesel engines continues and is only technologically limited by the key areas of material, lubrication, fuel injection, combustion, and air handling equipment. Figure 1 shows the increase in liner wall temperature at the top ring reversal (TRR) point as the diesel engine output continues to climb. The two lines show the temperature region for all engines between the uncooled adiabatic and the water cooled diesel engine. The top ring reversal point is the top dead center position of the piston where the piston ring temperature and cylinder liner wall is expected to be the highest in an adiabatic engine as shown in Figure 2.



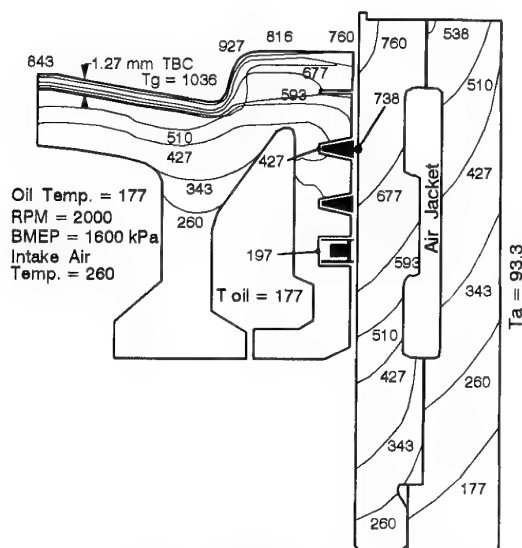


Figure 2: Predicted Piston - Cylinder Temperature Distribution (°C).

The polyol ester base lubricating oil is the current limit of the hydrodynamic liquid lubricant. Development work is underway with aromatic esters, polyphenolesters, etc. yet none appears viable from the standpoint of performance and cost.

For an uncooled "adiabatic" diesel engine, Figure 3 shows the probable approach to engine lubrication over the next generation as a function of heat rejection ratio in btu/bhp-min. In this Figure, 17 btu/bhp-min. represents the limit of the polyol ester base synthetic lubricant. A 315°C to 425°C area will represent a major challenge to any cost effective liquid lubricant. Much work is going on in the field of solid lubricants, especially for high temperature application. The problem with the solid lubricant to date has been its high coefficient friction and high wear rates. Low friction has been reported infrequently but only for a certain temperature regime. However, the research in solid lubricant continues and many good high temperature solid lubricants are becoming available. The solid lubricants may bridge the gap between solid lubricant materials and polyol esters shown in Figure 3.

#### LIQUID LUBRICANTS

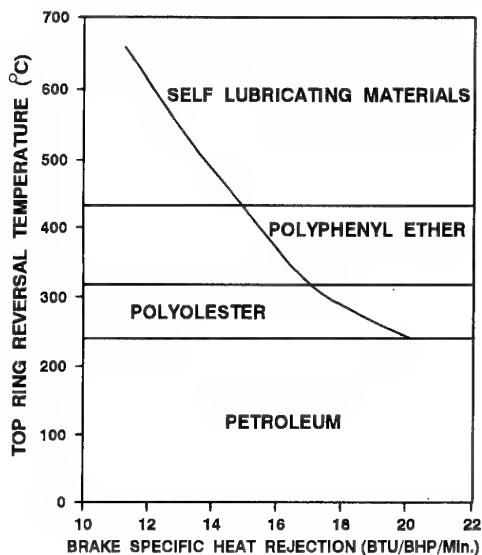
In the LHR adiabatic diesel engine, the need for a tribological system to provide adequate lubrication and life to the top ring reversal (TRR) area in the combustion chamber is critical. Conventional petroleum base lubricants are only capable of 180°C TRR capability. Because of its inadequacy, a synthetic lube oil program was started.

The desired characteristics of a high temperature lubricant for engines are many. The most important performance parameters in their descending order are:

- 1) Deposit formation, 2) Thermal stability/ volatility, 3) Oxidative stability, 4) Corrosion control, 5) Wear and friction control and 6) Viscometrics.

In 1985, two lubricant- development programs were initiated, one by TACOM and one by the Department of Energy (DOE), to address the needs of high temperature engines. In

FIGURE 3: PISTON RING and CYLINDER LINER LUBRICATION of an ADIABATIC DIESEL ENGINE



TACOM's lubricant development program, targets were set for a sump temperature of over 177°C and a top ring reversal liner temperature of over 593°C. As a result of this program, a series of fluids with excellent stability were developed (1,2,3). This series of lubricants, especially MRI -1, were successfully field tested in a 5 ton truck equipped with an uncooled 14 liter 6-cylinder engine from Cummins. The sump temperature of this uncooled engine was 114°C, with top ring reversal liner temperature being 293°C.

The DOE sponsored high temperature lubricant program was launched in anticipation of reaping the energy saving benefits from a low heat rejection engine. The original target was a temperature even higher than that of the TACOM program. This program was concluded in 1992. The final lubricant tests used a modified Cummins L10 engine rated at 231 kW. The final test condition was a sump temperature of 120°C and the top ring reversal cylinder liner temperature of 263°C. Two of the lubricants tested passed a 100 hour endurance test.

#### LABORATORY BENCH TESTS

To minimize deposit formation on the upper cylinder area of a low heat rejection engine is of paramount importance. Screening tests used by the DOE Cummins/Akzo team were a.) Falex panel coker test b.) Alcor deposition test c.) Penn State micro-oxidation test, and d.) NIST DSC two peak deposit test.

#### WEAR STUDIES

Another objective of laboratory tests was wear studies of aromatic ester based lubricants. Wear tests could be conducted with a four ball wear test to gain better understanding of the wear phenomena observed in engine tests. A block and roller tester was also used with excellent simulation to actual engine wear.

#### ENGINE TESTS

The DOE program culminated in two test oils formulated for tests based on the result of the laboratory development work.

The final two lubricants were identified as HTL-4 and HTL-5. Both of these lubricants were multi-grade 15W-40 synthetic blended with earlier base stock. HTL-4 was blended with a low ash additive package and supplemental anti-oxidant (2000 ppm Cu). For HTL-5 the base stock was blended with an alternative low ash additive package. Table 1 shows the final lubricant properties.

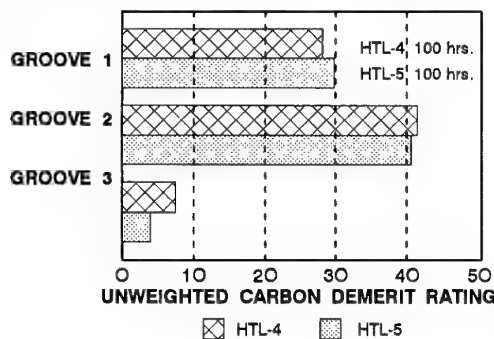
TABLE 1: Test Lubricant Properties

	HTL-4	HTL-5
Viscosity (cSt) at 40°C	99.8	110.9
Viscosity (cSt) at 100°C	12.6	13.4
Viscosity Index	122	120
TAN (mg KOH/g)	0.93	0.46
TBN (mg HOK/g)	5.9	8.8

The engine tests were run on a Cummins L40 engine at 1200 rpm with a 150°C-120°C sump temperature, 66°C intake manifold temperature and coolant temperature of 93°C. The engine torque was 1630/1695 N-m. A typical piston ring groove deposit ratings for the final HTL-4 and HTL-5 lubricants are shown in Figure 4. The HTL-4 (15W-40 synthetic) was the best overall lubricant in terms of stability, wear control, deposit control, dispersion and particulate emissions.

FIGURE 4: Piston Ring Groove Deposit Ratings (Final Engine Operating Conditions)

PISTON REGION



## SURFACE INTERACTING MATERIALS

Equally important in a desired tribological system are the interacting materials. Friction and wear are important parameters to deal with between cylinder liner and piston rings. After many years of development and engine running, Cr<sub>2</sub>O<sub>3</sub> has been found to be an excellent candidate for cylinder liner surface. There may be some other materials surpassing the friction properties of Cr<sub>2</sub>O<sub>3</sub> by a small margin but when wear is considered, Cr<sub>2</sub>O<sub>3</sub> will be difficult to beat.

One interesting approach to piston ring design is the ion-implantation technique on the piston ring. It is necessary that the piston ring material be of hard material such as M2-steel. Ductile iron rings are adequate. Table 2 shows the superiority of the TiN and CrN<sub>2</sub> on M2-steel against a Cr<sub>2</sub>O<sub>3</sub> cylinder liner.

TABLE 2: SCA-1000 CHROME OXIDE COATED ROLLER

TEMP. (°C)	BAR MATL	COAT PROC	TEST No.	$\mu_f$	Wear Rate (mg/HR.)
					+1 0 -1 -2 -3 -4 -5 -6 -7 -8 -9 -10 -11 -12
550	M-2 Steel	-	77	0.22	BAR
550	M-2 SiH+TiN	I.M.	78	0.20	ROLLER
550	Cr2O3	P.S.	79	0.28	
550	Cr3C2	P.S.	80	0.40	
RT	M-2 Steel	-	81	0.36	
RT	M-2 SiH+TiN	I.M.	82	0.36	
RT	M-2 SiH+CrN	I.M.	83	0.35	
RT	D.I.	-	84	0.40	
RT	DI+TiN	I.M.	85	0.44	
RT	DI+CrN	I.M.	86	0.44	
RT	DI + N	I.M.	88	0.42	
RT	Cr2O3	P.S.	89	0.41	
RT	Cr3C2	P.S.	89	0.41	
RT	SCA-1000	-	70	0.47	

Operating Condition: Dry In air  
Roller to Bar Contact Force = 5 lba. = 12,000 psi  
2.0" dia. Roller Speed = 1000 RPM, Bar Stroke = 0.5" @ 4 in./min.  
Friction Wear Bar-on Roller Test Results

## OTHER HIGH TEMPERATURE TRIBOLOGICAL SYSTEMS

Since the current liquid lubricants are not able to progress much higher than 300°C top ring reversal temperature, three approaches to high temperature lubrication of engines are being investigated for 480°C to 540°C TRR in the United States of America. They are: 1) Vapor phase lubrication. 2) Catalytically formed solid lubricant film and 3) Hybrid piston.

### Vapor Phase Lubrication

Vapor phase lubrication obtains its lubrication by introducing tricresylphosphate (TCP) on to the hot walls. TCP is being introduced in a chamber space between the top piston crown and the lower piston. It is also suggested that TCP can be introduced through the injector or through the intake system.

Thus Klaus (3) and coworkers vaporize liquid lubricants, such as phosphate esters, pass the vapors or mists through heated tubes in a nitrogen or other gas stream and bring them to the hot friction surfaces where they can condense and react to form solid lubricating residues. The system can be started at ambient temperatures with little wear because a liquid lubricant is provided. One of the problems with the Klaus concept is high wear.

### Catalytically Generated Lubricant

Lauer and Dwyer (4) suggested a different concept. Ethylene or another thermally stable carbonaceous gas is passed to the hot tribosurfaces, where it decomposes to form only hydrogen and carbon. The hydrogen is rapidly oxidized to water. The carbon will stick to the surfaces until it is worn off mechanically. A fresh surface will be exposed and the cycle will be repeated. To be able to decompose ethylene the surfaces must be catalytically active or tribochemically active. Any alloy containing nickel will do, and so will the ceramics Si<sub>3</sub>N<sub>4</sub> and SiC. The bonding surfaces are not chemically worn since they are not reagents, but catalysts, and the lubricating



investigated for friction and wear. Most solid lubricants indicate high coefficients of friction, i.e.  $\mu_f > 0.2$ . Wear has also been excessive. Recently solid lubricants have been developed which are capable of approaching coefficients of friction values of hydrodynamic lubrication. Among these are WSe/GaIn vs.  $\text{Cr}_2\text{O}_3$  and organometallic compound with  $\text{Cr}_2\text{O}_3$  intermediates and elemental carbon achieving coefficient of friction value from 0.03 to 0.06. Table 3 shows the results of our tests on many solid lubricants tested against M2-steel rollers (8). The same specimen materials were also tested with SDL-1 polyol ester base synthetic lubricant. The difference in coefficient of friction is an order of magnitude.

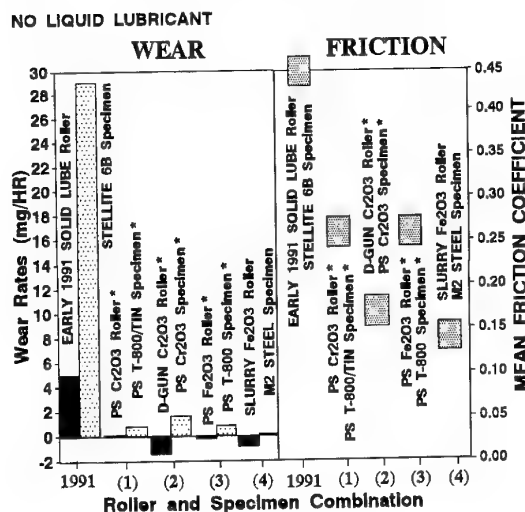
**TABLE 3: SUMMARY OF FRICTION COEFFICIENTS IN DRY AND LUBRICATED MODE**

SPECIMEN Material	ROLLER Material	Dry Not Lubricated Temperature °C				Liquid Lubricant Temperature °C			
		NO EXTERNAL HEATING				NO EXTERNAL HEATING			
		1 hr. 6 hr. 18 hr.	1 hr. 6 hr. 18 hr.	1 hr. 6 hr. 18 hr.	1 hr. 6 hr. 18 hr.	1 hr. 6 hr. 18 hr.	1 hr. 6 hr. 18 hr.	1 hr. 6 hr. 18 hr.	1 hr. 6 hr. 18 hr.
M2 Steel	Silicon a	0.82 0.88 0.89	0.51 0.56 0.58	0.04 0.04 0.08	0.04 0.25 0.82	M2+Cu/LIF	0.46 0.54 0.56	0.51 0.38 0.53	0.07 0.38 0.39
	Nitr.(1) b	0.55 0.50 0.50	0.46 0.38 0.38	0.04 0.04 0.04	0.04 0.19 0.18		0.41 0.50 0.53	0.46 0.19 0.40	0.04 0.19 0.18
Cr <sub>2</sub> O <sub>3</sub>	a	0.87 0.81 0.83	0.45 0.61 0.59	0.03 0.04 0.04	0.04 0.43 0.45	Cr <sub>2</sub> C <sub>3</sub>	0.65 0.39 0.38	0.38 0.38 0.33	0.06 0.38
	b	0.55 0.39 0.38	0.38 0.38 0.33	0.05 0.07 0.04	0.05 0.30 0.38		0.72 0.70	0.49 0.55 0.59	0.07 0.10
Cr <sub>2</sub> C <sub>3</sub>	a	0.72 0.70	0.49 0.55 0.59	0.03 0.05 0.05	0.06 0.15 0.86	Silicon Nitr.(1)	0.59 0.50	0.31 0.38 0.39	0.07 0.49
	b	0.59 0.50	0.31 0.38 0.39	0.03 0.05 0.05	0.06 0.15 0.86		0.98 1.05	0.79 0.90	0.07 0.49
Silicon Nitr.(1)	a	0.98 1.05	0.79 0.90	0.03 0.05 0.05	0.06 0.15 0.86	M2 Steel	0.75 0.63	0.49 0.48	0.07 0.49
	b	0.75 0.63	0.49 0.48	0.03 0.05 0.05	0.06 0.15 0.86		Silicon a	0.54 0.56 0.55	0.05 0.31 0.58
M2 Steel	Nitr.(2) b	0.54 0.56 0.55	0.44 0.39 0.36	0.05 0.31 0.58	0.06 0.16	M2+Cu/LIF	0.52 0.49 0.39	0.43 0.31 0.29	0.13 0.40 0.31
		0.52 0.49 0.39	0.43 0.31 0.29	0.13 0.40 0.31	0.07 0.23		0.44 0.76	0.43 0.48	0.05 0.57 0.48
Cr <sub>2</sub> O <sub>3</sub>	a	0.44 0.76	0.43 0.48	0.05 0.57 0.48	0.08 0.28	Cr <sub>2</sub> C <sub>3</sub>	0.54 0.56	0.43 0.43	0.04 0.28 0.48
	b	0.43 0.48	0.43 0.43	0.04 0.28 0.48	0.13 0.36		0.84 0.98	0.50 0.48	0.04 0.24 0.08
Cr <sub>2</sub> C <sub>3</sub>	a	0.54 0.56	0.43 0.43	0.04 0.28 0.48	0.13 0.36	Silicon Nitr.(2)	0.84 0.98	0.50 0.48	0.06 0.05
	b	0.43 0.43	0.43 0.43	0.04 0.28 0.48	0.13 0.36		0.50 0.48	0.50 0.48	0.06 0.05

a = Upper Limit b = Lower Limit

Most recently, a new  $\text{Fe}_2\text{O}_3$  coating has been developed which possesses excellent friction and wear lubrication. The  $\text{Fe}_2\text{O}_3$  coatings all proved to yield the lowest coefficient of friction and lowest wear rate as shown in Table 4. This densified coating takes the mechanically bonded plasma sprayed coating having an inherent minimum 15% open porosity in the surface

**TABLE 4: Graph of Combined Wear Rates and Friction Coefficients at 540°C**



layer. These coatings are then saturated with a chrome oxide forming densifying agent and heated to fill in fine open porosity and also enhance the cohesive and adhesive bond strength of the coating layer. Residual porosity is quickly filled and bonded by using an organic chrome aluminum phosphate solution.

The hybrid densified  $\text{Fe}_2\text{O}_3$  coating for cylinder liners, and densified Tribaloy T-800 coating for piston rings showed good results on the tribology test rig. It also did well in a corresponding small bore engine test. This wear combination provided dramatic wear improvements over the baseline slurry  $\text{Cr}_2\text{O}_3$  cylinder liner and M-2 steel piston ring. The hybrid  $\text{Fe}_2\text{O}_3$  cylinder liner wear improvement was nearly 3 times better than the baseline slurry  $\text{Cr}_2\text{O}_3$ . Wear data for top and intermediate rings yielded decreased wear rates over the baseline slurry  $\text{Cr}_2\text{O}_3$ .

With solid lubricants, no liquid lubricant is available to provide a film separating two mating surfaces. Without the liquid lubricant, vital heat transfer functions can no longer be performed. Coefficient of friction must be extremely low so as to minimize heat generation.

#### Solid Lubricant Dispersion

One method of alleviating the heat generation of solid lubricants will be to use a high temperature lubricant as the carrier for the solid lubricant particle. A number of tests were performed with graphites, carbon fluorides and inorganic sulfides. The friction and wear properties of the 3 wt percent dispersion of these solid lubricants are shown in Table 5. This work was shelved since the performance of the lubricant with the solid lubricant dispersion was no better than the liquid lubricant at the elevated temperatures.

**Table 5: Wear Rates and Steady State Friction Coefficients for Steel Lubricated With MRI-1 Ester Base Stock and Formulated Lubricant With and Without 3 wt.% Dispersion of Three Solid Lubricants**

Lubricant	Wear Rate x 10 <sup>7</sup> (mm <sup>3</sup> /Nm)		Friction Coefficient	
	21°C	260°C	21°C	260°C
Base stock (B)	<u>51.2</u>	<u>89.0</u>	<u>0.15</u>	<u>0.22</u>
Lubricant (L)	<u>151.0</u>	<u>5.9</u>	<u>0.11</u>	<u>0.05</u>
B + Graphite	1.52	72.7	0.02	0.19
L + Graphite	27.0	61.4	0.07	0.15
B + Carbon Fluoride	2.04	<u>40.3</u>	0.01	<u>0.11</u>
L + Carbon Fluoride	2.41	23.2	0.01	0.10
B + Inorganic Sulfide	1.58	<u>44.7</u>	0.14	<u>0.15</u>
L + Inorganic Sulfide	1.38	61.4	0.02	0.10

\* Underlined Numbers are Averages of Three Results.

carbon will stick since carbon is partly soluble in all transition metals such as nickel or iron.

Lauer's catalytic approach uses ethylene gas impinging on a hot tribological surface with a nickel catalyst to generate solid lubricants. Drastic reduction in friction is noted. The technique has reduced the coefficient of friction,  $\mu_f$  from 0.40 (dry) to 0.04 with catalytically generated solid lubricant film. Lauer's approach is still in the laboratory stage with no known application for high temperature diesel engine.

Another similarly interesting high temperature lubrication effort was reported by Y.S. Jin and C.H. Zhou (11). The so called oiliness boundary film could be transformed into reacted films during an extremely short period under certain conditions of reactive kinetics such as temperature, pressure and velocity. The concept is still in the developmental stage and further investigation is warranted.

### Hybrid Piston

The hybrid piston being developed by Kamo and Bryzik (5) used solid lubricant top ring on the piston where the temperature is highest. On the same piston a hydrodynamically lubricated lower ring is located where the temperature is low enough and the oil is thermally stable.

Figure 5 illustrates the working principle of the two piece hybrid articulated piston. The temperature along the axis at the critical region is shown. The solid lubricant top ring travel is shown between the Top Dead Center (TDC) and Bottom Dead Center (BDC). The top ring can now be located as close as possible to the piston top to minimize the dead air space for good engine performance (brake specific fuel consumption).

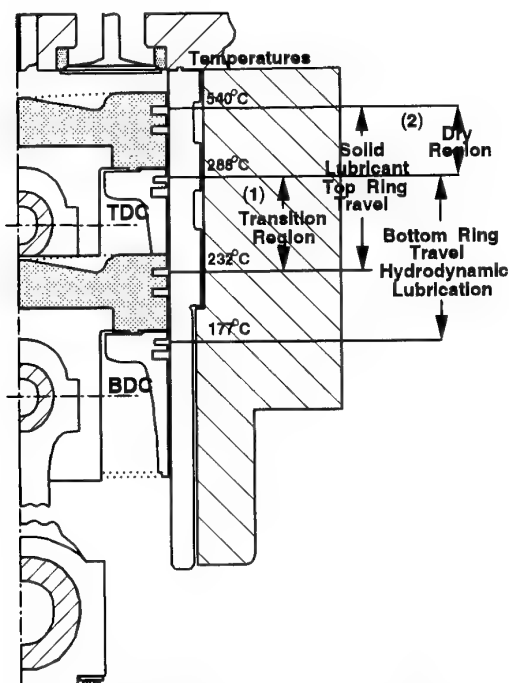


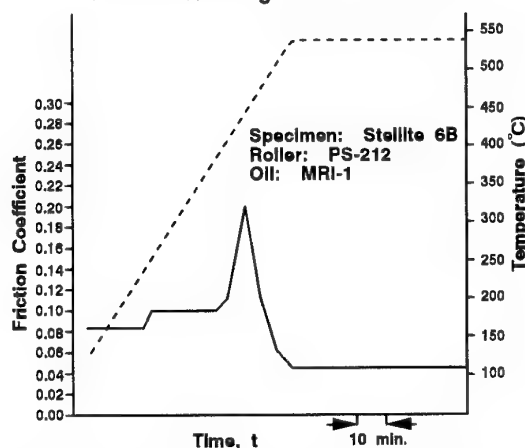
Figure 5: Essentials of the Hybrid Piston Shown at Top Dead Center and Bottom Dead Center

The bottom oil ring pack travel is identified as the hydrodynamic lubrication region between the top dead center and bottom dead center. The region between the TDC solid lubricated ring and TDC of bottom ring is identified as the so called dry region. Note that in a hybrid piston concept, oil consumption is minimal and the so called dry region with solid lubricant film offers very low chances of forming particulates. The difference between the TDC hydrodynamic bottom ring and the BDC of the top solid lubricant ring is shown as the transition region.

In actual operation it is conceivable that the solid lubricant top ring traveling through the transition can drag some oil into the dry region and form oil film in the dry region. Of course the oil film is now in the region converting the oil film into a solid lubricant film. This solid lubricant film provides very low friction coefficient and very low wear.

The formation of thin solid lubricant film in the hot dry region needs to be shown. A solid lubricant material developed by NASA was subjected to a ring and roller friction and wear test in the laboratory at temperatures up to 540°C. An electric oven around the ring and roller was used to heat the specimen. Figure 6 shows the laboratory test results. The block in this test of Stellite 6B and the roller were coated by NASA's PS-212 (6). The solid line shows the roller temperature and the dotted line indicates the friction coefficient  $\mu_f$  at each corresponding temperature. The rig was lubricated with polyol ester base lube oil MRI-1 with a known thermal stability of 288°C. At 371°C the friction increases rapidly due to formation of undesirable carbon species. However, as the test is continued, the friction coefficient drops to a point below the starting room temperature until at temperatures beyond 480°C, the  $\mu_f$  is now 0.04 (compared to 0.08 at room temperature). The specimen wear is nonexistent. Based on these findings it was felt the hybrid piston was conceptually viable.

FIGURE 6: Ring and Roller Tests



### FUTURE ADVANCED TRIBOLOGICAL SYSTEM

#### Solid Lubricants

Perhaps solid lubricant material stands high on the list for future high temperature tribological systems to be developed for engines. There are many solid lubricant materials

### Gas Lubricant

Gas lubricated tribological systems were investigated. The cylinder liner, ringless piston and partially stabilized wrist pin offer some benefits. With clearance of 0.005 inches between the cylinder liner and piston, the gas lubricated tribological system was designed, fabricated and tested in a 5 bhp Kohler gasoline engine (See Figure 7). The mechanical friction was reduced by 50%. A larger 5-1/2 inch bore diesel engine gas lubricated tribological system was subsequently designed, fabricated and tested. The test ended in disaster with severe scuffing of silicon nitride components. All further work was suspended. Gas lubricated piston ring development was also reported by MIT.

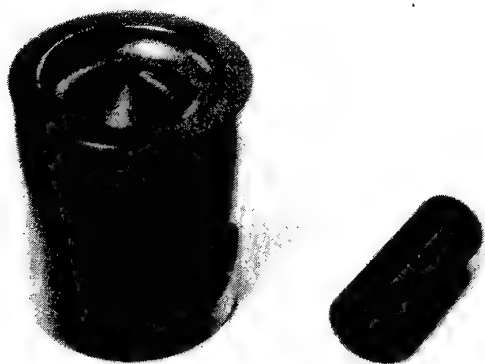


Figure 7: Gas Lubricated Minimum Friction Engine Piston and Pin Components.

### CONCLUSIONS

We have just begun to develop higher temperature tribological systems for future diesel engines. The results presented in this paper show the many concepts and approaches possible to develop a viable system to advance the tribology technology. Based on the above findings, the following conclusions are formulated:

1. High temperature tribological system for engines to meet 540°C top ring reversal temperature will be possible within the next ten (10) years.
2. Solid lubricants hold much promise but may require more than 10 years developmental time.
3. Hybrid piston approach is an intermediate approach with high probability of success.
4. Synthetic lubricants will be necessary and polyol ester base stock is demonstrating outstanding performance in the field with the MRI-1.
5. Thin film generation from lubricants at high temperature or catalysts may offer interesting possibilities for 540°C TRR.
6. The next generation high output high temperature diesel engine tribological needs combined with synthetic polyol ester base formulated lubricant.
7. Hybrid piston design higher liquid lubricant and better solid lubricant need to be developed.
8. A laboratory coefficient of friction of  $\mu_f < 0.06$  must be achieved in order to maintain acceptable brake specific fuel consumption.

### ACKNOWLEDGMENT

The authors would like to thank the sponsor (U. S. Army Tank Automotive Command) who made this tribological system development program possible. Acknowledgment and appreciation are given to P. Sutor, E. Bardasz, M. E. Woods and L. Kamo for their major contributions to the tribological development. C. Young and M. S. Kamo are acknowledged for preparation of the manuscript.

### REFERENCES

- (1) P. Sutor and W. Bryzik: Laboratory Development and Engine Performance of New High Temperature Diesel Engine Lubricants, SAE Paper 890145 in Worldwide Progress on Adiabatic Engine, SAE SP- 785 (1989) 41.
- (2) P. Sutor, E. A. Bardasz, and W. Bryzik: Improvement of High Temperature Diesel Engine Lubricants, SAE Paper 900687, Detroit, Michigan (1990) Feb./Mar.
- (3) E. E. Klaus, J. Phillips, S. C. Lin, N. L. Wu, and L. Duda: Structure of Films Formed During the Deposition and Lubrication Molecules of Iron and Silicon Carbide, STLE Paper No. 88-TC-5A-2, Technical Reprinting of the Society of Tribologists and Lubrication Engineers, ASME/STLE Tribology Conference, Baltimore (1988) October.
- (4) J. L. Lauer and S. R. Dwyer: Continuous High Temperature Lubrication of Ceramics by Carbon Generated Catalytically from Hydrocarbons Gases, submitted for presentation at the Tribology Conference, Fort Lauderdale (1989) October.
- (5) R. Kamo and W. Bryzik: Solid Lubricants for Advanced Heat Engines, STLE Annual Meeting, Calgary, Alberta, Canada (1993) May 18.
- (6) H. Sliney: Hot Piston Ring/Cylinder Liner Materials Selection and Evaluation, SAE Paper 880544, J. Vac Sci. Technical A 466 (1986) Nov./Dec.
- (7) Y. S. Jin, L. L. Cao, W. M. Xia, and X. H. Ma: Examination of Antifriction Characteristics of Cr<sub>2</sub>O<sub>3</sub>-Coated Cylinder Liner of an Adiabatic Engine Under Boundary Lubrication, 6th International Conference and Exhibition on Thermal Spray, Orlando, Florida (1992) June.
- (8) P. Moorhouse, R. Kamo, and B. Mortimer: Solid Lubrication Studies for Adiabatic Diesel Engines, SAE Paper 50508 (1985).

(9) J.C. Wang and M.A. Sublette: High Temperature Liquid Lubricant Development Part I: Engine Tests; SAE Paper 932842; Phil., PA, Oct 18-21, 1993.

(10) P.Wiczynski, T.A. Marolewski: Development of High Temperature Liquid Lubricants for Low Heat Rejection Heavy Duty Diesel Engines, DOE/NASA 10373-1 NASA CR-19497; March 1993.

(11) Y.S. Jin and C.H. Zhou: An Approach to Characterization of Producibility and Lubricity of Reacted Films Under Boundary Lubrication., First International Symposium on Tribology, Beijing, China, Oct.. (1993).

## Tribological assessments and concepts for an oilfree internal combustion engine

82<sup>nd</sup> Meeting of the Advisory Group for Aerospace Research & Development  
(NATO-AGARD)  
06 - 10 May 96, Sessimbra, Portugal

M. Woydt  
Federal Institute for Materials Research and Testing (BAM)  
Unter den Eichen 44-46  
12200 Berlin  
Germany

### Abstract

Unlubricated engines can be realized from the tribological point of view, if wear coefficients of sliding couples lower than  $5 \cdot 10^{-8} \text{ mm}^3 / (\text{N}\cdot\text{m})$  can be demonstrated, which are independent from ambient temperature and sliding speed. A review of published tribological data and the search in a data base provided no couples with such low wear coefficient at 22°C and 400°C. Known unlubricated sliding couples with wear coefficients around  $10^{-7} \text{ mm}^3 / \text{N}\cdot\text{m}$  opens the frame to built up such engines for basic studies.

### 1. Introduction

Since about 20 years all over the world, programs for unlubricated engines were started. The main problem of concepts like adiabatic engines [1, 2] low heat rejection engines [3], two stroke engines [4] and hydrogen engines [5] is the tribology of many tribosystems, especially of the system „piston ring / cylinder liners“ [6, 7, 8,]

Today, the driving forces to develop unlubricated engines are related to severe exhaust emission regulations [9], environmental legislation [10], waste management restrictions for used oils [11] and the new german product recycling law [12] as well as inquiries of customers to reduce operating costs.

With respect to this, the question arises whether transformation of common, fully oil lubricated engines to unlubricated ones is possible from the tribological point of view. An unlubricated combustion engine is of interest because:

- a. A causal relationship exists between exhausts emissions and the „piston ring / cylinder“ and „valve schaft / valve guide“ tribosystems [13].
- b. The oilfree engine will be more compact in its basic construction (with less parts) and avoids some problems related to the environment due to oil leakage, oil burning and used oil removal.

## 2. Tribology

### 2.1. System analysis of tribosystems

Before the feasibility of unlubricated tribosystems in combustion engines can be discussed, the needed volumetric wear coefficient must be analysed. The necessary data for operating conditions were collected by questioning experts from automotive companies. This analysis shows the average volumetric wear coefficients which occurred today in a oil lubricated running four stroke engine. If one will select new materials from Literature or based on any kind of non-engine screening test (e. g. DIN 50 324 or ASTM G-99) the candidate materials must exhibit a lower minimum wear level in these unlubricated screening tests than lubricated, real tribosystems in engines.

Table I summarises the volumetric wear coefficient (or specific wear rate) for the main relevant tribosystems of a combustion engine which occurred during a steady-state operation of 2000 hours. For this evaluation it is assumed, that the engine runs at 3000 rpm and the normal force is either the maximum force (calculated from the combustion pressure) or the average force during one crankshaft cycle. The calculated volumetric wear coefficient according DIN 50323 indicates, that the wear limit for the selection of unlubricated candidate materials is smaller than  $5 \cdot 10^{-8} \text{ mm}^3 / (\text{N}\cdot\text{m})$  and should be independent from sliding velocity, and ambient temperature. During this operation time, each tribosystems encounters around 400 million sliding or rolling cycles.

### 2.2 Unlubricated wear coefficient

The quickest way to get an overview on candidate materials for an unlubricated engine is the search in the numerical, tribological data base „Tribocollect V1.0“ [14] with more than 10.400 data sets.

For the present summary all unlubricated sets for non-polymeric materials tested at 22°C and 400 °C were selected. 400 °C is the minimum level of ambient temperature which has to be considered for unlubricated engines. A component temperature of 600 °C or 800 °C would be more realistic.

Figs. 1 and 2 shows the 532 resulting data points plotted volumetric wear coefficient versus friction coefficient and sliding velocity, respectively. It can easily be seen that, with respect to the requirements of Table I, no appropriate sliding couple with a volumetric coefficient below  $5 \cdot 10^{-8} \text{ mm}^3 / (\text{N}\cdot\text{m})$  at 400 °C and sliding velocity above 0,5 m/s is found in the tribological database.

Note, however that, at sliding speeds below 0,1 m/s and 22 °C, some couples exhibit volumetric wear coefficients around  $5 \cdot 10^{-8} \text{ mm}^3 / (\text{N}\cdot\text{m})$ .

### 2.3 Unlubricated coefficient of friction

It is well known, that engine oils lubricates under hydrodynamic or EHD conditions the tribosystems with coefficient of friction between  $10^{-2}$  and  $10^{-3}$ . The question, if unlubricated tribocouples exhibits similar low coefficient of friction than those under hydrodynamic or EHD conditions, can be easily answered with a search in the data base „Tribocollect“.

Figure 3 shows a plot of coefficient of friction versus sliding speed. Above 22°C, no data with coefficient of friction lower than  $10^{-2}$  could be found. In order to minimize the frictional losses, it can be concluded, that an unlubricated engine will not run efficient.

In the last few years, some results with coefficient of friction in the milli-range were published for dry lubricated couples [15]. Such a superlubricity requires the following conditions:

- atomistically smooth surfaces (Roughness  $\leq 2$  nm)
- frictional power losses  $\leq 1 \text{ mW/mm}^2$
- elastic microcontact
- no surface contamination
- defined and constant ambient conditions
- small surface interactions
- parallel again each other oriented, crystallographic shear layers at the surface

Such conditions can only be found in micromechanics or space applications and not in automotive applications, where the tribosystem runs in a wide range of normal force, temperature and sliding speed.

Another promising, in oxidizing atmospheres theoretical possible technology to reduce dry friction are the so called „Magnezi - Phases“, which are oxides and exhibit crystallographic layers with a crystalline slip ability [16].  $\text{TiO}_2$  represents such a substance and is stable in air. The shear stress depends from the stoichiometry and is shown in the following:

Substance	Shear stress (MPa)
$\text{MoS}_2$	7 - 10
$\text{TiO}_{1.93-1.98}$	8
$\text{TiO}_{1.80}$	81
$\text{TiO}_2$	21

Actual it is unclear, if for an automotive application these phases can be synthesised and are stable in their tribological properties under the operation conditions in an engine.

### 3. Tribological high-temperature applications

The main operational problems of constructions working in their tribosystems at temperatures above 400 °C are caused by the fact, that liquid lubricants are not stable at stock temperatures above 200 °C and at short peak temperatures above 400 °C, so that the triboelement must operate oil-free.

Liquid lubricants are essential in Tribosystems

- to separate the mating surface for low wear and friction,
- to remove wear particles,
- to cool the surfaces and components and
- to avoid adhesive wear (mainly for metals).

If the lubricants cannot be used, their functions must be taken over by other mechanisms or materials, which are insensitive to temperature.

A general dry lubrication mechanism can be seen in the transfer of the shearing of the liquid film into the upper surface area.

In Fig. 4 high-temperature tribosystems with the materials used for dry friction are presented.

Product	Tribosystem	Component Temperature °C	Gaseous ambient	Materials
Adiabatic diesel engine or oilfree engine	Piston ring / cylinder	≈ 700	CO, HC <sub>x</sub> , NO <sub>x</sub> , CO <sub>2</sub> , N <sub>2</sub> , C	ZrO <sub>2</sub> , SiC, Al <sub>2</sub> O <sub>3</sub> -SiC-Whisker, Si <sub>3</sub> N <sub>4</sub> , PS200, Si <sub>3</sub> N <sub>4</sub> -TiN, Si <sub>3</sub> N <sub>4</sub> -TiC, Vapor phase lubrication
Gas turbine heat exchanger	Shroud / Cordierit wheel	≈ 600 - 900	CO <sub>2</sub> , CO, N <sub>2</sub>	Cordierit, NiO-CaF <sub>2</sub> , Graphit, PbO-SiO <sub>2</sub>
Stirling engine	Piston ring / cylinder	600 - 1000	H <sub>2</sub> , He	PS200 (Cr <sub>3</sub> C <sub>2</sub> -Ag-BaF <sub>2</sub> /CaF <sub>2</sub> -NiAl), SiC, SiSiC
Hypersonic engine	Wall / seal ring	≥ 1000	H <sub>2</sub> , O <sub>2</sub> , H <sub>2</sub> O	Al <sub>2</sub> O <sub>3</sub> -SiC-Whisker/Fiber, SiC
Gas sliding seal	Ring / ring	900	CH <sub>x</sub>	TiC, PS 200, Si <sub>3</sub> N <sub>4</sub> , SiC
Oilfree turbine rolling bearing	Ball / rings / cages	600	air	Ga/In/WSe <sub>2</sub> , Si <sub>3</sub> N <sub>4</sub> , M50, Vapor phase lubrication

Fig. 4: High-temperature tribosystems in application and prototypes

Only ceramic materials were used in the tribosystems presented in Fig. 4, because they operate between 600 °C and 1000 °C. The experience with these applications has shown, that metallic materials fail by adhesive wear and are not suitable.

Full-ceramic materials were not only applied for tribological reasons but additionally for structural, thermodynamic and design considerations.

It is noticeable, that the components were only built out of monolithic materials or of sintered solid lubricant composites. These technical solutions give a high wear stock pile, which stands for high wear clearances and must be taken into consideration during design, because at high temperatures the wear coefficients are high.

The wear behaviour of couples can only be improved by intrinsic solid lubricants in those applications, where reducing, or oxygen free, atmospheres exist (s. Fig. 4). In the compilation in Fig. 4 the gas film lubricated seal ring represents an exception, because the mating surface contact only under start-stop-conditions.



If the wear reducing velocity accommodation between two sliding surfaces by liquid lubrication is not possible or must be avoided, dry lubrication concepts have to be developed to reach specific wear coefficients lower than  $5 \cdot 10^{-8} \text{ mm}^3 / \text{N.m}$ .

#### 4. Dry Lubrication concepts for high temperatures

Table II summarizes four main dry lubrication mechanisms applicable for engines, which were already applied in prototypes, test rigs or some rare products. The following dry lubrication concept will be validated with respect to the operating conditions of an engine.

##### 4.1 Lubricious oxides

Publicly founded European and German research projects were investigated by means of modern surface analysis dry sliding couples of commercial ceramics and new development ceramic composites the surface composition from low wear regions. From these results the formation of „lubricious oxides“ as wear reducing dry lubrication mechanisms were deducted [17, 18]. In this context, tribooxidation will be understood by the authors as lubricating mechanism and not as „wear mechanism“.

Tribochemically, on a hard substrate formed lubricating soft oxide layer, with a low shear strength, results under unlubricated conditions in a considerable wear reduction and sometimes in a decrease of friction.

In the self-formation of lubricious oxides a dry lubrication mechanism to enhance wear resistance can be seen, when oils must be avoided.

The friction force  $[F_f]$  of such tribosystems is defined by equation (1)

$$F_f = \frac{F_N \cdot \tau_s}{H(T)} \quad (1)$$

where  $F_N$  is the normal force,  $\tau_s$  is the shear strength of the oxide layer and  $H(T)$  is the hardness of the substrate as function of temperature.

Figure 5 summarizes pin-on-disk results with new self-mated ceramic-ceramic and ceramic fibre reinforced glasses against ceramics compared with commercial ceramics and illustrates the progress made on reducing the total volumetric wear coefficients of ceramics and ceramic composites. At room temperature, the total volumetric wear coefficient (TVWC = the sum of pin and disc wear coefficient), formerly widely regarded as the application limit for dry sliding couples, namely  $10^{-6} \text{ mm}^3 / (\text{N.m})$ , has been significantly lowered, and the wear behaviour depends only marginally on the sliding velocity. Materials for sliding applications are of interest, when the volumetric wear coefficient is lower than  $10^{-6} \text{ mm}^3 / (\text{N.m})$ . For ambient temperatures between  $400^\circ\text{C}$  and  $800^\circ\text{C}$  the TVWC approaches or undergoes the  $10^{-6} \text{ mm}^3 / (\text{N.m})$  threshold value. The incorporation of Ti-compounds, which can form by tribooxidation a self lubricating  $\text{TiO}_{2-x}$  surface layer, have considerably improved the wear resistance. The materials characterized were: SiC-TiC,  $\text{Si}_3\text{N}_4$ -TiN, (Ti, Mo) (C, N) and SiC-TiB<sub>2</sub>, which gave the same bending strength and higher toughness as the Ti-compound free ceramics and they are electrical conductive [17,18].

## **4.2 Incorporation of solid lubricants in a matrix**

For some decades, the incorporating of specific solid lubricants in materials and matrices were pursued in the United States for high temperature applications. The solid lubricants achieved no success under long term operation (except in space applications), but are still considered as candidate materials for e. g. dry turbine main shaft rolling bearing, unlubricated engines and others.

This situation is not surprising, because on one hand any solid lubricant weakens the materials structure and therefore the strength or fatigue life. On the other hand, under normal atmospheres the typical effective non-oxide solid lubricants oxidize and lose their beneficial properties. As an example the tribological results achieved with  $\text{Si}_3\text{N}_4$ -hex. BN are cited here [18] (s. Fig.5).

All together, many intrinsic or extrinsic solid lubricants begin to fail in their tribological effectiveness with increasing temperatures through oxidation, melting or decomposition.

## **4.3 Transfer film lubrication**

The favourable tribological behaviour of most polymer materials under dry sliding conditions is determined by the fact, that the polymers form a thin transfer film on the counter part surface, which depends on the surface roughness of the counter part and on the sliding velocity. High P-V-values as well as temperatures above 300°C hinder these mechanisms.

Glasses [20], carbon materials [21] and ceramic fibre reinforced glasses- or Cordierit-matrices [20] can operate as alternatives at up to 500°C. From these materials at room temperature friction coefficients low as 0.1 and sliding wear coefficients around  $10^{-7} \text{ mm}^3/\text{N}\cdot\text{m}$  were reported [20].

Any type of liquid interrupts this transfer film mechanism. As a consequence from the lubricious transfer film formation, a certain running-in-wear in the range of 1  $\mu\text{m}$  to 5  $\mu\text{m}$  of clearance, sometimes more, must be taken into account.

Fine grained turbostratic carbon prepared from  $\delta$ -mesophase offers for the design a promising perspective, because this material exhibits for the requirements of a piston both appropriate tribological and mechanical properties and has a key role also on the way to an oil-free engine [23, 24]. Recent two-stroke engine results [23] showed a guaranteed 1000 hour endurance life with a 1:200 oil-to-fuel ratio using a combination of wear-resistant and self-lubricating sliding couples (e. g.; a carbon piston against coated or ceramic liners).

## **4.4 Vapour phase lubrication**

A gaseous transport media or a gas mixture will be supplied to the tribocontact and will form a lubricious substance on the rubbing surfaces by decomposition or reaction. This mechanism can be applied to a wide range of temperature up to the highest temperature and is only effective under dry friction [25 - 27].

Many used substances, which were mixed to the gas, are critical from the ecological and toxic point of view.

In addition, this mechanism requires a supply system and a control device, which adds weight and needs to be refilled. Such a system can only be used in military and space applications.

The volumetric wear coefficient published by E. Klaus et al. [27] for plasma-sprayed ceramic coatings against cast iron with these vapor delivered lubricants was greater than  $10^{-7} \text{ mm}^3/(\text{N}\cdot\text{m})$ . Another principle proposed by J. Lauer et al. [26] is the catalytic decomposition of gaseous hydrocarbons on hot ceramic surfaces to form graphitic lubricants. No wear data from these tests were found in the literature.

## Conclusions

Unlubricated engines can be realized from the tribological point of view, if wear coefficients of sliding couples lower than  $5 \cdot 10^{-8} \text{ mm}^3/\text{N}\cdot\text{m}$  can be demonstrated, which are independent from ambient temperature and sliding speed. Known unlubricated sliding couples with wear coefficients around  $10^{-7} \text{ mm}^3/\text{N}\cdot\text{m}$  opens the frame to built up such engines for basic studies. To further improved the wear resistance, different dry lubricating mechanisms must be checked with respect to the required life-time, the allowable costs and operating conditions as well as the customer needs. In any case, the outstanding wear resistance of some materials can be used to increase the operation time of oils. An energy efficient engine, with less frictional power losses, will only be able to be realized, from the point of state-of-the-art of today with tribosystems, where the surfaces are separate through a liquid film.

## LITERATURE

- [1] N.N.: A review of the state of the art and projected technology of low heat rejection engines. National Academy Press, Washington, D. C. 1987
- [2] R. Kamo: Ceramic engines and their cost effectiveness. *Ceramica Acta*, Vol. 3, No. 1, 1991, pp. 49-65
- [3] H. Kawamura and H. Matsuoka: Low heat rejection engine with thermos structure. SAE paper 950978
- [4] P. Greiner: Entwicklung von Motoren und Apparaten mit keramischen Bauteilen. International Congress High-Tec-Materials and Finishing, march 1989, Berlin  
Publisher: Praxis-Forum TCI, 14089 Berlin, Germany
- [5] A. Tanaka: New types engines and their tribological assignments. Proc. of the Int. Tribology Conference, Nagoya, Japan, 1990, P. 1339
- [6] H. Kita, H. Kawamura, Y. Unno and S. Sekiyama: Low frictional ceramic materials. SAE paper 950981
- [7] R. Kamo and W. Bryzik: High temperature lubrication of adiabatic engine. Synopses 3S1-7, International Tribology Conference, November 1995, Yokohama
- [8] M. Woydt and K.-H. Habig: Tribological criteria and assessments for the life of unlubricated engines. *Lubrication Engineering*, 1994, July, Vol. 50, No 7, p. 519-522
- [9] Schadstoffemission leichte Kraftwagen, PkW, Stufe 2.

70/220/EWG, EG-Amtsblatt Nr. L 100 vom 19.04.1994

- [10] N.N.: Committee of experts for environmental questions „Waste Management“. Special expertise, September 1990, ISBN 3-8246-0073-0, Metzler-Poeschel-Verlag Stuttgart, Germany
- [11] Verordnung über das Einsammeln und Befördern sowie über die Überwachung von Abfällen und Reststoffen (AbfResÜberV) vom 03.04.1990
- [12] Rückstand- und Abfallwirtschaftsgesetz vom 06.10.1994, Bundesgesetzblatt (BGBl. I. S. 2705).
- [13] W. Platzer: Auswirkungen zukünftiger Emissionsvorschriften für NFZ-Dieselmotoren auf die Tribologie im Motor.  
Congress „Tribotechnische Werkstoffe im Kraftfahrzeug“, April 1990, Bad Nauheim; Praxis-Forum, Ritterfelddamm 82 h+i, D-14089 Berlin, Germany
- [14] „Tribocollect - A numerical, tribological database for materials, coatings and lubricants“. BAM, Dept. VIII.1, Unter den Eichen 87, 12200 Berlin, Germany
- [15] J.-M. Martin, C. Donnet, T. Le Mogne and M. Belin: How to reduce friction coefficients in the millirange by solid lubrication  
Proc. of the Int. Tribology Conference, 29.10 - 03.11.1995, Yokohama, Japan
- [16] M.N. Gardos: The effect of anion vacancies on the tribological properties of rutile.  
Tribol. Trans. 32 (1988), pp. 427-436
- [17] M. Woydt, J. Kadoori, H. Hausner and K.-H. Habig: Werkstoffentwicklung an Ingenieurkeramik nach tribologischen Gesichtspunkten.  
Cf/Ber. Dt. keram. Gesellschaft, Vol. 67, 1990, No. 4, p. 123-130
- [18] M. Woydt and A. Skopp: Ceramic and ceramic composite materials with improved friction and wear properties, Tribology Transactions, Vol. 38, 1995, No. 2, p. 233-242
- [19] R. Wäsche and K.-H. Habig: Physikalisch-chemische Grundlagen der Feststoffschmierung.  
BAM-Forschungsbericht 158, April 1989, ISBN 3-88314-889-x
- [20] R. Brückner, T. Klug, A. Skopp and M. Woydt: Festkörpergleitreibung und -verschleiß von keramikfaserverstärkten Glas-komposites gegen Ingenieurkeramik.  
BMFT-project contact 03M1035; WEAR 1993, Vol. 169, pp. 243-250
- [21] W. Thiele: Tribologisches Verhalten von Kohlegraphit  
Company paper, SGL Carbon GmbH, Werk Ringsdorff, Drachenburgstr. 1, D-53170 Bonn, Germany, 1993
- [22] E. Minford and K. Prewo „Friction and Wear of Graphite Fiber-Reinforced Glass Matrix Composites, „Wear. 102, pp. 253-264, (1985)
- [23] P. Greiner: „Use of Ceramic Parts of SiSiC and Carbon for Engines and Condensers and

Securing of Function in Long-Time Tests.“ Annual Report, BMFT, ISSN 0724-1771, (1991)

[24] M. Koch: „Pistons Made of Carbon“, Auto, Motor, Sport, No. 3, pp. 36-38, (1993)

[25] E.E. Klaus, G.S. Jeng and J.L. Duda: A study of tricresyl phosphate as a vapour delivered lubricant.  
Lubrication Engineering, November 1989, pp. 717-723

[26] J.L. Lauer and S.R. Dwyer: Regeneration of solid lubricants by chemical reaction on tribological surfaces.  
Rensselaer Polytechnic Institute, Troy, New York, 12180-3590, USA

[27] M. Groeneweg, G.C. Barber and E. Klaus: Vapor delivered lubrication of diesel engines  
Cylinder Kit Rig Simulation.  
J. of the Soc. f. Tribologists and Lubrication Engineers, Dec. 1991, pp. 1035-1039

n = 3000 rpm; life = 2000 h; 4 cylinder, 2000 ccm							
	Normal force		Sliding speed	Wear volume	Sliding distance	Necessary volumetric wear	
	N		m/s	mm <sup>3</sup>	in 2000 h km	coefficient mm <sup>3</sup> /(N*m)	
	Cycle average	Maximum				Maximum	Minimum
1. Piston ring <sup>2</sup>	283	3956	8	113	57600	$7 * 10^{-9}$	$5 * 10^{-10}$
2. Piston ring <sup>3</sup>	42	593	8	113	57600	$4,7 * 10^{-8}$	$3,3 * 10^{-9}$
Valve guide <sup>1</sup>	700	1000	0,5	67	3600	$2,6 * 10^{-8}$	$1,8 * 10^{-9}$
Cam / follower	1000	3000	2,3	6	16500	$3 * 10^{-10}$	$1,2 * 10^{-10}$
<sup>3)</sup> Gas pressure max. 15 % of 1 <sup>st</sup> piston ring <sup>2)</sup> Bore = 90 mm; stroke = 80 mm; thickness piston ring = 2 mm; wear length radial = 0.200 mm; gas pressure max. = 70 bar <sup>1)</sup> Wear of valve shaft set = 0; shaft diameter = 7 mm; guide length = 30 mm; stroke = 10 mm; wear length radial = 0.100 m							

Table I: Estimation of the volumetric wear coefficient of tribosystems in an oil lubricated international combustion engine

Tribo-oxidative formation of lubricious oxides	Incorporation of intrinsic solid lubricants in a matrix
Incorporation of Ti-compounds, which can form in oxidative environments by tribo-oxidation a thin $\text{TiO}_{2-x}$ layer. The mechanical properties are slightly affected. The wear stock pile is high. Hard substrates achieves the maximum effect.	The incorporated, soft solid lubricant particles weakens the mechanical properties of matrix and disturbs sintering or thermal spraying. The non-oxide phases loses their properties by oxidation. The wear stock pile is high.
TiC, TiN, (Ti, Mo) (C, N)	hex-BN, $\text{MoS}_2$ , $(\text{CF}_x)_n$ , graphite, $\text{WSe}_2$
Transfer film formation	Vapor phase Lubrication
Depending from surface roughness, sliding velocity and normal force, the triboelement forms an adhesive, thin film on the counterpart surface. Any liquid interrupts this mechanism.	Surface active substances can be delivered through a vapor or as vapor and form a film by decomposition on the surface or by reaction with the surface. The mechanism operates effective up to very high temperatures. This technique requires an additional supply system. Many of the known substances are toxic or neurotoxic.
Polymers, glasses, graphite, C- and SiC-fibers	Tricresylphosphate, ethylen, $\text{CO-H}_2$ , phthalocyanin, O-phatolonitril, PFPE, arylphosphate, tricyclophe-phazene.

Table II. Dry lubrication mechanisms for tribosystems operating at high-temperatures

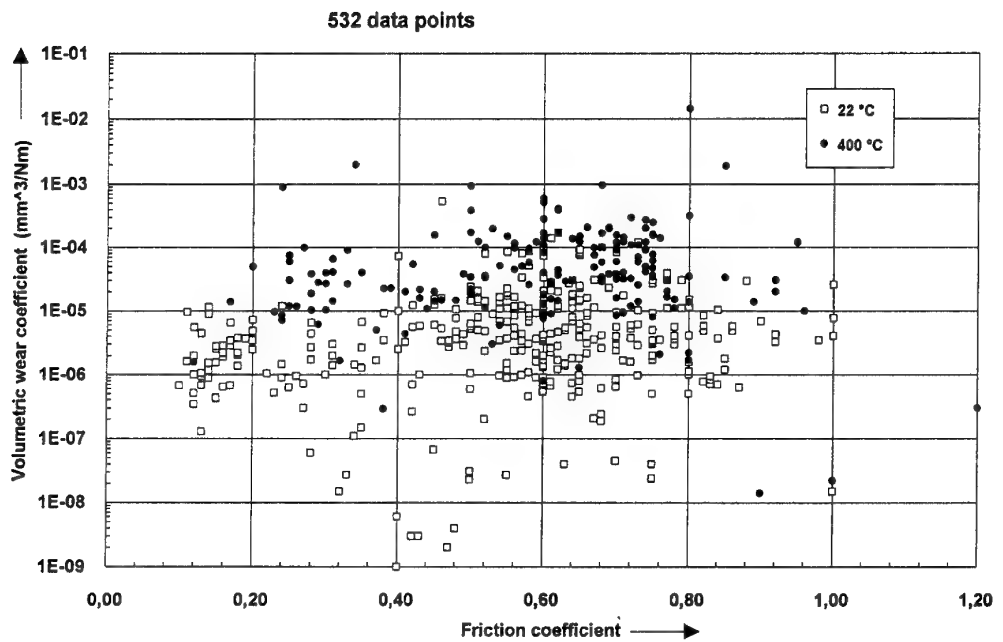


Fig. 1: Plot of volumetric wear coefficient versus solid state friction coefficient of sliding couples found in the tribological data base of BAM

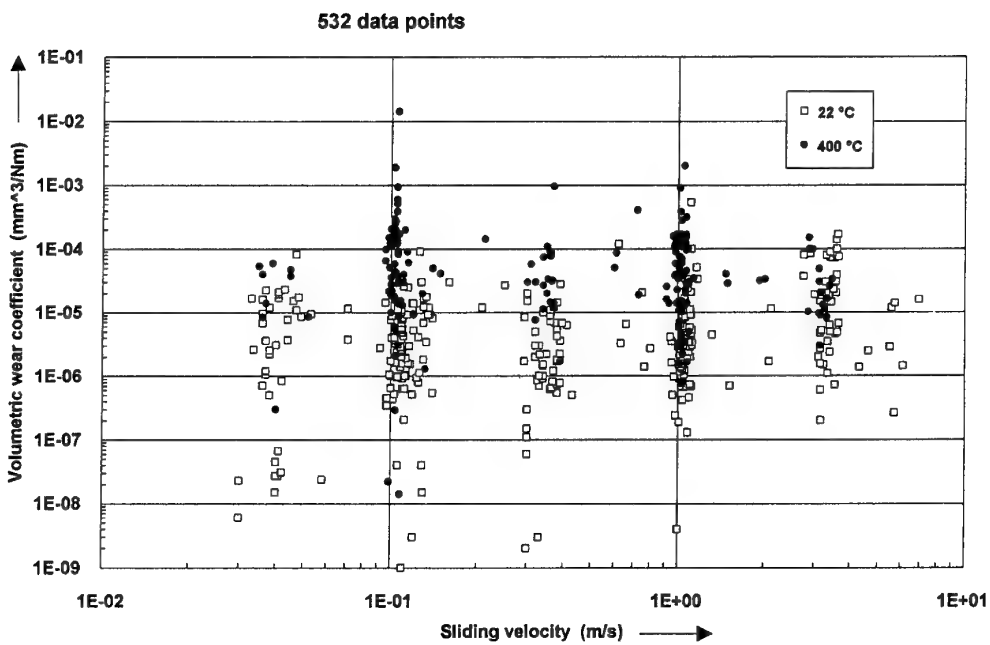


Fig. 2: Plot of volumetric wear coefficient versus sliding speed of couples found in the tribological data base of BAM under solid state friction

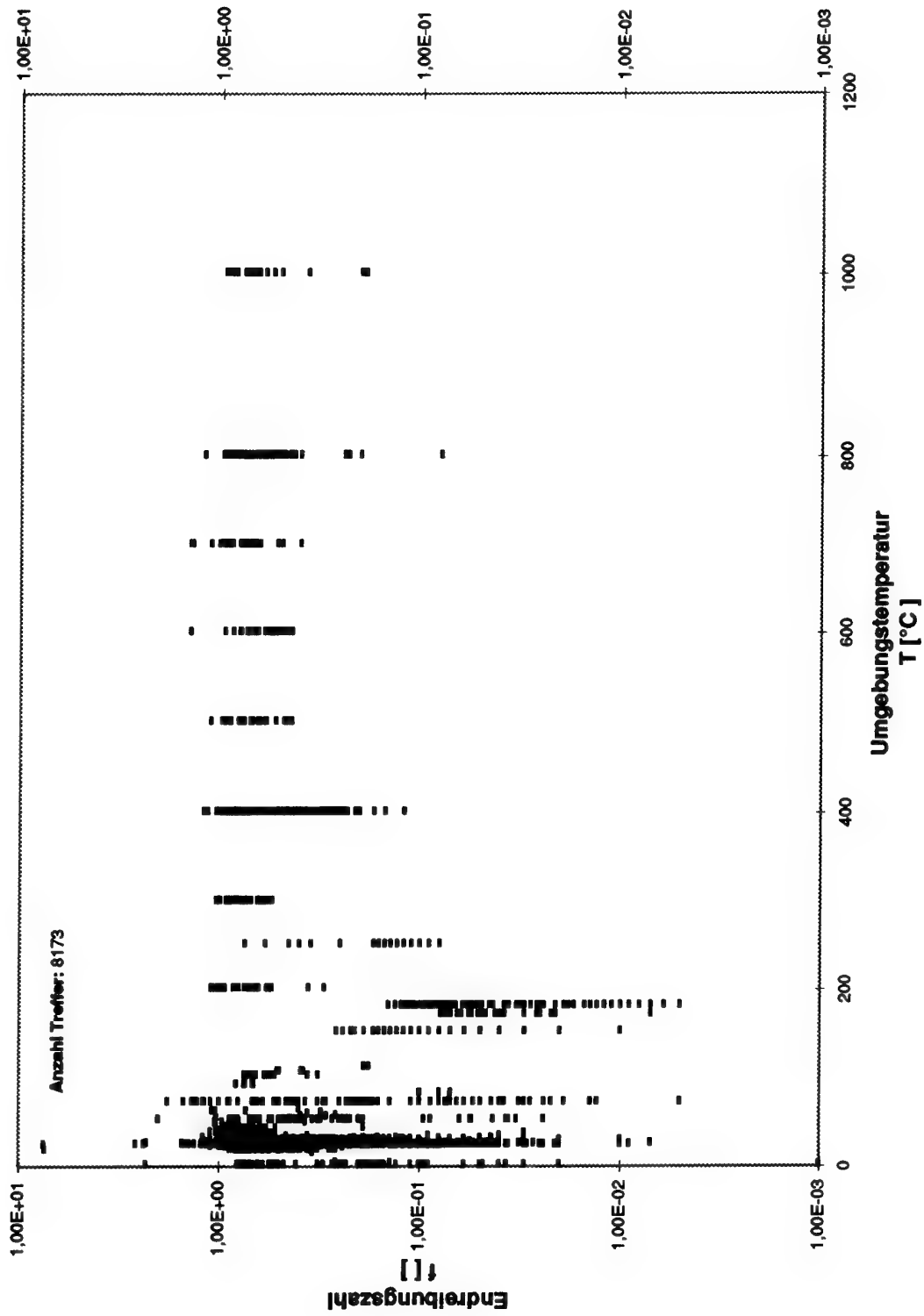


Fig. 3: Plot of coefficient of friction at test and versus ambient temperature from tests according DIN 50 324 found in Tribocollect



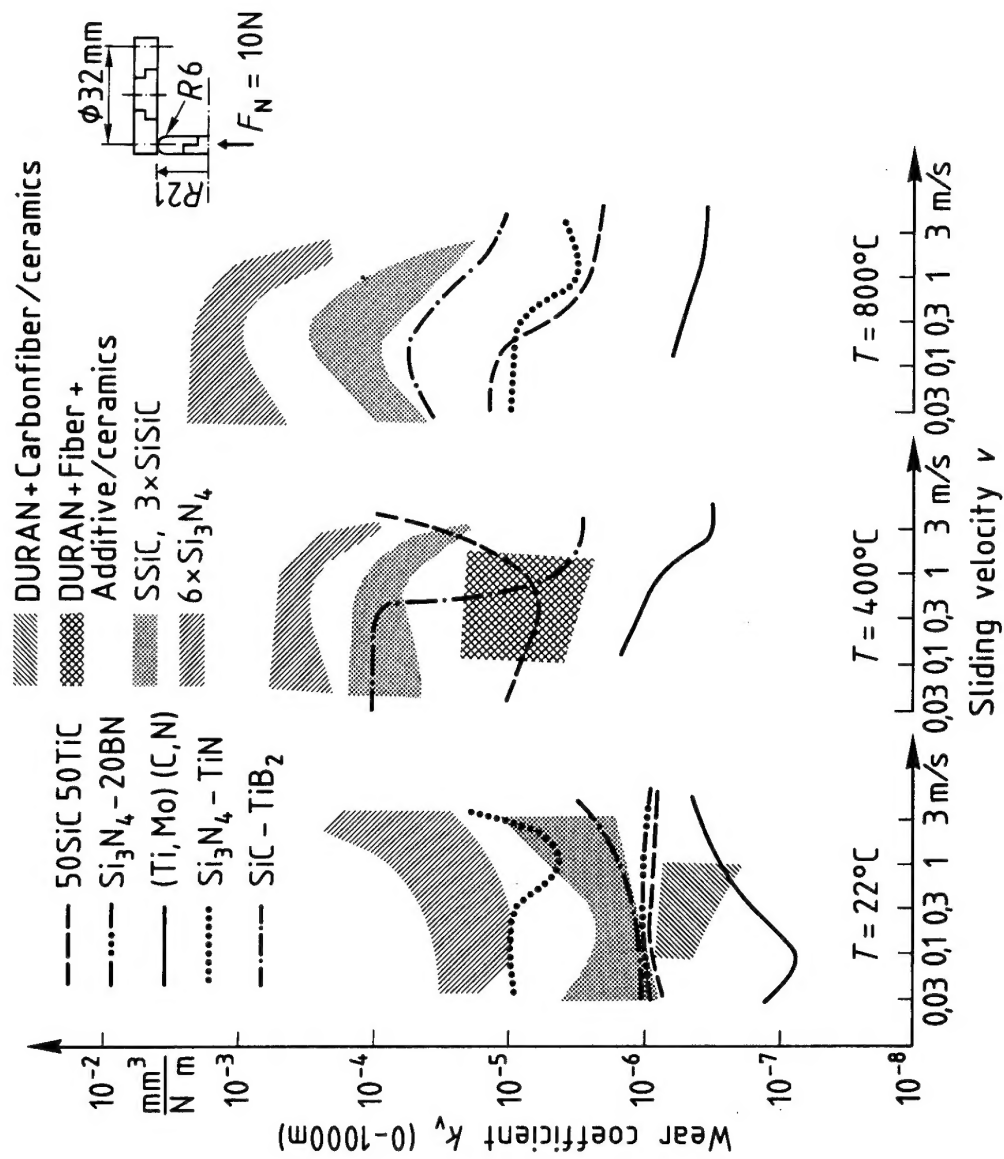


Fig. 5: Total volumetric wear coefficient of self-mated couples under dry friction in tests according to DIN 50324

## REPORT DOCUMENTATION PAGE

<b>1. Recipient's Reference</b>	<b>2. Originator's Reference</b> AGARD-CP-589	<b>3. Further Reference</b> ISBN 92-836-0029-0	<b>4. Security Classification of Document</b> UNCLASSIFIED/ UNLIMITED																
<b>5. Originator</b> Advisory Group for Aerospace Research and Development North Atlantic Treaty Organization 7 rue Ancelle, 92200 Neuilly-sur-Seine, France																			
<b>6. Title</b> Tribology for Aerospace Systems																			
<b>7. Presented at/sponsored by</b> The 82nd Meeting of the AGARD SMP, held in Sesimbra, Portugal, from 6-7 May 1996.																			
<b>8. Author(s)/Editor(s)</b> Multiple			<b>9. Date</b> October 1996																
<b>10. Author's/Editor's Address</b> Multiple			<b>11. Pages</b> 198																
<b>12. Distribution Statement</b> There are no restrictions on the distribution of this document. Information about the availability of this and other AGARD unclassified publications is given on the back cover.																			
<b>13. Keywords/Descriptors</b> <table><tr><td>Tribology</td><td>Bearings</td></tr><tr><td>Technology</td><td>Gears</td></tr><tr><td>Design</td><td>Maintenance</td></tr><tr><td>Friction</td><td>Fatigue (materials)</td></tr><tr><td>Wear</td><td>Coatings</td></tr><tr><td>Lubrication</td><td>Interactions</td></tr><tr><td>Engines</td><td>NATO</td></tr><tr><td>Airframes</td><td></td></tr></table>				Tribology	Bearings	Technology	Gears	Design	Maintenance	Friction	Fatigue (materials)	Wear	Coatings	Lubrication	Interactions	Engines	NATO	Airframes	
Tribology	Bearings																		
Technology	Gears																		
Design	Maintenance																		
Friction	Fatigue (materials)																		
Wear	Coatings																		
Lubrication	Interactions																		
Engines	NATO																		
Airframes																			
<b>14. Abstract</b> <p>Fretting and wear of hinges, tracks, bearings, gearboxes in airframes and engines is a constant problem for aircraft or other defense systems, as they induce failures and jamming, necessitating costly in-service inspections and replacement of parts.</p> <p>At the 82nd Meeting of the AGARD Structures and Materials Panel a Specialist's Meeting was held on Tribology for Aerospace Systems.</p> <p>The meeting was split into three sessions (18 papers):</p> <ul style="list-style-type: none"><li>— new technologies such as coatings, new materials, lubrication and their behaviour;</li><li>— practical applications in airframes and their mechanical systems;</li><li>— practical applications to engines, both jet engines and reciprocal engines.</li></ul> <p>The meeting was ended by a round table discussion.</p>																			

Aucun stock de publications n'a existé à AGARD. A partir de 1993, AGARD détiendra un stock limité des publications associées aux cycles de conférences et cours spéciaux ainsi que les AGARDographies et les rapports des groupes de travail, organisés et publiés à partir de 1993 inclus. Les demandes de renseignements doivent être adressées à AGARD par lettre ou par fax à l'adresse indiquée ci-dessus. *Veuillez ne pas téléphoner.* La diffusion initiale de toutes les publications de l'AGARD est effectuée auprès des pays membres de l'OTAN par l'intermédiaire des centres de distribution nationaux indiqués ci-dessous. Des exemplaires supplémentaires peuvent parfois être obtenus auprès de ces centres (à l'exception des Etats-Unis). Si vous souhaitez recevoir toutes les publications de l'AGARD, ou simplement celles qui concernent certains Panels, vous pouvez demander à être inclu sur la liste d'envoi de l'un de ces centres. Les publications de l'AGARD sont en vente auprès des agences indiquées ci-dessous, sous forme de photocopie ou de microfiche.

CENTRES DE DIFFUSION NATIONAUX

## ALLEMAGNE

Fachinformationszentrum Karlsruhe  
D-76344 Eggenstein-Leopoldshafen 2

## BELGIQUE

Coordonnateur AGARD-VSL  
Etat-major de la Force aérienne  
Quartier Reine Elisabeth  
Rue d'Evere, 1140 Bruxelles

## CANADA

Directeur, Services d'information scientifique  
Ministère de la Défense nationale  
Ottawa, Ontario K1A 0K2

## DANEMARK

Danish Defence Research Establishment  
Ryvangs Allé 1  
P.O. Box 2715  
DK-2100 Copenhagen Ø

## ESPAGNE

INTA (AGARD Publications)  
Carretera de Torrejón a Ajalvir, Pk.4  
28850 Torrejón de Ardoz - Madrid

## ETATS-UNIS

NASA Goddard Space Flight Center  
Code 230  
Greenbelt, Maryland 20771

## FRANCE

O.N.E.R.A. (Direction)  
29, Avenue de la Division Leclerc  
92322 Châtillon Cedex

## GRECE

Hellenic Air Force  
Air War College  
Scientific and Technical Library  
Dekelia Air Force Base  
Dekelia, Athens TGA 1010

## ISLANDE

Director of Aviation  
c/o Flugrad  
Reykjavik

## ITALIE

Aeronautica Militare  
Ufficio del Delegato Nazionale all'AGARD  
Aeroporto Pratica di Mare  
00040 Pomezia (Roma)

## LUXEMBOURG

Voir Belgique

## NORVEGE

Norwegian Defence Research Establishment  
Attn: Biblioteket  
P.O. Box 25  
N-2007 Kjeller

## PAYS-BAS

Netherlands Delegation to AGARD  
National Aerospace Laboratory NLR  
P.O. Box 90502  
1006 BM Amsterdam

## PORTUGAL

Estado Maior da Força Aérea  
SDFA - Centro de Documentação  
Alfragide  
2700 Amadora

## ROYAUME-UNI

Defence Research Information Centre  
Kentigern House  
65 Brown Street  
Glasgow G2 8EX

## TURQUIE

Millî Savunma Başkanlığı (MSB)  
ARGE Dairesi Başkanlığı (MSB)  
06650 Bakanlıklar-Ankara

**Le centre de distribution national des Etats-Unis ne détient PAS de stocks des publications de l'AGARD.**

D'éventuelles demandes de photocopies doivent être formulées directement auprès du NASA Center for AeroSpace Information (CASI) à l'adresse ci-dessous. Toute notification de changement d'adresse doit être fait également auprès de CASI.

AGENCES DE VENTE

NASA Center for AeroSpace Information  
(CASI)  
800 Elkridge Landing Road  
Linthicum Heights, MD 21090-2934  
Etats-Unis

The British Library  
Document Supply Division  
Boston Spa, Wetherby  
West Yorkshire LS23 7BQ  
Royaume-Uni

Les demandes de microfiches ou de photocopies de documents AGARD (y compris les demandes faites auprès du CASI) doivent comporter la dénomination AGARD, ainsi que le numéro de série d'AGARD (par exemple AGARD-AG-315). Des informations analogues, telles que le titre et la date de publication sont souhaitables. Veuillez noter qu'il y a lieu de spécifier AGARD-R-nnn et AGARD-AR-nnn lors de la commande des rapports AGARD et des rapports consultatifs AGARD respectivement. Des références bibliographiques complètes ainsi que des résumés des publications AGARD figurent dans les journaux suivants:

Scientific and Technical Aerospace Reports (STAR)  
publié par la NASA Scientific and Technical  
Information Division  
NASA Langley Research Center  
Hampton, Virginia 23681-0001  
Etats-Unis

Government Reports Announcements and Index (GRA&I)  
publié par le National Technical Information Service  
Springfield  
Virginia 22161  
Etats-Unis  
(accessible également en mode interactif dans la base de données bibliographiques en ligne du NTIS, et sur CD-ROM)



AGARD holds limited quantities of the publications that accompanied Lecture Series and Special Courses held in 1993 or later, and of AGARDographs and Working Group reports published from 1993 onward. For details, write or send a telefax to the address given above. *Please do not telephone.*

AGARD does not hold stocks of publications that accompanied earlier Lecture Series or Courses or of any other publications. Initial distribution of all AGARD publications is made to NATO nations through the National Distribution Centres listed below. Further copies are sometimes available from these centres (except in the United States). If you have a need to receive all AGARD publications, or just those relating to one or more specific AGARD Panels, they may be willing to include you (or your organisation) on their distribution list. AGARD publications may be purchased from the Sales Agencies listed below, in photocopy or microfiche form.

NATIONAL DISTRIBUTION CENTRES**BELGIUM**

Coordonnateur AGARD — VSL  
Etat-major de la Force aérienne  
Quartier Reine Elisabeth  
Rue d'Evere, 1140 Bruxelles

**CANADA**

Director Scientific Information Services  
Dept of National Defence  
Ottawa, Ontario K1A 0K2

**DENMARK**

Danish Defence Research Establishment  
Ryvangs Allé 1  
P.O. Box 2715  
DK-2100 Copenhagen Ø

**FRANCE**

O.N.E.R.A. (Direction)  
29 Avenue de la Division Leclerc  
92322 Châtillon Cedex

**GERMANY**

Fachinformationszentrum Karlsruhe  
D-76344 Eggenstein-Leopoldshafen 2

**GREECE**

Hellenic Air Force  
Air War College  
Scientific and Technical Library  
Dekelia Air Force Base  
Dekelia, Athens TGA 1010

**ICELAND**

Director of Aviation  
c/o Flugrad  
Reykjavik

**ITALY**

Aeronautica Militare  
Ufficio del Delegato Nazionale all'AGARD  
Aeroporto Pratica di Mare  
00040 Pomezia (Roma)

**LUXEMBOURG**

See Belgium

**NETHERLANDS**

Netherlands Delegation to AGARD  
National Aerospace Laboratory, NLR  
P.O. Box 90502  
1006 BM Amsterdam

**NORWAY**

Norwegian Defence Research Establishment  
Attn: Biblioteket  
P.O. Box 25  
N-2007 Kjeller

**PORTUGAL**

Estado Maior da Força Aérea  
SDFA - Centro de Documentação  
Alfragide  
2700 Amadora

**SPAIN**

INTA (AGARD Publications)  
Carretera de Torrejón a Ajalvir, Pk.4  
28850 Torrejón de Ardoz - Madrid

**TURKEY**

Millî Savunma Başkanlığı (MSB)  
ARGE Dairesi Başkanlığı (MSB)  
06650 Bakanlıklar-Ankara

**UNITED KINGDOM**

Defence Research Information Centre  
Kentigern House  
65 Brown Street  
Glasgow G2 8EX

**UNITED STATES**

NASA Goddard Space Flight Center  
Code 230  
Greenbelt, Maryland 20771

**The United States National Distribution Centre does NOT hold stocks of AGARD publications.**

Applications for copies should be made direct to the NASA Center for AeroSpace Information (CASI) at the address below.

Change of address requests should also go to CASI.

SALES AGENCIES

NASA Center for AeroSpace Information  
(CASI)  
800 Elkridge Landing Road  
Linthicum Heights, MD 21090-2934  
United States

The British Library  
Document Supply Centre  
Boston Spa, Wetherby  
West Yorkshire LS23 7BQ  
United Kingdom

Requests for microfiches or photocopies of AGARD documents (including requests to CASI) should include the word 'AGARD' and the AGARD serial number (for example AGARD-AG-315). Collateral information such as title and publication date is desirable. Note that AGARD Reports and Advisory Reports should be specified as AGARD-R-nnn and AGARD-AR-nnn, respectively. Full bibliographical references and abstracts of AGARD publications are given in the following journals:

Scientific and Technical Aerospace Reports (STAR)  
published by NASA Scientific and Technical  
Information Division  
NASA Langley Research Center  
Hampton, Virginia 23681-0001  
United States

Government Reports Announcements and Index (GRA&I)  
published by the National Technical Information Service  
Springfield  
Virginia 22161  
United States  
(also available online in the NTIS Bibliographic  
Database or on CD-ROM)

